

Northumbria Research Link

Citation: Hajirasouliha, Farzaneh (2022) Nanosized pollutants at the air-liquid interface under dynamic conditions: interfacial tension and rheology. Doctoral thesis, Northumbria University.

This version was downloaded from Northumbria Research Link:
<https://nrl.northumbria.ac.uk/id/eprint/51662/>

Northumbria University has developed Northumbria Research Link (NRL) to enable users to access the University's research output. Copyright © and moral rights for items on NRL are retained by the individual author(s) and/or other copyright owners. Single copies of full items can be reproduced, displayed or performed, and given to third parties in any format or medium for personal research or study, educational, or not-for-profit purposes without prior permission or charge, provided the authors, title and full bibliographic details are given, as well as a hyperlink and/or URL to the original metadata page. The content must not be changed in any way. Full items must not be sold commercially in any format or medium without formal permission of the copyright holder. The full policy is available online: <http://nrl.northumbria.ac.uk/policies.html>



**Northumbria
University**
NEWCASTLE

**Nanosized Pollutants at the Air-
Liquid Interface under Dynamic
Conditions: Interfacial Tension and
Rheology**

Farzaneh Hajirasouliha

PhD

2022

Nanosized Pollutants at the Air-Liquid Interface under Dynamic Conditions: Interfacial Tension and Rheology

Farzaneh Hajirasouliha

A thesis submitted in partial fulfilment of the requirements of the University of Northumbria at Newcastle for the degree of Doctor of Philosophy

Faculty of Engineering and Environment

July 2022

Abstract

Human health has been adversely affected by air pollution. Ambient (outdoor) air pollution causes 4.2 million deaths every year. Moreover, each year, 3.8 million people die from indoor air pollution. Air pollution is considered as a silent killer which threatens human lives around the world by its invisible weapons called air particulate matter. Among the various air particulate matter, nano-sized pollutants with diverse qualities can easily enter the respiratory system of the human and cause respiratory diseases. They can also penetrate the blood circulation and affect other organs such as liver, kidneys, and spleen. Understanding the mechanism of interactions of nanoparticles with pulmonary surfactant is crucial to predict the fate of nanoparticles based on their characteristics such as concentration, size, shape, hydrophilicity/hydrophobicity, and surface charge.

This thesis has explored these mechanisms of interactions between a single-component model of pulmonary surfactant, i.e., Dipalmitoylphosphatidylcholine, and three types of nanoparticles (i.e., anatase form of titanium dioxide, rutile form of titanium dioxide, and carbon nanotube) with different surface properties. To establish a reasonable understanding of the systems containing surfactants and nanoparticles, this research starts with investigating the systems containing nanosized pollutants in contact with the industrial surfactants applicable in many fields such as formulations of detergents, foams, and emulsions. Accordingly, the interactions of single-type nanoparticles with different types of surfactants including the industrial surfactants (Cetyltrimethylammonium Bromide and Sodium Dodecyl Sulfate) and a model of pulmonary surfactant have been investigated and the mechanisms of the interactions have been proposed.

For the industrial surfactants such as CTAB and SDS, their types and concentrations affect their interactions with nanoparticles such as titanium dioxide. In case of the model of pulmonary surfactant, i.e., DPPC, different surface properties of nanoparticles result in various types of interactions between DPPC and nanoparticles. The interactions between DPPC and titanium dioxide nanoparticles are affected by the crystal form and concentration of nanoparticles. At the similar concentration of nanoparticles, different crystal forms of titanium dioxide, i.e., anatase and rutile, show

different interfacial tension and zeta potential values in the solutions with constant concentration of DPPC. It means that these two crystal forms of the same chemical formula result in different interfacial properties of the air-liquid interface and various types of interactions with DPPC molecules. These results related to industrial surfactants are useful for industrial applications. Moreover, the findings about the nanosized pollutants and pulmonary surfactant are clear evidence about the effects of nanomaterials on the interfacial behaviour of the pulmonary surfactant. The different concentrations of nanoparticles used in this study are the representative of the time of the exposure to nano-pollutants. These results combined with toxicity studies are helpful in revising the environmental regulations. Moreover, the outcomes about the interactions between pulmonary surfactant and nanoparticles can be used in the applications such as drug delivery to lungs.

This thesis has also established and developed a robust systematic method of measuring the physicochemical effects of the mixtures of nanoparticles on DPPC as a model of pulmonary surfactant. This innovative approach simulates the real conditions when a mixture of nanosized pollutants reach the lungs. The composition of the mixture and the mixing method are the factors that affect the behaviour of these mixture of nanoparticles in contact with DPPC. The stability of the colloidal phase and the interfacial tension of the air-liquid interface for the mixture of nanoparticles interacting with DPPC depends on the composition of the mixture and the mixing method. The results of this part of study related to the mixture of nanoparticles has identified which nanoparticles can have the most dominant effect in interactions with pulmonary surfactant.

Finally, this thesis has used a nonlinear interfacial rheology approach as a complementary tool to understand the microstructures of the pulmonary surfactant-nanoparticles at the air-liquid interface under dynamic conditions such as the breathing cycles. All types of nanoparticles affect the interfacial performance of DPPC as a model of pulmonary surfactant. However, based on the surface properties of nanoparticles, their effect on the interfacial properties of DPPC under dynamic conditions are different. For nanoparticles with the same size and chemical formula, the shape and surface charge are the most important surface properties affecting the interfacial behaviours.

Table of Contents

Abstract	iii
Table of Contents.....	v
Acknowledgements.....	viii
Declaration	ix
List of Abbreviations and Terms	x
List of Symbols.....	xii
List of Figures.....	xv
List of Tables.....	xxv
Publications	xxvi
1 Introduction and Scope of the Thesis	1
1.1 Research Motivation	1
1.2 Research Aims and Objectives	5
1.3 Distinctiveness and Novelty of the Thesis	8
1.4 Outline of the Thesis	10
2 Literature Review	13
2.1 Introduction	13
2.2 Air pollution	14
2.3 Nano-Pollutants	15
2.4 Effects of Air pollution on Human Health	15
2.5 Air Pollution and Human Respiratory System	17
2.5.1 Anatomy of Respiratory System.....	17
2.5.2 Deposition of Air Particulate Matter and Nano-Pollutants in Respiratory System.....	19
2.5.3 Stability of Alveolar Region.....	20
2.5.4 Pulmonary Surfactant: Composition and Function.....	21
2.5.5 Proposed Model of Pulmonary Surfactant: DPPC.....	22
2.6 Effects of Nanoscale Materials/Pollutants on the Interfacial Properties of the Systems of Pulmonary Surfactant and Industrial Surfactants.....	24
2.6.1 Surface Charge.....	25
2.6.2 Hydrophilicity/Hydrophobicity.....	26
2.6.3 Size.....	28
2.6.4 Concentration.....	28
2.6.5 Shape	29
2.7 Pulmonary Surfactant under Dynamic Conditions	30
2.7.1 Dynamic Conditions versus Static Assumptions	31
2.7.2 Mixture of Nanoparticles versus Single-Type Nanoparticles.....	32
2.7.3 Interfacial Rheology: A Potential Method for Investigation of Pulmonary Surfactant under Real Conditions.....	34
2.8 Summary	36
3 Experimental Work and Analytical Methods.....	38
3.1 Preparation of Solutions / Dispersions.....	38
3.1.1 Solutions of Ionic Surfactants.....	38

3.1.2	Dispersions of Nanoparticles in Ionic Surfactants	39
3.1.3	Solutions of DPPC as a Single-Component Model of Lung Surfactant ..	40
3.1.4	Dispersions of Nanoparticles in DPPC Solutions	44
3.2	Characterisation of Nanoparticles.....	46
3.2.1	Dried Nanoparticles.....	47
3.2.2	Bulk Characterisation_Surface Charge of Nanoparticles.....	48
3.2.3	Hydrophilicity/Hydrophobicity of Nanoparticles	48
3.3	Preparation and Characterisation of Foams.....	53
3.4	Nanoparticles-DPPC Interactions	54
3.4.1	Adsorption of DPPC onto the Surface of Nanoparticles	54
3.4.2	Surface Charge of the Nanoparticles Interacted with DPPC.....	55
3.5	Dynamic Interfacial Tension Measurement	55
3.5.1	Profile Analysis Tensiometer (PAT).....	56
3.5.2	Method of Analysis	60
3.5.3	Limitations of Profile Analysis Tensiometer (PAT).....	64
3.6	Spectrum Width Measurement	66
3.7	Interfacial Rheology Measurement.....	67
3.7.1	Design of Experiments based on Breathing Patterns (Amplitude and Frequency)	71
3.7.2	Methods of Analysis.....	73
4	Surface Properties of the Agglomerates of Nano-Pollutants	74
4.1	Results and Discussion.....	75
4.1.1	Shapes of Nanoparticles and Agglomerates	75
4.1.2	Surface Charge.....	85
4.1.3	Hydrophilicity/Hydrophobicity.....	87
4.2	Summary	97
5	Nano-Pollutants in Contact with Industrial Surfactants	99
5.1	Results and Discussion.....	100
5.1.1	Adsorption Isotherms and Models	100
5.1.2	Alternative Method of CMC Measurement: Optical Fibre	105
5.1.3	Effects of Nano-Pollutants on the Solutions of Different Industrial Surfactants.....	111
5.2	Summary	124
6	Interactions of Nano-Pollutants with DPPC in the Bulk of Solution and at the Air-Liquid Interface	126
6.1	Results and Discussion.....	127
6.1.1	Adsorption and Structure of DPPC onto the Surface of Nanoparticles .	127
6.1.2	Effects of the Single-Type Nano-Pollutants on the DPPC.....	136
6.1.3	Effects of the Mixture of Nano-Pollutants on the DPPC	145
6.2	Summary	170
7	Dynamic Responses of DPPC Monolayers to Nano-Pollutants Impact Studied using Interfacial Rheology	173
7.1	Results and Discussion.....	174
7.1.1	Linear (Traditional) Approach: Fourier Analysis	175
7.1.2	Total Harmonic Distortion (THD) Measurement	191
7.1.3	Interfacial Rheology of Nanoparticles-DPPC Systems: Non-Linear Approach.....	194
7.1.4	Interfacial Rheology of DPPC Solution without Nanoparticles	199

7.1.5 Mechanism of the Interactions between Nanoparticles and DPPC under Sinusoidal Perturbations	207
7.2 Summary	221
8 Conclusions and Future Work.....	224
8.1 Conclusions	224
8.2 Future Work.....	232
References	235
Appendix A: Data related to Chapter 6.....	258
Appendix B: MATLAB Codes.....	261
Appendix C: Data related to Chapter 7	262
Appendix D: Published Work	303

Acknowledgements

First, I would like to thank my principal supervisor, Dr. Dominika Zabiegaj, and co-supervisors, Dr. Michael Deary and Professor Richard Fu, for their guidance and support throughout this project. If there has been any personal and professional development during this PhD journey, I owe it to my supervision team.

For an experimental researcher, working in the laboratories is a significant part which cannot be done without the support of technical staff. I appreciate all the support and patience of technical staff at Northumbria University, Rebecca Payne, Gavin Warburton, Dr. Pietro Maiello, Matthew Torelli Moynihan, and Stephen Reed.

I am very grateful because I have had the pleasure of working with staff, academics, and fellow PhD students at Northumbria University.

I would like to thank Dr. Kristina Cabanova and Professor Daniela Placha from Centre of Advanced Innovation Technologies and Nanotechnology Centre, VŠB - Technical University of Ostrava, Ostrava, Czech Republic for their collaboration and permission for using their equipment.

I would like to thank Northumbria University for this amazing PhD opportunity and funding this PhD studentship.

I want to thank my best friends - Faezeh Tarassoli, Faeze Fayyazi, David - and my cousin - Masoumeh Nourollah - for their consistent support even from a very long distance.

I also want to thank three deceased members of my family - my uncle, grandmother, and grandfather – who supported me during the first two years of this journey. If it was not for their pure love, I would not be able to overcome the difficulties especially arisen from their loss.

Last, but definitely not least, I would love to thank my parents and younger brother who have always been there for me and inspired me to get stronger. I owe them my whole life including my PhD. I could not have done it without their emotional and mental support. So, I want to dedicate this work to my beloved family, Mohsen, Azita, and Mohammad Javad.

Declaration

I declare that the work contained in this thesis has not been submitted for any other award and that it is all my own work. I also confirm that this work fully acknowledges opinions, ideas and contributions from the work of others.

Any ethical clearance for the research presented in this thesis has been approved. Approval has been sought and granted by the University Ethics Committee on 27/10/2019.

I declare that the Word Count of this thesis is 46,929 words.

Name: Farzaneh Hajirasouliha

Date: 28/07/2022

List of Abbreviations and Terms

PM	Particulate Matter
GBD	Global Burden of Diseases
CNS	Central Nervous System
ADHD	Deficit Hyperactivity Disorder
COPD	Chronic Obstructive Pulmonary Diseases
SP	Surfactant Protein
DPPC	Dipalmitoylphosphatidylcholine
CGMD	Coarse-Grained Molecular Dynamics
CTAB	Cetyltrimethylammonium Bromide
SDS	Sodium Dodecyl Sulfate
TiO ₂	Titanium Dioxide; Titanium (IV) Oxide
DI Water	Deionised Water
OD	Outside Diameter
ATD	Anatase form of Titanium Dioxide (TiO ₂)
RTD	Rutile form of Titanium Dioxide (TiO ₂)
CNT	Carbon Nanotube
IPA	Isopropyl Alcohol, Isopropanol
SEM	Scanning Electron Microscope
GTT	Gel Trapping Technique
PDMS	Polydimethylsiloxane
EDTA	Ethylenediamine Tetraacetic Acid
AFM	Atomic Force Microscopy
NMR	Nuclear Magnetic Resonance
PAT	Profile Analysis Tensiometer
ADSA	Axisymmetric Drop Shape Analysis
CCD Camera	Charge-Coupled Device Camera
R-squared	Coefficient of Determination

CMC	Critical Micelle Concentration
PTFE	Polytetrafluoroethylene
SNCS	Single mode-No Core-Single mode
SLD	Super Luminescent Diode
OSA	Optical Spectrum Analyser
THD	Total Harmonic Distortion
TEM	Transmission Electron Microscopy (TEM)
CPP	Critical Packing Parameter
DLS	Dynamic Light Scattering
EDX	Energy Dispersive X-Ray Analysis
XPS	X-ray Photoelectron Spectroscopy
SSE	Sum of Squares due to Error
RMSE	Root Mean Square Error
SST	Total Sum of Squares
DFT	Discrete Fourier Transform
SD	Standard Deviation
ANOVA	Analysis of Variance
ARDS	Acute Respiratory Distress Syndrome

List of Symbols

mm	Millimetre (Length Unit)
m ²	Square Metre (Surface area unit)
μm	Micrometre (Length Unit)
γ	Surface Tension; Interfacial Tension
A	Surface Area
Hz	Hertz (Frequency Unit)
g/mol	Gram per Mole (Molecular Weight Unit)
MΩ.cm	Megaohms-cm (Resistivity Unit)
°C	Degree Celsius; Degree Centigrade (Temperature Unit)
mN.m ⁻¹	Millinewtons per Meter (Surface/Interfacial Tension Unit)
M	Molar Concentration; Molarity (Concentration Unit)
nm	Nanometre
m ² /g	Square metre per Gram (Specific Surface Area Unit)
wt %	Weight Percent
mg/ml	Milligram per Millilitre (Concentration Unit)
mg/L	Milligram per Litre (Concentration Unit)
μL	Microlitre
v/v	Volume/Volume Percentage
MHz	Megahertz
Δp	Pressure Difference across the Interfacial Layer
R_1, R_2	Principal Radii of the Curvature
ϕ	Angle of Tangent to the Profile
S	Arc Length along the Profile
x, z	Coordinate Axes
b	Radius of the Curvature at the Drop Apex
$\Delta\rho$	Density Difference between the Drop and its Surrounding Medium
g	Gravitational Acceleration Constant

S^*	Dimensionless Arc Length
z^*	Dimensionless Vertical Coordinate
x^*	Dimensionless Horizontal Coordinate
$Bo.$	Bond Number; Eötvös Number
mm^3, mm^3	Cubic Millimetre (Volume Unit)
g/cm^3	Gram per Cubic Centimetre (Density Unit)
mm^2	Square Millimetre (Surface Area Unit)
r	Radius of the Sphere
T	Temperature
λ_c	Spectrum Width Centre
s	Second (Time Unit)
t	Real Time
τ	Dummy Time in the Convolution Integral
ε	Interfacial Dilatational Modulus, Complex Viscoelastic Modulus
$\Delta A/A_0$	Relative Surface Area Change
ω	Angular Frequency
ν	Frequency
θ	Phase Difference between $\Delta\gamma$ and ΔA
ε'	Real Part of the Viscoelastic Modulus, Dilatational Surface Elasticity
ε''	Imaginary Part of the Viscoelastic Modulus, Dilatational Surface Viscosity
a	Amplitude
mV	Millivolt
ζ	Zeta Potential
σ_{eff}	Effective Charge Density
c	Ion Concentration (Chapter 4)
N	Avogadro Constant
ε_r	Dielectric Constant
ε_0	Vacuum Permittivity

k_B	Boltzmann's Constant
ζ_{eff}	Effective Zeta Potential of the Agglomerates of Nanoparticles In this equation
p	Porosity
Br^-	Bromide Ion
Na^+	Sodium Ion
v	Volume of Hydrocarbon Chain of Lipid
a_0	Surface Area of the Polar Headgroup of Lipid
l_c	Length of Hydrocarbon Chain of Lipid
ppm	Parts per Million
μm^2	Square Micrometre
Al	Aluminium
Na	Sodium
Cu	Copper
Si	Silicon
deg	Degree
dB	Decibel (dB)
π	Surface Pressure
γ_{eq}	Equilibrium Interfacial Tension before Oscillation
S	Strain-Stiffening Ratio
G_L	Large Strain Modulus
G_M	Minimum Strain Modulus
S_{exp}	Strain-Stiffening ratio for Expansion
$E_{L,E}$	Large Strain Modulus in Expansion
$E_{M,E}$	Minimum Strain Modulus in Expansion
S_{com}	Strain-Stiffening ratio for Compression
$E_{L,C}$	Large Strain Modulus in Compression
$E_{M,C}$	Minimum Strain Modulus in Compression

List of Figures

Figure 1.1 Air pollution effects throughout the lifetime [1].....	1
Figure 1.2 Estimations of the global deaths from the air pollution published in recent studies of authentic resources. ‘All sources’ means natural and anthropogenic sources [4].	2
Figure 2.1 Human respiratory system [51]. The alveolar region exists at the end of the branches of the airways [5].....	18
Figure 2.2 Deposition fraction of particles in different regions of the respiratory system according to the particle size. Head, TB, and P are the representatives of extra-thoracic, tracheobronchial, and alveolar regions, respectively. Total means the overall deposition in the three regions [53, 54].	19
Figure 2.3 The structure of alveoli [56]. The tissue barrier consists of two layers of cells: the endothelium layer faces the capillary lumen and the epithelium faces the alveolar lumen [55]. The first barrier that inspired air meets is the alveolar lining fluid called pulmonary surfactant (green layer).....	20
Figure 2.4 Breathing cycle consisting of inspiration and expiration. (a) The plot of surface tension (γ) vs. surface area (A) which shows surface tension hysteresis, and (b) adsorption/desorption of the surfactant at the air-liquid interface [58]. ..	22
Figure 2.5 Chemical structure of DPPC.....	23
Figure 2.6 (a) Positioning of a particle in a fluid-fluid interface according to the contact angle, θ , and (b) change of the hydrophobicity of a negatively charged particle due to the interactions with a cationic surfactant [109].....	27
Figure 2.7 Different types of the structure at the air-liquid interface for pure DPPC monolayer (a-c), mixed monolayer of DPPC and hydrophilic silica nanoparticles (d-f), and mixed monolayer of DPPC and hydrophobic silica nanoparticles (g-i) [63].....	27
Figure 2.8 The perturbation of the pulmonary surfactant by hydrophobic particles including (a) cuboid nanoparticles with different lengths and the same width and (b) nanoparticles of various shapes [114].	30
Figure 2.9 Lissajous plot obtained during the amplitude sweep of the air-water interface stabilized by the oligofructose ester with the mono-unsaturated fatty acid <i>cis</i> -9-hexadecenoic acid as the hydrophobic group at 25 °C [20].....	36
Figure 3.1 Molecular structures of (a) CTAB and (b) SDS.	38
Figure 3.2 The deposition of the DPPC from the chloroform solution on the surface of the water droplet [135].....	42
Figure 3.3 The specific home-made chamber in the tensiometer set-up. The different parts include (a) camera, (b) pendant drop in the chamber, (c) light source, (d) chamber, (e) specific optical glass, and (f) micro-syringe which enters the measurement chamber through the orifice [135].	43

Figure 3.4 Scanning Electron Microscope (SEM) TESCAN, MIRA3.	48
Figure 3.5 Schematic diagram of GTT for (A) air-water and (B) oil-water interfaces [150].	50
Figure 3.6 The upside-down vial containing the gel based on KELCOGEL® F gellan gum. The gel strength and its clarity are visible.	50
Figure 3.7 Samples prepared with Gel Trapping Technique (GTT). Each Petri dish is related to a single type of nanoparticle including ATD, RTD, and CNT.	51
Figure 3.8 Samples of nanoparticles entrapped on the surface of PDMS for SEM imaging in two positions: (a) top view, and (b) side view.	53
Figure 3.9 The deuterated structure of DPPC-d ₆₂ [154].	55
Figure 3.10 The set-up of the PAT1M, SINTERFACE Technologies, Germany.	56
Figure 3.11 A schematic diagram of the profile analysis tensiometer (PAT) set-up.	57
Figure 3.12 Coordinate system for a drop.	58
Figure 3.13 A pendant drop and a family of the theoretical curvatures fitting the experimental points (red points) in the PAT [159].	59
Figure 3.14 An example of typical plot of the dynamic interfacial tension vs. time for the aqueous solution of SDS with the concentration of 1e-5 M at 25 °C.	60
Figure 3.15 Surface tension of water against temperature.	63
Figure 3.16 The set-up for aluminium cell and the optical fibre sensor sunk in the surfactant solution.	67
Figure 3.17 Example of the augmented image of the oscillation at the frequency of 0.1 Hz and amplitude of 1% area deformation. Red and blue dots correspond to the surface area and interfacial tension, respectively.	70
Figure 3.18 Static lung volumes and capacities [170].	72
Figure 4.1 SEM images of ATD after the evaporation of IPA at different resolutions. The dashed square in image (a) has been magnified in image (b).	76
Figure 4.2 SEM images of RTD after the evaporation of IPA at different resolutions. The dashed square in image (a) has been magnified in image (b). These images remind either bi-porous or fractal structures.	77
Figure 4.3 TEM image of RTD nanoparticles provided by the supplier.	78
Figure 4.4 SEM image of CNTs after the evaporation of IPA.	79
Figure 4.5 SEM images of the top view of surface of the PDMS prepared by GTT for the agglomerates of ATD nanoparticles. Both images are related to ATD nanoparticles on the surface of PDMS.	81
Figure 4.6 SEM images of the top view of surface of the PDMS prepared by GTT for the agglomerates of RTD nanoparticles. Both images are related to RTD nanoparticles on the surface of PDMS.	82

Figure 4.7 SEM images of the top view of surface of the PDMS prepared by GTT for (a) ATD and (b) RTD nanoparticles.....	82
Figure 4.8 SEM images of the top view of surface of the PDMS prepared by GTT for an individual CNT particle. Both images are related to CNT particles on the surface of PDMS.....	84
Figure 4.9 SEM images of the top view of surface of the PDMS prepared by GTT for the agglomerates of CNT particles. Both images are related to CNT particles on the surface of PDMS.	85
Figure 4.10 SEM images of the side view of surface of the PDMS prepared by GTT for the agglomerates of ATD nanoparticles when the top surface is observed.	88
Figure 4.11 SEM images of the side view of surface of the PDMS prepared by GTT for the agglomerates of RTD nanoparticles when the top surface is observed. Both images are related to RTD nanoparticles on the surface of PDMS.	88
Figure 4.12 SEM images of the side view of surface of the PDMS prepared by GTT for the agglomerates of CNT particles when (a) the top surface is observed and (b) the tilting angle is -14°	89
Figure 4.13 SEM images of the edge of surface of the PDMS prepared by GTT for the agglomerates of CNT particles when the tilting angle is (a) -7° , (b) 0° , and (c) -7°	91
Figure 4.14 The possible positions of CNT particles or agglomerates at air-water interface. The positions include (a) nanotubes lying down on the plane of interface, (b) nanotubes crossing each other and forming agglomerates, (c) bent nanotubes in the aqueous phase, and (d) nanotubes along the interface with their end sticking to the aqueous phase.....	93
Figure 4.15 Dynamic interfacial tension of the dispersions of nanoparticles with the concentration of 0.01 wt % in DI water at 37°C in log-log coordinates. The dashed line is the representative of the interfacial tension of DI water at 37°C . The hollow purple dots were used for data related to RTD so that the green data points related to ATD can be recognised.	95
Figure 5.1 Equilibrium interfacial tension against concentration of the CTAB in aqueous solutions at 25°C . The standard deviation for each point has been shown on the graph, but it is not clearly visible due to the small amount. The solid line is the best fitted curve of the Frumkin model for the experimental results in this study. Dashed line is the representative of reaching CMC point. The arrow shows the CMC value equal to 1.30×10^{-3} M.	102
Figure 5.2 Equilibrium interfacial tension against concentration of the SDS in aqueous solutions at 25°C . The standard deviation for each point has been shown on the graph, but it is not clearly visible due to the small amount. The solid line is the best fitted curve of the Frumkin model for the experimental results in this study. Dashed line is the representative of reaching CMC point. The arrow shows the CMC value equal to 4.23×10^{-3} M.	103
Figure 5.3 Molecular structure of (a) CTAB and (b) SDS.....	104

Figure 5.4 Schematic diagram of the optical fibre set-up [212].....	105
Figure 5.5 A typical spectrum as the output of the optical spectrum analyser...	106
Figure 5.6 Spectrum width centre against concentration of the CTAB in aqueous solutions at room temperature. The black and red dashed lines are the linear and logarithmic trends, respectively. The arrow shows the CMC value.	107
Figure 5.7 Spectrum width centre against concentration of the SDS in aqueous solutions at room temperature. The black and red dashed lines are the linear and logarithmic trends, respectively. The arrow shows the CMC value.	108
Figure 5.8 The main considerations for the future studies on CMC measurement using optical fibre [212].	110
Figure 5.9 Equilibrium interfacial tension (a) and zeta potential (b) of the dispersions of ATD nanoparticles against concentration of the CTAB in aqueous solutions at 25°C. The concentration of ATD nanoparticles is constant and 0.1 wt % in all experiments. The solid line in (a) is the best fitted curve of the Frumkin model for the interfacial tension results for bare surfactant solutions. Dashed line is the representative of reaching CMC point. The green line is the representative of the surface charge of ATD nanoparticles in water. The grey line indicates the zero surface charge.	112
Figure 5.10 Schematic likely mechanism of interactions between ATD nanoparticles and surfactant molecules of CTAB. The bromide ions shown by yellow circles are released into the solution after dissolving CTAB in water. ..	114
Figure 5.11 Equilibrium interfacial tension (a) and zeta potential (b) of the dispersions of ATD nanoparticles against concentration of the SDS in aqueous solutions at 25°C. The concentration of ATD nanoparticles is constant and 0.1 wt % in all experiments. The solid line in (a) is the best fitted curve of the Frumkin model for the interfacial tension results for bare surfactant solutions. Dashed line is the representative of reaching CMC point. The green line is the representative of the surface charge of ATD nanoparticles in water. The grey line indicates the zero surface charge.	116
Figure 5.12 Schematic likely mechanism of interactions between ATD nanoparticles and surfactant molecules of SDS. The sodium ions shown by blue circles are released into the solution after dissolving SDS in water.	118
Figure 5.13 Foam formation in CTAB solutions (a, b) and dispersions with a fixed concentration of ATD nanoparticles equal to 0.1 wt % in CTAB (c, d)...	119
Figure 5.14 Foam formation in SDS solutions (a, b) and dispersions with a fixed concentration of ATD nanoparticles equal to 0.1 wt % in SDS (c, d).....	120
Figure 5.15 The bubbles observed at the initial time after formation at different concentrations of surfactants for (a) CTAB, (b) ATD-CTAB, (c) SDS, and (d) ATD-SDS. All the scale bars are representing a length of 100 μm . Blank spaces are related to the situations where no foams were formed.	121
Figure 5.16 Normal distribution of bubble size based on the diameter of the bubbles for (a) CTAB solutions and (b) ATD-CTAB dispersions at different concentrations of CTAB and a fixed concentration of ATD nanoparticles (0.1 wt %).	122

Figure 5.17 Normal distribution of bubble size based on the diameter of the bubbles for (a) SDS solutions and (b) ATD-SDS dispersions at different concentrations of SDS and a fixed concentration of ATD nanoparticles (0.1 wt %).	123
Figure 6.1 Self-assembly of the phospholipid molecules and formation of the bilayer upon using the ethanol injection method.	128
Figure 6.2 The Critical Packing Parameter (CPP) and structure of the aggregates of the surfactant and lipid molecules [222].	129
Figure 6.3 Self-assembly of the DPPC molecules into the structure of (a) cylindrical micelle and (b) flexible bilayer.	130
Figure 6.4 ^1H NMR spectrum of aqueous solution of the DPPC-d ₆₂ without nanoparticles. The sample was prepared in the laboratory and the ^1H NMR analysis was done on the sample. The labels (a) to (e) on the spectrum are the representative of singular tertiary proton at the <i>sn</i> -2 position on the glycerol backbone (a), protons of water (b), protons positioned between the quaternary amine and the phosphate group (c), protons of the three methyl groups in the quaternary amine part of the hydrophilic head of DPPC (d), and protons of the methyl groups at the endpoints of the tail groups in the structure of the DPPC (e), respectively. Due to the size of peaks, the regions of (a) and (c) have been zoomed.	131
Figure 6.5 The labelled hydrogens in the structure of DPPC.	132
Figure 6.6 ^1H NMR spectra of DPPC-d ₆₂ with different concentrations of ATD nanoparticles (right vertical axis). The concentration of the DPPC is constant at 5.38×10^{-8} M in all solutions and dispersions.	133
Figure 6.7 ^1H NMR spectra of DPPC-d ₆₂ with different concentrations of RTD nanoparticles (right vertical axis). The concentration of the DPPC is constant at 5.38×10^{-8} M in all solutions and dispersions.	134
Figure 6.8 ^1H NMR spectra of DPPC-d ₆₂ with different concentrations of CNT particles (right vertical axis). The concentration of the DPPC is constant at 5.38×10^{-8} M in all solutions and dispersions.	135
Figure 6.9 Dynamic interfacial tension of the dispersions of ATD nanoparticles with different concentrations in the DPPC solutions at 37°C. The concentration of the DPPC is constant at 5.38×10^{-8} M in all solutions and dispersions. The red dots, as a reference, are related to the DPPC solution without nanoparticles.	138
Figure 6.10 Equilibrium interfacial tension (a) and zeta potential (b) of the dispersions of ATD nanoparticles in the DPPC solutions against the concentration of nanoparticles at 37°C. The concentration of the DPPC is constant at 5.38×10^{-8} M in all solutions and dispersions. The blue and red dashed lines in (a) are the representative of the interfacial tension of DI water without DPPC and with DPPC, respectively. The green line and the triangle on it in (b) are the representative of the surface charge of ATD nanoparticles in water.	139
Figure 6.11 Dynamic interfacial tension of the dispersions of RTD nanoparticles with different concentrations in the DPPC solutions at 37°C. The concentration of the DPPC is constant at 5.38×10^{-8} M in all solutions and dispersions. The red	

dots, as a reference, are related to the DPPC solution without nanoparticles. The scratched part on the graph of RTD 0.01 wt % is because this experiment was done for 4000 s to reach the equilibrium. Therefore, the data of the last 1000 s has been shifted from the interval of 3000-4000 s in the main experiment. 142

Figure 6.12 Equilibrium interfacial tension (a) and zeta potential (b) of the dispersions of RTD nanoparticles in the DPPC solutions against the concentration of nanoparticles at 37°C. The concentration of the DPPC is constant at 5.38×10^{-8} M in all solutions and dispersions. The blue and red dashed lines in (a) are the representative of the interfacial tension of DI water without DPPC and with DPPC, respectively. The purple line and the triangle on it in (b) are the representative of the surface charge of RTD nanoparticles in water. 143

Figure 6.13 Visual inspection of the colloids (side view) and the structure of the sediments (bottom view) for the mixture of ATD+CNT nanoparticles with the concentration of 0.01 wt % in DPPC solution prepared using (a) method i, (b) method ii, and (c) method iii. 147

Figure 6.14 Optical microscopy images of the solid agglomerates in the colloid phase (left column including a-1, b-1, and c-1) and the structure of the sediments (right column including a-2, b-2, and c-2) for the mixture of ATD+CNT nanoparticles with the concentration of 0.01 wt % in DPPC solution prepared using (a) method i, (b) method ii, and (c) method iii. There were no visible solid agglomerates in the sediments prepared using mixing method iii under optical microscope. 149

Figure 6.15 Histogram and normal distribution of the surface area of solid agglomerates in the colloid phase for the mixture of ATD+CNT nanoparticles with the concentration of 0.01 wt% in DPPC solution prepared using (a) mixing method i and method ii, and (b) methods i, ii, and iii. The results for method iii have been excluded from part (a) to obtain a better view in the part (b). 150

Figure 6.16 Visual inspection of the colloids (side view) and the structure of the sediments (bottom view) for the mixture of RTD+CNT nanoparticles with the concentration of 0.01 wt % in DPPC solution prepared using (a) method i and (b) method ii. 152

Figure 6.17 Optical microscopy images of the solid agglomerates in the colloid phase (left column including a-1 and b-1) and the structure of the sediments (right column including a-2 and b-2) for the mixture of RTD+CNT nanoparticles with the concentration of 0.01 wt % in DPPC solution prepared using (a) method i and (b) method ii. There were no visible solid agglomerates in the colloid phase prepared using mixing method i under optical microscope. 153

Figure 6.18 Histogram and normal distribution of the surface area of solid agglomerates in the colloid phase for the mixture of RTD+CNT nanoparticles with the concentration of 0.01 wt% in DPPC solution prepared using mixing method ii. There were no visible solid agglomerates in the colloid phase prepared using mixing method i under optical microscope. 154

Figure 6.19 Visual inspection of the colloids (side view) and the structure of the sediments (bottom view) for the mixture of ATD+RTD+CNT nanoparticles with the concentration of 0.01 wt % in DPPC solution prepared using (a) method i and (b) method ii. 155

Figure 6.20 Optical microscopy images of the solid agglomerates in the colloid phase (left column including a-1 and b-1) and the structure of the sediments (right column including a-2 and b-2) for the mixture of ATD+RTD+CNT nanoparticles with the concentration of 0.01 wt % in DPPC solution prepared using (a) method i and (b) method ii. There were no visible solid agglomerates in the colloid phase prepared using mixing method ii under optical microscope.	156
Figure 6.21 Histogram and normal distribution of the surface area of solid agglomerates in the colloid phase for the mixture of ATD+RTD+CNT nanoparticles with the concentration of 0.01 wt% in DPPC solution prepared using mixing method i. There were no visible solid agglomerates in the colloid phase prepared using mixing method ii under optical microscope.....	157
Figure 6.22 SEM images of the droplet of the mixture of ATD+CNT nanoparticles with the concentration of 0.01 wt % in DPPC solution prepared using mixing method i.....	158
Figure 6.23 SEM images of the droplet of the mixture of ATD+CNT nanoparticles with the concentration of 0.01 wt % in DPPC solution prepared using mixing method ii.....	159
Figure 6.24 SEM images of the droplet of the mixture of ATD+CNT nanoparticles with the concentration of 0.01 wt % in DPPC solution prepared using mixing method iii.	160
Figure 6.25 SEM images of the droplet of the mixture of RTD+CNT nanoparticles with the concentration of 0.01 wt % in DPPC solution prepared using mixing method i.....	161
Figure 6.26 SEM images of the droplet of the mixture of RTD+CNT nanoparticles with the concentration of 0.01 wt % in DPPC solution prepared using mixing method ii.....	162
Figure 6.27 SEM images of the droplet of the mixture of ATD+RTD+CNT nanoparticles with the concentration of 0.01 wt % in DPPC solution prepared using mixing method i.....	163
Figure 6.28 SEM images of the droplet of the mixture of ATD+RTD+CNT nanoparticles with the concentration of 0.01 wt % in DPPC solution prepared using mixing method ii.....	164
Figure 6.29 SEM image of the needle-shaped structure in the mixture of ATD+RTD+CNT nanoparticles with the concentration of 0.01 wt % in DPPC solution prepared using mixing method i.....	165
Figure 6.30 SEM image of the needle-shaped structure in the mixture of ATD+RTD+CNT nanoparticles with the concentration of 0.01 wt % in DPPC solution.	166
Figure 6.31 EDX analysis of the spectrum 1 (a) and spectrum 3 (b) of the SEM image in Figure 6.30 for the mixture of ATD+RTD+CNT nanoparticles with the concentration of 0.01 wt % in DPPC solution. There were no visible solid agglomerates in the colloid phase prepared using mixing method ii under optical microscope.....	167

Figure 6.32 Equilibrium interfacial tension for the mixture of nanoparticles with the concentration of 0.01 wt % in DPPC solution using mixing methods i, ii, and iii describes in Section 3.1.4.2. The dashed lines are the representative of the interfacial tension of DPPC solution without nanoparticles and with single-type nanoparticles at 37 ± 0.2 °C. 169

Figure 7.1 A typical plot of the dynamic interfacial tension and surface area vs. time during oscillation. Red and blue dots correspond to the surface area and interfacial tension, respectively. The sample is related to DPPC solution without nanoparticles. 174

Figure 7.2 An example of the Fourier curve fitting using MATLAB for (a) surface area, and (b) interfacial tension, versus time. 175

Figure 7.3 The dynamic interfacial tension against time during oscillation at the amplitude of 1% and frequency of 0.1 Hz for DPPC without nanoparticles, ATD 0.01 wt % + DPPC, and RTD 0.01 wt % + DPPC. The double-headed arrows on the data points related to RTD 0.01 wt % + DPPC show the range of data scattering. 180

Figure 7.4 Complex viscoelastic (dilatational) modulus of air-liquid interface of (a) DPPC solution without particles, (b) ATD 0.01 wt% + DPPC, and (c) RTD 0.01 wt% + DPPC. 183

Figure 7.5 The main effects plots for the mean of complex viscoelastic modulus versus frequency and amplitude as the effective factors for (a) DPPC solution without particles, (b) ATD 0.01 wt% + DPPC, and (c) RTD 0.01 wt% + DPPC. . 185

Figure 7.6 The volume versus pressure known as pressure-volume curve of lung during inspiration (expansion) and expiration (compression) in the breathing cycle. Reprinted by permission from Springer Nature Customer Service Centre GmbH: Springer, Cham, Basic Sciences in Anesthesia. © 2018 Springer International Publishing AG [247]. 186

Figure 7.7 The example of the surface area and interfacial tension signals in MATLAB interface during the oscillation at the amplitude of 1% and frequency of 0.1 Hz. The sample is related to the DPPC solution without particle. 187

Figure 7.8 Phase difference between interfacial tension and surface area signals for (a) DPPC solution without particles, (b) ATD 0.01 wt% + DPPC, and (c) RTD 0.01 wt% + DPPC. 189

Figure 7.9 The main effects plots for the mean of phase difference versus frequency and amplitude as the effective factors for (a) DPPC solution without particles, (b) ATD 0.01 wt% + DPPC, and (c) RTD 0.01 wt% + DPPC. 190

Figure 7.10 The example of the THD measurement for the surface area signal in MATLAB interface. The output of the code is in both dB unit and percentage. This example is related to the oscillation at the amplitude of 1% and frequency of 0.1 Hz. The sample is related to the DPPC solution without particle. 192

Figure 7.11 THD percentage for surface area (left column) and interfacial tension (right column) for DPPC solution without particles (a-b), ATD 0.01 wt% + DPPC (c-d), and RTD 0.01 wt% + DPPC (e-f). 193

Figure 7.12 An example of the Lissajous plot for DPPC solution without particles at the amplitude of 10% and the frequency of 0.5 Hz. The hollow dots and filled dots are related to the expansion and compression, respectively. 196

Figure 7.13 The fourth order polynomial curve fitted on the data of Lissajous plots for DPPC solution without particles at the amplitude of 10% and the frequency of 0.5 Hz. The blue and red dashed lines are related to the expansion and compression, respectively. 198

Figure 7.14_Part 1 Lissajous plots for DPPC solution without particles at the amplitudes of 1% (a-b), 2% (e-f), 5% (i-j), and 10% (m-n). The data were obtained for all frequencies including 0.1 Hz (left column) and 0.125 Hz (right column). The hollow dots and filled dots are related to the expansion and compression, respectively. 200

Figure 7.15_Part 1 The fourth order polynomial curve fitted on the data of Lissajous plots for DPPC solution without particles at the amplitudes of 1% (a-b), 2% (e-f), 5% (i-j), and 10% (m-n). The data were obtained for all frequencies including 0.1 Hz (left column) and 0.125 Hz (right column). The blue and red dashed lines are related to the expansion and compression, respectively. 203

Figure 7.16 The S-factor of Lissajous plots for DPPC solution without particles at various amplitudes for the frequencies of 0.1 Hz (a), 0.125 Hz (b), 0.25 Hz (c), and 0.5 Hz (d). The grey and black colours are related to the expansion and compression, respectively. 206

Figure 7.17 Pressure-volume curve for healthy lungs, emphysematous, and fibrotic lungs [257]. 207

Figure 7.18 Colour maps related to the R-squared values of the fourth order polynomial curve fitted on the data of Lissajous plots for ATD+DPPC and RTD+DPPC with different concentrations during expansion (a) and compression (b). The red, yellow, blue, and green colours are the representative of the R-squared values in the ranges of 0-0.4, 0.4-0.6, 0.6-0.8, and 0.8-1, respectively. 209

Figure 7.19 Equilibrium interfacial tension of the dispersions of ATD nanoparticles (a) and RTD nanoparticles (b) in the DPPC solutions against the concentration of nanoparticles at 37°C. The concentration of DPPC in the solution is constant. The blue and red dashed lines are the representative of the interfacial tension of DI water without DPPC and with DPPC, respectively. ... 211

Figure 7.20 Lissajous plots and the fourth order polynomial curve fitted on the data of Lissajous plots for DPPC solution without particles (a-b), ATD 0.01 wt%+DPPC (c-d), and RTD 0.01 wt%+DPPC (e-f) at the amplitude of 1% and the frequency of 0.1 Hz. The hollow dots and filled dots are related to the expansion and compression, respectively. The blue and red dashed lines are related to the expansion and compression, respectively. 213

Figure 7.21 The S-factor of Lissajous plots for ATD+DPPC dispersion with the nanoparticle concentrations of (a) 0.02 wt%, (b) 0.03 wt%, and (c) 0.04 wt% at various amplitudes. Blue, orange, grey, and yellow colours represent the frequencies of 0.1, 0.125, 0.25, and 0.5 Hz, respectively. The patterned and non-patterned columns are related to the expansion and compression at each frequency, respectively. 214

Figure 7.22 The S-factor of Lissajous plots for RTD+DPPC dispersion with the nanoparticle concentrations of (a) 0.02 wt%, (b) 0.03 wt%, and (c) 0.04 wt% at various amplitudes. Blue, orange, grey, and yellow colours represent the frequencies of 0.1, 0.125, 0.25, and 0.5 Hz, respectively. The patterned and non-patterned columns are related to the expansion and compression at each frequency, respectively. 216

Figure 7.23 The dynamic interfacial tension and surface area vs. time for CNT 0.01 wt%+DPPC during oscillation. Red and grey dots correspond to the surface area and interfacial tension, respectively. 219

Figure 7.24 The dynamic interfacial tension and surface area vs. time for ATD+RTD+CNT 0.01 wt%+DPPC (mixing method i) during oscillation. Red and blue dots correspond to the surface area and interfacial tension, respectively. 220

List of Tables

Table 2.1 The summary of the characteristics of the alveolar region, pulmonary surfactant, and DPPC molecule.	23
Table 3.1 The composition of the different mixtures of nanoparticles and the mixing methods used for their preparation. The final concentration of the nanoparticles in the solution before adding the DPPC was 0.01 wt % in all cases.	45
Table 3.2 Nanoparticles' characteristics provided by the supplier.	46
Table 3.3 The general settings of PAT and the quantity of the parameters for two categories of experiments, i.e. ionic surfactants and lung surfactant model.	61
Table 3.4 Breathing frequency in quiet and deep breathing at different age groups.	72
Table 4.1 Comparisons between the dried nanoparticles' characteristics provided by the supplier and analysed in the laboratory using SEM.	76
Table 4.2 Zeta potential of nanoparticles or their agglomerates.	86
Table 4.3 Interfacial tension of the dispersions of nanoparticles with the concentration of 0.01 wt % in DI water at 37°C.	96
Table 5.1 Adsorption isotherm parameters obtained as best fit values from the Frumkin model and CMC at 25°C obtained by the tensiometry and optical fibre methods.	103
Table 7.1 The R-squared values of the fitted curves of interfacial tension and surface area as functions of time.	177
Table 7.2 The SSE values of the fitted curves of interfacial tension and surface area as functions of time.	179
Table 7.3 The RMSE values of the fitted curves of interfacial tension and surface area as functions of time.	181
Table 8.1 Summary of experimental results, findings and conclusions related to CTAB and SDS interacting with ATD nanoparticles.	226
Table 8.2 Summary of experimental results, findings and conclusions related to DPPC interacting with ATD, RTD, and CNT nanoparticles.	229
Table 8.3 Summary of findings and conclusions related to DPPC interacting with nanoparticles and their mixtures under dynamic conditions.	232

Publications

Journals:

- **Hajirasouliha, F.**, Yang, H., Wu, Q., Zabiegaj, D., “Can optical fiber compete with profile analysis tensiometry in critical micelle concentration measurement?”, *Zeitschrift für Physikalische Chemie*, 235(12), 2021.
- Zabiegaj, D., **Hajirasouliha, F.**, Duilio, A., Guido, S., Caserta, S., Kostoglou, M., Petala, M., Karapantsios, T., Trybala, A., “Wetting/spreading on porous media and on deformable, soluble structured substrates as a model system for studying the effect of morphology on biofilms wetting and for assessing anti-biofilm methods”, *Current Opinion in Colloid & Interface Science*, 2021.
- **Hajirasouliha, F.**, Zabiegaj, D., “Effects of Titanium Dioxide Nanoparticles and Concentration of Ionic Surfactants on Air-Liquid Interfacial Properties: Surface Tension and Foamability”, 2022. (Under Preparation)
- **Hajirasouliha, F.**, Cabanova, K., Placha, D., Zabiegaj, D., “Effect of Two Different Forms of Titanium Dioxide Nanoparticles on the Interfacial Rheology of Dipalmitoyl Phosphatidylcholine (DPPC) Monolayers: Linear and Nonlinear Approaches”, 2022. (Under Preparation)
- **Hajirasouliha, F.**, Gunda, A., Alajmi, E., Zabiegaj, D., “The Structure and Stability of the Oil-in-Water Emulsions of Vegetable Oils in Aqueous Phase”, 2022. (Under Preparation)

Book Chapters:

- **Hajirasouliha, F.**, Zabiegaj, D., “Effects of Environmental Emissions on the Respiratory System: Secrets and Consequences”, In *Environmental Emissions*. IntechOpen., 2020. (Published)
- **Hajirasouliha, F.**, Zabiegaj, D., “Nano-structured Polymer-based Composites”, 2022. (Under Preparation)

Conferences:

- Oral Presentation, **Hajirasouliha, F.**, Cabanova, K., Placha, D., Zabiegaj, D., “Impact of the Air Pollutants on the Lung Surfactant: Interfacial Study”, EUFOAM 2022 Conference, Krakow, Poland, 3rd-6th July 2022
- Oral Presentation, **Hajirasouliha, F.**, Cabanova, K., Placha, D., Fu, R., Zabiegaj, D., “Impact of the air pollutants on the Lung Surfactant based on Interactions of the Carbon Nanotubes and TiO₂ Nanoparticle mixtures with Dipalmitoyl Phosphatidylcholine Monolayers (DPPC)”, International

Marangoni Association Conference (IMA10), Iasi, Romania, 12th-16th June 2022

- Oral Presentation, **Hajirasouliha, F.**, Zabiegaj, D., “Is the shape of air particulate matter important? A study on the interactions of the two shapes of titanium dioxide nanoparticles with a model of pulmonary surfactant”, UK Fluids Conference 2021 (Online Conference), University of Southampton, UK, 8th-10th September 2021
- Poster Presentation, **Hajirasouliha, F.**, Zabiegaj, D., “Optical Fiber: A Potential Method for Critical Micelle Concentration Measurement”, 5th International Conference on Droplets 2021 (Online Conference), Technische Universitat Darmstadt, Germany, 16th-18th August 2021
- Poster Presentation, **Hajirasouliha, F.**, Zabiegaj, D., “Effect of Titanium Dioxide Nanoparticles on the Wet Foams Produced by Ionic Surfactants: A Study on Air-Liquid Interfacial Properties”, International E-Conference on Advanced Materials Science and Graphene Nanotechnology, United Research Forum, UK, 25th-26th November 2020
- Flash Presentation, **Hajirasouliha, F.**, Zabiegaj, D., “Effect of the Surfactant Concentration on the Adsorption of TiO₂ Nanoparticles at the Air-Liquid Interface: A Promising Method to Control the Photocatalytic Activity”, An e-Symposium on: Reforming Multi-disciplinary Engineering Innovation for the New Normal, Northumbria University and Royal Society of Chemistry (NuTNEC), UK, 28th August 2020
- Poster Presentation, **Hajirasouliha, F.**, Zabiegaj, D., “Analysis of air-liquid interfacial layer of a phospholipid as a model of lung surfactant in presence of solid particles”, North East Postgraduate Conference, Newcastle Civic Centre, Newcastle University, UK, 22nd November 2019
- Poster Presentation, Zabiegaj, D., **Hajirasouliha, F.**, “Materials based on Polymer-Particle-Oil Emulsions: Droplet Stabilisation and Evolution”, Droplets 2019 Conference, UK Fluids Network (UKFN), Durham University_Department of Physics, UK, 16th-18th September 2019
- Poster + Flash Presentation, **Hajirasouliha, F.**, Zabiegaj, D., “Effects of surfactant concentrations on the drop behaviour on solid surfaces”, Droplets 2019 Conference, UK Fluids Network (UKFN), Special Interest Group (SIG) on “Droplet and Flow interactions with bio-inspired and smart surfaces”, Durham University_Department of Physics, UK, 15th September 2019

Award:

- Poster Award, **Hajirasouliha, F.**, Zabiegaj, D., “Carbon Materials based on Waste for the CO₂ Capturing”, Future Opportunities for CO₂: The Chemistry of Carbon Dioxide and its Role in decarbonisation, SCI, UK, November 2020
- Outstanding Presentation Award for the Flash Presentation, **Hajirasouliha, F.**, Zabiegaj, D., “Effect of the Surfactant Concentration on the Adsorption

of TiO₂ Nanoparticles at the Air-Liquid Interface: A Promising Method to Control the Photocatalytic Activity”, An e-Symposium on: Reforming Multi-disciplinary Engineering Innovation for the New Normal, Northumbria University and Royal Society of Chemistry (NuTNEC), UK, 28th August 2020

Chapter 1

Introduction and Scope of the Thesis

1.1 Research Motivation

Human health has been adversely affected by air pollution, which is now regarded as the most serious environmental challenge. In the UK, public health is at high risk of the poor air quality. The long-term exposure to air pollution causes chronic conditions such as lung cancer. Therefore, it reduces the life expectancy. Short-term exposure to air pollution also causes various health impacts such as increasing the cardiovascular and respiratory hospital admissions and mortality. The effects of the air pollution throughout people's lifetime have been shown in Figure 1.1 [1].

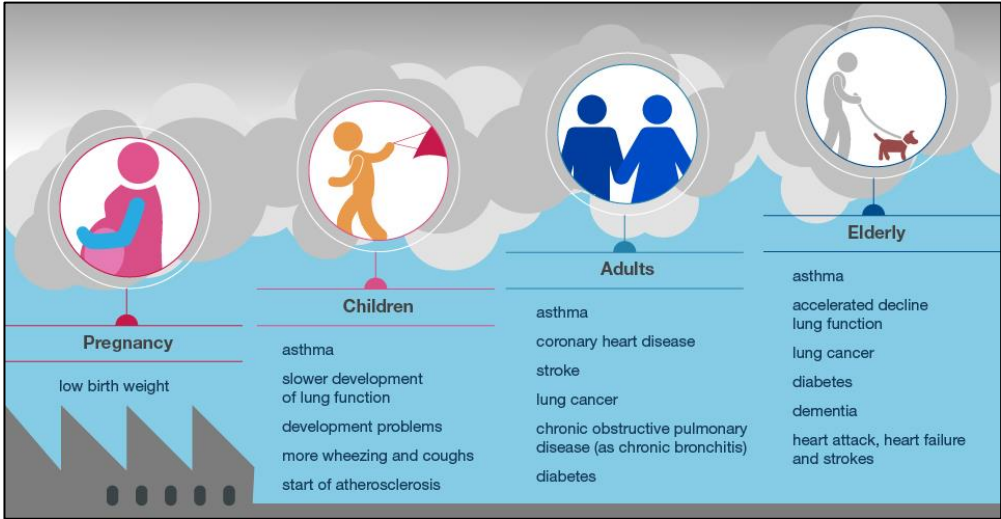


Figure 1.1 Air pollution effects throughout the lifetime [1].

In 2010, it was estimated that the cost of health impacts of the air pollution was £8 to 20 billion [1]. In 2019, in the UK, the mortality burden attributed to long-term exposure to air pollution was estimated to be 29,000 to 43,000 deaths for adults aged 30 and over [2]. On a global scale, ambient (or outdoor) air pollution causes 4.2 million deaths every year. Moreover, each year, 3.8 million people die from indoor air pollution caused by household exposure to smoke from fuels and dirty cook stoves [3].

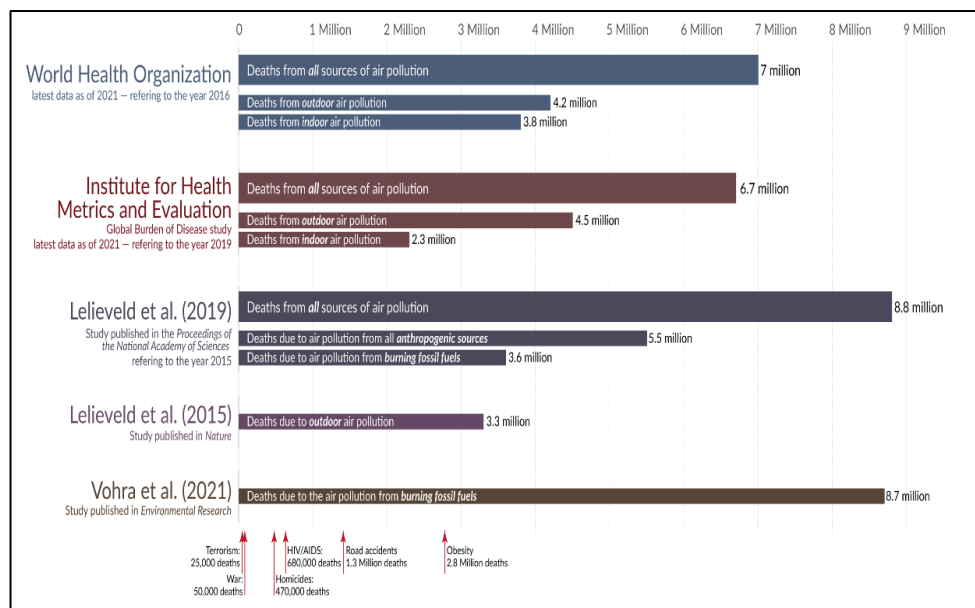


Figure 1.2 Estimations of the global deaths from the air pollution published in recent studies of authentic resources. ‘All sources’ means natural and anthropogenic sources [4].

As shown in Figure 1.2, the number of deaths related to the air pollution overtakes that of obesity, HIV/AIDS, road accidents, homicides, and war. In fact, air pollution is regarded as a silent killer which kills many human beings around the world by its invisible weapons called air particulate matter.

It has been proven that air pollution causes and/or exacerbates many diseases including skin, heart, neurological, and lung ones. Some associated noncommunicable diseases such as ischaemic heart disease, stroke, pneumonia, chronic obstructive pulmonary disease, and lung cancer are examples of these diseases which affect the people’s lives and/or result in premature deaths [5].

Among the air particulate matter, nano-sized pollutants with diverse qualities are being emitted into the environment. These nano-pollutants are originated from combustion sources (such as engines and power generation plants) or non-exhaust sources (such as brake wear) [6]. The other source of the emission of nanoparticles into the environment is the increased manufacturing, processing, and handling of nanomaterials due to the popularity and potential applications of nanotechnology as a useful scientific discipline. Despite unique properties and applications of nanomaterials in different fields such as pharmaceuticals, cosmetics, healthcare, agriculture, and food processing, these materials present risks toward the environmental issues and human health. These risks arise from the nanoparticles' eventual fate and toxicity [7]. Therefore, evaluating the toxic effects of these nanoparticles on human health is a key issue for health and environmental regulatory authorities to put more strict regulations on the nano-sized pollutants in place [8].

Upon inhalation, the air with nano-pollutants dispersed in it enters the human body through the respiratory system. These nano-sized pollutants enter the respiratory system of a person, pass the airways, and change into a danger for the human health. These nanoparticles may cause respiratory diseases, or they can penetrate the blood circulation and affect other organs such as liver, kidneys, and spleen. For example, accumulation of the nanoparticles in kidneys, liver, spleen and central nervous system through the penetration of the epithelial barrier of the alveolar region of the lungs has been observed [9, 10].

The lungs are the responsible organs for gas exchange with blood. This function is performed in the alveolar sacs called alveoli located in the deepest region of the lung. There are almost 500 million alveoli in the human lungs. Because of the liquid film on the alveoli's walls, this great number of alveoli sacs can be considered as a network of 500 million bubbles in the lungs. Due to the interfacial tension effects arising from the mentioned liquid film, this great number of bubbles which possesses large air-liquid interfaces are potential to collapse. Therefore, the structure of the alveoli's network is intrinsically unstable.

To prevent this problem, some cells in the alveolar region secrete a material called pulmonary surfactant or lung surfactant which decreases the interfacial

tension and prevents the possibility of collapse of bubbles by being adsorbed at the air-liquid interfaces in the alveoli. This means that the air-liquid interface existing in the alveoli is the last barrier against the inhaled nanosized pollutants before penetrating the lung barrier into the blood circulation. Investigating the interactions of these nano-pollutants with pulmonary surfactant is crucial to understand the fate of the inhaled nanosized pollutants, whether it is about their retention time in the lungs or it is about penetrating the blood circulation. The results of such studies can be used either in the context of environmental toxicology or pulmonary drug delivery [11, 12]. Moreover, the mechanics of the breathing is critically affected by the interactions of nanoparticles with the pulmonary surfactant. The irreversible attachment of particles (such as asbestos fibres) to the air-liquid interface of the lung surfactant means that these particles remain in the lungs due to their physicochemical properties. During the breathing cycle, these particles cause the rigidity of the air-liquid interface in the alveoli sacs as the area of gas exchange. Consequently, the mechanics of breathing during the expansion and compression is affected by these particles. The real particles (such as dust) entering the lungs, are not homogeneous in their size, shape, and concentration. This non-homogeneity in the physicochemical properties makes these particles more complicated in terms of their interactions with the lung surfactant and their adverse effects on the human health. It has been proven that the exposure to dust causes the change of the pulmonary function parameters. Asbestos also causes diseases such as lung fibrosis (asbestosis), malignant mesothelioma cancer, and lung cancer [13, 14].

In brief, the adverse effects of nanoparticles inhaled through the respiratory system on human health is the main motivation of this study. Investigation of the interactions of nanoparticles with pulmonary surfactant will result in understanding the mechanisms behind these interactions. These results can be used to predict the fate of nanoparticles based on their characteristics such as concentration, size, shape, hydrophilicity/hydrophobicity, and surface charge.

To establish a reasonable understanding of the systems containing surfactants and nanoparticles in the context of interfacial science, this study starts with investigation of the nanosized pollutants in contact with the industrial surfactants applicable in many fields. In the following work, one of the main constituents of

the lung surfactant, i.e., dipalmitoylphosphatidylcholine (DPPC), is chosen as a single-component model of the lung surfactant to study the effects of three different types of nanosized pollutants on the air-liquid interfaces containing DPPC [15, 16].

1.2 Research Aims and Objectives

In systems consisting of two fluids (air and liquid) and a solid material of the nanometric dimension, partial wettability properties of particles give a nonhomogeneous character to interfacial layers due to the formation of three interfaces among solid, liquid, and air. It is important to define appropriate quantities of mechanical characteristics of these microscopic layers so that it can be useful to describe such characteristics at a macroscopic scale. Effective interfacial tension is one of these properties which can be measured by tensiometric methods based on the Laplace equation [17]. This study also uses an axisymmetric drop shape analysis technique in which the shape analysis of the droplets is conducted to measure the interfacial tension. The instrument applied in this study is called the profile analysis tensiometer (PAT). For the systems containing surfactants and nanoparticles, measuring the interfacial properties such as interfacial tension and rheology can be an effective tool to understand the effects of the nanoparticles on these systems.

In general, the main aim of this research is to investigate the interactions between the surfactants and nanosized materials at air-liquid interface and in the bulk of the solution. The main topics based on this aim are as follows:

The first topic of the aim is to investigate the interactions of single-type nanoparticles with different types of surfactants including the industrial surfactants and a model of pulmonary surfactant. The design of the experiments is directly based on the applications of each type of surfactant. Therefore, the first part of results related to the industrial surfactants can be used for the industrial applications such as formulation of cleaning products. The second part of results related to the pulmonary surfactant model can be used by linking them with *in vivo* toxicology. The experimental set-up used in this study, i.e., PAT, is

a reliable device especially in simulating the air-liquid interface in the alveoli sacs and its dynamic condition during the breathing cycle. Therefore, the outcomes of this part of research are useful in finding the physical chemistry principles behind the results of the *in vitro* and *in vivo* studies focused on the interactions of particles and lung.

The second topic of the key aim is to establish and develop a robust systematic method of measuring the physicochemical effects of the mixtures of nanoparticles on the DPPC as a model of pulmonary surfactant. This is an area that has been overlooked even in terms of the toxicity measurements. The results coupled with the toxicity can be a good reference for the regulatory authorities to revise the regulations in case that the mixture of nanoparticles is elevating the hazards toward the human health.

The third topic of the key aim is to apply the nonlinear interfacial rheology approach for the DPPC systems with and without nanoparticles under dynamic conditions. The nonlinear interfacial rheology can be used as a complementary tool to understand the microstructure of the surfactant-nanoparticles at the interface under dynamic conditions applied to the real case studies such as the human breathing cycles.

To achieve the mentioned key aim, the detailed objectives of this thesis are listed as follows:

- Characterisation of the nanoparticles and their agglomerates in the dried state and at the air-water interfaces using a three-phase contact angle measurement method to establish highly possible backup information about the properties of nanoparticles. Identification of some complicated positions of nanoparticles at the air-water interfaces based on the microscopic observations.
- Investigation of the most applicable industrial surfactants and one type of nanoparticles comprehensively used in the industrial/commercial formulations and processes. Design of the experiments based on the challenges that might be faced in the industries. Measurement of the effects for a specific nanoparticle on two different surfactants using interfacial tension, zeta potential, and foaming properties measurements.

Understanding of the mechanism of interactions between nanoparticles and each type of surfactant.

- Proposing a potential method based on the optical fibre for measuring the critical micelle concentration as one of the important features of the surfactants. Comparing the results of the previously approved methods with the new technique. Suggesting the modifications of the hypotheses and designs of the experiments for the next phase of the method development.

The below objectives are focused on the mimicking of the real impact of the nanosized pollutants on the respiratory system using lung surfactant. The real conditions are simulated using (a) different concentrations of nanoparticles (which mimic the time of the exposure to pollutants), (b) mixture of nanoparticles (which mimics the real status of the pollutants entering the lung upon each inhalation), and (c) oscillation studies of the rheological parameters (which mimic the dynamic conditions of lungs). These objectives are listed as follows:

- Studying the interactions of three different nanoparticles with DPPC in the bulk of the solution.
- Investigating the interfacial behaviour of the solutions of DPPC without and with nanoparticles at different concentrations as a representative of the time of the exposure to the nanosized pollutants in real case scenario. Integrating the results related to the air-liquid interfaces with the data acquired from bulk studies. Understanding the mechanism of interactions of nanoparticles with DPPC.
- Analysing the effects of the shape and surface properties of nanoparticles with the same chemical compositions on their interactions with DPPC molecules. In the real life, nanoparticles with the same chemical formula and different surface properties (such as size, shape, and surface functionalisation) are inhaled. It is important to study the effect of different physicochemical factors and understand the most dominant factors.

- Evaluating the behaviour of the mixture of nanoparticles in contact with the DPPC in both colloidal phase and air-liquid interface. Studying the effects of the composition of the mixture and mixing method.
- Analysing the interfacial rheology of the air-liquid interfaces containing DPPC and a single-type nanoparticle using the linear method. Discussing the insufficiency of this method for the specific systems in this study. The linear method using the Fourier transform does not necessarily make realistic results for all systems. Based on the composition of the system (chemical composition and concentration of particles and surfactants) and the dynamic conditions (frequency and amplitude), various systems such as the systems in this study might be deviated from the linear regime in which a harmonic multi-frequency change in the surface area results in the similar harmonic multi-frequency composition for the system's response, i.e., interfacial tension.
- Investigating the interfacial rheology of the air-liquid interfaces containing DPPC and nanoparticles using the nonlinear method which applies Lissajous plots to understand the behaviour of the interfaces and their microstructure at the regimes beyond the linear ranges. Providing qualitative arguments about the effects of the nanoparticles at the air-liquid interface of the DPPC under the dynamic condition of the breathing cycle at different frequencies and amplitudes.

1.3 Distinctiveness and Novelty of the Thesis

In this thesis, the studies of the interfacial behaviour of the DPPC-nanoparticle systems have been conducted in conditions that simulate the real operating conditions of lung and the states of the nanoparticles as much as possible. To achieve that, the real operating state (working regime) of the lungs has been simulated using the harmonic oscillation. The device used in this study has been set up to work in appropriate ranges of the frequencies and amplitudes, which in turn, simulates the breathing cycle in the human lungs.

When it comes to the effects of the nanosized pollutants, most of the previous studies have been only focused on one single-type nanoparticle in each set of measurement. However, this is not what happens in the real world. Upon every inhalation, a mixture of particles (differentiated in size, shape, and surface functionalisation) enters the respiratory system and meet the DPPC or lung surfactant. Majority of the previous studies are focused on a model of airborne particulate matter, usually known as diesel particulate matter, to investigate their interactions with the pulmonary surfactant [18, 19]. However, due to the very complex composition and heterogeneity of these models of the airborne particulate matter, it is difficult to understand the mechanisms for the interactions of particles with DPPC molecules. This means that it is a very complex and multi-layered process to clarify which types of particles have the most dominant effects on the lung surfactant.

In this thesis, for the first time, a robust systematic way has been used to understand the effects of the mixture of nanoparticles on the DPPC in the bulk of the solution and at the air-liquid interface. Moreover, to mimic the different possible ways of mixing of the nanoparticles, three methods of mixing have been used to show the interfacial effects they might have on the lung surfactant. Results of this investigation are extremely important for environmental regulations and can provide a guidance on pulmonary drug delivery mechanisms.

The other novelty of this research is related to taking the nonlinear approach in the interfacial rheology measurements of the DPPC-nanoparticle systems. This method has been previously used for some other surfactant-containing systems [20, 21]. To our knowledge, this is the first time that a nonlinear method is used for DPPC systems. Using this method, some valuable qualitative results have been achieved that can distinguish the effect of nanoparticles at each part of the breathing cycle, i.e., expansion and compression.

This thesis also introduces a potential method based on the optical fibre for measuring the critical micelle concentration of surfactant. The preliminary outcomes represent a compliance between the optical fibre method and profile analysis tensiometry (PAT) technique. To develop an optical fibre-based sensor able to measure the critical micelle concentration of the surfactants, the

suggestions for future designs of experiments and controlling the effective factors have been provided.

1.4 Outline of the Thesis

This thesis includes eight chapters as follows:

Chapter 1 introduces the motivation and scope of the research, as well as the aims and objectives that have been targeted. Moreover, the novelty and distinctiveness of the thesis as the contribution to the research field are mentioned in this chapter.

Chapter 2 reviews the literature to highlight the scientific gaps in the field and the necessity of this research. Due to the main application of this research in the biological field and specifically in human respiratory system, an overview of the respiratory system and its structure are provided to establish the required fundamentals for understanding the research. In the next step, the literature related to the interactions of surfactants and nanoparticles and the effective factors on these interactions are reviewed. The pulmonary surfactant under the dynamic conditions and the reasons of using the current experimental device are discussed based on the literature review. The importance of considering the mixture of nanoparticles in the toxicological studies and the lack of physicochemical studies in this area are mentioned. Finally, the interfacial rheology as a tool to understand the microstructure of the interfaces is reviewed.

Chapter 3 focuses on the details of the experimental work and the analytical methods used in this research. In this chapter, the methods of preparation of the solutions of surfactants and dispersions of nanoparticles in the surfactant solutions are explained precisely due to the importance of the effects of preparation methods on the obtained results. Moreover, the characterisation of nanoparticles and foams are described. The experimental methods (such as gel trapping technique) used in understanding the interactions of surfactant and nanoparticles are also introduced. A comprehensive explanation about the profile analysis tensiometer, its principles, related equations, and the limitations/considerations of this device is provided. At the end, the design of

experiments for the interfacial rheology measurements based on the dynamic conditions of lung are explained. To avoid any confusion, the details of the methods of analysis are described in the related chapter, i.e., Chapter 7.

Chapter 4 presents the results related to the characterisation of the nanoparticles and their agglomerates. The shape, surface charge, and hydrophilicity/hydrophobicity of these particles are discussed through analysing the results of related experimental work.

Chapter 5 covers the interactions of industrial surfactants and nanoparticles. The adsorption isotherms of two ionic surfactants including a cationic and an anionic surfactant are derived. A potential method based on the optical fibre for measuring the critical micelle concentrations (CMC) of these surfactants is proposed and the results are compared to those obtained using a tensiometry method. The effects of one type of nanoparticle with a fixed concentration on the solutions of each surfactant at different concentrations are evaluated using interfacial tension measurement and analysing their foaming properties. As a result, the probable mechanisms of interactions of each surfactant with that specific nanoparticle are suggested.

Chapter 6 investigates the interactions of three different nanosized materials with the DPPC in the bulk of solution and at the air-liquid interface. Because of the method of preparing the dispersions of nanoparticles in the DPPC solution, the interactions of the DPPC and each type of nanoparticles in the bulk should not be ignored. Therefore, this chapter starts with the analysis of the results related to the DPPC and nanoparticles in the bulk. Then, the interfacial tension of the mentioned samples is measured to propose the possible mechanism of interactions of each single type of nanoparticle with DPPC. In this chapter, to mimic the real situation related to the time of exposure to the nanoparticles, the concentration of nanoparticles is varied and the concentration of DPPC is maintained constant. The main part of this chapter analyses the mixture of nanoparticles and their interactions with DPPC to reveal the effects of the composition of the mixture and mixing method on the interfacial behaviour of these systems and their colloidal phase. The mixture of particles mimics the real situation in which the nanosized pollutants are inhaled in real life. The nanoparticles might mix and interact with each other before reaching the

pulmonary system or after it. The different mixing methods used in this study simulate the various states of mixing of nano-pollutants in the real life.

Chapter 7 uses the interfacial rheology to understand the mechanisms of interactions between nanoparticles and DPPC under the dynamic conditions representing the breathing cycle. The presence of nanoparticles and their interactions with pulmonary surfactant increase the rigidity of the system and cause anomalies in the breathing cycles. As a consequence, part of the normal respiratory mechanics of breathing related to the liquid layer containing the lung surfactant [22] is adversely affected. Interfacial rheology is used to understand the possible anomalies, caused by nanoparticles, in the mechanical properties of the lung surfactant system. In this chapter, the analysis of the data starts with conducting the linear approach in the interfacial rheology. However, based on the logic reasoning, it is concluded that the special systems of this study are not in the linear regime. Therefore, the nonlinear approach for the interfacial rheology measurements is conducted to describe these systems under the dynamic conditions. As this research is one of the first studies using this method for DPPC-nanoparticle systems, the details of this nonlinear approach have been described precisely.

Chapter 8 presents the conclusions of this research and suggests the future directions to extend this research.

Chapter 2

Literature Review

2.1 Introduction

This chapter firstly introduces the air pollution (which is now becoming a serious environmental challenge) and some environmental terms and concepts. Then, the nanomaterials as one of the most important air pollutants are introduced. The effect of the air pollution on human health, and specifically on human respiratory system, will be discussed. To clarify the reasons behind the design of the experiments and applying a specific device in this research, i.e., profile analysis tensiometer, the anatomy of the respiratory system and the deposition of nano-sized pollutants in the deepest areas of this system are explained. The composition of the pulmonary surfactant in the alveolar region is also expressed in detail to highlight the reason of choosing one of its components as the model of lung surfactant.

As this research includes both industrial surfactants (Chapter 5) and pulmonary surfactant (Chapter 6 and Chapter 7), the previous studies focused on the measurements of the interfacial properties of the systems containing any industrial or pulmonary surfactant and nanoscale materials/pollutants are reviewed in order to find out the main effective characteristics of such systems on the interfacial tension of the air-liquid interface. In the next step, the pulmonary surfactant under the dynamic conditions is scrutinised to explore the reason of using profile analysis tensiometer in this study. Finally, the literature review is finished by introducing the importance of studying the mixture of nanoparticle-lung surfactant system in a systematic way. Moreover, the nonlinear interfacial rheology approach which has been previously studied for the systems other than nanoparticle-lung surfactant is introduced as a potential

method to be used for studying the microstructure of the lung surfactant under the dynamic conditions.

It should be noted that this chapter is a combination of the literature review and the explanations of importance for the great concerns leading to this study. The basic concepts and principles of the experimental methods and the novel approaches have been explained in more details in the following chapters. Moreover, each result chapter (Chapters 4-7) contains an introduction which reviews specific literature only closely related to that chapter.

2.2 Air pollution

Air pollution has become one of serious environmental issues. Every year, 3.8 million deaths occur because of people's exposure to the smoke from fuels and dirty cookstoves. Moreover, 4.2 million deaths occur annually due to the exposure to outdoor air pollution [3]. The ambient or outdoor air pollution mainly arises from anthropogenic activities such as combustion of fossil fuels, power generation, usages of vehicles, and industrial contaminations [23-25]. In fact, air pollution is the result of extensively environmental emissions discharged into the air. The pollutants can be categorised into four groups as below:

- Gaseous pollutants (such as carbon monoxide, nitrogen oxides, sulphur dioxide, and volatile organic compounds),
- Heavy metals (such as chromium, lead, mercury, vanadium),
- Persistent organic pollutants (such as dioxins and pesticides), and
- Particulate matter (PM) [5, 26].

The PM is the collection of solid and/or liquid substances classified based on their aerodynamic diameters [27]. By definition, the particles with diameters less than or equal to 10, 2.5, and 0.1 μm are categorised as PM_{10} , $\text{PM}_{2.5}$, and $\text{PM}_{0.1}$, respectively [28]. The focus of this study is on $\text{PM}_{2.5}$ and particularly nanoparticles, because these particles have a high deposition fraction in the deeper sections of the lung [29].

2.3 Nano-Pollutants

Emission of different nanoparticles with diverse qualities into the environment is also due to the consequences of the fast-growing nanotechnologies. These nanoparticles can be classified into organic and inorganic nanoparticles based on their chemical compositions. They can also be natural or synthetic ones. In addition, they can be generated from different sources. For example, in traffic-influenced environments, nano-pollutants can be emitted from combustion sources (such as engines and power generation plants) or they can be originated from non-exhaust sources (such as brake wear) [6].

Nano-pollution as an invisible pollution is the most serious one to be controlled and managed. The nano-pollutants are easily released into soil, water, and air. The nanoparticles transported into the soil can be accumulated in the plants and enter the human body through the food chain. Drinking water, breathing the air, and contacting skins are also the other ways that the nano-pollutants can enter the human body. The small size of the nano-pollutants leads to their easy penetration into the cells of plants, animals, and human beings. Therefore, assessing the toxic effects of nanoparticles and adverse effects of nano-pollutants on human health is crucial for environmental and health regulators to put more strict regulations on the nano-pollutants in place [8].

2.4 Effects of Air pollution on Human Health

There are huge risks of skin, heart, and neurological diseases as well as lung diseases or even cancers resulted from the air pollution. These pollutants affect our brain, heart and lungs using its invisible weapons named particulate matter (PM), especially the nano-pollutants. Our exposure to the air pollutants could cause Central Nervous System (CNS) [30], cardiovascular [31], and lung diseases [32].

Skin as the largest organ in human body is one of the first barriers against these nano-sized pollutants. However, several types of diseases such as eczema, psoriasis, acne, and atopic dermatitis may happen to skin if it is exposed to nano-

pollutants for a long time [33]. Studies on specific populations , such as workers for chimney sweeps, asphalt-roofing, coke oven, and asphalt-paving show that the air pollutants directly affect their skins [34].

The main morbidity and mortality related to the air pollution are because of the severe effects of these pollutants on the cardiovascular system. Based on the Global Burden of Diseases (GBD) study, in 2015, the air pollution caused 19 % of all cardiovascular deaths [35]. Moreover, if the exposure to PM is increased, the relative risk of the cardiovascular diseases will be significantly increased. The direct translocation of PM and their penetration into the systemic circulation is one of the primary pathways which initiate the secondary pathways through which the air pollution leads to the cardiovascular diseases [31]. The short-term exposure to PM affects the acute cardiovascular diseases such as myocardial infarction and cardiac arrhythmia whereas the long-term exposure to the air pollutants results in the coronary events [36].

Air pollution also affects the central nervous system (CNS) and exacerbate the neurodegenerative conditions such as Alzheimer's and Parkinson's diseases. There is an apparent link between air pollution and the incidence of dementia, white matter injury, and cognitive impairment [30]. The traffic-related air pollution with an increased concentration enhances the Attention Deficit Hyperactivity Disorder (ADHD) and autism [37].

The risk of stroke which can be categorised as both neurological and cardiovascular disorders is elevated by exposure to air pollution [38, 39]. Due to the high danger of air pollutants in the case of stroke, the air pollution is often regarded as silent killer. Therefore, serious actions related to environmental regulations and public health policies should be taken [40, 41].

The incidence of the lung cancer is also associated with air pollution. Moreover, Chronic Obstructive Pulmonary Disease (COPD) and asthma are the other examples of the lung diseases caused by the air pollution [32, 42-44].

It is well-agreed that one of the most important pathways through which the air pollutants cause a danger for human health is the respiratory system. The PM can either stay in the lungs and/or diffuse through the lung barrier and enter the blood circulation. This will result in the disturbance to normal functions of the human body. For example, these particles can block the vessels, which in turn,

causes blood clotting and stroke. Titanium dioxide and carbonate compounds in submicron and micron sizes were found in the mucosa of the patients diagnosed with hypertrophic rhinitis [45].

Among the air pollutants, nano-pollutants are of a great importance due to their large surface areas, high alveolar deposition fractions, and strong ability to enter the bloodstream [46, 47]. Due to the high rate of the nanoparticles' emission into the environment, the studies on the nanotoxicity are becoming more crucial [48, 49].

The accumulation of the nanoparticles in various human organs such as liver, spleen, kidneys, and CNS has been previously observed. These nanoparticles were the ones which had previously penetrated through the epithelial barrier of the alveolar region in the lungs [5, 9, 10].

These observations demand a comprehensive study of the fate of the air pollutants, especially nano-sized ones, reaching to the respiratory system and the deepest areas of the human lungs. Therefore, the next section focuses on the human respiratory system, its details related to the context of this research, and the deposition of nano-pollutants in this system.

2.5 Air Pollution and Human Respiratory System

As mentioned before, the air pollutants can enter the respiratory system, pass the airways, and change into a danger for the human health. To clarify the whole journey of the air PM in the respiratory system, some fundamental knowledge about the unique anatomy and physiology of the respiratory system is required. Therefore, in the next section, the anatomy of the respiratory system is explained.

2.5.1 Anatomy of Respiratory System

The respiratory system procures the necessary oxygen to provide energy for body and removes carbon dioxide produced by the metabolism. When we breathe, air enters the mouth or nose, where it is filtered, humidified, and warmed

to 37°C. Then, the conditioned air travels through the airways. The main air passage is *trachea* subdividing to the two *bronchi*. Each one of these *bronchi* leads to one lung. To simplify the general image of the respiratory system, it can be considered as a collection of branching tubes. As these tubes penetrate deep into the lungs, they are divided more, become narrower and shorter. The final divisions of the respiratory tubes are *alveolar ducts* consisting of *alveoli*, the small air sacs with an enormous number about 500 million in the human lungs (Figure 2.1). The gas exchange as the cardinal function of the lungs takes place in alveoli [50]. Therefore, the alveolar region of the lungs is called the *respiratory zone*.

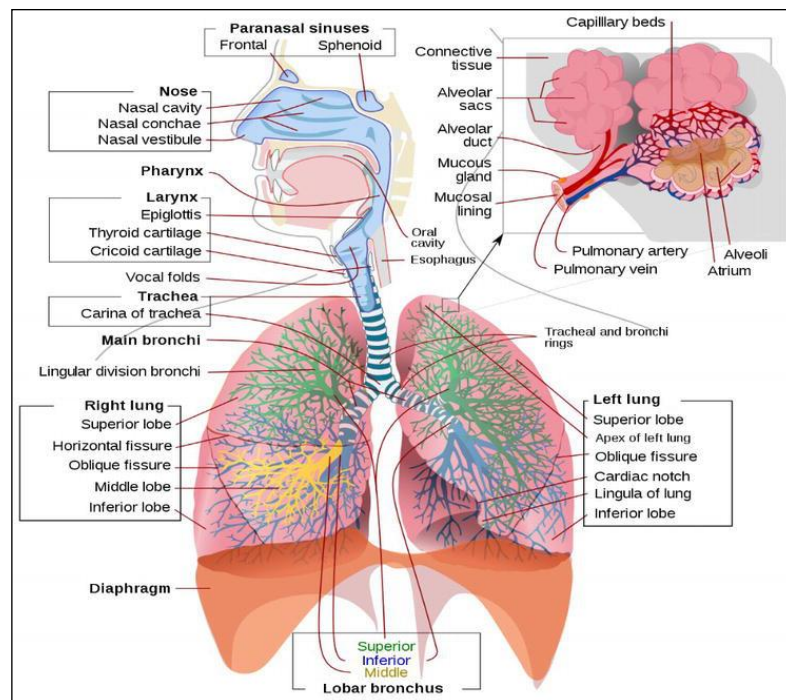


Figure 2.1 Human respiratory system [51]. The alveolar region exists at the end of the branches of the airways [5].

The diameter of each alveolus located in the alveolated region is about 0.3 mm. When the inhaled air with its components and particles flows down toward the alveoli, its velocity becomes small. Hence, the dominant mechanism of ventilation in the alveolar region is gas diffusion [52].

2.5.2 Deposition of Air Particulate Matter and Nano-Pollutants in Respiratory System

Upon inhalation (inspiration), a lot of particles with different size enter our respiratory system. The deposition of these particles in different areas of the respiratory system depends on the size of the particles. Figure 2.2 shows that the deposition fractions of the particles at extra-thoracic (head), tracheobronchial (TB), and alveolar regions (P) of the respiratory system depend on the particle size.

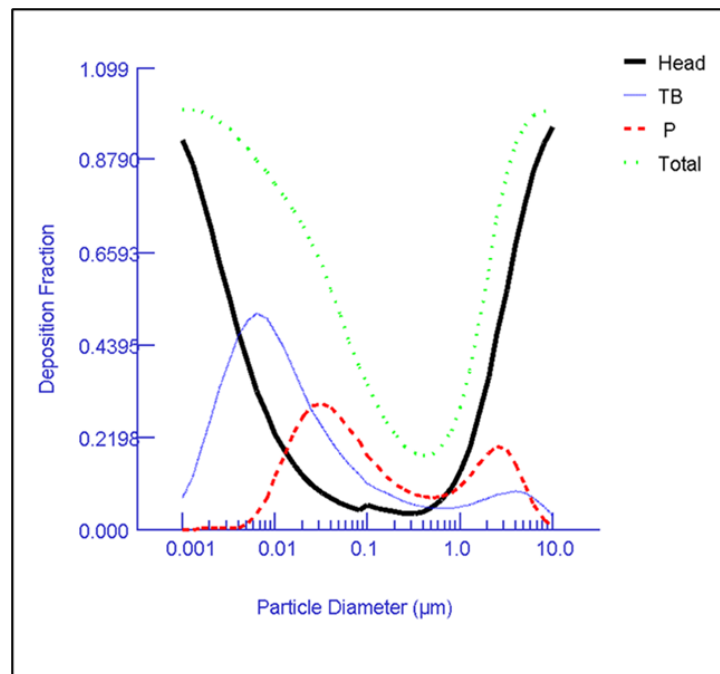


Figure 2.2 Deposition fraction of particles in different regions of the respiratory system according to the particle size. Head, TB, and P are the representatives of extra-thoracic, tracheobronchial, and alveolar regions, respectively. Total means the overall deposition in the three regions [53, 54].

The smallest and largest particles deposited in the respiratory tract are of the size of ~ 1 nm and ~ 10 μm . These particles are mostly deposited in extra-thoracic region as the first line of defence against the inhaled particles. This region includes the nasal and oral passages, pharynx, and larynx. The highest deposition in the alveolar region is related to the particles with the diameter of 20-30 nm

and 2-3 μm [54]. This shows that $\text{PM}_{2.5}$ and, particularly, nano-pollutants will reach the alveolar region and deposit there.

2.5.3 Stability of Alveolar Region

The structure of the inter-alveolar septum has been designed in a specific form for an efficient gas diffusion between the air and blood compartments. It provides a large surface area, for example approximately 140 m^2 in the human lungs, and a thin layer considered as the diffusion barrier with a thickness of about $2\text{ }\mu\text{m}$ in the human lungs [55]. The alveoli's walls, surface on which gas exchange takes place, are covered by liquid. Therefore, the lungs can be considered as a network of 500 million bubbles with a prodigious surface area. This structure is intrinsically unstable. The liquid lining the inside surface of the alveoli creates the surface tension which results in the development of large forces tending to collapse the alveoli. To prevent this problem, alveolar type II cells lining the alveoli secrete a lipoprotein material called pulmonary surfactant or lung surfactant (the thin green layer in Figure 2.3).

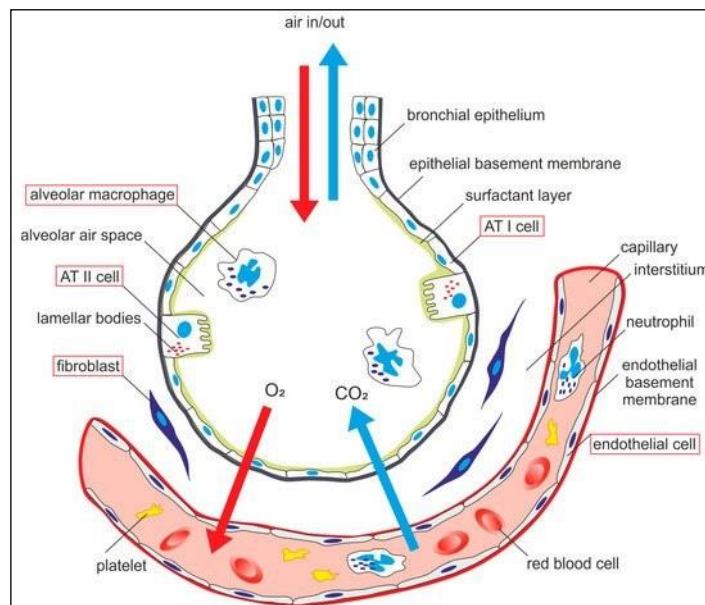


Figure 2.3 The structure of alveoli [56]. The tissue barrier consists of two layers of cells: the endothelium layer faces the capillary lumen and the epithelium faces the alveolar lumen [55]. The first barrier that inspired air meets is the alveolar lining fluid called pulmonary surfactant (green layer).

In fact, the primary function of this surfactant is to lower the surface tension in the alveoli. Therefore, the stability of the alveolar region is enhanced [15].

2.5.4 Pulmonary Surfactant: Composition and Function

Pulmonary surfactant or lung surfactant comprises phospholipid and protein components. The thin lipid-protein film of the lung surfactant consists of 90% lipids and 10% proteins. The surfactant proteins (SP) can be divided to the hydrophilic proteins, SP-A and SP-D, and hydrophobic proteins, SP-B and SP-C. The main lipid components of the lung surfactant are phospholipids, and saturated Dipalmitoylphosphatidylcholine (DPPC) constitutes 40% of the mass. It has been reported that the biophysical properties of the models with 40% DPPC were close to the calf lung surfactant extract.

This surfactant is responsible for reducing the surface tension to values below 2 mN/m at the alveoli air-liquid interface considered as the first barrier that inspired air meets before entering the blood circulation. Decreasing the surface tension in the aqueous hypophase lining the alveoli results in the reduction of total work related to the inspiration in the breathing cycle [16, 57]. Due to the periodic expansion-compression of the air-liquid interface arising from the breathing cycle, the surface tension of this interface never reaches the equilibrium state. Sequential inspiration-expiration phases result in the air-liquid interface deformation, and, in turn, the continuous perturbations in the surface tension. Upon inspiration, the area expands due to the lung inflation (expansion). This causes a local decrease of the surfactant molecules at the interface. Consequently, a driving force for the mass transfer of the molecules of the pulmonary surfactant from the aqueous subphase to the air-liquid interface is created and surfactant adsorption at the interface occurs. During expiration, the interface contracts and becomes oversaturated with the pulmonary surfactant molecules. This oversaturation leads to the desorption of surfactant at the interface. These changes in the adsorption of surfactant molecules at the interface results in the continuous variation of surface tension. In fact, there is a surface tension hysteresis in this system which manifests its viscoelastic behaviour (Figure 2.4).

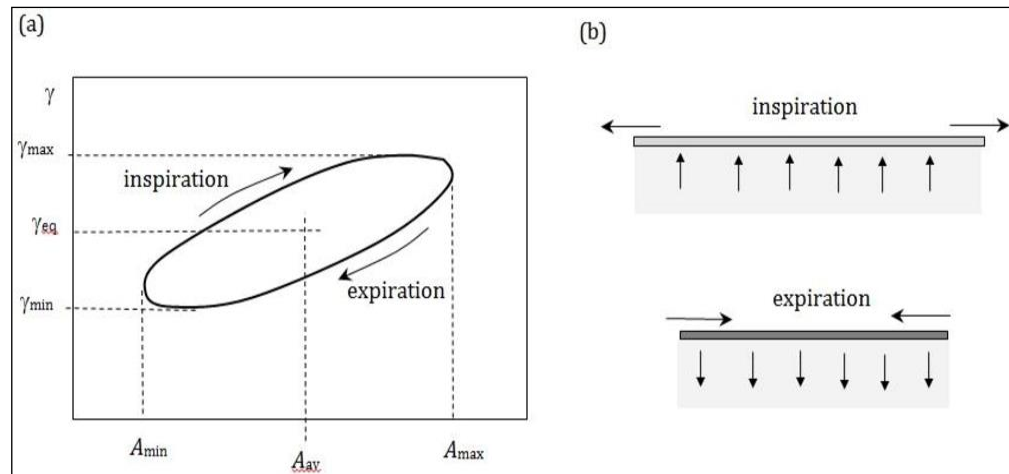


Figure 2.4 Breathing cycle consisting of inspiration and expiration. (a) The plot of surface tension (γ) vs. surface area (A) which shows surface tension hysteresis, and (b) adsorption/desorption of the surfactant at the air-liquid interface [58].

The kinetics of the adsorption/desorption of the surfactant molecules at the air-liquid interface must be preserved within a certain regime. This surface tension can be altered by different reasons, such as lung diseases or inhaled materials. These materials change the surface concentration of the surfactant and/or cause inactivation of the pulmonary surfactant which, in turn, affect the surface tension and its hysteresis shape [58]. In fact, the mechanics of breathing and the lifetime/fate of the air particulate matter are critically affected by the interactions of these particles with the layer of the pulmonary surfactant.

2.5.5 Proposed Model of Pulmonary Surfactant: DPPC

To investigate the effects of nano-pollutants on the interface covered by lung surfactant, DPPC monolayers are used as a model [16, 59-63]. DPPC, mostly known as 1,2-dipalmitoyl-sn-glycero-3-phosphocholine, is a type of lecithin. It is a zwitterionic surfactant with phosphocholine as the hydrophilic head group located in the position 3 of the backbone of glycerol (Figure 2.5).

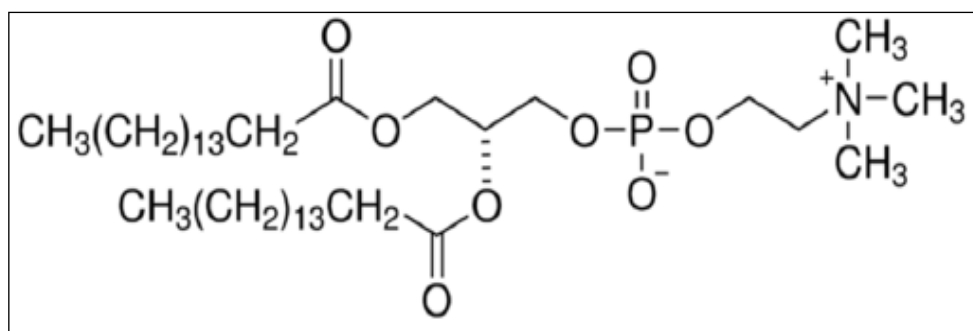


Figure 2.5 Chemical structure of DPPC.

As Figure 2.5 shows, this glycerophospholipid possesses two straight saturated acyl chains or fatty acid residues in the positions 1 and 2. Therefore, during the compression of the air-liquid interface, it can form a highly lateral packed monolayer to achieve the near-zero surface tension [64, 65].

Table 2.1 The summary of the characteristics of the alveolar region, pulmonary surfactant, and DPPC molecule.

Number of Alveoli	500 million [15]	Thickness of the Liquid Layer of Pulmonary Surfactant	0.1–0.9 μm [66]	Diameter of the Hydrophilic Head of DPPC	0.63 nm^2 [67]
Total Surface Area of the Inter-Alveolar Septum in Human Lungs	140 m^2 [55]	Percentage of the Phospholipids in the Pulmonary Surfactant	90% [16]	Length of the Hydrophilic Head of DPPC	1 nm [67]
Thickness of the Gas Diffusion Barrier in Alveoli	2 μm [55]	Percentage of DPPC in the Pulmonary Surfactant	40% of the mass of the Phospholipids [16]	Length of the Hydrophobic Tail of DPPC	2.9 nm [67]

Table 2.1 summarises the properties of the alveolar region, pulmonary surfactant, and DPPC molecule.

2.6 Effects of Nanoscale Materials/Pollutants on the Interfacial Properties of the Systems of Pulmonary Surfactant and Industrial Surfactants

It is important to define appropriate quantities of characteristics for the microscopic layers consisting of nanoparticles and air-liquid interfaces, so that the description of such characteristics at a macroscopic scale can be useful. Interfacial tension is one of these properties which can be measured (using methods described in Section 2.7) after inducing nanoparticles onto the air-liquid interfaces of a system containing surfactant. These properties, considered as the indicators of the system's behaviour after stresses caused by nanoparticles entrance, are dependent on different factors, which will be discussed in this section.

In systems consisting of two fluids and solid particles, partial wettability properties of particles give a nonhomogeneous character to interfacial layers due to the formation of three interfaces. The behaviour of nanoparticles and their toxicity are influenced by their physical and chemical properties [68]. When they enter the respiratory system, these nanoparticles affect the physicochemical properties of the air-liquid interface of the lung surfactant. Therefore, evaluation of the interactions between nanoparticles and lung surfactant provides a fundamental basis of the mechanism for the adverse effects of nano-pollutants on the respiratory system and their toxicity. These interactions affected by the particles' surface characteristics play an important role in nanomedicine and nano-safety issues [69, 70]. It has been demonstrated that surface properties of engineered nanoparticles change their aggregation, which in turn, alters their toxicity and their environmental impact [71, 72]. To assess these types of interactions, the DPPC as a component of the lung surfactant has been frequently used in the context of both nano-safety and physicochemical studies [73, 74].

In addition to the pulmonary surfactant, the interactions of industrial surfactants with nanoparticles have been studied comprehensively. A wide range of technologies and industries are dependent on comprehending and harnessing the interfacial behaviour of the gas and liquid in the structure of the foams. Enhanced oil recovery (EOR) [75, 76], wastewater treatment [77, 78], food [79],

cosmetic [80], and pharmaceutical [81] industries are benefiting from the foams in their operation plants and/or product formulations.

In many of these applications, nanoparticles are often used, and often accompany with a surfactant known as the main foaming agent. In fact, this combination is used to produce foams of intended strength and stability [82-85]. Silica (SiO_2) [83, 86-94], iron oxide (Fe_2O_3) [83], gliadin [84], and aluminium oxide (Al_2O_3) [86] nanoparticles, as well as multi-walled carbon nanotubes (MWCNTs) [95] and nano-clay [82] are the examples of nanomaterials which have been used in this field of research.

In the systems where only surfactants are used as the agent for producing foams, the type of surfactant and its concentration are two important factors which control the foaming and interfacial properties of the solution [96]. The alteration of surfactant concentrations affects its adsorption at the interface, and in turn, the interfacial tension. When solid nanoparticles are utilised in the dispersions of two immiscible fluids such as foams, there are changes in interfacial characteristics of the system. These changes are due to not only the existence of the surfactant, but also the result of surfactant/nanoparticles interactions at the gas-liquid interface [97-100]. Besides the concentration and type of the surfactants [101], the concentration [17, 102], size [103], surface charge [104], and hydrophilicity/hydrophobicity [63] of the nanoparticles will also affect the interfacial interactions of particles and surfactants such as pulmonary surfactant and industrial surfactants.

In this section, the reported studies related to the nanoparticles' characteristics effective on the interactions between nanoparticles and surfactants such as pulmonary surfactant and industrial surfactants at the air-liquid interface are presented.

2.6.1 Surface Charge

The surface charge of nanoparticles can be considered as a characteristic of nanoparticles' surface which is linked to their interfacial behaviour at the air-liquid interface. It has been shown that the translocation of nanoparticles across

the monolayer of the pulmonary surfactant is regulated by the particles' surface charge [105]. Based on models of pulmonary surfactant, it has been observed that the nanoparticle–vesicle aggregates are resulted from electrostatic interactions [104].

In a study which evaluated the effects of surface charge of particles on a lipid bilayer as the biomimetic lung surfactant, adsorption of negatively charged particles onto the bilayer was observed whereas positively charged ones were not adsorbed onto this bilayer [106]. In other studies, the effect of the surface charge density on the translocation of nanoparticles across the pulmonary surfactant was investigated using molecular dynamics simulations [107, 108].

2.6.2 Hydrophilicity/Hydrophobicity

The procedure through which the complexes of surfactant-solid particles are formed and positioned at the air-liquid interface strongly depends on the hydrophilicity or hydrophobicity of the particles. The value of the three-phase contact angle varies between 0° and 180° . The angles of 0° and 180° are related to absolutely hydrophilic and hydrophobic solid particles, respectively. In these two extreme cases, the particle is immersed only in one of the fluidic phases, i.e., the hydrophilic and hydrophobic phases. The only particles which may be located at the interface are those ones classified as partially hydrophobic or hydrophilic particles with contact angles of $0^\circ < \theta < 180^\circ$. Therefore, the surface nature of the particle affects the degree of wettability because it influences the contact angle [109]. It means that the hydrophilicity and hydrophobicity of particles affect their adsorption and agglomeration onto the interfacial layer which affect the toxicity of particles when it comes to the biological systems.

It should be noted that hydrophilicity/hydrophobicity can also be changed through interactions with a surfactant. Figure 2.6 shows that the hydrophobicity of a negatively charged colloidal particle is altered due to the interactions with the molecules of a cationic surfactant. At higher concentrations of the surfactant, another layer of surfactant molecules can be adsorbed onto the previous layer. This new layer will result in the formation of hydrophilic particles.

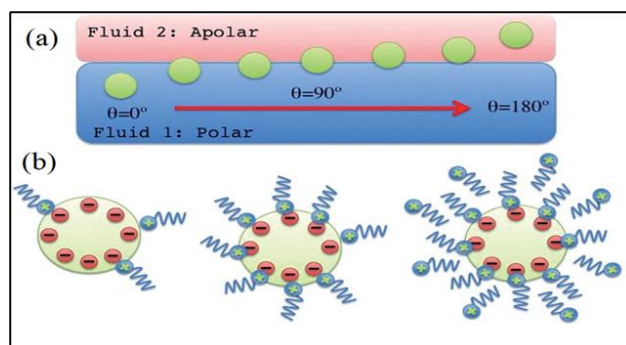


Figure 2.6 (a) Positioning of a particle in a fluid-fluid interface according to the contact angle, θ , and (b) change of the hydrophobicity of a negatively charged particle due to the interactions with a cationic surfactant [109].

In the systems containing pulmonary surfactant, increasing the hydrophobicity of nanoparticles intensifies the particles' retention at the surfactant monolayer, which in turn, causes deterioration in the surface activity of pulmonary surfactant [110]. It has also been reported that different nanoparticles with various hydrophilicity/hydrophobicity features change the structures of the monolayer of the DPPC in different ways (Figure 2.7).

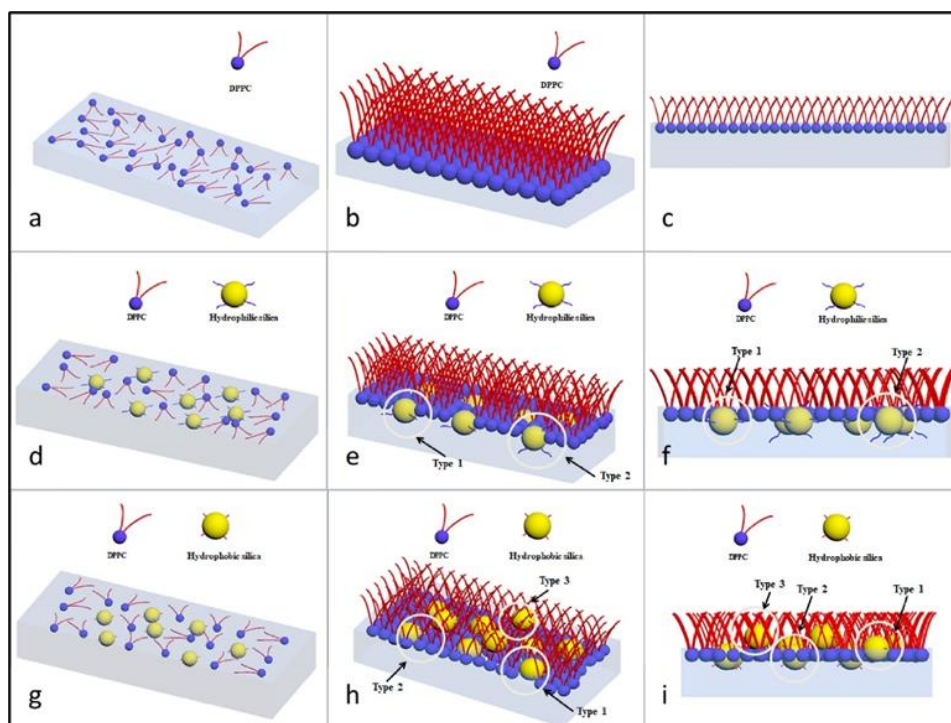


Figure 2.7 Different types of the structure at the air-liquid interface for pure DPPC monolayer (a-c), mixed monolayer of DPPC and hydrophilic silica nanoparticles (d-f), and mixed monolayer of DPPC and hydrophobic silica nanoparticles (g-i) [63].

As shown in Figure 2.7 in [63], both types of hydrophilic silica nanoparticles are in water and covered by the DPPC molecules. However, the hydrophobic nanoparticles can be arranged into different ways (Figure 2.7, g-i). Some of them can stay partially in water (see type 1 and type 2 in Figure 2.7, h-i) and some tend to stay on the top of the DPPC monolayer (see type 3 in Figure 2.7, h-i) [63]. The reason is due to the squeezing effects among particles and also the interactions between the hydrophobic groups of silica nanoparticles and hydrophobic tails of DPPC [63].

2.6.3 Size

The size of nanoparticles is a significant factor in the study of the interactions between particles and pulmonary surfactant. Studies have shown that the phase transition behaviour of the pulmonary surfactant under compression depends on the size of the particles [9, 111]. The effects of different sizes of nanoparticles on surface activity, line tension, and domain morphology of both pure DPPC monolayers and pulmonary surfactant model systems have been studied. The functional and structural behaviour of the pure DPPC system depends on the size of nanoparticles. For the nanoparticles of small size (~12 nm), the phase transition is not visibly disturbed whereas a drastic disruption of the domain structures were observed for larger nanoparticles (~136 nm) [103]. Effects of the size of nanoparticles on the interactions between particles and air-liquid interfaces have been investigated through molecular dynamics simulations. The hydrophobic nanoparticles with the size of 3 nm were immersed into the aqueous phase deeper than those nanoparticles with the size of 5 nm [112].

2.6.4 Concentration

The interfacial tension of a three-phase system consisting of the air-liquid interface and silica nanoparticles from equilibrium and dynamic points of view has been investigated [17]. Results indicated that the equilibrium surface tension

is a function of particle's concentration, and there is a critical quantity of particle concentration, beyond which all the surfactant (CTAB) content is removed from the bulk due to the interactions of surfactant molecules with nanoparticles [17].

Effects of different concentrations of polyorganosiloxane (AmorSil20) on a model of lung surfactant monolayer have been investigated [102]. It was assumed that nanoparticles were coated with surfactant molecules in a self-assembly manner, remained at the air-liquid interface and showed hydrophobic surface characteristics [102].

The impact of different concentrations of polystyrene particles on DPPC in terms of surface pressure, the structure of surfactant and its topology has been evaluated [60]. Moreover, the particle placement after interaction with surfactant was visualised in this paper. It was shown that in the presence of particles, smaller condensed domains of DPPC with a larger quantity form. The particles also remained closely associated with the condensed domains [60].

2.6.5 Shape

The role of the particles' shape has been overlooked in many of the previous studies that investigate the interactions between the particles and air-liquid interface of pulmonary surfactant. There were a few studies in which the researchers have used coarse-grained molecular dynamics (CGMD) simulation (Figure 2.8) to find out effects of different shapes of nanoparticles on their translocation across the surfactant monolayer during breathing cycle simulated by compression and expansion [10, 113-115]. They reported that shape anisotropy, initial orientation and rotation processes are important parameters in the interactions between particles and lipid bilayers.

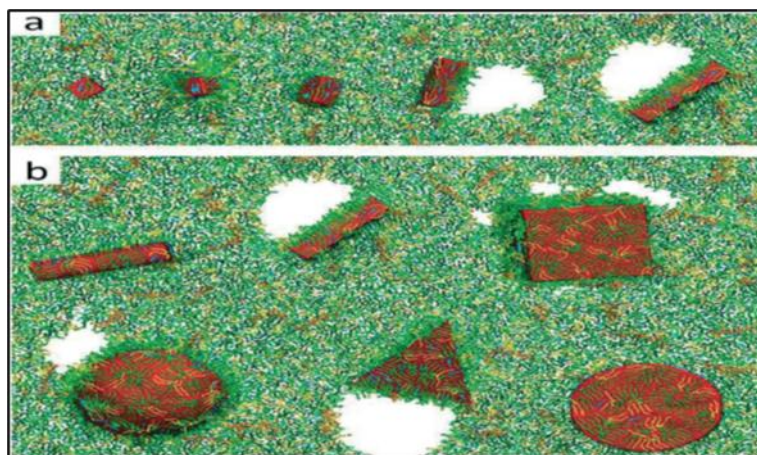


Figure 2.8 The perturbation of the pulmonary surfactant by hydrophobic particles including (a) cuboid nanoparticles with different lengths and the same width and (b) nanoparticles of various shapes [114].

However, it should be addressed that despite the acceptable number of simulation-based studies on the effect of the shape of particles, it is difficult to find sufficient experimental studies for verifying the accuracy of these simulations.

2.7 Pulmonary Surfactant under Dynamic Conditions

In the interfacial system of the pulmonary surfactant, the kinetics play an important role. Many of the previous studies have used Langmuir trough to simulate the lung conditions and/or study the interactions of particles with pulmonary surfactant at its air-liquid interfaces [116-119]. The Langmuir trough is mainly used to understand the quasi-static mechanical function and structure of the pulmonary surfactant or the lipid films [120]. The rate of the expansions and compressions in the Langmuir trough are as slow as 8 minutes per cycle [121]. This slow speed in the Langmuir trough makes it a suitable instrument to characterise the surfactant films under the quasi-equilibrium conditions. However, it can also be considered as a drawback when it comes to the studies related to the breathing cycles. The real physiological rates of expansion and compression of the lung surfactant are considerably faster than the rates

occurring in the Langmuir trough [122]. As mentioned before, due to this continuously periodic expansion-compression of the interface, the interfacial tension of the air-liquid interface in the alveolar region of the lungs never reaches the equilibrium state [58]. Therefore, using the methods that simulate the dynamic conditions of the lungs becomes of a great importance. The drop/bubble tensiometers are the effective techniques to investigate the pulmonary surfactant under the dynamic conditions because these instruments can make oscillations at a much higher speed and being much closer to the actual physiological rates [120].

2.7.1 Dynamic Conditions versus Static Assumptions

The static interfacial tension refers to the value of interfacial tension in the thermodynamic equilibrium. This interfacial tension is independent of time. The dynamic interfacial tension depends on the time of surface age. The surface age is the time from the start of the formation of an interface to the time when the measurement is conducted [123]. Although the Langmuir trough with the Wilhelmy plate is a popular and convenient method for measuring dynamic interfacial tension over time [124], its low speed of the expansion-compression is not perfectly simulating the dynamic conditions of lungs and the interfacial changes happening during the breathing cycle. This characteristic depends on the type of the testing device. Some Langmuir trough devices are working at the frequencies from 0.005 Hz to 0.03 Hz whereas some other Langmuir troughs can work in the range of frequencies as high as 4 Hz [125-127].

In the studies related to the pulmonary surfactant or its models, the best instruments are the ones that can simulate the expansion-compression cycles of the breathing cycles in terms of both area perturbation and frequency. The profile analysis tensiometer used in this study is suitable to simulate the frequencies of the breathing cycles related to different age groups. These frequencies including 0.1 Hz, 0.125 Hz, 0.25 Hz, and 0.5 Hz, can simulate the range of breathing frequencies from adults to 5-year-old age group. Therefore, the dynamic

oscillatory conditions of the air-liquid interface of the pulmonary surfactant are fulfilled using the profile analysis tensiometer.

In the Langmuir trough device, the monolayer consists of only one lipid leaflet [128]. Moreover, during the oscillation in the Langmuir trough device, this monolayer is the target of perturbation and surface area deformation. Therefore, this method may not perfectly reflect the complex phenomena happening between the subphase and the interface during the oscillation. In contrast, when the drop profile analysis tensiometer is used, the oscillation of the whole droplet containing the pulmonary surfactant and/or nanoparticles and the subphase is conducted. This oscillatory-related way of operation is another reason to use tensiometers to simulate the dynamic conditions of the lung in this study.

Overall, it is difficult to state which method of the interfacial tension measurement is the best technique. In fact, choosing the method is dependent on the nature of the interface, rheology of the liquid, range of the temperature, range of the interfacial tension, requirements of precision, accuracy, speed, and cost, as well as the practical considerations of the convenience of the technique [124]. It should also be noted that the combination of the different methods can provide the complementary possibilities of studying the air-liquid interface of the pulmonary surfactant and/or DPPC as a representative model of the pulmonary surfactant [129].

2.7.2 Mixture of Nanoparticles versus Single-Type Nanoparticles

Most of the previous studies evaluating the effects of the nanoparticles on the pulmonary surfactant or DPPC monolayers are only considering a single-type nanoparticle at a time. It means that these studies consider only one or more types of nanoparticles. Then, using different interfacial tension measurement techniques, they often measured the effect of each type of nanoparticle on the structure and the interfacial tension of the interface [61, 74, 125, 130, 131].

There are also some studies using a model of airborne particulate matter to investigate their interactions with the pulmonary surfactant or DPPC as a model

of this surfactant [18]. These studies show that the $PM_{2.5}$ affects the morphology and phase behaviour of the DPPC monolayer. The model of the $PM_{2.5}$ used in these studies was usually diesel particulate matter. The average size of these particles was between 200 nm to 951 nm which makes them to be considered as $PM_{2.5}$. The investigation of the elemental composition of these model airborne particulate matter shows the presence of many elements including carbon, nitrogen, hydrogen, sulphur, oxygen, magnesium, aluminium, silicon, potassium, calcium, phosphorus, zinc, lead, copper, nickel, iron, manganese, calcium, and chromium [18, 19]. Due to the complex composition and heterogeneity of these models, it is difficult to understand the mechanism for the interactions of particles with the DPPC molecules. Moreover, the surface properties of each type of particles in these mixture models are different. Therefore, it is impossible to understand which types of particles have the most dominant effect on the lung surfactant or the DPPC.

It is important to understand the effects of the mixture of nanoparticles on the DPPC as a model of lung surfactant. However, it is more critical to build a fundamental understanding and a methodology about these effects. These studies and the obtained results should help the prediction of the most dangerous nanoparticles in the mixtures in terms of toxicity and adverse effects on the lung surfactant. Moreover, these studies should be a good indicator for the actual compositions of the mixed nanoparticles that have the most adverse effect on the lung surfactant due to the interparticle interactions and nanoparticle-surfactant interactions. To achieve this aim, effects of the mixture of nanoparticles on the DPPC in the bulk of the solution and at the air-liquid interface should be studied systematically. Although the toxicity of these mixtures in the lungs has been studied in some previous research [132], the interfacial properties of the mixed nanoparticles interacting with DPPC have not been investigated before.

2.7.3 Interfacial Rheology: A Potential Method for Investigation of Pulmonary Surfactant under Real Conditions

Using a profile analysis tensiometer, the surface area of a drop can be oscillated. The advantage of this method over the Langmuir trough is the more homogeneous distribution of the expansion and compression of the monolayer over the whole area. The studies related to the drop oscillation are used to measure the dilatational rheology parameters of the fluid-fluid interfaces. These parameters include elasticity and viscosity [133, 134]. The physiology of breathing highlights the importance of studying the rheological properties of the DPPC monolayers at the air-liquid interface.

The normal respiratory mechanics of the lungs is determined by different factors including the liquid layer containing the lung surfactant. Therefore, measuring the rheological properties of the air-liquid interface covered by the lung surfactant is of a great importance. The interfacial tension and rheology of this interface are all clinically important in different aspects such as lung diseases and drug/gene delivery to the respiratory system [22].

For the cholesterol and other phospholipid monolayers such as DPPC, the dependence of the dilatational elasticity and viscosity on the dynamic parameters such as the amplitude of the surface area oscillation and frequency has been studied using the tensiometer and linear approach [135]. Moreover, the rheological properties for the monolayers of the mixed cholesterol and phospholipids have been investigated for their comprehensive applications in preparing liposomes used in medicine [136].

To simulate the real conditions of lungs, these types of oscillatory studies should also be done when it comes to the interactions of nanoparticles and DPPC molecules. These studies are important from two main aspects. The first is related to the nano-sized pollutants and their interactions with the lung surfactant during the breathing cycles. The second aspect is attributed to the drug delivery to the lungs in which the drug deposition and retention under the dynamic breathing cycles are important [137].

Upon inhalation of nanosized pollutants, these particles meet the lung surfactant as the first contact line. The interactions of these particles with the lung surfactant change the normal interfacial rheology of the lung surfactant

which, in turn, affects the respiratory performance [135]. Therefore, the study of interfacial rheology of the lung surfactant in the presence of nanoparticles not only reveals the diverse effects of these particles on the lung surfactant, but also clarifies the significant characteristics of these particles that mainly affect the normal performance of the lung surfactant. The major characteristics can be their concentrations, sizes, shapes, and surface properties [138]. It has been reported that nanocarbons with different wettability properties and surface areas affect the rheological properties of the lung surfactant in different ways [129].

Most of previous studies on the interactions of the nanoparticles and lung surfactant or DPPC as a model of the lung surfactant have used the linear approach of the Fourier transform to measure and interpret the rheological parameters [74]. Some studies have shown that the linearity or nonlinearity of the system are dependent on the composition of the system in terms of the presence and absence of nanoparticles. For example, it has been shown that incorporating the silica nanoparticles into the lipid monolayers results in deviation from the linearity even at the amplitudes as low as 5% [139].

It should be mentioned that the linearity and nonlinearity of these interfacial systems must be checked before the studies. The chemical composition of the system and the operational conditions such as frequency and amplitudes affect the degree of nonlinearity of system. In the case of nonlinearity, the use of a linear approach related to the Fourier transform will not lead to any accurate results. Therefore, nonlinear approaches for these interfacial systems should be applied. In fact, the nonlinear interfacial dilatational rheology can be used as a useful tool to understand the microstructure of the air-liquid interfaces [20].

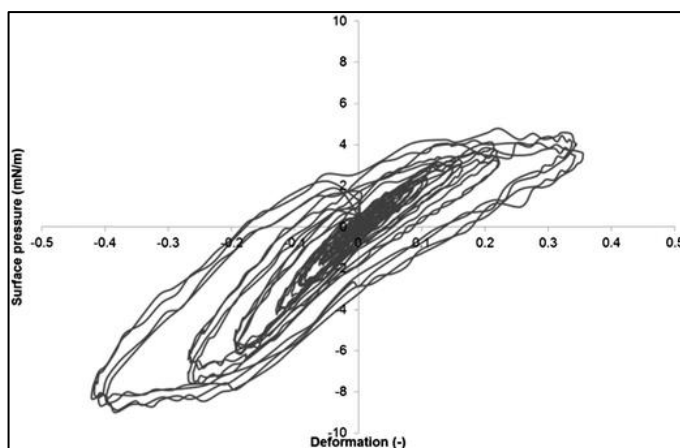


Figure 2.9 Lissajous plot obtained during the amplitude sweep of the air-water interface stabilized by the oligofructose ester with the mono-unsaturated fatty acid *cis*-9-hexadecenoic acid as the hydrophobic group at 25 °C [20].

Figure 2.9 shows that Lissajous plots are used in the nonlinear interfacial dilatational rheology approach. Using this method, the behaviour of the interfaces and their microstructure can be understood even at the regimes beyond the linear ranges [21]. The details of this approach will be described in Chapter 7.

2.8 Summary

This chapter has demonstrated the serious environmental concerns about the air pollution and, specifically nano-sized pollutants which can adversely affect the human health. Based on the fundamental knowledge provided on the anatomy of the respiratory system, it has been shown that the fate of the air pollutants, especially nano-sized ones, is dependent on their interactions with the lung surfactant. It has also been shown that the interactions of the nanoparticles and different types of surfactants are dependent on different factors such as surface charge, hydrophilicity/hydrophobicity, size, concentration, and shape of the nanoparticles.

The reasons behind choosing the profile analysis tensiometer for this study have also been discussed. The novelty aspects of this research study in comparisons to the previous studies have also been discussed. In this study, the

evaluation of the mixture of nanoparticles in contact with DPPC has been done in a systematic way. Moreover, the nonlinear interfacial rheology approach has been suggested to use for the interfacial systems of nanoparticles-DPPC.

Chapter 3

Experimental Work and Analytical Methods

3.1 Preparation of Solutions / Dispersions

3.1.1 Solutions of Ionic Surfactants

The ionic surfactants were cetyltrimethylammonium bromide (CTAB) and sodium dodecyl sulfate (SDS) as cationic and anionic surfactants, respectively. CTAB (Figure 3.1, a) with the chemical formula of $[\text{CH}_3(\text{CH}_2)_{15}(\text{CH}_3)_3\text{NBr}]$, a molecular weight of 364.46 g/mol, and a purity of 99%, under the brand name of AnalaR was supplied by BDH Chemical Ltd., United Kingdom. SDS (Figure 3.1, b), with $\text{CH}_3(\text{CH}_2)_{11}\text{SO}_4\text{Na}$ as its chemical formula, a molecular weight of 288.38 g/mol, and the minimum assay of 99% was purchased from SIGMA-ALDRICH CHEMIE GmbH, China.

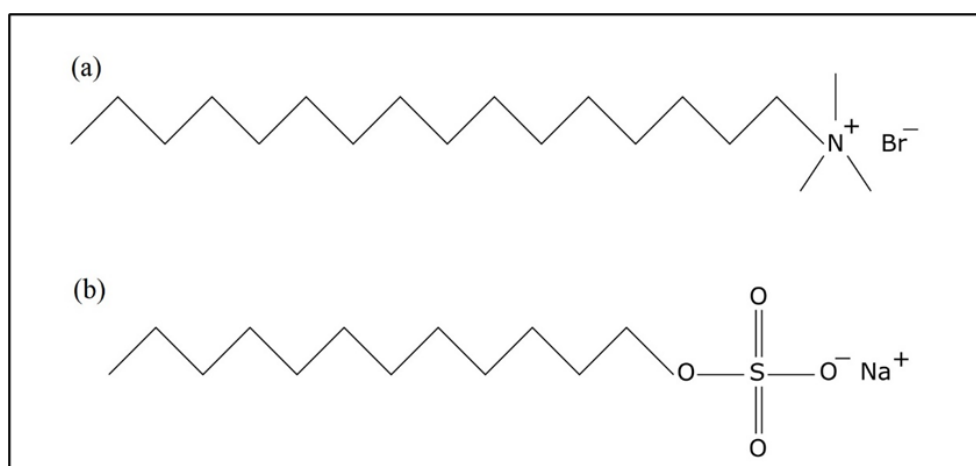


Figure 3.1 Molecular structures of (a) CTAB and (b) SDS.

Due to the reliable solubility of both these ionic surfactants in water, the aqueous solutions of them were prepared. The water purification system was PURELAB® Option-Q7 (ELGA LabWater, United Kingdom). This machine provides ultrapure water or deionised (DI) water. The bulk resistivity of the produced water was greater than 18 MΩ.cm. This DI water was the one used in all the following sections.

According to the molecular weight of CTAB, a certain amount of its powder was weighed and dissolved in the ultrapure water to achieve the main stock solution with a concentration of 1×10^{-1} M. The mixing operation was performed on a magnet stirrer at the room temperature and under the fume hood. Then, using the dilution method, other aqueous CTAB solutions with concentrations of 1×10^{-2} , 5×10^{-3} , 2.5×10^{-3} , 1×10^{-3} , 5×10^{-4} , 1×10^{-4} , 5×10^{-5} , 1×10^{-5} , 5×10^{-6} , and 1×10^{-6} M were prepared. Because of the nature of CTAB as the surfactant, the bubbles were formed during adding water and mixing process. Therefore, after preparing each solution, specially at high concentrations, it was required to put the sealed container of the sample in the ultrasonic bath to make sure of degasification. An ultrasonic bath of Fisher brand (FB15053, Fisher Scientific, United Kingdom) was utilised for mixing, homogenising, and degassing of the bubble-contained solutions. To check the complete elimination of the bubbles in solutions, a visual test was done. Then, the degassed sample of the desired concentration was diluted to prepare the next solution. The same procedure was applied for SDS solutions.

3.1.2 Dispersions of Nanoparticles in Ionic Surfactants

To prepare the dispersions of nanoparticles in ionic surfactants, i.e., CTAB and SDS, titanium dioxide (TiO₂) nanoparticles, known as Titanium (IV) Oxide nanoparticles, with anatase crystal form were chosen. This choice is based on the comprehensive applications of this crystal form of TiO₂ nanoparticles in the industries (Section **Error! Reference source not found.**). The anatase form of TiO₂ has a lower surface energy in comparison with the other crystal form called rutile [140].

These nanoparticles were purchased from Ionic Liquids Technologies GmbH (IoLiTec), Germany. The purity of this white powder and the size of nanoparticles were 99.5% and 20 nm, respectively. Based on the supplier's confirmation, the particle was spherical. The specific surface area of the particles was more than 120 m²/g (Table 3.2).

The dispersions of TiO₂ nanoparticles with anatase form in the ionic surfactants (CTAB and SDS) were prepared by adding the aqueous matrix (surfactant solution) to the dry powder of the nanoparticles upon continuous stirring on the magnet stirrer in the glovebox at room temperature. This procedure was done in a volumetric flask. Therefore, the amount of aqueous solution added to the dry powder was based on the level line of the flask. To ensure the proper homogenisation of the mixture and avoid any nanoparticle agglomeration, the samples were left to be stirred overnight at room temperature. The concentration of TiO₂ nanoparticles at the solutions was fixed at 0.1 wt %, in both CTAB and SDS solutions with variable concentrations of the surfactants.

Each solution and dispersion described in sections 3.1.1 and 3.1.2 were put in an ultrasonic bath at room temperature for 30 minutes. Then, the interfacial tension of each sample was measured and repeated three times to obtain the average amount and calculate the standard deviation. The results related to the ionic surfactant solutions and the dispersions of TiO₂ (anatase) have been reported in Chapter 5.

3.1.3 Solutions of DPPC as a Single-Component Model of Lung Surfactant

DPPC, introduced in section 2.5.5, was purchased from Avanti[®] POLAR LIPIDS Inc., USA. The physical state of this phospholipid was powder. Its chemical formula and molecular weight are C₄₀H₈₀NO₈P and 734.039 g/mol, respectively. Based on the certificate of analysis for this product, its purity was more than 99%. The critical micelle concentration (CMC) of DPPC is equal to 0.46×10⁻⁹ M [141].

The DPPC was dissolved in ethanol (99.8% purity, Fisher Scientific, United Kingdom) with a concentration of 1 mg/ml or 1.4×10^{-3} M using the ultrasonic bath. A 25 ml volumetric flask was used for this purpose. To measure the interfacial tension, 400 μ L (0.4 ml) of the mentioned DPPC in ethanol solution was added into 10 ml of DI water. This means that 5.6×10^{-7} mol of the DPPC was put into a total amount of 10.4 ml of solution consisting of both DI water and DPPC in an ethanol solution. Therefore, the final concentration of the DPPC in the aqueous solution was 5.38×10^{-8} M.

The procedures of selecting the solvent for DPPC have been discussed as below:

This phospholipid (DPPC) is only slightly soluble in water. Therefore, organic solvents such as chloroform is normally used for dissolving this powder.

At first, chloroform was chosen as the solvent. According to the previous studies on DPPC monolayers used in the Langmuir-Blodgett Trough method, the concentrations of DPPC in chloroform, as the stock solution, can be varied from 0.10 mg/ml to 1.22 mg/ml [60, 116, 131, 142-144]. In the cases of microfilm based techniques such as pendant drop and captive bubble methods, the DPPC concentrations in chloroform have been reported to be in the range of 0.09 mg/ml to 0.15 mg/ml [135, 145]. Therefore, this study also used the DPPC concentration of 0.1 mg/ml in the chloroform. It should be noted that the concentration of DPPC in the lung is more than 15 mg/L [146].

40 μ L of the mentioned solution of the DPPC in chloroform was added to 10 mL DI water. This solution was put in an ultrasonic bath at room temperature for 15 minutes before measuring the interfacial tension using a profile analysis tensiometer. Upon the preparation of samples, it was observed that the organic phase was separated from the aqueous phase. In fact, due to the higher density of chloroform (1.49 g/cm^3) in comparison with water, this phase separation easily happens, which results in the formation of a non-homogeneous solution. When this solution is pumped into the tensiometer's chamber, the composition of the droplet at the tip of the capillary is variable and dependent on the specific point of sample where the solution was pumped using the tubes and syringe of the equipment.

Another way to use the DPPC in chloroform in the tensiometer was to inject the chloroform solution to the water droplet formed at the tip of the capillary. Figure 3.2 shows injection of the chloroform solution and withdrawal of the micro-syringe afterwards. It has been stated that a time of 15 min was required for the evaporation of the solvent, i.e., chloroform, which resulted in the formation of lipid monolayer on the droplet [135, 145].

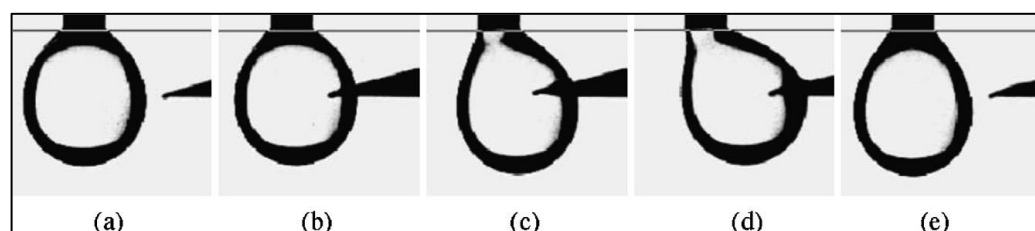


Figure 3.2 The deposition of the DPPC from the chloroform solution on the surface of the water droplet [135].

To conduct this method, an orifice in the chamber of the tensiometer is required. This orifice is used to put the needle of the micro-syringe inside the chamber and deposit the DPPC solution into the droplet as shown in Figure 3.2. This type of measurement chamber was normally performed using a home-made one. As the chamber in the tensiometer used in this study did not contain any orifice (Figure 3.3), it was not possible to use this method of the DPPC deposition.

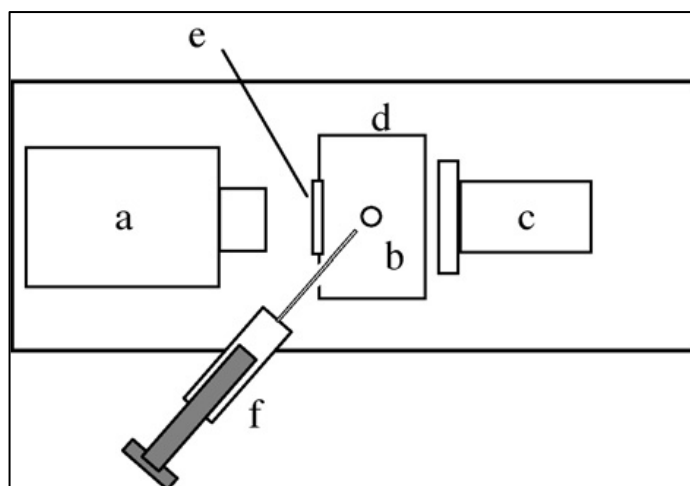


Figure 3.3 The specific home-made chamber in the tensiometer set-up. The different parts include (a) camera, (b) pendant drop in the chamber, (c) light source, (d) chamber, (e) specific optical glass, and (f) micro-syringe which enters the measurement chamber through the orifice [135].

In the tensiometer of this study, the chamber does not contain any orifice. Therefore, the capillary was taken out of the chamber before the start of the experiment. Then, it was attempted to deposit DPPC in chloroform solution on the droplet. However, the movement of capillary and locating it in the chamber after the deposition resulted in the falling and failure of the droplet. Therefore, the methods such as using the chloroform in the procedure of preparing the DPPC solution were not suitable for profile analysis tensiometer set-up. This is because of the phase separation of the organic phase, when the bulk of the solution was prepared, and/or lack of the orifice in the tensiometer set-up when the deposition was supposed to be used.

To avoid these drawbacks, a substitution of the chloroform as the solvent of DPPC was considered. Ethanol was chosen because it is a polar solvent which is miscible with water. Moreover, the DPPC was dissolved well in this organic solvent, therefore, there was no phase separation between organic and aqueous phase.

3.1.4 Dispersions of Nanoparticles in DPPC Solutions

Two categories of nanoparticle dispersions in DPPC solutions were prepared and studied in this work. The first category was the dispersion of each individual type of nanoparticles with its different concentrations in the DPPC solution, and the second one was the mixture of different types of nanoparticles in the DPPC solution. For the second category, only one concentration of nanoparticles was considered whereas the mixing methods and types of nanoparticles were varied in the dispersions. The details of the preparation methods are described in Sections 3.1.4.1 and 3.1.4.2.

3.1.4.1 Individual Nanoparticles in DPPC Solutions

Three types of nanoparticles (purchased from Ionic Liquids Technologies GmbH-IoLiTec), Germany with their detailed specifications in Table 3.2) were used in this study. The dispersions of each type of nanoparticles, i.e., anatase form of TiO₂, rutile form of TiO₂, and carbon nanotubes, with their concentrations of 0.01, 0.02, 0.03, 0.04, and 0.05 wt % were prepared in DI water. The mixing was done by dropwise addition of water to the powder under a continuous stirring. To avoid the formation of particles agglomerates, the magnet-stirring process was continued for overnight (with a total time of 24 hours). All the above-mentioned samples were prepared at room temperature.

To prepare the samples for measurements using tensiometer, 400 μ l (0.4 ml) of DPPC in ethanol solution with a concentration of 1 mg/ml (Section 3.1.3) was added to 10 ml of each individual dispersion of nanoparticles in DI water using a Hamilton micro-syringe. These samples were ultrasonically agitated for 15 min prior to the interfacial tension and interfacial rheology measurements.

3.1.4.2 Mixture of Nanoparticles in DPPC Solutions

The mixtures of dispersed nanoparticles with a concentration of 0.01 wt % were prepared using three different methods as following:

- i. The separated dispersions of each individual nanoparticle with a concentration of 0.01 wt % in water were prepared. Then, 400 μ L of the DPPC in ethanol solution (1 mg/ml) was added to each one of them (see Section 3.1.4.1). 5 mL of each prepared sample of nanoparticle-DPPC was collected and mixed with each other. Using the same portion of each dispersion, the final concentration of nanoparticles was maintained at 0.01 wt %.
- ii. The separated dispersions of each individual nanoparticle with a concentration of 0.01 wt % in DI water were prepared. 5 mL of each sample was collected and mixed with each other. The concentration of nanoparticles in the final sample was 0.01 wt %. Finally, 400 μ L of the DPPC in ethanol solution (1 mg/ml) was added to this mixture of nanoparticles.
- iii. The nanoparticles were weighed and mixed firstly. Then, the DI water was added to this mixture so that the final concentration of the mixture of nanoparticles in DI water was maintained at 0.01 wt %. Finally, 400 μ L of the DPPC in ethanol solution (1 mg/ml) was added to this mixture.

It should be noted that the process of water addition was done drop-by-drop and under a constant stirring for all three methods. These samples were further put inside the ultrasonic bath for 15 min before interfacial tension measurements. The composition of the various mixtures of nanoparticles and the related mixing methods used for each one of them have been listed in Table 3.1.

Table 3.1 The composition of the different mixtures of nanoparticles and the mixing methods used for their preparation. The final concentration of the nanoparticles in the solution before adding the DPPC was 0.01 wt % in all cases.

Composition of the Mixture	Mixing Method		
	(i)	(ii)	(iii)
TiO₂ (Anatase) + Carbon Nanotubes	√	√	√
TiO₂ (Rutile) + Carbon Nanotubes	√	√	
TiO₂ (Anatase) + TiO₂ (Rutile) + Carbon Nanotubes	√	√	

It should be noted that the mentioned methods of mixing of nanoparticles are actually the simulation of possible ways of the interaction of nanoparticles which happens in the real life. The nanoparticles can be inhaled individually, interact with the lung surfactant, and then become mixed with each other in the alveoli (method i). The nanoparticles can also adsorb the humidity from the environment or respiratory tract, interact with each other, become mixed, then reach the alveoli, and finally interact with the lung surfactant (method ii). Or the solid nanoparticles can interact firstly while they are suspended in the air, then be inhaled into lung, and finally interact with the lung surfactant (method iii).

These mixtures were used to measure their interfacial tension using a tensiometer (Chapter 6). Moreover, one droplet of each sample was put on the SEM stub and dried, before putting into SEM for morphology observation. The SEM images of all the samples were obtained and compared.

3.2 Characterisation of Nanoparticles

Three types of nanoparticles including anatase crystal form of TiO₂ (spherical shape), rutile crystal form of TiO₂ (rod-like shape), and carbon nanotubes were purchased from Ionic Liquids Technologies GmbH (IoLiTec), Germany. The details and characteristics of nanoparticles based on the certificates of analysis, safety data sheet, and product packages provided by the supplier are listed in Table 3.2. In this table, for multi-walled carbon nanotubes, the OD and L show the outside diameter and length, respectively.

Table 3.2 Nanoparticles' characteristics provided by the supplier.

Nanoparticles	Crystal Form	Shape	Size (nm)	Specific Surface Area (m ² /g)	Purity (%)
Titanium Dioxide (TiO ₂)	Anatase	Sphere	20	>120	99.5
Titanium Dioxide (TiO ₂)	Rutile	Rod-like	10-30	50-150	99.5
Carbon	Not Applicable	Multi-walled Nanotube	OD: 10-30 (L: 1-2 μm)	40-300	>95

The name of the nanoparticles in this thesis will be abbreviated as below:

- ATD for Anatase form of Titanium Dioxide (TiO₂),
- RTD for Rutile form of Titanium Dioxide (TiO₂), and
- CNT for Carbon Nanotubes.

To characterise the nanoparticles and obtain more detailed information, both in dried (powder) form and at the air-liquid interface, various procedures were conducted as described in sections 3.2.1 to 3.2.3.

3.2.1 Dried Nanoparticles

The dispersions of the nanoparticles with a concentration of 0.1 wt % in isopropyl alcohol (IPA) were prepared. To decrease the chance of agglomerations, the IPA (Fisher Scientific, United Kingdom) was added to the weighed nanoparticles drop-by-drop while the stirring was done at room temperature. The samples were left to be stirred overnight at room temperature.

Then, using a glass Pasteur pipette, one droplet of each sample was transferred onto each individual stub of Scanning Electron Microscope (SEM) (Figure 3.4). Then, the samples were left under fume hood for 30 minutes so that the IPA was evaporated.

The stubs containing the particles were observed under SEM (TESCAN MIRA3) directly and without any further coating.

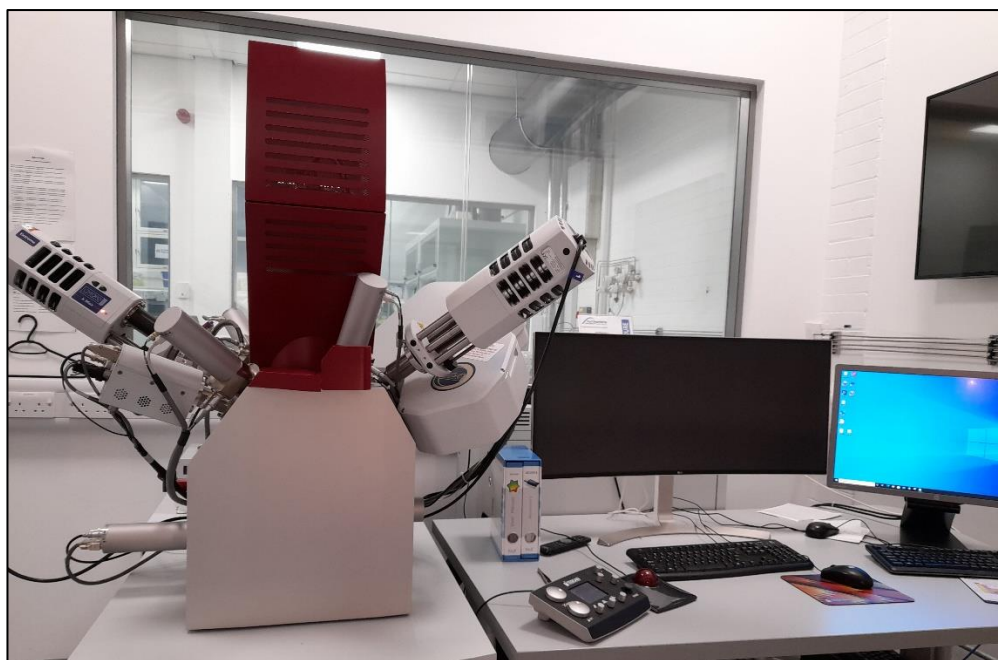


Figure 3.4 Scanning Electron Microscope (SEM) TESCAN, MIRA3.

It should be noted that the images from SEM were analysed using ImageJ Software [147].

3.2.2 Bulk Characterisation_Surface Charge of Nanoparticles

The dispersions of the nanoparticles in surfactant solutions mentioned in Section 3.1 as well as the dispersions with a concentration of 0.1 wt % in DI water were prepared. The surface charge of nanoparticles was measured using SZ-100 Nano Partica Analyser (Horiba, Japan). Therefore, the zeta potential of nanoparticles and/or their agglomerates before interaction with surfactants at different concentrations and after it were measured and reported.

3.2.3 Hydrophilicity/Hydrophobicity of Nanoparticles

The hydrophilicity/hydrophobicity of particles at fluid-fluid interfaces affects the position of particles at interface. The position of particles at interface is describe by the contact angle of particles at fluid-fluid interface. Therefore, the

hydrophilicity/hydrophobicity of particles can be described by measuring the contact angle of particles at interface.

Young's equation (Eq. 3-1) is used to measure the contact angle of particles, θ , at interfaces:

$$\cos \theta = \frac{\gamma_{sg} - \gamma_{sl}}{\gamma_{gl}} \quad \text{Eq. 3-1}$$

where γ_{sg} , γ_{sl} , and γ_{gl} are the interfacial tensions of solid-gas, solid-liquid, and gas-liquid phases, respectively [148].

Based on Young's equation, changes in interfacial tension indicates the change in the contact of particles at interface which, in turn, shows the hydrophilicity/hydrophobicity of particles.

Therefore, measuring the three-phase contact angle of particles at air-liquid interface as well as investigating the effects of particles on the air-liquid interfacial tension of pure water can be reliable indicators of hydrophilicity/hydrophobicity of particles. The experimental methods for these measurements have been described in sections 3.2.3.1 and 3.2.3.2.

3.2.3.1 Three-Phase Contact Angle of Nanoparticles at Air-Water Interface: Gel Trapping Technique (GTT)

The Gel Trapping Technique (GTT) developed to measure the three-phase contact angle of microparticles and nanoparticles at fluid-fluid interfaces was used in this study. The three-phase contact angle of particles at fluid-fluid interface describes the particle hydrophobicity [149].

The schematic diagram of the GTT has been shown and summarised step-by-step in Figure 3.5 [150]. This method can be used for measuring the three-phase contact angle of particles at both air-water and oil-water interfaces.

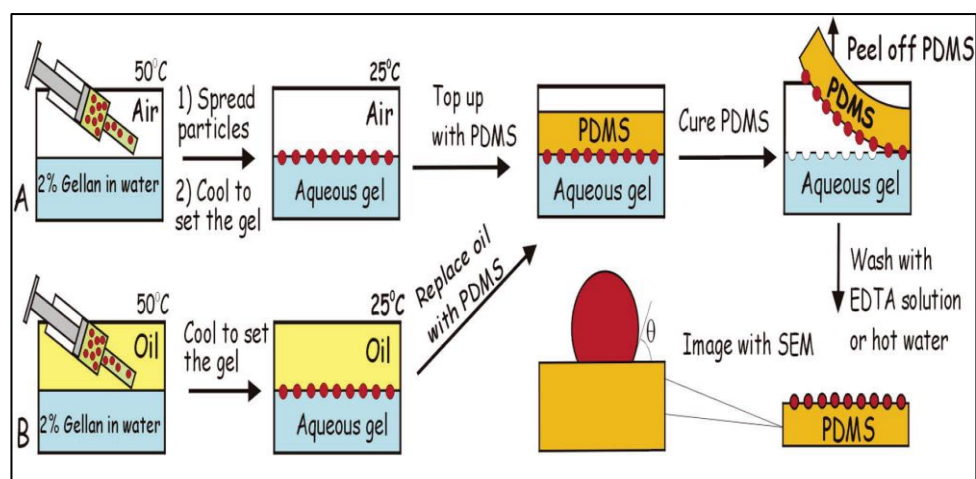


Figure 3.5 Schematic diagram of GTT for (A) air-water and (B) oil-water interfaces [150].

To use this method, the gellan gum as a gift sample was supplied from CPKelco US Inc., USA. The brand name and type of the gellan gum was KELCOGEL[®] F which is a fine mesh gelling agent and polysaccharide secreted by the microorganism *Sphingomonas elodea*. KELCOGEL[®] F is a low acyl gellan gum with heat stability and the molecular weight of 2×10^5 to 3×10^5 Daltons. Based on the data sheet provided by the supplier, this gellan gum has a high level of stability, gel strength, and clarity. The clarity and gel strength were checked and approved during the experiments (Figure 3.6).



Figure 3.6 The upside-down vial containing the gel based on KELCOGEL[®] F gellan gum. The gel strength and its clarity are visible.

To prepare the gel, gellan gum was dispersed in DI water with a concentration of 2.00 wt %. The dispersion was heated to 65-70 °C in the ultrasonic bath mentioned in section 3.1.1 for 15 minutes. At this temperature, the gellan gum was fully dissolved and hydrated in DI water and a clear aqueous solution was obtained. This aqueous solution was transferred to the Petri dish.

A suspension of each type of nanoparticles with a concentration of 0.5 wt % in an aqueous solution containing 35% v/v isopropyl alcohol (IPA) was prepared. IPA was used as the spreading agent. 10 µL of each suspension of nanoparticles was injected onto the hot surface of gellan gum solution in the Petri dish [151].

To set the gel, the system was cooled within 30 minutes at room temperature. To avoid any evaporation at the gel surface, the Petri dish was sealed during the mentioned time.

Polydimethylsiloxane (PDMS) under the brand name of SYLGARD™ 184 Silicone Elastomer (Dow Europe GmbH, Germany) was mixed with the curing agent with a ratio of 10:1. Then, degassing was done using a vacuum pump so that the bubbles are removed. This curable silicon elastomer was poured over the surface of the cooled gel with the entrapped particles at the air-liquid interface. The role of PDMS is to mould this interface. The samples in sealed Petri dishes were kept at room temperature for 48 hours to cure the PDMS layer (Figure 3.7).

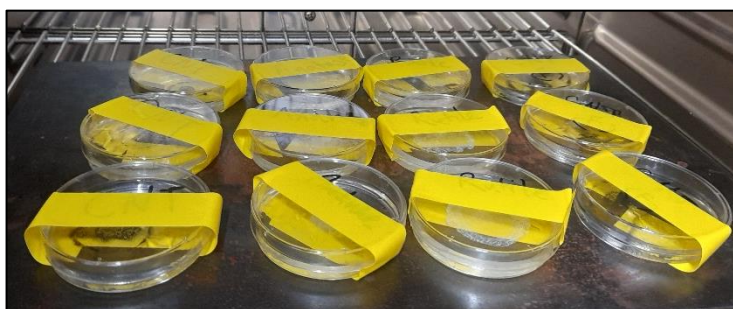


Figure 3.7 Samples prepared with Gel Trapping Technique (GTT). Each Petri dish is related to a single type of nanoparticle including ATD, RTD, and CNT.

After 48 hours, the cured PDMS layer was peeled off the gel together with the entrapped nanoparticles. Then, the PDMS was washed with hot DI water with a temperature of 65-70 °C to remove any possible traces of gel. As the

gellan gum had shown complete solubility in the mentioned range of temperature, we did not use any other solvents such as ethylenediamine tetraacetic acid (EDTA) to remove the gel residues. The other reason was to avoid any possible interactions between EDTA and entrapped nanoparticles at the surface of PDMS, especially titanium dioxide nanoparticles [152]. There are also studies that do not use EDTA in GTT [153].

The PDMS layer with particles was dried and observed under SEM by coating with platinum nanolayer (5 nm thickness) in a rotary pumped coating system (Q150R, Quorum Technologies Ltd., United Kingdom).

It should be noted that, in GTT, the SEM imaging method has been used when the entrapped particles were micro sized. The Atomic Force Microscopy (AFM) has been suggested and used for the nanoparticles. However, there are some drawbacks of using AFM in GTT. For example, for polydisperse samples, the contact angle cannot be calculated directly from AFM method as this method cannot measure the protrusion of particle and its radius simultaneously. In this case, particles should be spread on a solid surface, e.g., silicon wafer, to determine their radius by AFM scanning. Using AFM and supplier's information about the radius and size of the particles cannot be considered a suitable option as the data are not necessarily corresponding to each other [150].

Although the particles in this study were nanosized particles, the preliminary results from AFM (Nanoscope IV, Veeco Metrology Group, Dimension™ 3100 Controller, Digital Instruments, USA) in contact mode were showing a lot of noises. Therefore, SEM was used, and it showed better results for our samples.

In some cases, the detection of particles on PDMS were difficult. Therefore, the samples were prepared in two positions for SEM. First, the samples which could be observed under SEM from the top view (Figure 3.8, a). Second, the samples that had been cut so that the side view of them would be possible (Figure 3.8, b).

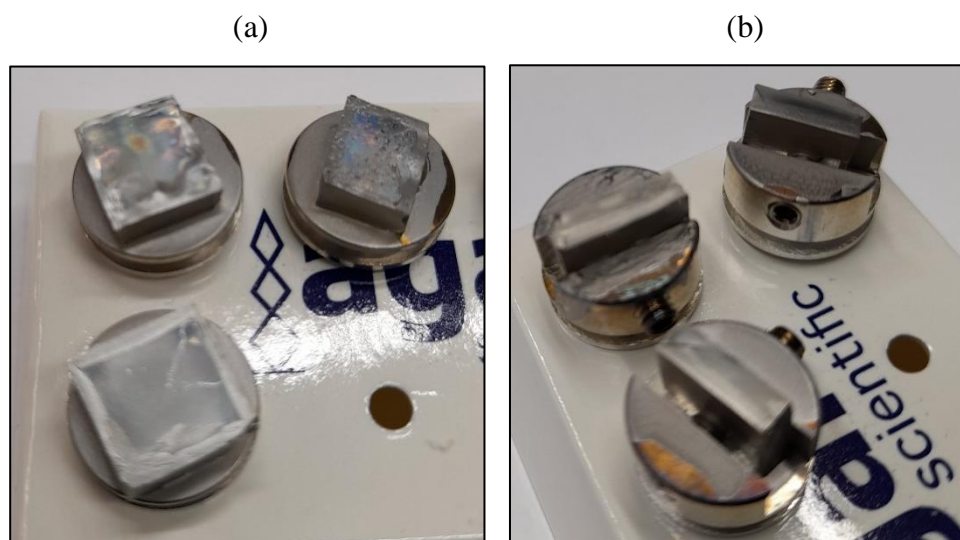


Figure 3.8 Samples of nanoparticles entrapped on the surface of PDMS for SEM imaging in two positions: (a) top view, and (b) side view.

Using the second set of samples, it was possible to image the nanoparticles and/or their agglomerates at the edges of PDMS and measure their height of protrusion. To our knowledge, cutting the samples and observing the edges in GTT have not been studied extensively in these conditions.

3.2.3.2 Interfacial Tension Measurement

The dispersions of nanoparticles with a concentration of 0.01 wt % in DI water were prepared. The interfacial tension of these dispersions at 37 ± 0.2 °C was measured during 4,000 s according to the method described in Section 3.5 in details.

3.3 Preparation and Characterisation of Foams

The wet foams of the aqueous solutions of CTAB and SDS, as well as the dispersions of anatase form of TiO₂ nanoparticles were prepared using manual shaking. Before foaming, all surfactant solutions at given concentration and nanoparticles-surfactant dispersions with a concentration of 0.1 wt % were transferred into separated glass containers and put into ultrasonic bath for 10

minutes. Then, the containers were shaken up and down vigorously for one minute and at a rate of 180 ± 4 shake.min⁻¹, at room temperature.

Afterwards, created wet foams, one by one, were transferred onto microscope glass slides to be observed under optical microscope.

The 3*2 stage optical microscope ECLIPS LV 100, Nikon, Japan was used to observe the shapes and sizes of the created bubbles and foams.

ImageJ Software [147] was used as an image processing programme to analyse the images obtained from optical microscopy method.

3.4 Nanoparticles-DPPC Interactions

Upon the interactions of DPPC and nanoparticles (Section 3.1.4), the surface properties of nanoparticles will change. To investigate these interactions, NMR analysis and zeta potential measurements were conducted as described in Section 3.4.1 and Section 3.4.2.

3.4.1 Adsorption of DPPC onto the Surface of Nanoparticles

Mechanism of the interactions between the nanoparticles and DPPC was investigated using a JEOL 400 MHz NMR Spectrometer. The proton spectra of nanoparticle dispersions containing DPPC (mentioned in Section 3.1.4.1) were recorded at the operating frequency of 399.78 MHz for ¹H NMR. ³¹P-NMR was also done at an operating frequency of 161.83 MHz. Using NMR spectroscopy, it is possible to assess the molecular interactions between DPPC molecules (with a fixed concentration), and nanoparticles (with different concentrations).

After doing the preliminary tests on the samples, the peaks on the NMR spectra were not clear and recognisable. Therefore, the samples were prepared with the same procedure as explained in Section 3.1.4.1 whereas the deuterated DPPC-d₆₂ (Avanti[®] POLAR LIPIDS Inc., USA) was used instead of DPPC in the solutions and dispersions.

In the structure of DPPC-d₆₂ (1,2-dipalmitoyl-d₆₂-sn-glycero-3-phosphocholine), deuteriums are on the alpha carbon attached to the carbonyl group (Figure 3.9). Therefore, the DPPC-d₆₂ is deuterated at alpha positions.

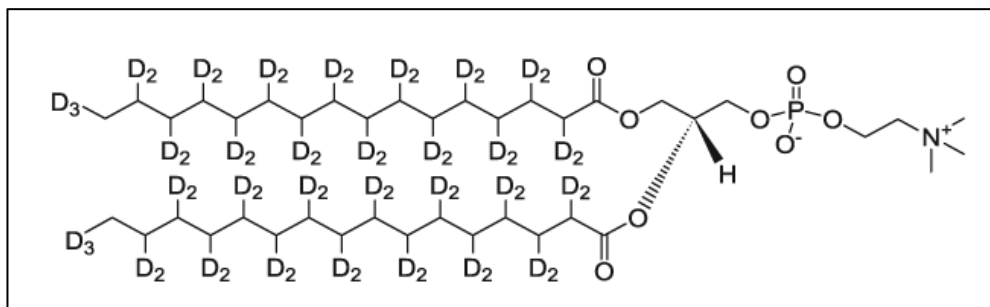


Figure 3.9 The deuterated structure of DPPC-d₆₂ [154].

This deuterated structure (Figure 3.9) helps the simplification of ¹H NMR spectroscopy and convenient detection of the peaks and signals [155].

It should be noted that the data obtained from ¹H NMR spectroscopy were analysed using Delta 6.1.0 software to evaluate the peaks and integrals [156].

3.4.2 Surface Charge of the Nanoparticles Interacted with DPPC

The surface charges of nanoparticles in the dispersions mentioned in Section 3.1.4.1 were measured using SZ-100 Nano Partica Analyser (Horiba, Japan). Accordingly, the zeta potentials of nanoparticle values with different concentrations after their interactions with the same amount of DPPC were measured and reported.

3.5 Dynamic Interfacial Tension Measurement

3.5.1 Profile Analysis Tensiometer (PAT)

The Profile Analysis Tensiometer (PAT) is the high end full-automatic instrument utilised for surface / interfacial tension measurement. Moreover, this instrument can be used for studying the interfacial rheology. The PAT system used in this research was PAT1M, SINTERFACE Technologies, Germany (Figure 3.10).

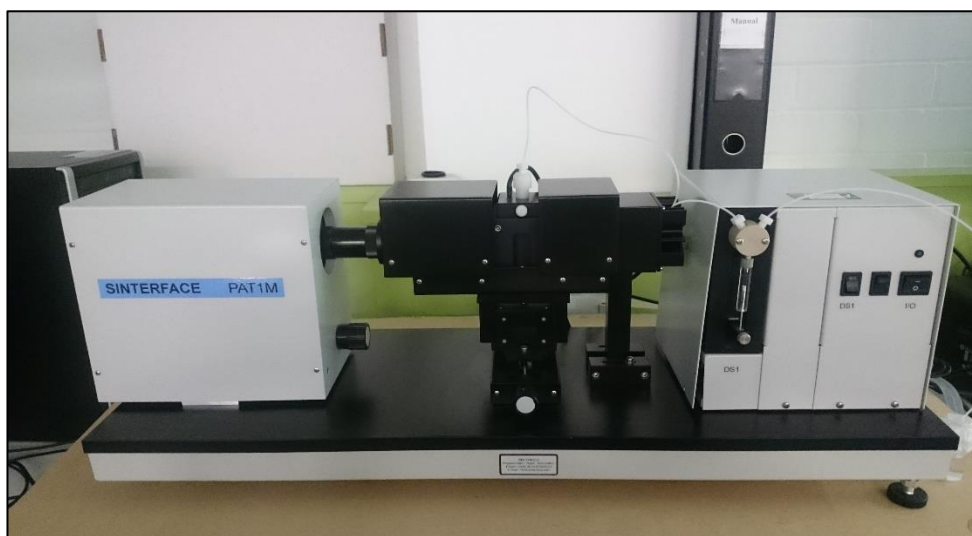


Figure 3.10 The set-up of the PAT1M, SINTERFACE Technologies, Germany.

The principle used in PAT is based on the shape analysis of droplets and bubbles. The technique is called Axisymmetric Drop Shape Analysis (ADSA) [135]. This instrument has a capacity to work in any of these four modes: (a) pendant drop, (b) sessile drop, (c) buoyant bubble, and (d) captive bubble modes. A schematic diagram of its set-up has been depicted in Figure 3.11. The liquid sample is pumped into the syringe of the instrument and pumped out of it to pass through the tube and reach the steel capillary. Then, the drop is formed at the tip of this capillary. Using the automatic dosing system of this instrument, it is possible to keep either the area or volume of the drop constant. An external thermostatic water bath is used to control the inside temperature of the measuring cell. To visualise and obtain the images of the drop, a light source and a charge-coupled device (CCD) camera are used in opposite sides of the measuring cell.

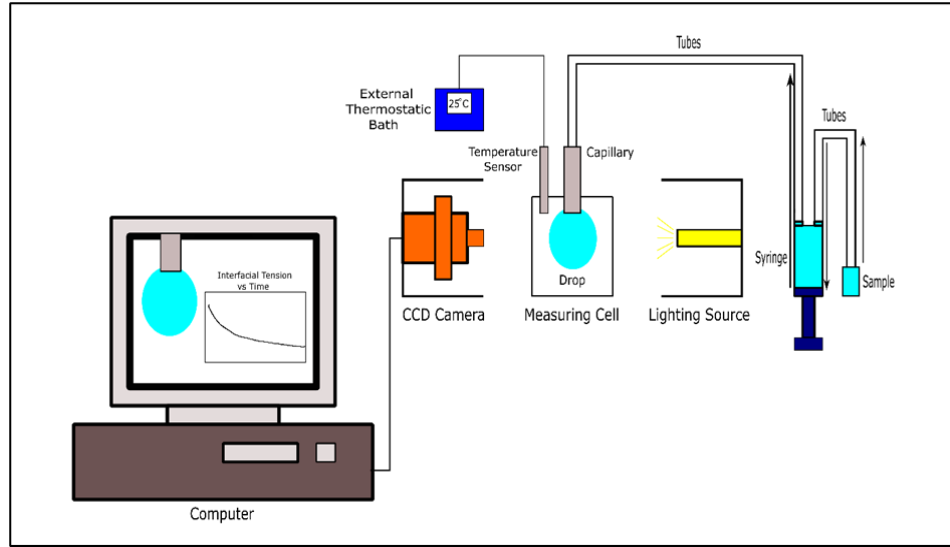


Figure 3.11 A schematic diagram of the profile analysis tensiometer (PAT) set-up.

The efficient and highly accurate software connected to the PAT specifies the coordinates of the drop and fits the Gauss-Laplace equation to the formed profile drop. The Gauss-Laplace equation (Eq. 3-2) describes the relationship between the curvature of the liquid meniscus and the surface tension [157, 158]:

$$\Delta p = \gamma \left(\frac{1}{R_1} + \frac{1}{R_2} \right) \quad \text{Eq. 3-2}$$

where Δp is the pressure difference across the interfacial layer, γ is the surface/interfacial tension, and R_1 and R_2 are the principal radii of the curvature (Figure 3.12). The meridional and azimuthal curvatures are defined as $\frac{1}{R_1}$ and

$\frac{1}{R_2}$, respectively, and are given by Eq. 3-3 and Eq. 3-4 [157, 158]:

$$\frac{1}{R_1} = \frac{d\phi}{dS} \quad \text{Eq. 3-3}$$

$$\frac{1}{R_2} = \frac{\sin \phi}{x} \quad \text{Eq. 3-4}$$

where ϕ and S are the angle of tangent to the profile and the arc length along the profile, respectively. Considering the effect of gravity as an external field, the weight of the column of the liquid with a height of z is added to Eq. 3-2.

Therefore, under the constant density of both phases, the equation will be demonstrated as below [157, 158]:

$$\frac{2\gamma}{b} - \Delta\rho g z = \gamma \left(\frac{d\phi}{dS} + \frac{\sin \phi}{x} \right) \quad \text{Eq. 3-5}$$

where b is the radius of the curvature at the drop apex, $\Delta\rho$ is the density difference between the drop and the medium surrounding it, and g is the gravitational acceleration constant. For axisymmetric profiles, the two principal radii become equal at the drop apex where $z = 0$. Therefore, the parameter 2γ comes into the equation.

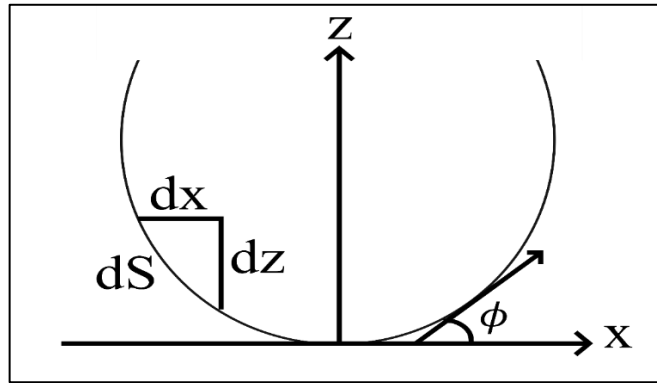


Figure 3.12 Coordinate system for a drop.

If we divide both sides of Eq. 3-5 by $\frac{\gamma}{b}$, the starting point for the calculation algorithm will be obtained:

$$\frac{d\phi}{dS^*} = 2 - \frac{\Delta\rho g b^2 z^*}{\gamma} - \frac{\sin \phi}{x^*} \quad \text{Eq. 3-6}$$

where S^* , z^* , and x^* are the dimensionless arc length, vertical and horizontal coordinates, respectively, and are shown as below:

$$S^* = \frac{S}{b} \quad \text{Eq. 3-7}$$

$$z^* = \frac{z}{b} \quad \text{Eq. 3-8}$$

$$x^* = \frac{x}{b} \quad \text{Eq. 3-9}$$

The Eq. 3-6 can also be rewritten as:

$$\frac{d\phi}{dS^*} = 2 - Bo \cdot z^* - \frac{\sin \phi}{x^*} \quad \text{Eq. 3-10}$$

in which, **Bo**. is the dimensionless Bond number (Eötvös number). This number which compares the gravitational and surface tension forces is defined as below:

$$Bo. = \frac{\Delta\rho g b^2}{\gamma} \quad \text{Eq. 3-11}$$

When the drop is formed at the tip of the capillary, the extracted profile coordinates will be compared with the theoretical profiles obtained from the Gauss-Laplace equation (Figure 3.13). Then, the best fitting curve for the experimental points corresponds to the optimal surface tension and it is calculated as the only free parameter [157, 158].

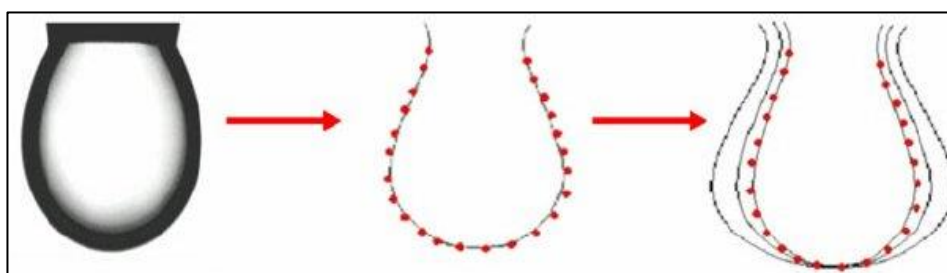


Figure 3.13 A pendant drop and a family of the theoretical curvatures fitting the experimental points (red points) in the PAT [159].

Using PAT, the dynamic interfacial tension is measured continuously as a function of time (Figure 3.14). When the adsorption equilibrium is reached, the surface tension plot vs. time gets plateau, and the quantity of the surface tension can be attributed to the solution or dispersion.

As it is demonstrated in Figure 3.14, the software installed on the system also plots the volume of drop during time if we keep the surface area of the drop as one of the constant parameters.

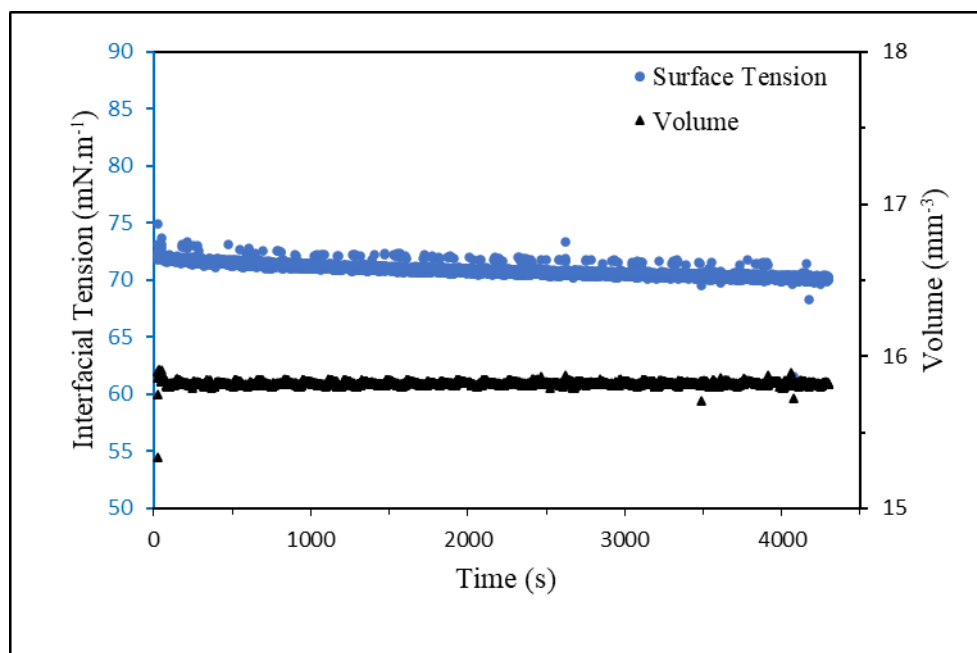


Figure 3.14 An example of typical plot of the dynamic interfacial tension vs. time for the aqueous solution of SDS with the concentration of $1e-5$ M at 25 °C.

3.5.2 Method of Analysis

In PAT, there are some general parameters that must be defined by the user. The mode of the equipment, the second phase in which the drop or bubble is formed, i.e., the surrounding medium, and the density difference between these two phases are defined by the user. Moreover, the temperature inside the measuring cell, the diameter of the steel capillary (e.g., 2 mm in this study), and the controlled parameter which can be either the volume or the surface area of the drop and/or bubble are other parameters that must be defined by the user.

As it is demonstrated in Table 3.3, we worked on two categories of experiments. The first one was the ionic surfactants, i.e., CTAB and SDS, with and without particles. Based on the applications of these surfactants which mainly included the products used in room temperature, the working temperature was set at 25 ± 0.2 °C. For the second category of the experiments related to the lung surfactant model, the temperature was kept constant at 37 ± 0.2 °C which simulates the lung temperature [160]. Other parameters were equal in both categories of the experiments.

Table 3.3 The general settings of PAT and the quantity of the parameters for two categories of experiments, i.e. ionic surfactants and lung surfactant model.

Parameters Category of Experiments	Mode	Surrounding Medium	Density Difference (g/cm³)	Temperature (°C)	Capillary Diameter (mm)	Constant Area (mm²)
Ionic Surfactants (CTAB and SDS)	Pendant drop	Air	0.997	25 ± 0.2	2	25
Lung Surfactant Model (DPPC)	Pendant drop	Air	0.997	37 ± 0.2	2	25

The internal density related to the liquid phase was assumed as equal to the density of water. Therefore, the density difference was the difference between water density and the density of air as the external phase. To avoid the complexities related to the relationships between the temperature, vapor pressure, and density, the density difference in all cases in the experiments was considered the same and equal to the quantity mentioned in Table 3.3.

As mentioned in section 2.5.1, if we consider the diameter of the alveoli as 0.3 mm with a spherical shape, its surface area is calculated using the below equation:

$$A = 4\pi r^2 \quad \text{Eq. 3-12}$$

where r is the radius of the sphere, and A is the surface area of the sphere. Therefore, the surface area of one single alveoli will be:

$$A = 4 * 3.14 * \left(\frac{0.3}{2}\right)^2 = 0.28 \text{ mm}^2$$

The surface area of the real alveoli is very small. Because of the instrumental limitations, we had to use the optimum quantity of surface area. This quantity must be as large as it does not cause any failure during the experiment time. The examples of the failure are the evaporation of the drop because of its extremely small size and the difficult visualisation of that drop by the software. Therefore, the constant surface area of 25 mm² was considered in our experiments.

This magnitude is almost 100 times more than the real scale for the experiments on the lung surfactant model. In addition, the interfacial tension, i.e., the surface tension at the interface, is one of the macroscopic mechanical properties of the fluid-fluid interfaces. However, the effective interfacial tension, which can be measured by PAT, is one of the operationally valid properties for description of interfacial layers at smaller scales, even microscopic interfaces which have been changed to non-homogeneous interfacial layers by the adsorption of nanoparticle onto them [17].

Before starting the experiments with surfactant-contained solutions and dispersions, all parts of the tensiometer in contact with the liquid samples were cleaned using isopropyl alcohol (IPA) and ultrapure water. To avoid any contamination, the PAT was run with the ultrapure water for at least one day, at different intervals.

Surface tension of water is a function of temperature. Using the experimental data in scientific literature [161], we plotted the surface tension of water against temperature over the range of 5–100 °C (Figure 3.15). Over this range, there is a linear relationship between the surface tension and temperature. Therefore, the linear equation will be:

$$\gamma = -0.1691T + 76.183 \quad \text{Eq. 3-13}$$

where T represents the temperature. The coefficient of determination, also called R-squared, was greater than 0.99. It shows that the linear model in this range of temperature is an appropriate fit. Using interpolation, the surface tensions of water at the temperatures of 25°C and 37°C were calculated as 71.99 mN.m⁻¹ and 69.93 mN.m⁻¹, respectively.

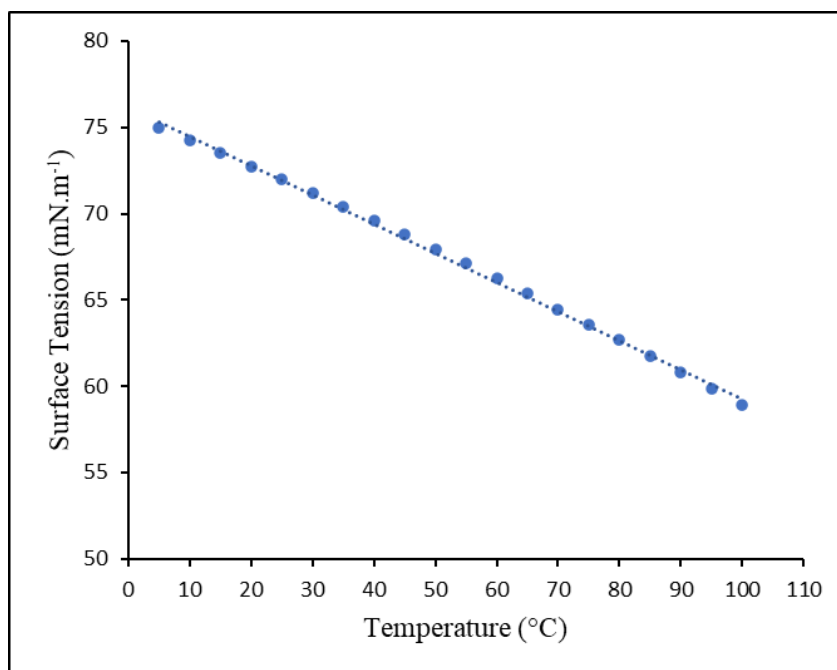


Figure 3.15 Surface tension of water against temperature.

When PAT is used for tests of DI water, it must show two features to make sure that there is no contamination or impurity in the system, and the instrument is calibrated:

- The surface tension must be equal to the standard quantity for each temperature (Figure 3.15).
- The surface tension must show no significant kinetics over several hours.

To avoid the evaporation of the drop during the experiments which took more than 2500 s, based on the category of the experiments, the surrounding air in the measuring cell should be saturated with water vapor. So, at the start of each experiment, we assured that there is a layer of water with a thickness of at least 3 mm at the bottom of the measuring cell (glass chamber).

It should be noted that the time interval, i.e., the time between measured points, was 1 s in all experiments (Figure 3.14). Minitab[®] 18 Statistical Software as well as Microsoft Excel Software were utilised for data analysis and statistical studies of the data [162]. For fitting the best adsorption isotherm model to experimental data, the IsoFit programme was applied [163].

3.5.3 Limitations of Profile Analysis Tensiometer (PAT)

The PAT instrument has been widely used for measuring the interfacial tension of the air-liquid and liquid-liquid systems containing solid particles. However, this instrument has its own limitations that should be considered during its operation and data interpretation. Some of these limitations encountered in this study are mentioned here:

- This instrument is significantly sensitive to the surrounding noises, such as light, movement, and sounds. The best place to put this instrument in the laboratory would be on the vibration control tables and, possibly, in the dark rooms or areas. Otherwise, the calibration must be done every time before starting a new series of tests. Moreover, the chamber, camera, and light source should be carefully insulated using aluminium foils.
- The over-sensitivity of the PAT instrument to the noise will result in the out-of-range data whilst measuring the interfacial tension. If those out-of-range individual points are seen in the interfacial tension graph, they must be removed by the software such as MATLAB or Minitab before analysing the data. This means that, based on the user and analyser, the accuracy of data obtained from PAT may be changed.
- Using liquid systems that contain two or more different immiscible solvents, such as water and chloroform, should be considered precautionarily. Putting the sample in its testing position (Figure 3.11) even immediately after the mixing procedure will probably result in the separation of the immiscible phases. This means that the tip of the tube may suck the solution from either phase in each experiment. Therefore, the variation of the results happens, and the obtained results are not reproducible or accurate. Even if someone puts the sample on a stirrer next to the PAT set-up, the sample will still be pumped in the syringe (Figure 3.11) which has a static position. This means that the phase separation will happen in this case as well.
- The temperature is another important factor that should be monitored carefully in this device. Although the external thermostatic bath (Figure

3.11) is used to control the temperature in the chamber, the final temperature in the chamber is not the one set on the thermostatic bath. The temperature shown on the control screen of the bath should normally be slightly (2-3 °C) higher than the desired temperature in the chamber. This is a normal calibration between the temperature inside the chamber and the bath temperature. However, it should be considered when the PAT equipment is used. The higher temperature of the bath might also depend on the temperature of the room where the bath is located. Therefore, this temperature must be controlled every time before the start of the experiments on each specific day. The temperature recorded by the software of the device is the one measured in the chamber and probed by the sensor.

- The next limitation of the PAT is also related to the temperature control. When the sample is located at the sample testing place (Figure 3.11), the temperature is the room temperature. Therefore, the droplet formed at the tip of the capillary is not initially at the desired operating temperature in the chamber unless the operating temperature is the room temperature. This means that, in case of interpreting the data before reaching the equilibrium, the effect of temperature and equilibrium of the droplet must always be considered as a variable. To avoid this problem or to minimise this effect, before starting each measurement in PAT, the first sample should be put in the ultrasonic bath in the temperature equal to the operating temperature in the chamber. It should be noted that the effect of temperature changes before reaching to the equilibrium conditions cannot be totally removed as the sample will be pumped in and out of the syringe. Therefore, the initial droplet is hardly at the desired temperature. It is noteworthy to consider the length of the metal capillary as an appropriate solution to this issue. This metallic capillary helps the liquid inside the capillary reach the desired temperature faster.
- In PAT, whenever a measurement is done, the tubes and the pumping syringe must be emptied before the start of the next test. Generally, to avoid any contamination in the stock of the first sample, all the liquid in the tubes and syringe will be disposed in the glass cell in the chamber.

That means that there is always sample waste in this instrument. Therefore, if someone needs to do experiments other than interfacial tension measurement on the same sample (for example, NMR and zeta potential measurement), a larger amount of stock solution of the samples is required for the sake of consistency among the results.

- When working with the dispersed solid particles in a liquid, the cleaning of the PAT instrument should be considered carefully. The internal diameter of the tubes of this instrument is 1.6 mm. This small size of tube and careless cleaning of the tubes will result in cross-contamination. To avoid such possible contaminations, especially when working with different nanoparticles, it is better to change those polytetrafluoroethylene (PTFE) tubes after each set of experiments on a specific particle.

Despite all the above-mentioned limitations, if they are seriously considered, the PAT could still provide accurate results at higher temperatures. Therefore, it can be a good choice specially when the dynamic interfacial tension and rheology measurements are required [145].

3.6 Spectrum Width Measurement

Optical fibre method will be used as an alternative method for measuring the critical micelle concentration (CMC) of surfactants in this work. The optical fibre sensor was a single mode-no core-single mode (SNCS) fibre structure. In this structure, a short section of silica no core was fusion spliced between two traditional single mode fibres [164]. The diameter of the silica no core was 125 μm . The length of the sensing region was 5 cm.

One of the equipment used for this purpose was super luminescent diode (SLD) as the light source of a class 1M laser working in the range of 1450-1660 nm. The optical spectrum analyser (OSA), model AQ6370C, Yokogawa Test & Measurement Corporation, Japan, was the other machine applied in this study. The working range of the OSA was 600-1700 nm.

An aluminium cell with one open facet to air was used as the container of the surfactant solutions in direct contact with the optical fibre (Figure 3.16). The

response of this set-up was spectrum width centre, λ_c . The λ_c was measured four times for each solution at room temperature.

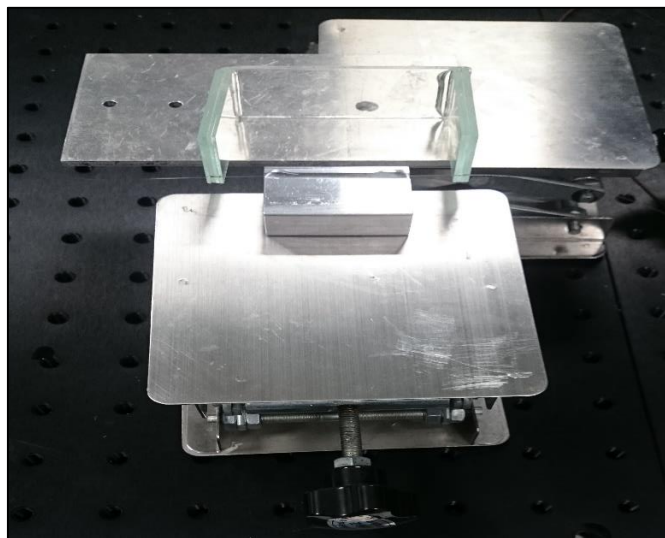


Figure 3.16 The set-up for aluminium cell and the optical fibre sensor sunk in the surfactant solution.

3.7 Interfacial Rheology Measurement

Interfacial rheology of the monolayers of DPPC was studied using the same device for interfacial tension measurement, i.e. PAT (section 3.5.1). In fact, the perturbation of the interfacial area for the systems containing surfactants affects the adsorption of these molecules onto the interface, and this will result in a change of the interfacial tension measured as a function of time. As discussed before, the option of controlling the surface area and/or the volume of the drop allows the investigation of the dynamic interfacial tension and interfacial responses to the perturbations in the surface area of the drop. These studies, known as drop oscillation methods or perturbation-response methods, are used to measure the viscoelastic properties of the adsorption layers. This means that the PAT allows the measurement of dilatational elasticity and viscosity.

The viscoelastic parameters are calculated via Fourier analysis. In mathematical point of view, the linear viscoelasticity is defined either in the time domain (Eq. 3-14) or in the frequency domain (Eq. 3-15).

$$\Delta\gamma(t) = \gamma(t) - \gamma_0 = \int_0^t F^{-1}\{\varepsilon(\omega), \tau\} \Delta A(t - \tau) / A_0 d\tau \quad \text{Eq. 3-14}$$

$$\Delta\gamma(\omega) = \varepsilon(\omega) \Delta A(\omega) / A_0 \quad \text{Eq. 3-15}$$

where t and τ are the real time and dummy time in the convolution integral, respectively. F is the Fourier transform operator, ε is the interfacial dilatational modulus, $\Delta A/A_0$ is the relative area change, and ω is the angular frequency. It should be noted that:

$$\Delta\gamma(\omega) = F\{\Delta\gamma(t)\} \quad \text{Eq. 3-16}$$

$$\Delta A(\omega) = F\{\Delta A(t)\} \quad \text{Eq. 3-17}$$

When the perturbations of the interfacial area are small and not far from the equilibrium state, Eq. 3-14 and Eq. 3-15 provide this possibility to express the periodic or transient processes by a linear time-invariant distributed-parameter dissipative system. This assumption can be taken into consideration when the response amplitude is directly proportional to the amplitude of the perturbation.

In such a linear model, $\varepsilon(\omega)$, interfacial dilatational modulus, is an intrinsic characteristic of the system which describes the dynamic of the adsorption layers by making the relationship between the surface area changes and the interface response obtained as the changes in surface tension within time. If a system is within the linear regime, a harmonic multi-frequency change in the surface area, $\Delta A(t)/A_0$, results in the similar harmonic multi-frequency composition for the system's response, $\Delta\gamma(t)$. In fact, in a linear system, it is important to assume that all the perturbations are small enough. As quantitative criteria, the below conditions are considered:

$$\Delta A \ll A_0 \quad \text{and} \quad \Delta\gamma \ll \gamma_0 \quad \text{Eq. 3-18}$$

where ΔA is the amplitude of the surface area oscillation, A_0 is the equilibrium surface area, and γ_0 is the equilibrium interfacial tension [165].

In real interfacial systems, a nonlinear dynamic behaviour is observed by increasing the time scale and amplitude of the interfacial strain. This behaviour depends on the chemical composition of the system. In fact, there is the memory resulted from the relaxation processes in these systems. One of the mathematical resources to describe the behaviour of these systems is Volterra series (Eq. 3-19).

$$\gamma(t) = \gamma_0 + \sum_{n=1}^{n=\infty} \frac{1}{n!} \int_0^t \dots \int_0^t k_n(\tau_1, \tau_2, \dots, \tau_n) \times \prod_{i=1}^n \Delta A(t - \tau_i) / A_0 d\tau_1 d\tau_2 \dots d\tau_n \quad \text{Eq. 3-19}$$

where k_n is the mathematical n -th order Volterra kernel. This equation includes the terms for the memory, linearity, and nonlinearity. However, because of the lack of the efficient numerical algorithm and experimental techniques for the kernel measurement, simplifying approaches are sought to describe the behaviour of such systems.

One of these approaches is to consider the system as a weakly nonlinear case with memory. In this system, the nonlinearity extent is described by the Total Harmonic Distortion (THD) parameter. This parameter can be used as an index to assess either the validity of linearity assumption or quantitative assessment of nonlinearity of the interfacial systems.

As mentioned before, in studies conducted by PAT, Fourier series (Eq. 3-14 and Eq. 3-15) is usually used to analyse the viscoelastic parameters in a weakly nonlinear interfacial system. Based on the specific assumptions mentioned above for Eq. 3-18, the systems in this study could also be potentially considered as linear ones. Using Eq. 3-15 from Fourier analysis, the dilatational modulus or viscoelastic modulus is obtained as below:

$$|\varepsilon(\omega)| = \frac{\Delta\gamma(\omega)}{\Delta A(\omega)/A_0} \quad \text{Eq. 3-20}$$

in which, ω is defined by the below equation:

$$\omega = 2\pi\nu \quad \text{Eq. 3-21}$$

where ν is the frequency. Two parts of the dilatational modulus, i.e., the real and imaginary parts, are defined from below equations:

$$\varepsilon' = |\varepsilon(\omega)| \cos \theta \quad \text{Eq. 3-22}$$

$$\varepsilon'' = |\varepsilon(\omega)| \sin \theta \quad \text{Eq. 3-23}$$

where θ is defined as the phase difference between $\Delta\gamma$ and ΔA . The schematic diagram of the mentioned parameters has been shown in Figure 3.17. The phase difference or the loss angle, θ , between the interfacial tension and surface area can be defined as below:

$$\theta = \tan^{-1}\left(\frac{\varepsilon''}{\varepsilon'}\right) \quad \text{Eq. 3-24}$$

where ε' and ε'' are the real and imaginary parts of the viscoelastic modulus, respectively. The real part accounts for the dilatational surface elasticity, and the imaginary part can be defined as below:

$$\varepsilon'' = \omega\mu \quad \text{Eq. 3-25}$$

where μ is the dilatational surface viscosity.

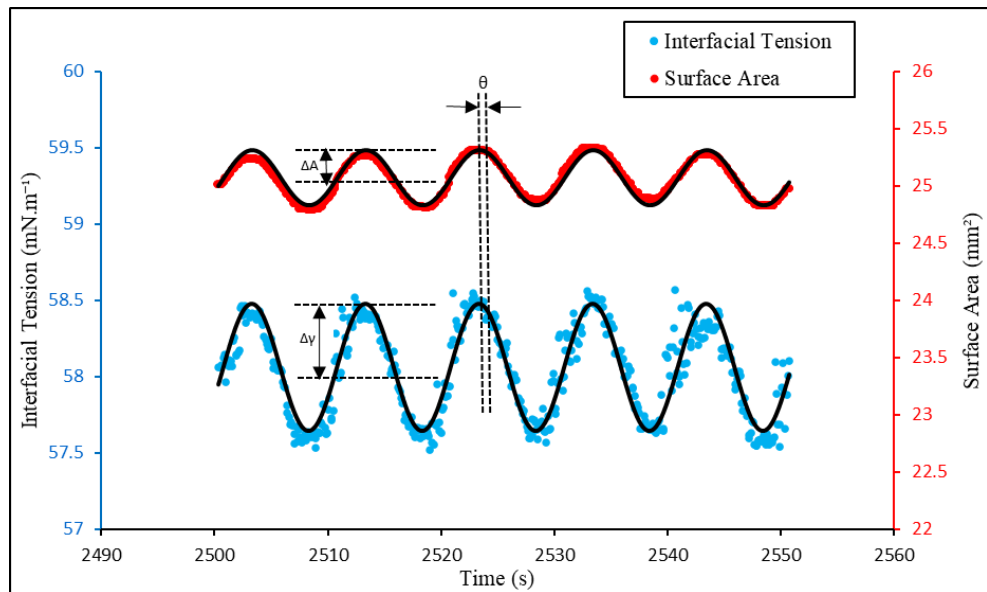


Figure 3.17 Example of the augmented image of the oscillation at the frequency of 0.1 Hz and amplitude of 1% area deformation. Red and blue dots correspond to the surface area and interfacial tension, respectively.

The THD is another parameter in such interfacial systems, and it is defined as the ratio of the amplitude values of higher harmonics ($\mathbf{a}_2, \mathbf{a}_3, \dots, \mathbf{a}_n$ in Eq. 3-26) to the amplitude related to the measured fundamental frequency (\mathbf{a}_1 in Eq. 3-26).

$$THD = (a_2^2 + a_3^2 + \dots + a_n^2)^{1/2}/a_1 \quad \text{Eq. 3-26}$$

The THD is also stated as a percentage of the amplitude of the fundamental frequency. For linear systems, when there are small-amplitude disturbances, the THD values are small and less than 5%. The THD values more than 5% show the nonlinearity.

To propose a reliable model that can distinguish between significant signals and noises, it is assumed that the response signal is the result of the fundamental oscillation and higher harmonics up to the fifth order. So, the remainder terms are considered as noise [133].

Based on the above-mentioned principles, the rheology experiments were conducted using the PAT. It should be noted that the range of the smooth oscillation provided by the piezo system of this device (PAT1M, SINTERFACE Technologies, Germany) was 0.001 to 1 Hz [166]. The details about the design of the rheology experiments have been described in Section 3.7.1.

3.7.1 Design of Experiments based on Breathing Patterns (Amplitude and Frequency)

The interfacial tension of the air-liquid interface of the solutions and dispersions containing DPPC (Section 3.1.3 and Section 3.1.4.1) was determined using PAT with the details mentioned in Section 3.5.2. The measurement of interfacial tension and dilatational rheology for each sample was repeated three times based on the following protocol:

After the equilibration condition was achieved at 37 ± 0.2 °C, the sinusoidal oscillations were applied at 2500 s using the piezo system of PAT. For some of the samples that did not reach the equilibrium condition within 2500 s, the experiments were performed at 4000 s, when it becomes an equilibrium condition.

In PAT, the option of controlling the surface area of the drop allows the investigation of the dynamic interfacial tension and interfacial responses to the perturbations in the surface area of the drop. To do this study, the amplitude sweeps were performed at amplitudes of 1%, 2%, 5%, and 10%, where the frequency was increased step-by-step from 0.1 Hz to 0.125 Hz, 0.25 Hz, and 0.5 Hz. At any defined frequency and amplitude, five compression-expansion cycles were performed.

It should be noted that the frequencies were chosen based on the details of breathing patterns of healthy human beings with different gender and age groups

[167, 168]. The breathing frequency related to the various age groups has been listed in Table 3.4. The frequencies selected in this study, i.e., 0.1 Hz to 0.125 Hz, 0.25 Hz, and 0.5 Hz, simulate the range of breathing frequencies from adults (both normal and deep breathing) to 5-year-old age group.

Table 3.4 Breathing frequency in quiet and deep breathing at different age groups.

Breathing Pattern Frequency	Age Group			
	1 year	5 years	15 years	Adult
Quiet or Normal Breathing Frequency (Hz)	0.72	0.5	0.31	0.24
Deep Breathing Frequency (Hz)	---	---	---	0.12*

* With 0.002 Hz difference between women and men.

The quantities of amplitudes were selected based on the lung parameters, such as tidal volume and functional residual capacity [169]. Figure 3.18 shows that the tidal volume, defined as the volume that is inhaled and exhaled during normal or quiet breathing, is 8-10% of the total lung capacity. However, this amount can be increased to more than the tidal volume, i.e., to the inspiratory reserve volume during inhalation (expansion) and to the expiratory reserve volume during exhalation (compression) [170].

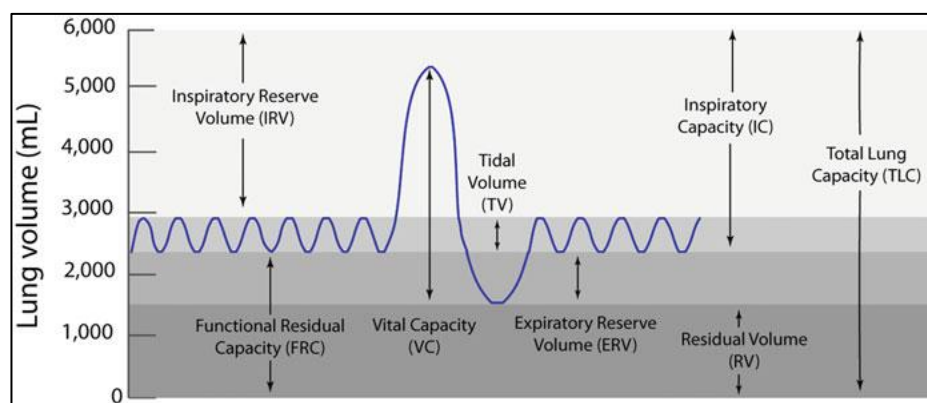


Figure 3.18 Static lung volumes and capacities [170].

Based on the above-mentioned lung volumes and other experimental factors such as instrument maintenance, the maximum perturbations, reliability, and validity of the results, the amplitudes of 1%, 2%, 5%, and 10% were selected in this study.

3.7.2 Methods of Analysis

The data analysis for the rheology measurements was done based on the Fourier transform analysis with a linear approach. However, the analysis of the total harmonic distortion and the curve fitting method to measure the first harmonic Fourier moduli showed that the linear approach did not produce realistic results for calculating the viscoelasticity parameters including the complex viscoelastic modulus and the phase difference between interfacial tension and surface area signals [21, 134]. Therefore, a nonlinear and more realistic approach was considered to re-analyse the data. To our knowledge, it is the first time that this method for the DPPC systems has been applied. Both linear and nonlinear methods of analysis have been described in details in Chapter 7.

Chapter 4

Surface Properties of the Agglomerates of Nano-Pollutants

Nanoparticles possess a large surface area to volume ratio. This characteristic results in tremendously reactive interfaces among nanoparticles, or with other components in the local environment. The high surface energy of nanoparticles results in the strong tendency of these particles to form agglomerates [171]. Therefore, sizes and surface properties of nanoparticles determine their agglomeration states and interactions with the surrounding medium, especially those living matters under physiological conditions.

The agglomerates of nanoparticles are important for the biological media and environment. The assembly of nanoparticles with different geometries at fluid-fluid interfaces could have many applications in different fields such as detergents, coatings, pharmaceuticals, and oil refining [172]. Therefore, characterisation of surface properties of nanoparticles and their agglomerates is essential to understand the nature of these agglomerates and elucidate fluid-fluid interfacial behaviours of those agglomerates.

In this chapter, three types of nanoparticles including anatase form of titanium dioxide (ATD), rutile form of titanium dioxide (RTD) and multi-walled carbon nanotube (CNT) were characterised. In addition to the shape characterisation of these nanoparticles' agglomerates, their surface charges were also measured and reported.

The Gel Trapping Technique (GTT) was primarily used to calculate the three-phase contact angle of nanoparticles at air-water interfaces. Therefore, the geometry and attachment of some of the agglomerates of nanoparticles at air-water interface were investigated using GTT. Furthermore, understanding the details of the agglomerates of nanoparticles at air-water interface is critical in

elaborating their behaviour in more sophisticated systems containing surfactants. For this purpose, the interfacial tension of the aqueous dispersions of nanoparticles was also measured in this chapter.

4.1 Results and Discussion

4.1.1 Shapes of Nanoparticles and Agglomerates

The shapes of the nanoparticles and/or their agglomerates have been analysed in two different ways.

The first one is to check the shape in their dried states, and it was conducted to understand the shapes of the particles or their agglomerates before they were put in aqueous solutions. The method for this dried state was mentioned in the Section 3.2.1.

The second one is to check the shapes of the agglomerates for the nanoparticles at air-water interfaces. Based on the principles of GTT for measuring the three-phase contact angle, the specified method (in the Section 3.2.3.1) results in a replica of air-water interface [151]. Any individual particles and/or agglomerates observed on the PDMS replica will be the reliable representatives of the shapes of that particle and/or agglomerates at the air-water interfaces.

In this section, results of the shape analysis are reported for both the dried agglomerates and the entrapped agglomerates at air-water interfaces obtained from the PDMS replica using the GTT.

4.1.1.1 Dried Agglomerates of Nanoparticles

Based on the method mentioned in the Section 3.2.1, the SEM images of the nanoparticles after the evaporation of IPA from the surface of the stubs were obtained and analysed. The obtained results of the image analysis are shown in Figure 4.1, Figure 4.2, and Figure 4.4. Moreover, the sizes of nanoparticles

provided by the supplier were compared with those measured from the SEM images in the laboratory. The comparative data are summarised in Table 4.1.

Table 4.1 Comparisons between the dried nanoparticles' characteristics provided by the supplier and analysed in the laboratory using SEM.

Nanoparticles	Shape by Supplier	Size by Supplier (nm)	Shape by Internal Analysis	Size by Internal Analysis (nm)
ATD	Sphere	20	Sphere*	38-68*
RTD	Rod-like	10-30	Sphere and Rod-like*	40-73*
CNT	Multi-walled Nanotube	OD: 10-30 (L: 1-2 μm)	Entwined Nanotubes	OD: 45-103 (L: Not Reliable)

* Due to the limitations of SEM analysis, these results cannot be considered with 100% certainty for individual nanoparticles.

Using SEM, the shape of the agglomerates of ATD nanoparticles was detected (Figure 4.1). The agglomerates are clearly porous. The shapes of individual nanoparticles appear spherical as shown in Figure 4.1, a. However, the exact size of these particles is difficult to obtain due to their agglomeration. These nanoparticles were reported to be of the size of 20 nm by the supplier (Table 4.1).

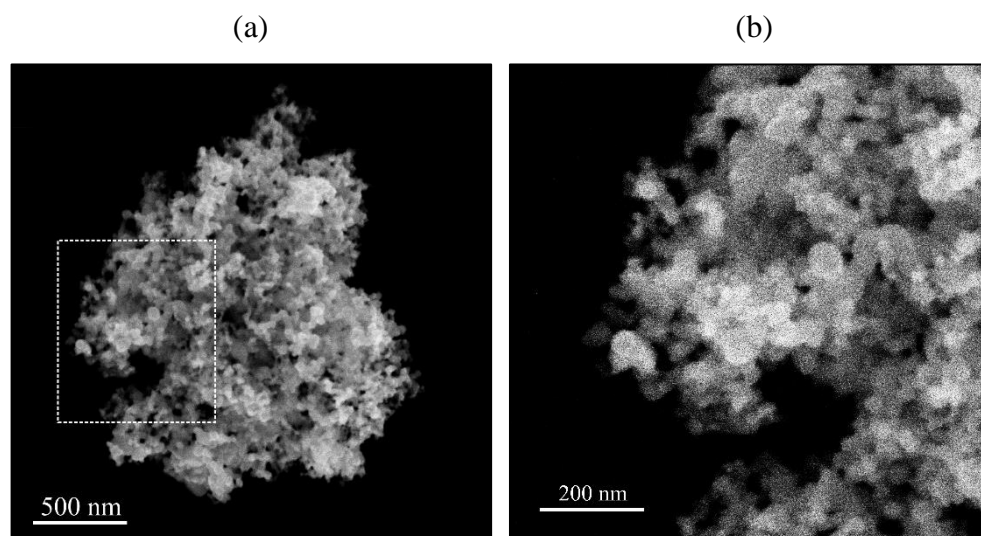


Figure 4.1 SEM images of ATD after the evaporation of IPA at different resolutions. The dashed square in image (a) has been magnified in image (b).

Figure 4.1, b shows a higher magnification of part of the agglomerate of ATD nanoparticles. Due to the limitations of SEM, the shape of individual nanoparticles was unclear. However, for some detectable particles, the diameter of those particles measured using ImageJ software was estimated as 38-68 nm. As those particles might not be necessarily the individual nanoparticles, this size range in Table 4.1 has been shown by an asterisk sign.

SEM images of the agglomerates of RTD nanoparticles are shown in Figure 4.2. The structure of the agglomerates was bi-porous or fractal. As shown in Figure 4.2, a, the agglomerate of RTD nanoparticles seems to be more dense than that of ATD nanoparticles (Figure 4.1, a).

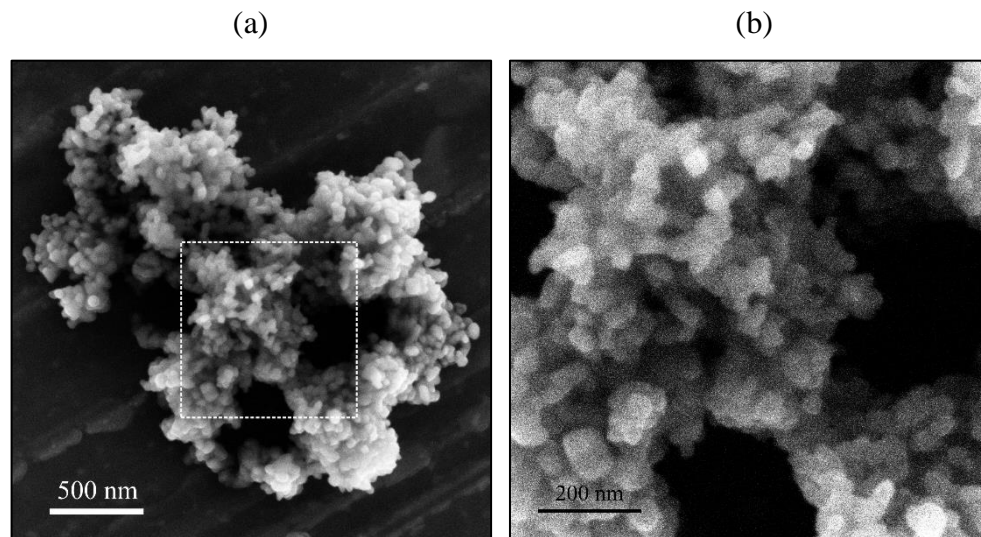


Figure 4.2 SEM images of RTD after the evaporation of IPA at different resolutions. The dashed square in image (a) has been magnified in image (b). These images remind either bi-porous or fractal structures.

According to Figure 4.2, the shape of the individual nanoparticles is varied between spheres and rods. However, it seems that the rod shape is more dominant because there are more particles with angular shapes. This can also be seen from the Transmission Electron Microscopy (TEM) image provided by the supplier (Figure 4.3).

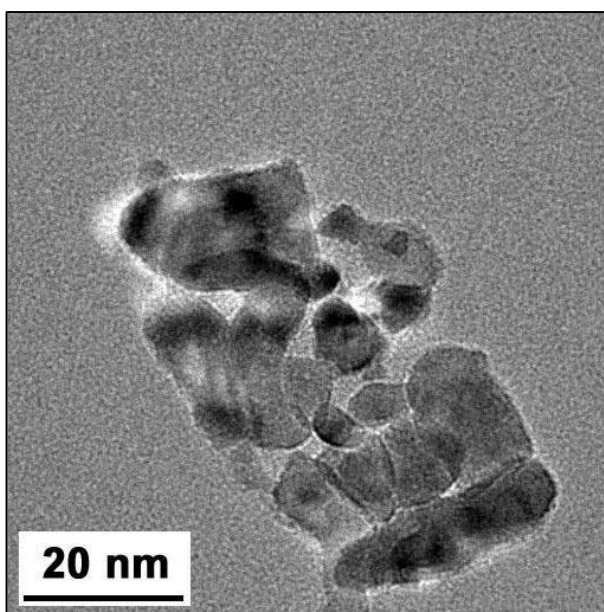


Figure 4.3 TEM image of RTD nanoparticles provided by the supplier.

To measure the size of the individual RTD nanoparticles, the equivalent diameter method was used. The equivalent diameter is defined as the diameter of a circle with an equal surface area of the measured area of a particle obtained using the ImageJ software [173]. Based on this method, the size range of RTD particles was obtained as 40-73 nm. As mentioned before, due to the limitations of the resolution in SEM, this size range should not be considered accurate for individual nanoparticles, as the particles can be either a single nanoparticle or agglomerate of 2-3 nanoparticles.

SEM image analysis was also done for CNT agglomerates (Figure 4.4).

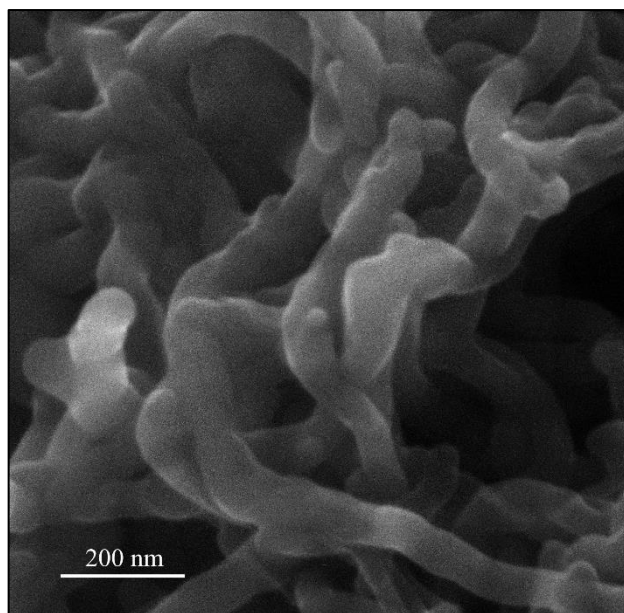


Figure 4.4 SEM image of CNTs after the evaporation of IPA.

Images of CNT particles show that the nanotubes are entwined among each other, and the agglomerates of CNT have shown irregular structures with nanopores (Figure 4.4). The outside diameters (ODs) of the nanotubes were measured at randomly selected points as shown in Figure 4.4. The range of the OD obtained using SEM images was 45-103 nm, which is approximately 3.4-4.5 times larger than those of ODs provided by supplier (Table 4.1). This difference might be due to either the actual size deviation from supplier's information or lateral agglomeration of the cylindrical shells of multi-walled carbon nanotubes. These types of agglomerates are formed due to π - π interactions and van der Waals interactions between nanotubes [174]. This hypothesis can be confirmed using a high-resolution microscopy methods such as TEM, but unfortunately this is not currently available in our laboratories.

Apart from the ODs for the agglomerates of CNT particles, the lengths of the nanotubes were also measured. The obtained length range was between 0.73-1.11 μm which is smaller than the one reported by the supplier (1-2 μm). The reason of the smaller length obtained by image analysis could be that the entwined (tangled) nanotubes penetrated the core of the agglomerates, which, in turn, were difficult to be observed from the SEM analysis. For this reason, the

obtained lengths of CNTs listed in Table 4.1 which were obtained internally in the laboratory might not be reliable.

It should be noted that the sonication of the dispersions containing CNTs may also cause the shortening of the nanotubes from the cap (i.e., the end-defect). Therefore, the shorter length of the CNT particles observed from the SEM is not necessarily due to the penetration of the nanotubes into the core of the agglomerates. These sorts of defects can also happen at the surface of the sidewall of CNT particles. The holes in the sidewall and open ends are considered as the defect sites on the CNTs [174, 175].

4.1.1.2 Agglomerates at Air-Water Interface: PDMS Replica

Observation of the top views of PDMS replica obtained from GTT using the SEM revealed the shapes of agglomerates of nanoparticles at air-water interfaces. The SEM images of the agglomerates of the nanoparticles of ATD, RTD, and CNT are shown in Figure 4.5, Figure 4.6, and Figure 4.8, respectively. These images clearly show that for the ATD and RTD nanoparticles, it was difficult to find the agglomerates of nanoparticles on the surface of PDMS. This indicates that a large fraction of ATD and RTD nanoparticles has not been attached to the air-water interface and could be remained in the aqueous phase. Therefore, there were only some agglomerates detected (Figure 4.5 and Figure 4.6).

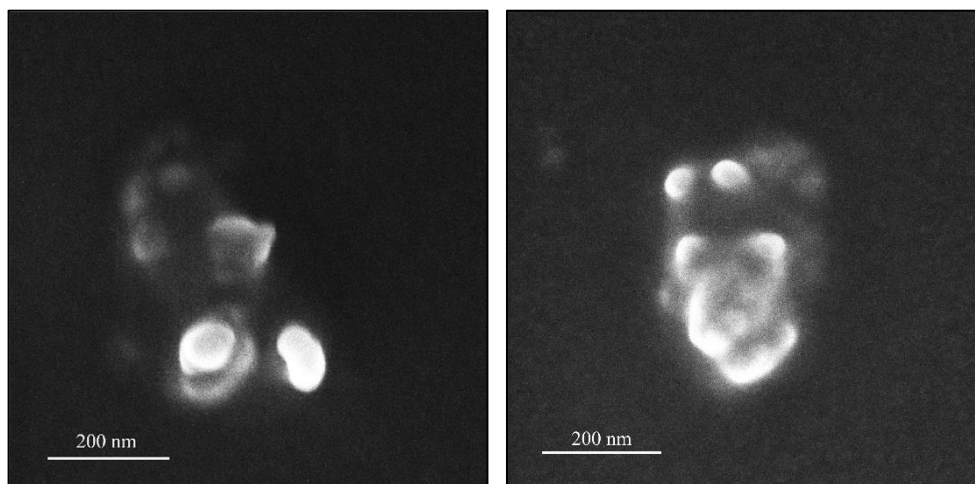


Figure 4.5 SEM images of the top view of surface of the PDMS prepared by GTT for the agglomerates of ATD nanoparticles. Both images are related to ATD nanoparticles on the surface of PDMS.

As shown in Figure 4.5, the agglomerates of ATD nanoparticles have irregular structures with a significant surface roughness, as the brightness of the detected agglomerates is changed significantly from one position to another. This can be a representative of their porous structures as well. The analysis of the images related to the agglomerates of ATD nanoparticles at the air-water interface on the PDMS replica show that the sizes of the agglomerates are in the range of 99-509 nm at different locations. Although this size range is much larger than those of raw nanoparticles of ATD, the size range is still less than 2.5 μm , which is the size range of particles that can arrive to the alveolar region of the human lungs. That means that these agglomerates of ATD nanoparticles are the appropriate representatives of nano-pollutants that can reach the alveolar region of the human lungs [54].

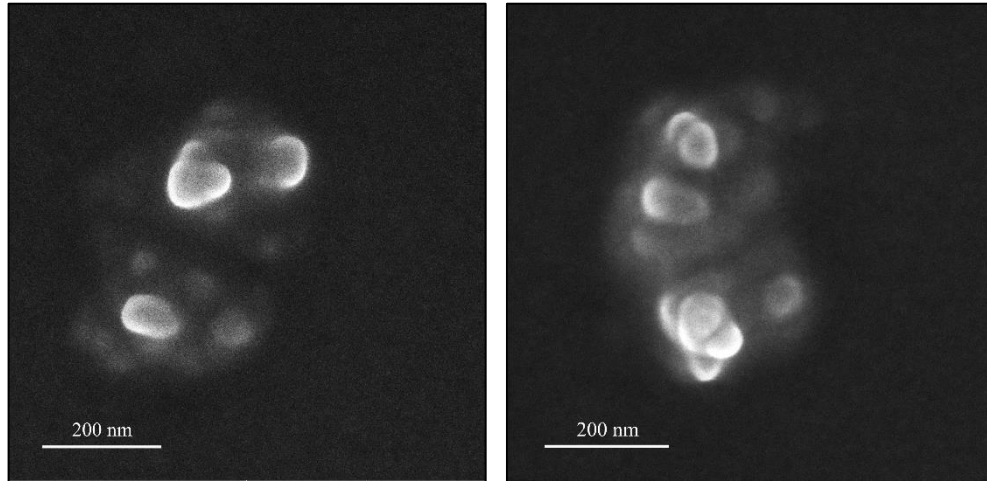


Figure 4.6 SEM images of the top view of surface of the PDMS prepared by GTT for the agglomerates of RTD nanoparticles. Both images are related to RTD nanoparticles on the surface of PDMS.

Figure 4.6 shows the SEM images of the agglomerated RTD nanoparticles casted with PDMS. The structure of the RTD agglomerates is irregular and also appears porous. The size of the agglomerates of RTD nanoparticles is in the range of 69-512 nm at different locations.

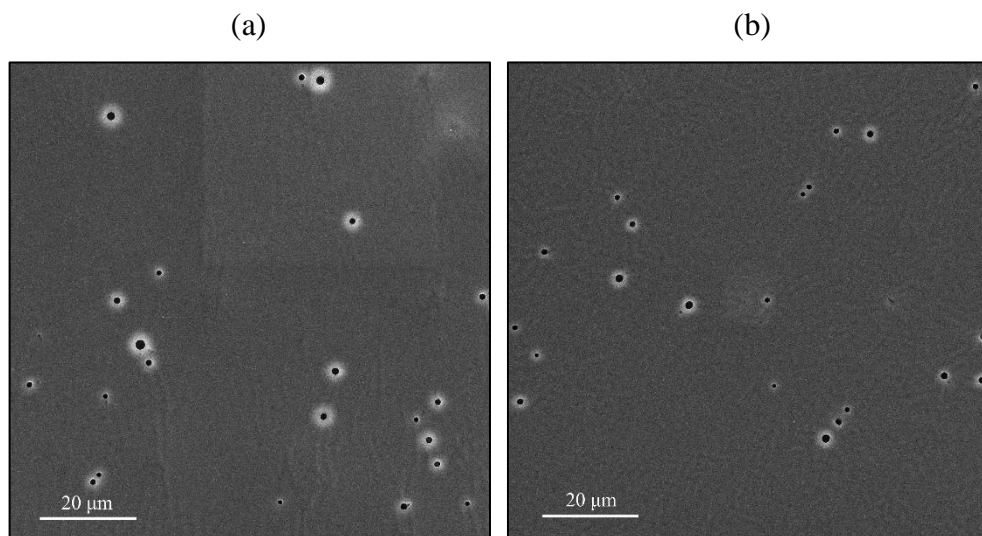


Figure 4.7 SEM images of the top view of surface of the PDMS prepared by GTT for (a) ATD and (b) RTD nanoparticles.

As mentioned before, finding a single nanoparticle or even agglomerates of ATD and RTD on the surface of PDMS is difficult. Instead, there were a notable number of holes on the surface of the PDMS in both cases of ATD and RTD (Figure 4.7, a and b).

The considerable numbers of holes for both the ATD and RTD cases and the difficulties in finding their agglomerates on the PDMS can be associated with the hydrophilicity of these particles and/or their agglomerates. The contact angles of these agglomerates of ATD and RTD nanoparticles at the air-liquid interface might have been small. Therefore, the hydrophilic agglomerates have not been sufficiently protruded from the air-liquid interface. This has resulted in much less entrapped agglomerates of ATD and RTD nanoparticles in the casted PDMS.

The other reason for the presence of these holes might be associated with the mechanical stretching during the preparation of the PDMS in GTT. It has been reported that local stretching of the PDMS in GTT resulted in the formation of microcavities on the surface of PDMS because some of the particles are pulled out. It is also a method of preparing microporous surfaces [153, 176, 177].

Based on the above discussions about the presence of the holes in PDMS replica of ATD and RTD, the average size of the holes can be used as a non-direct indicator of the size of the agglomerates of ATD and RTD nanoparticles.

Based on the analysis of the diameters of the observed holes, the size range of the agglomerates for the ATD and RTD nanoparticles are 1,022-2,030 nm and 850-1,686 nm, respectively. Although this magnitude of size of the holes is considerably larger than those obtained by finding the real agglomerates entrapped in the PDMS, the values obtained using the holes analysis might be more statistically reliable because the number of analysed holes was more than the number of real agglomerates of ATD and RTD found on PDMS.

Apart from the agglomerates of titanium dioxide nanoparticles, i.e., ATD and RTD, the agglomerates of CNT particles on the surface of PDMS were also observed using SEM to determine the structure and size of the agglomerates at the air-water interface.

In the case of CNT particles, some individual carbon nanotubes on the surface of PDMS (Figure 4.8) were detected when the SEM's magnification was

increased significantly with its high resolutions. However, the number of these individual nanotubes protruded from the surface of PDMS is negligible.

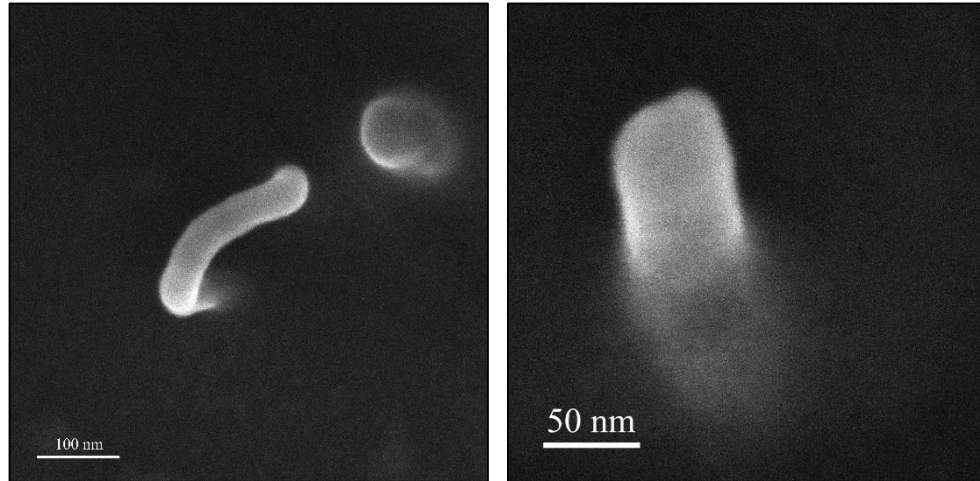


Figure 4.8 SEM images of the top view of surface of the PDMS prepared by GTT for an individual CNT particle. Both images are related to CNT particles on the surface of PDMS.

By measuring the diameter of different axial planes, the outer diameter of the individual nanotubes was estimated. The size range of ODs for these agglomerates of CNTs at air-water interface was 44-64 nm. This OD value is approximately within the size range for the dried agglomerates of CNTs as listed in Table 4.1.

It is impossible to measure the length of the nanotubes from the top view of PDMS because a large section of nanotubes has been trapped inside the PDMS.

Although finding individual nanotubes was difficult, the agglomerates of CNTs were clearly observed on the surface of PDMS (Figure 4.9). It was interesting to see that, despite ATD and RTD cases, there were no holes observed on the surface of PDMS for the CNT agglomerates. Instead, many protrusions from the surface of PDMS were found. The protruded areas in Figure 4.9 were related to the agglomerates of CNT particles.

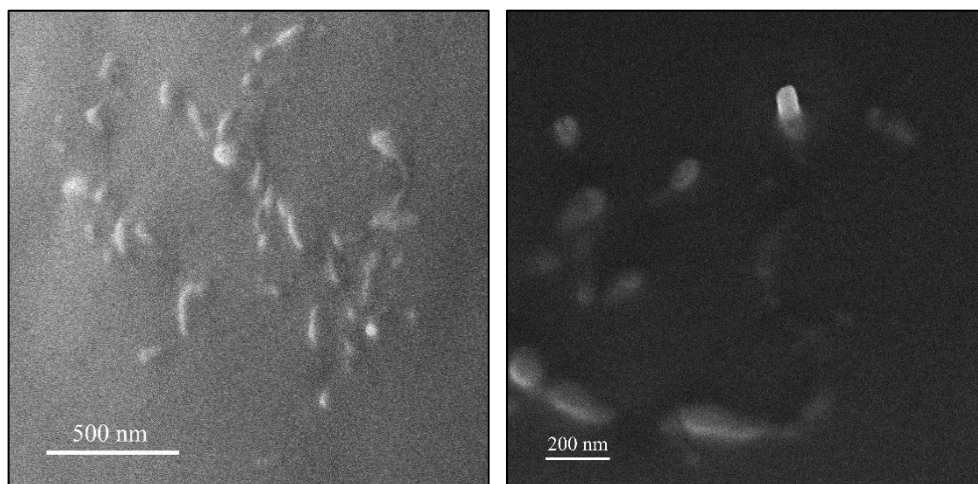


Figure 4.9 SEM images of the top view of surface of the PDMS prepared by GTT for the agglomerates of CNT particles. Both images are related to CNT particles on the surface of PDMS.

Figure 4.9 shows that the agglomerates of CNT particles are entrapped on the surface of the PDMS. The structure of the agglomerates is irregular. These agglomerates of CNT particles are formed due to van der Waals forces as mentioned in Section 4.1.1.1.

4.1.2 Surface Charge

As mentioned in Section 3.2.2, zeta potential measurement was used to measure the surface charges of nanoparticles (Table 4.2). The zeta potential or electrokinetic potential is the potential of a charged particle. This potential is not exactly a phase boundary potential. It is developed within the surrounding solution region. For a surface charged particle, the zeta potential is the potential difference between a point in the fluid medium at some distance from the surface of particle and one point at the plane of shear [178, 179]. In fact, each particle is surrounded by oppositely charged ions in a fixed layer called stern layer. Beyond this fixed layer, there is a cloud-like layer in which there are both positive and negative ions. The shear plane or slipping plane (under the diffusion layer) is the

plane defined by the distance at which the colloidal structure with its chemically bound ions move in the bulk through the solution.

Table 4.2 Zeta potential of nanoparticles or their agglomerates.

Nanoparticles	Zeta Potential (mV)
ATD	-31.46±7.11
RTD	-0.11±0.11
CNT	-49.02±8.21

Results of zeta potential measurement in Table 4.2 show that the ATD and CNT particles are negatively charged. The zeta potential values for these ATD and CNT particles are -31.46 mV and -49.02 mV, respectively.

The standard deviations of zeta potential of ATD and CNT particles are considerably high. This can be attributed to the different sizes of agglomerates which result in various surface areas. These varied surface areas of agglomerates cause different values of surface charge densities, defined as the quantity of charge per unit area. Based on a derivation from the Gouy-Chapman equation (Eq. 4-1), there is a direct relationship between zeta potential, ζ , and effective charge density, σ_{eff} [180, 181]:

$$\sigma_{eff} = \sqrt{8cN\varepsilon_r\varepsilon_0k_B T} \sinh\left(\frac{e\zeta}{2k_B T}\right) \quad \text{Eq. 4-1}$$

where c is the ion concentration, N is the Avogadro constant, ε_r is the dielectric constant, and ε_0 is the vacuum permittivity. The k_B and T stand for Boltzmann's constant and temperature, respectively.

In addition to the charge density, the porosity of the agglomerates affects the measured zeta potential known as effective zeta potential. The real zeta potential of the individual nanoparticles (ζ) can be estimated using the below equation:

$$\zeta_{eff} = \zeta(1 - p) \quad \text{Eq. 4-2}$$

where ζ_{eff} is the effective zeta potential of the agglomerates which is measured during the experiment. In this equation, p is the porosity. If the porosity is known, the real zeta potential of nanoparticles can be calculated. Due to the lack

of equipment, the measurement of the porosity was not possible. Moreover, the equations developed for the zeta potential of the porous materials are more complex than Eq. 4-2 suggested above [182]. It should be noted that zeta potential values measured in this study are the effective zeta potential values of the agglomerates of nanoparticles. For the sake of the brevity, the zeta potential term is used for these values.

Therefore, the size variation and shape nonuniformity, in case of ATD and CNT agglomerates, can be the sources of higher standard deviations of zeta potentials, arising from non-uniform effective charge densities for particles of the same composition in the dispersion.

In case of RTD particles, their values of zeta potential are negative. However, the standard deviation shows that the surface charge of RTD nanoparticles or their agglomerates has also been zero. This indicates that RTD nanoparticles do not contain surface charges, or else, some particles are carrying a very small amount of surface charges corresponding to the zeta potential of -0.11 mV.

4.1.3 Hydrophilicity/Hydrophobicity

4.1.3.1 Three-Phase Contact Angle at Air-Water Interface

The samples prepared for the top view under SEM (Figure 3.8, a) were not suitable to detect the ATD and RTD agglomerates and measure the three-phase contact angles of them at air-water interface (Figure 4.5, Figure 4.6, and Figure 4.7). Therefore, the samples were prepared for the side-view observations under SEM (Figure 3.8, b) to observe if there were nanoparticles or their agglomerates at the edges of the PDMS.

For the cases of the ATD and RTD, no nanoparticles or agglomerates were found at the edges of PDMS. Only by focusing on the top surface of the samples, one individual agglomerate of ATD nanoparticles could be found (Figure 4.10).

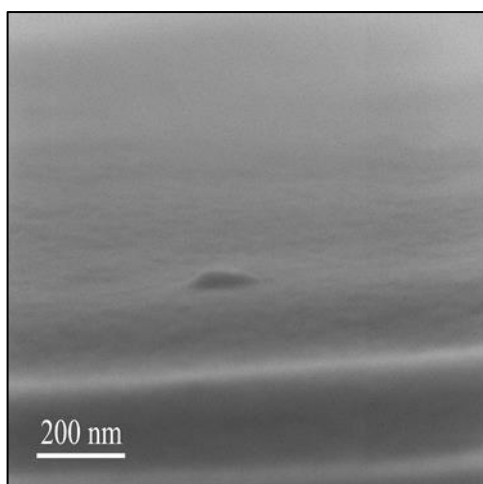


Figure 4.10 SEM images of the side view of surface of the PDMS prepared by GTT for the agglomerates of ATD nanoparticles when the top surface is observed.

The same observation method by focusing on the top surface of samples was used for RTD samples. In this case, individual agglomerates of nanoparticles were found (Figure 4.11).

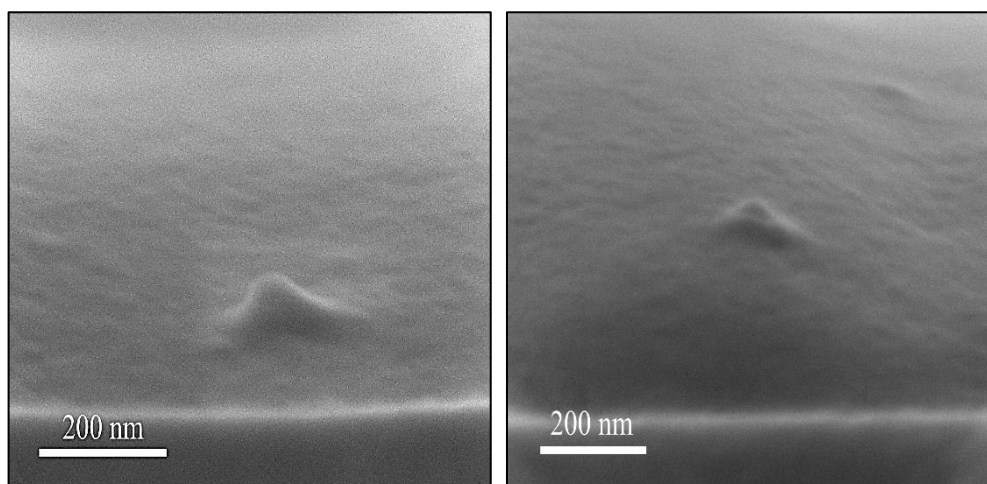


Figure 4.11 SEM images of the side view of surface of the PDMS prepared by GTT for the agglomerates of RTD nanoparticles when the top surface is observed. Both images are related to RTD nanoparticles on the surface of PDMS.

Using the data from only one or two nanoparticles and/or agglomerates of nanoparticles cannot be a reliable method to find and calculate the average value

of the contact angles of particles at the air-water interface from the statistical point of view. The difficulties in finding the agglomerates of the ATD and RTD nanoparticles on the surface of different samples of the PDMS and the presence of the holes on the surface of PDMS for ATD and RTD samples (Figure 4.7 discussed in Section 4.1.1.2) could be associated with the hydrophilicity of ATD and RTD nanoparticles.

In case of CNT particles and their agglomerates, the situation was different from those for ATD and RTD. Finding the aggregates of CNT particles at the edges of PDMS was more convenient (Figure 4.12 and Figure 4.13). By focusing on the top surface of the same samples and using stage tilting option in SEM, CNT particles were easily detected.

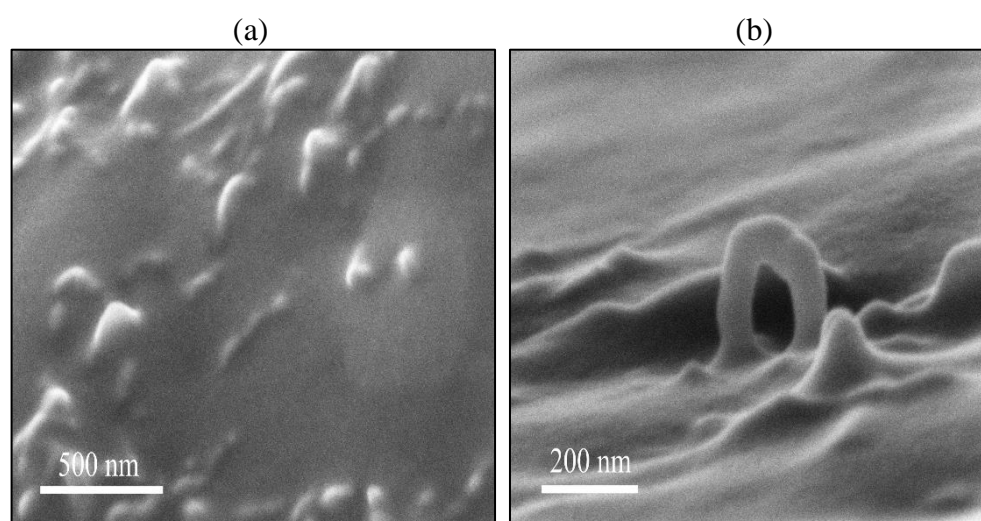


Figure 4.12 SEM images of the side view of surface of the PDMS prepared by GTT for the agglomerates of CNT particles when (a) the top surface is observed and (b) the tilting angle is -14° .

As shown in Figure 4.12, the agglomerates of CNT particles were detectable on the surface of the sample (Figure 4.12, a) which confirms what was observed in Figure 4.9. By tilting the stage and focusing on the surface of these samples, the protrusions of the CNT agglomerates from the surface of the PDMS can be recognised (Figure 4.12, b).

Figure 4.12, b clearly shows the differences in the shape and size of the agglomerated CNT particles at the surface of PDMS, which, in turn, demonstrates the diversity of the shapes and sizes of the CNT agglomerates at the air-water interface.

The other interesting point related to Figure 4.12, b is about the orientation of one nanotube or probably an agglomerate of nanotubes at the surface of PDMS. As it can be seen in this figure, there is a ring-like structure on the surface of PDMS. This nanostructure shows that how the CNTs can be bent into different curved shapes. The agglomerates with different shapes and sizes can affect the kinetics of the adsorption of particles at fluid-fluid interfaces even if the nature of nanoparticles is the same, i.e., CNT particles [183].

In addition to the surface of the samples of PDMS entrapping CNT agglomerates, their edges were also observed using the SEM (Figure 4.13).

It should be emphasized that, in Figure 4.13, the surface of PDMS is a replica of the air-water interface containing the agglomerates of CNT particles. In details, any protrusion from the surface of the PDMS represents those parts of the CNT agglomerates which tend to be at the air-water interface or even in the water phase.

Figure 4.13 a shows the agglomerates of CNT particles at the surface of PDMS, which was cut on its surface. There are several randomised shapes of the agglomerates, whereas finding single nanotubes and calculating their contact angle at the interface is not possible. Some places in Figure 4.13, a show the protrusion of the single nanotubes from the surface of PDMS (Figure 4.13, b and Figure 4.13, c).

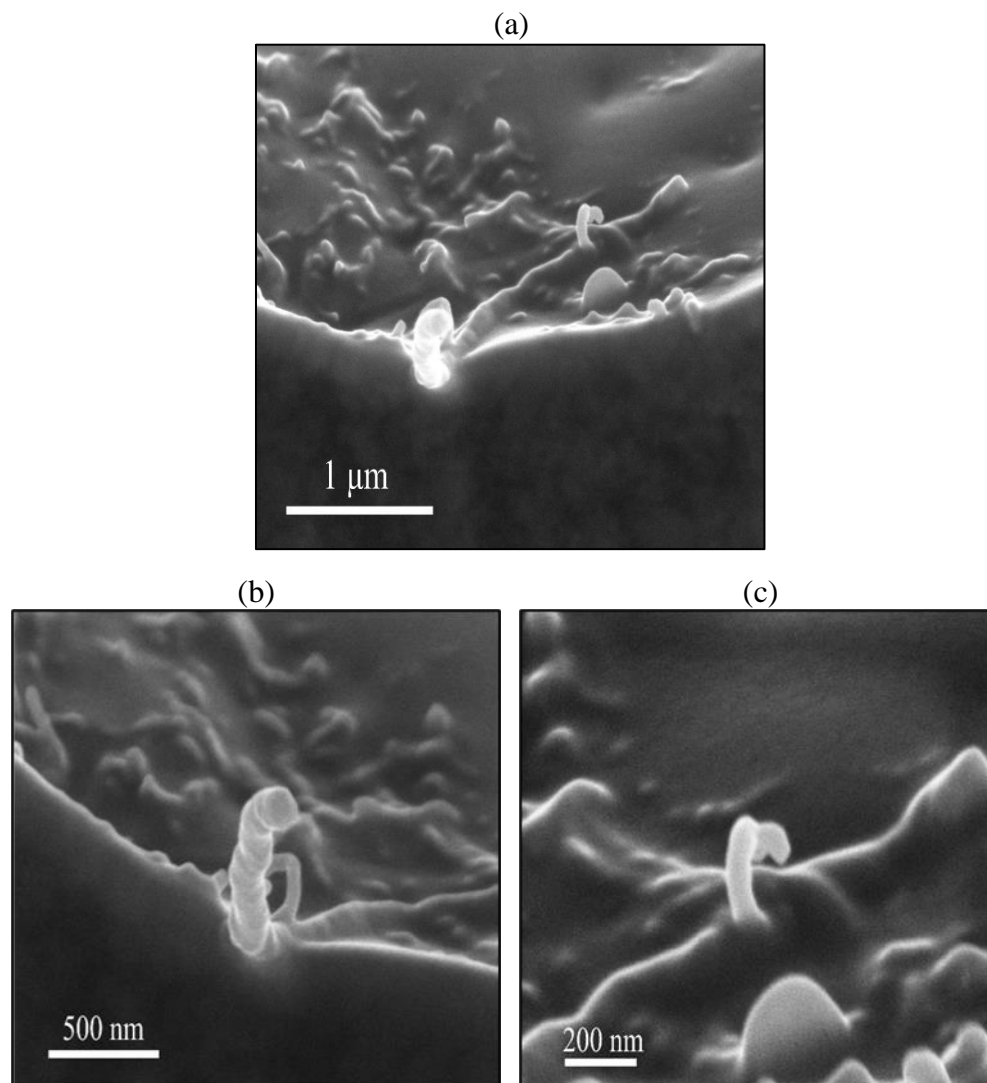


Figure 4.13 SEM images of the edge of surface of the PDMS prepared by GTT for the agglomerates of CNT particles when the tilting angle is (a) -7° , (b) 0° , and (c) -7° .

In Figure 4.13, b, the nanotube at the edge of the surface of PDMS is observed. This shows the tendency of some parts of the surface of the nanotubes toward the aqueous phase. It is seen that the nanotube has been tangentially located on the surface of the PDMS, meaning that the nanotubes are lying down on the plane of interface, and the end part of the nanotube has been protruded from the surface of PDMS. Behind that nanotube, a ring-like agglomerate such as the one observed in Figure 4.12, b is also seen.

This sort of protrusion from the surface cannot be the effect of cutting the surface of the PDMS and damaging the structure of the agglomerates at the edge.

Figure 4.13, c shows that the protrusion of the end part of nanotubes has also happened on the top surface which is far from the cutting edge.

As mentioned before, the measurements of the contact angles of CNT, ATD, and RTD nanoparticles or their agglomerates at the air-water interface were not successful. For calculating the contact angle, both height of the protrusion and average diameter (or radius) of the particles were required.

In cases of the ATD and RTD, the number of the agglomerates of particles entrapped and found at the surface of PDMS was not enough. Therefore, measuring the contact angle only based on one or two protrusions is not statistically reliable.

For the CNT particles, different shapes of the agglomerated CNTs of micron size were detected. These various shapes indicate the polydispersity of the CNT particles and non-uniformity of the system containing these nanoparticles. The range of the size of CNT particles provided by the supplier (Table 4.1) also confirms that the samples of CNT particles are naturally polydispersed. This polydispersity is in both diameter and length of the CNT particles. However, the larger polydispersity is expected to be related to the length of CNT particles as listed in Table 4.1, which was also previously confirmed in reference [184]. Due to the polydispersity of the CNT particles and the various shapes of their agglomerates at the interface, the estimation and calculation of the contact angle were not practical.

Despite the obstacles in measuring the contact angles of the aggregations of CNT particles using the GTT, it is possible to elaborate the attachment and orientation of these shape-anisotropic agglomerates at air-water interface using the robust method of GTT [177]. The visualisation of the microstructures on the PDMS surface elucidate the adsorption behaviour of the agglomerates at the air-water interface.

Based on the configurations distinguished for CNT agglomerates on the SEM images (Figure 4.12 and Figure 4.13), the possible orientations and attachment situations of CNT agglomerates are summarised in Figure 4.14.

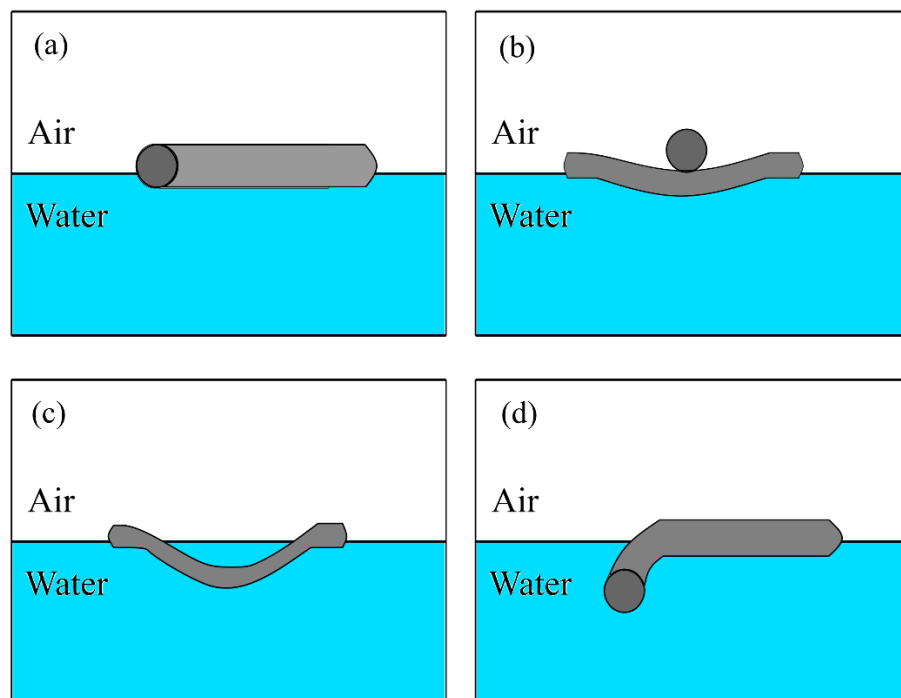


Figure 4.14 The possible positions of CNT particles or agglomerates at air-water interface. The positions include (a) nanotubes lying down on the plane of interface, (b) nanotubes crossing each other and forming agglomerates, (c) bent nanotubes in the aqueous phase, and (d) nanotubes along the interface with their end sticking to the aqueous phase.

As mentioned before, many nanotubes and their agglomerates tend to be orientated along the air-water interface (Figure 4.14, a). The protrusions from the surface of PDMS also show a possibility that nanotubes are crossing each other at the air-water interface (Figure 4.14, b). Moreover, some random ring-like shapes were found on the surface of PDMS. These rings represent the bent nanotubes in the water phase (Figure 4.14, c). In addition to these types of attachment at the interface, the end parts of some of the nanotubes tend to stick into the aqueous phase whilst their length is still along the air-water interface (Figure 4.14, d).

The types of the attachment of multi-walled CNT particles mentioned in Figure 4.14, b-d, are related to bend buckling behaviour of the multi-walled CNT particles. To the best of my knowledge, this type of configuration of CNT particles, i.e., bend buckling, at the air-water interface has not been reported

before. However, it has been proved that the multi-walled CNT particles show bend buckling behaviour under stress [185].

One might think that only the effect of the weight of the PDMS on the CNT particles or their agglomerates causes such an effect. However, there are other possible sources of the compressive stress on the CNT particles. For examples, this compressive force can arise from either the weight of the other nanotubes crossing the buckling bent nanotube or the weight of the trapped water in the holes formed by the CNT agglomerates.

The suggested ways of attachment and orientation of the CNT particles at air-water interface are based on the SEM images taken in this study. It should be noted that there might be other types of configurations. The surface properties such as surface charges and functional groups of the particles also strongly affect the shape of the agglomerates and their configurations at the interface [177].

4.1.3.2 Interfacial Tension

The interfacial tension at air-water interface of the dispersions of 0.01 wt % of nanoparticles in DI water was measured. The method was described in Section 3.2.3.2. To show the estimated equilibrium time, the examples of measurement results for each dispersion of nanoparticles are shown in the logarithmic scale in Figure 4.15. For clarity of data points, the out-of-range points obtained due to the noises in the laboratory were removed.

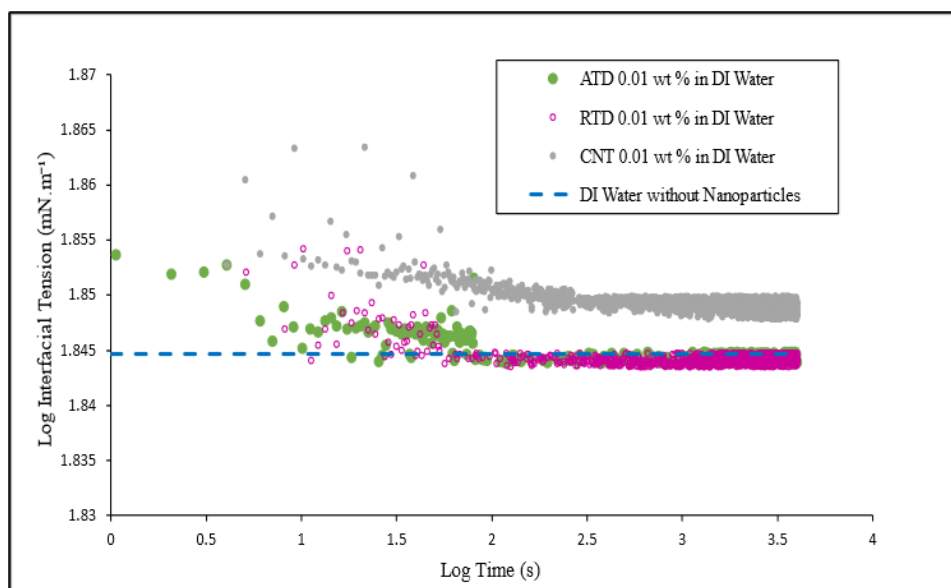


Figure 4.15 Dynamic interfacial tension of the dispersions of nanoparticles with the concentration of 0.01 wt % in DI water at 37°C in log-log coordinates. The dashed line is the representative of the interfacial tension of DI water at 37°C. The hollow purple dots were used for data related to RTD so that the green data points related to ATD can be recognised.

As shown in Figure 4.15, the equilibrium interfacial tension of the dispersions of the ATD and RTD nanoparticles are in the same range. Therefore, the data points for ATD and RTD are overlapping in the graph. After measuring the dynamic interfacial tension for three times, the average values of interfacial tensions for the dispersions of ATD and RTD nanoparticles are 69.96 mN.m^{-1} and 69.91 mN.m^{-1} , respectively. These values are corresponded to 1.8448 and 1.8445 of the log interfacial tension on Figure 4.15. The interfacial tension of DI water at the same temperature, i.e., 37 °C, is equal to 69.93 mN.m^{-1} (1.8447 in the logarithmic scale). Therefore, the interfacial tension of ATD dispersions is slightly higher than that of DI water, whereas the interfacial tension of RTD nanoparticles is slightly lower than that of DI water. Therefore, the deviation of interfacial tension of DI water upon adding ATD and RTD nanoparticles is from hundredths order of magnitude.

In case of the dispersions of the CNT particles, the equilibrium interfacial tension was considerably higher than that of DI water. The obtained average

value of the interfacial tension of CNT dispersion was 70.66 mN.m^{-1} (1.8492 on the log interfacial tension axis in Figure 4.15).

The first difference between the interfacial tension values of the dispersions of CNT and those of both crystal forms of TiO_2 nanoparticles was the order of magnitude of deviation from the interfacial tension of DI water. The deviation of the interfacial tension of CNT dispersion from that of DI water was from tenths order of magnitude, whereas it was of hundredths order of magnitude for the dispersions of ATD and RTD nanoparticles. The second difference was the time that it took for the dispersions to reach the equilibrium interfacial tension and plateau position of graph. As shown in Figure 4.15, the dispersions of ATD and RTD reached their plateau within 150 s (2.1761 on the log time axis), whereas it took 350 s (2.5441 on the log time axis) for the CNT dispersion to reach its plateau.

Table 4.3 Interfacial tension of the dispersions of nanoparticles with the concentration of 0.01 wt % in DI water at 37°C .

Nanoparticles	Interfacial Tension (mN.m^{-1})
ATD	69.96 ± 0.005
RTD	69.91 ± 0.03
CNT	70.66 ± 0.06

The results of the interfacial tension measurement of the dispersions of nanoparticles in DI water have been summarised in Table 4.3. This table also shows the value of standard deviation obtained from the multiple measurements. The largest standard deviation is associated to CNT dispersion in DI water. This can be due to the various shapes of the agglomerates of CNT particles at the air-water interface (Section 4.1.3.1) which cause more deviation in multiple measurements for the same sample.

4.2 Summary

In this chapter, characterisation of three different nanoparticles including anatase form of titanium dioxide (ATD), rutile form of titanium dioxide (RTD) and multi-walled carbon nanotube (CNT) was performed.

Analysis of the shapes of the above-mentioned nanoparticles and/or their agglomerates in the dried state showed the porous nature of the agglomerates of titanium dioxide nanoparticles either with anatase or rutile crystal forms. However, the agglomerates of the RTD nanoparticles were denser than those of ATD nanoparticles. This was consistent with the less surface charges of the RTD nanoparticles compared to those of ATD nanoparticles. As the surface charges of RTD nanoparticles were small, the repulsion forces between these particles were also small, which in turn, caused the denser agglomerates. No accurate information was obtained for the sizes of the individual nanoparticles due to the instrumental limitations. The shapes of the individual ATD and RTD nanoparticles were consistent with the information provided by the supplier, meaning that the ATD and RTD nanoparticles had spherical and rod-like shapes, respectively.

The CNT nanoparticles were entwined among each other resulting in the agglomerates with irregular structures containing nanopores. These structures of the agglomerates of CNT particles were not as dense as those of titanium dioxide nanoparticles. This was also consistent with the higher surface charges of the CNT particles, if compared with those of ATD and RTD. Therefore, the surface charges of the nanoparticles were the indicator of the porosity and/or the compactness of the final structure of their agglomerates.

The three-phase contact angle measurement at air-water interface using the GTT was not successful for the nanoparticles and/or their agglomerates in this study. However, useful qualitative information was provided using this technique. The hydrophilic features of the agglomerates of ATD and RTD nanoparticles and hydrophobic characteristic of the agglomerates of CNT particles were clearly proved based on the holes or entrapped nanoparticles on the surfaces of the PDMS used in GTT.

It was also revealed that the possible configurations for CNT agglomerates at the air-water interface are not limited to simple positions of nanotubes lying down on the plane of interface. More positions including nanotubes crossing each other, bent nanotubes in the aqueous phase, and nanotubes along the interfaces with their ends sticking to the aqueous phase were found. These structures at the air-water interface are arising from the bend buckling behaviour of the multi-walled CNT particles. These structures which have not been considered in the studies of air-liquid interfaces containing CNT particles, should be treated carefully in these interfacial studies because these structures are one of the sources of complexity in the interfacial systems.

Finally, the hydrophobic CNT particles with a concentration of 0.01 wt % in DI water showed a higher interfacial tension in comparison with hydrophilic ATD and RTD nanoparticles with the same concentration in DI water.

The results of this chapter can also be used as a reference of the potential characterisation methods for the studies investigating the nanoparticles at the fluid-fluid interfaces.

Chapter 5

Nano-Pollutants in Contact with Industrial Surfactants

Foams are defined as an aggregation of gas bubbles separated from each other by a thin layer of liquid called a liquid film [186]. The separated bubbles are connected through Plateau borders and nodes [187]. Different types of nanoparticles are used to improve the stability and characteristics of the foams.

Titanium dioxide (TiO_2) nanoparticle is one of the most ubiquitous nanoscale substances which have been widely applied in various fields including, but not limited to, paint, pigment, plastics, coating, cosmetics, food, paper and pharmaceutical industries [188, 189]. The nanoparticles of TiO_2 can be used to improve the stability of foams in the EOR techniques [190-193]. Moreover, TiO_2 is a cost-effective photocatalyst material for decomposition of wastes in liquid and gas phases. The wet foams stabilised by TiO_2 nanomaterials are potential options for the fabrication of photoactive macroporous/mesoporous structured TiO_2 foams which can be utilised for overcoming the environmental challenges such as air filtration [194-196]. Despite a lot of applications of TiO_2 nanoparticles in the dispersed systems, to our knowledge, the studies focused on the interfacial properties and foamability of such systems are relatively inadequate [197].

In this chapter, the adsorption isotherms and models of two commonly used industrial surfactants were obtained. The surfactants were CTAB and SDS, which are classified as cationic and anionic surfactants, respectively. The Critical Micelle Concentration (CMC) as a unique parameter for each surfactant was obtained from interfacial tension measurement. The CMC values of these two surfactants are well-documented in the literature. However, it has been proven that CTAB and SDS purchased from different suppliers show different CMC values [198]. Therefore, it was beneficial to measure the CMC values of these

two surfactants. The CMC affects interfacial phenomena such as interfacial tension and bulk properties, e.g., the detergency. Therefore, to measure the CMC, a potential method based on optical fibre was suggested and studied.

The adsorption of TiO₂ nanoparticles at the air-liquid interfaces of the aqueous solutions of the mentioned ionic surfactants was further studied. The crystal structure of the TiO₂ nanoparticles is anatase because this polymorph has shown a better photocatalytic activity in comparison to the other forms of TiO₂, e.g., rutile [199]. The concentration of nanoparticles was fixed, whereas the surfactants' concentrations were varied. The interactions between TiO₂ nanoparticles and each type of surfactant with varying concentrations were also investigated. Their foamability and foam properties were analysed through the foam formation and bubble size distribution in the foams. The outcome of this study will be promising for the industries in which amphiphilic systems of nanoparticles-surfactants and foam formation are used.

5.1 Results and Discussion

5.1.1 Adsorption Isotherms and Models

To investigate the performance of the surfactants at the air-liquid interface and, in turn, the related foaming properties, it is crucial to understand the adsorption behaviour of the surfactants. Using adsorption isotherms and their models is a well-known method to elaborate this behaviour. In this study, we applied Frumkin model as the adsorption isotherm and the equation of state for the adsorption layer. This model is suitable for the systems slightly deviated from ideal systems which can be described by the Langmuir adsorption isotherm [200].

The adsorption model proposed by Frumkin [201] can be used for individual ionic surfactant solutions such as CTAB and SDS. In the Frumkin model, the interactions between the adsorbed molecules of the surfactants at the interface have been considered. When this model is used for ionic surfactants without any

inorganic salt in the system, the equation of state and adsorption isotherm are [201]:

$$\gamma = \gamma_0 + \frac{2RT}{\omega} [\ln(1 - \theta) + a\theta^2] \quad \text{Eq. 5-1}$$

$$bcf = \frac{\theta}{1 - \theta} \exp(-2a\theta) \quad \text{Eq. 5-2}$$

where γ_0 , R , T , and c are the surface tension of the pure solvent, gas law constant, absolute temperature, and the bulk concentration of the ionic surfactant, respectively. The Frumkin interaction parameter and the adsorption equilibrium constant have also been shown as the parameters a and b . Moreover, ω is the partial molar area of the surfactant. The surface coverage, θ , is:

$$\theta = \Gamma\omega \quad \text{Eq. 5-3}$$

where Γ is the actual adsorption of the surfactant molecules at the interface [202]. The average activity coefficient, f , can be calculated by the Debye-Hückel equation which has been corrected for short-range interactions:

$$\log f = -\frac{0.5115\sqrt{I}}{1 + 1.316\sqrt{I}} + 0.055I \quad \text{Eq. 5-4}$$

where I is the ionic strength expressed in M and can be calculated as the sum of the surfactant concentration and inorganic salt concentration. Therefore, when there is no salt in the system, $I = c$ [203]. In our studies, there was no salt used in the system.

As it was mentioned in Chapter 3, the dynamic interfacial tension was measured by the PAT and plotted as a function of time for each concentration of CTAB and SDS individually. The equilibrium interfacial tension was considered as the interfacial tension attributed to the special concentration of the surfactant in the solution.

By plotting the interfacial tension versus concentration for each type of pure surfactant, two main regions can be recognised (Figure 5.1 and Figure 5.2). These regions are concave-shaped curve zone (solid line) and plateau-shaped zone (dashed line).

The first region with a concave-shaped curve is the zone in which an adsorption isotherm model can be suggested. In this region, when the

concentration of the surfactant in the solution is increased, more surfactant molecules are adsorbed at the interface, and thus interfacial tension decreases.

By adding more surfactant molecules to the system, the interface coverage is increased until it gets saturated by the surfactant molecules. At the concentrations above this amount, the remained surfactant molecules at the solution interact with each other and form clusters called micelles. The concentration at which these colloidal structures are formed in the solution is the critical micelle concentration (CMC).

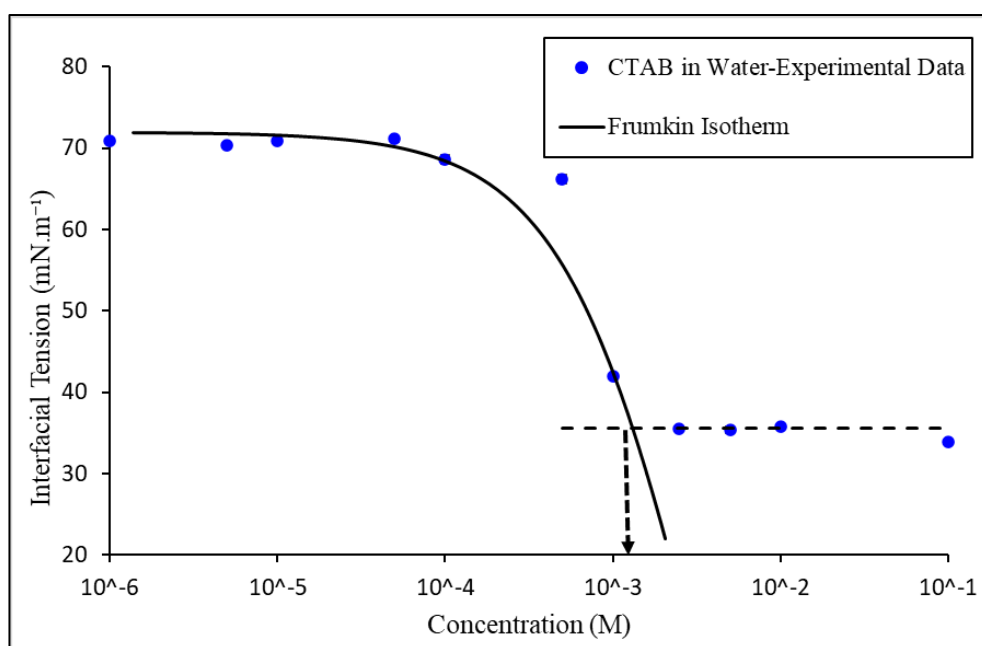


Figure 5.1 Equilibrium interfacial tension against concentration of the CTAB in aqueous solutions at 25°C. The standard deviation for each point has been shown on the graph, but it is not clearly visible due to the small amount. The solid line is the best fitted curve of the Frumkin model for the experimental results in this study. Dashed line is the representative of reaching CMC point. The arrow shows the CMC value equal to 1.30×10^{-3} M.

The surface tension will not decrease by increasing the concentration beyond CMC point. This is where the graph of interfacial tension versus concentration becomes a plateau shape. In Figure 5.1 and Figure 5.2, the concentration at which the solid line and dashed line cross each other is reported as the CMC. The arrow shows the CMC point.

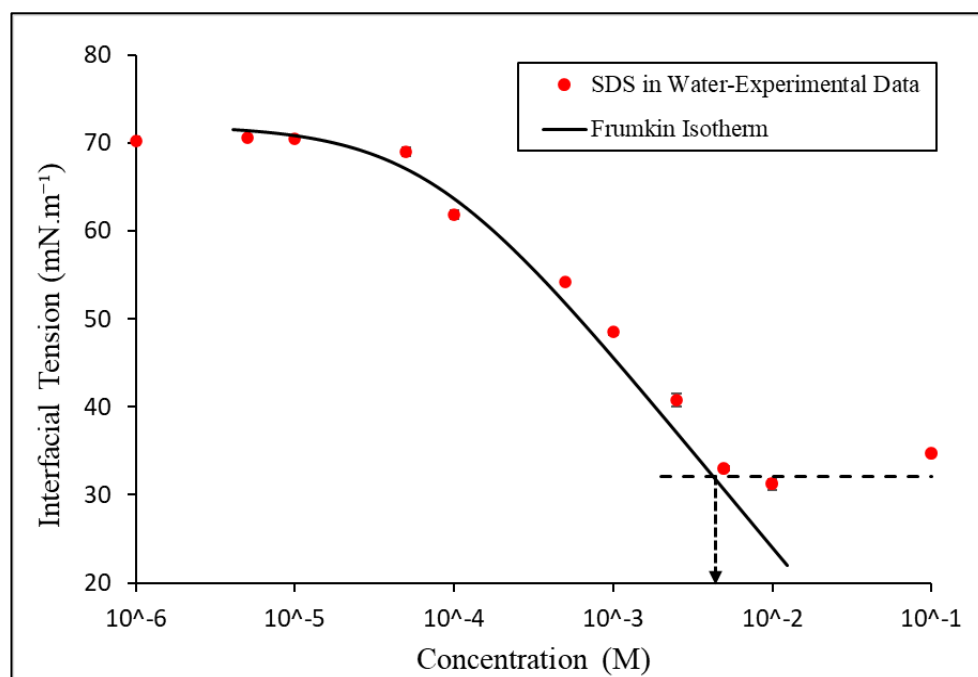


Figure 5.2 Equilibrium interfacial tension against concentration of the SDS in aqueous solutions at 25°C. The standard deviation for each point has been shown on the graph, but it is not clearly visible due to the small amount. The solid line is the best fitted curve of the Frumkin model for the experimental results in this study. Dashed line is the representative of reaching CMC point. The arrow shows the CMC value equal to 4.23×10^{-3} M.

Using the Frumkin model for ionic surfactants and IsoFit software, the related parameters of the model, i.e. ω , a , and b were derived and are summarised in Table 5.1. This table also shows the CMC amount for each surfactant at 25°C.

Table 5.1 Adsorption isotherm parameters obtained as best fit values from the Frumkin model and CMC at 25°C obtained by the tensiometry and optical fibre methods.

Surfactant	ω ($\text{m}^2 \cdot \text{mol}^{-1}$) [204]	a	b ($\text{m}^3 \cdot \text{mol}^{-1}$)	CMC (M) by Tensiometry	CMC (M) by Optical Fibre
CTAB	$1.00 \times 10^{+5}$	3.00×10^{-1}	7.35×10^{-1}	1.30×10^{-3}	1.60×10^{-3}
SDS	$5.00 \times 10^{+5}$	1.00×10^{-1}	$1.26 \times 10^{+1}$	4.23×10^{-3}	6.50×10^{-3}

Positive values of α for both the CTAB and SDS show that intermolecular attraction exists between surfactant molecules at the surface monolayer. This non-negligible amount of α represents that the attraction forces at the interface are mostly related to the hydrophobic tails of the surfactant molecules which cause a closer packing of the molecules. This can be attributed to the long-chain alkyl groups of both CTAB and SDS molecules. As it can be seen in Figure 5.3, the numbers of carbon atoms of the hydrophobic groups in the CTAB and SDS are 16 and 12, respectively, and thus they are categorised as the surfactants with a straight long-chain hydrophobic tail [205, 206].

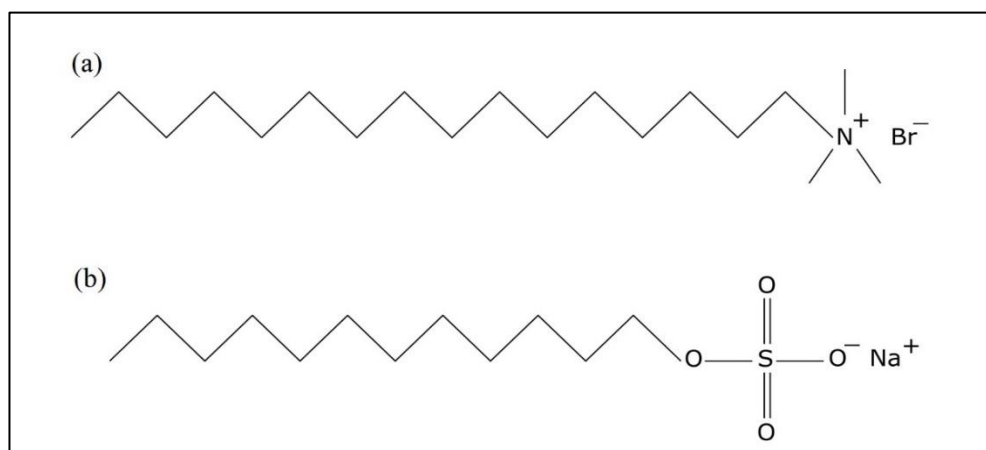


Figure 5.3 Molecular structure of (a) CTAB and (b) SDS.

The amount of molar area, ω , for the SDS is larger than that for the CTAB. The larger molar area of SDS molecules leads to a situation where, at a given concentration, SDS preferentially decreases the value of interfacial tension, compared with the CTAB. For example, at the concentration of 1.00×10^{-4} M, the value of interfacial tension for CTAB is 68.58 mN.m^{-1} (Figure 5.1), whereas at the same concentration, this value is 61.89 mN.m^{-1} for SDS (Figure 5.2).

Based on obtained results, the CMC for CTAB is 1.30×10^{-3} M at 25°C and the interfacial tension at this concentration is 35.55 mN.m^{-1} . Likewise, at 25°C , the CMC for SDS is 4.23×10^{-3} M at which the interfacial tension is 32.09 mN.m^{-1} .

In this study, we have used the tensiometry as one of the conventional and common methods of CMC measurement. Although this is a well-known method and a concise technique for measuring the CMC of surfactants, it demands a long time to complete the experiments using the PAT and obtain the results [17].

In addition to the tensiometry, analytical chemistry techniques such as titration [207], electrochemical methods such as conductometry, voltammetry, potentiometry, and electromigration techniques, have also been used to measure the CMC of surfactants [208]. However, most of the mentioned techniques are sample-consuming or their related experiments need a long time to be completed.

Therefore, in the next section, the details of a potential method based on optical fibre for measuring the CMC of surfactants have been presented and discussed.

5.1.2 Alternative Method of CMC Measurement: Optical Fibre

Optical fibre sensors have been comprehensively studied because of their small size, low cost, low amount of required sample for measurement, rugged construction, and possibility of *in-situ* measurements of chemical parameters [209-211]. Because of such advantages, optical fibre sensors can be an alternative method in measuring the CMC of surfactants.

The set-up details were explained in Chapter 3. Figure 5.4 shows a schematic diagram of the optical fibre set-up.

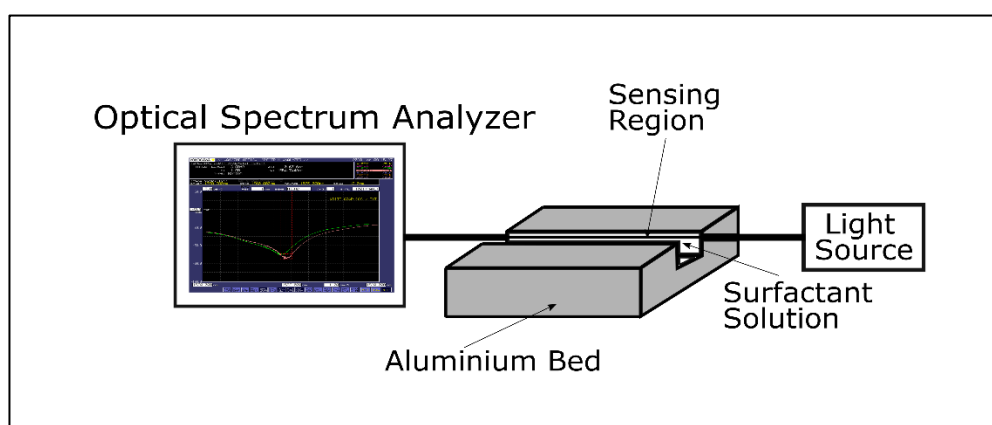


Figure 5.4 Schematic diagram of the optical fibre set-up [212].

The output of the optical spectrum analyser is a spectrum typically shown in Figure 5.5. The spectrum width centre, λ_c , is the quantified response of the optical spectrum analyser system using notch width measurement. A waveform of a filter with U-character or V-character type wavelength characteristics is measured. In the algorithm of notch width measurement when the type is bottom (Figure 5.5), a bottom level is obtained. Then, the notch width for this level and its centre wavelength (λ_c) is measured. As Figure 5.5 (horizontal axis) shows, λ_c is the average of λ_A and λ_B [213]. The value of λ_c is specific for each solution, and it can depend on different parameters such as temperature, concentration, and pH of the solution.



Figure 5.5 A typical spectrum as the output of the optical spectrum analyser.

The CMCs of both the CTAB and SDS were measured using the optical fibre method. Then, as a verification procedure, the results measured by the optical fibre sensor were compared with the results obtained by the PAT. This comparative approach was taken to evaluate the potential of optical fibre sensor

as a promising technique for measuring the CMC of surfactants in different industries.

To achieve this purpose, the spectrum width centre, λ_c , was plotted against the concentration of surfactant (Figure 5.6 and Figure 5.7). These figures show that the trend in the behaviour of spectrum width centre suddenly changes in the vicinity of a particular concentration (the arrows shown in Figure 5.6 and Figure 5.7). This sudden alteration was observed in both CTAB and SDS cases. It can be seen that at the concentrations lower than this particular concentration, there is a linear trend in the behaviour of λ_c . At higher concentrations, the relationship between λ_c and concentration is nonlinear and more of a logarithmic trend.

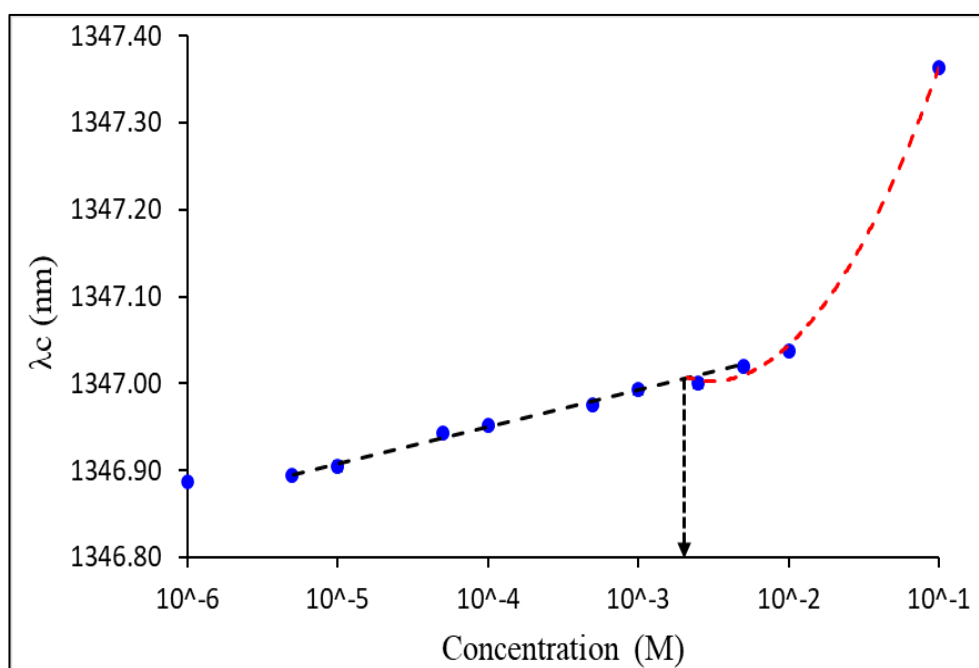


Figure 5.6 Spectrum width centre against concentration of the CTAB in aqueous solutions at room temperature. The black and red dashed lines are the linear and logarithmic trends, respectively. The arrow shows the CMC value.

If we intercept the linear and logarithmic trendlines, the concentration attributed to the interception point is very close to the value of CMC obtained by the tensiometry for each surfactant. The amounts of CMC attained by the optical fibre method were 1.60×10^{-3} M for CTAB and 6.50×10^{-3} M for SDS. The CMCs

for CTAB and SDS calculated from the profile analysis tensiometry were 1.30×10^{-3} M and 4.23×10^{-3} M, respectively (Table 5.1).

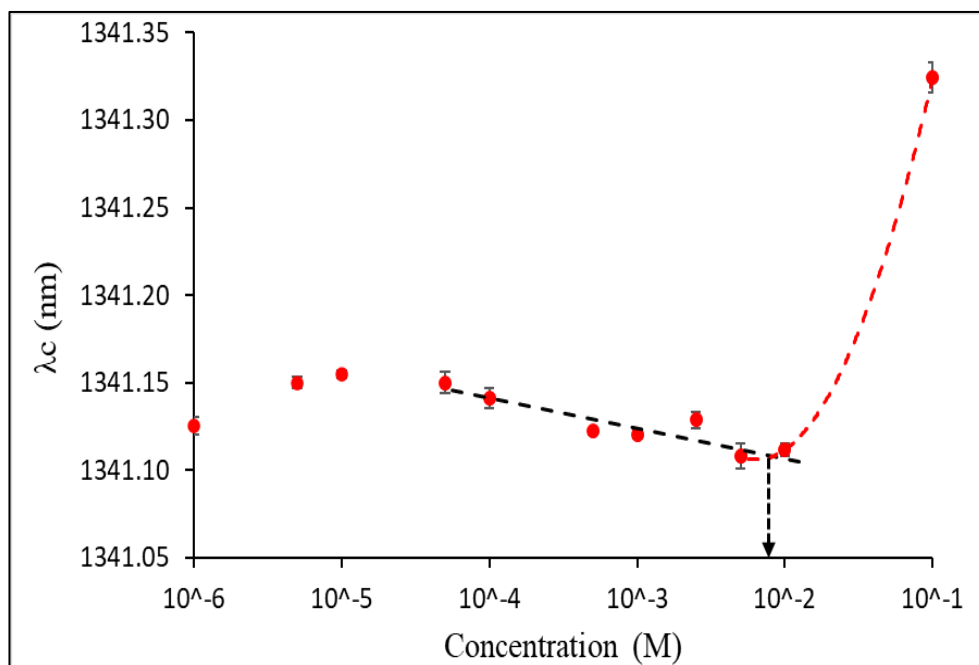


Figure 5.7 Spectrum width centre against concentration of the SDS in aqueous solutions at room temperature. The black and red dashed lines are the linear and logarithmic trends, respectively. The arrow shows the CMC value.

The similarity of the CMC values obtained by the tensiometry and optical fibre shows that the point of sudden change in the trendlines can be an indicator of CMC for both the CTAB and SDS. However, there are some differences between the results of CTAB and SDS when the optical fibre method is used. At the concentrations below CMC, when the concentration is increased, the λ_c is increasing for CTAB while it is decreasing for SDS.

This difference between CTAB and SDS might be due to the various mechanisms of adsorption of surfactant molecules onto the optical fibre. The mechanism of adsorption affects the refractive index and the effective diameter of fibre. Therefore, it will result in various wavelength shifts for each surfactant. Based on the materials constructing the solid surface of optical fibre, there might be electrostatic and/or hydrophobic interactions between surfactant molecules and the outer layer of the sensing region of optical fibre. Accordingly, the

mechanism of action depends on the functional groups of the solid surface of fibre.

The silica fibre used in this study can be either hydrophilic or hydrophobic. If the surface of silica is hydrophobic, the discrepancies between the CTAB and SDS can be attributed to the difference between the length of the hydrophobic group and size of the surfactant's head. These differences between the CTAB and SDS lead to different packing of surfactant molecules on the surface of the optical fibre. If the surface of optical fibre is hydrophilic or it contains electrostatic charges, they will affect its interactions with ionic surfactant molecules. At higher concentrations of surfactant, there is also a possibility of formation of the bilayer of surfactant molecules on the surface of the optical fibre.

To address the reason of opposite trends for the two surfactants at the concentrations below CMC, further studies are required. The design of the future studies should be based on the below considerations so that any possible mechanism of action and/or source of error can be detected:

1. The attachment of surfactant molecules on the surface of optical fibre results in changes in the refractive index and effective diameter of the sensor which, in turn, alters the measured wavelength shift [214-217]. Therefore, future studies should be focused on measuring the following factors and parameters:
 - The hydrophilicity / hydrophobicity of the surface of optical fibre using contact angle measurements,
 - The surface charge of the solid optical fibre using zeta potential measurements,
 - The thickness of the fibre after interactions with the molecules of each type of surfactant,
 - The refractive index differences between the surfactants, and,
 - The amount of the adsorbed surfactant molecules onto the surface of the fibre.
2. When we use the optical fibre technique, two different interfaces can be recognised. The first one is the solid-liquid interface between the optical fibre and solution of surfactant, and the second interface is the air-liquid

interface between air and surfactant solution. There might be an adsorption competition between these two interfaces due to the tendency of surfactant molecules toward them. In the future studies, air-liquid interface can be eliminated by introducing a closed volume as the cell of optical fibre and the liquid. Therefore, the aluminium bed in Figure 3.16 will not have an open facet on its top side. Moreover, the optical fibre will be immersed in the solution and the temperature can be controlled.

3. The opposite wavelength shifts before CMC can also be a result of a measurement error as the wavelength shifts before CMC are limited. To find out more about this hypothesis, a tapered SNCS fibre sensor with 10 times higher sensitivity than the previously used sensor can be utilised. This method can improve the measurement accuracy and minimise measurement errors [212].

Accordingly, the future studies can be summarised in Figure 5.8.

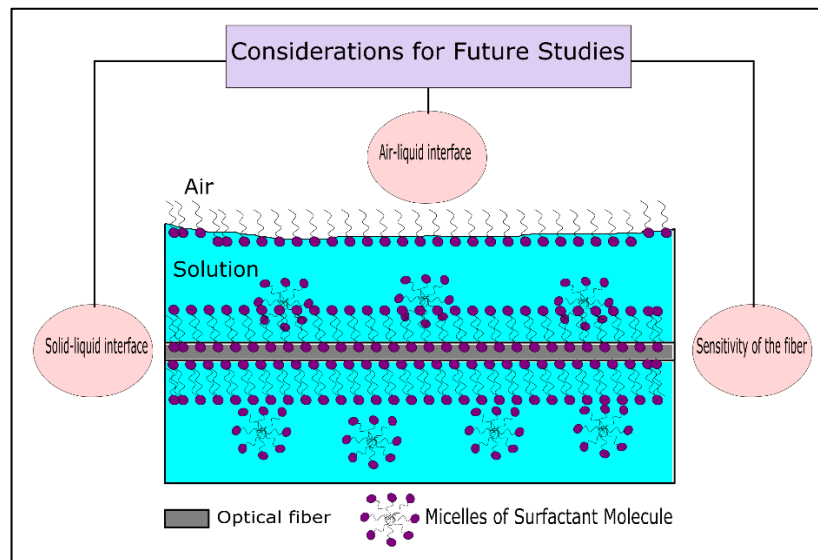


Figure 5.8 The main considerations for the future studies on CMC measurement using optical fibre [212].

The development of these optical fibre sensors for in-situ measurement of the CMC in the industries which require the CMC measurement during the

manufacturing process is helpful because these sensors have a small size and can be portable whereas the profile analysis tensiometer is a large equipment which needs to be put on a vibration control table. Moreover, most of the other methods of CMC measurement such as tensiometry are sample-consuming or take a long time to be performed [212]. The CMC measurement using optical fibre is a suitable method for the applications dealing with samples with small size.

Based on the results shown in Sections 5.1.1 and 5.1.2, we understood the effects of the nature and concentration of each surfactant on the interfacial tension. Moreover, a clear view on the CMC of each surfactant, i.e., CTAB and SDS, was achieved.

In the next section, the effect of a fixed concentration of TiO₂ nanoparticles with anatase crystal form on the surfactant solutions will be investigated. The importance of this part of the study is related to (a) the industrial formulations and processes containing surfactants and nanoparticles specifically TiO₂, and (b) industrial processes working with surfactants and struggling with the introduction of air suspended nano-pollutants in their processes.

5.1.3 Effects of Nano-Pollutants on the Solutions of Different Industrial Surfactants

5.1.3.1 Effects of the Type of Surfactant and its Concentration

The graphs related to the interfacial tension and zeta potential versus the concentration of surfactant at a fixed concentration of anatase TiO₂ nanoparticles (0.1 wt %) are shown in Figure 5.9 and Figure 5.11. The ATD is the abbreviation for anatase form of titanium dioxide (TiO₂) nanoparticles. To understand the mechanism of adsorption, the Frumkin isotherm related to the interfacial tension of bare surfactants and interfacial tension in presence of nanoparticles have been combined into a single graph. The graph of the zeta potential has been also shown in Figure 5.9 and Figure 5.11.

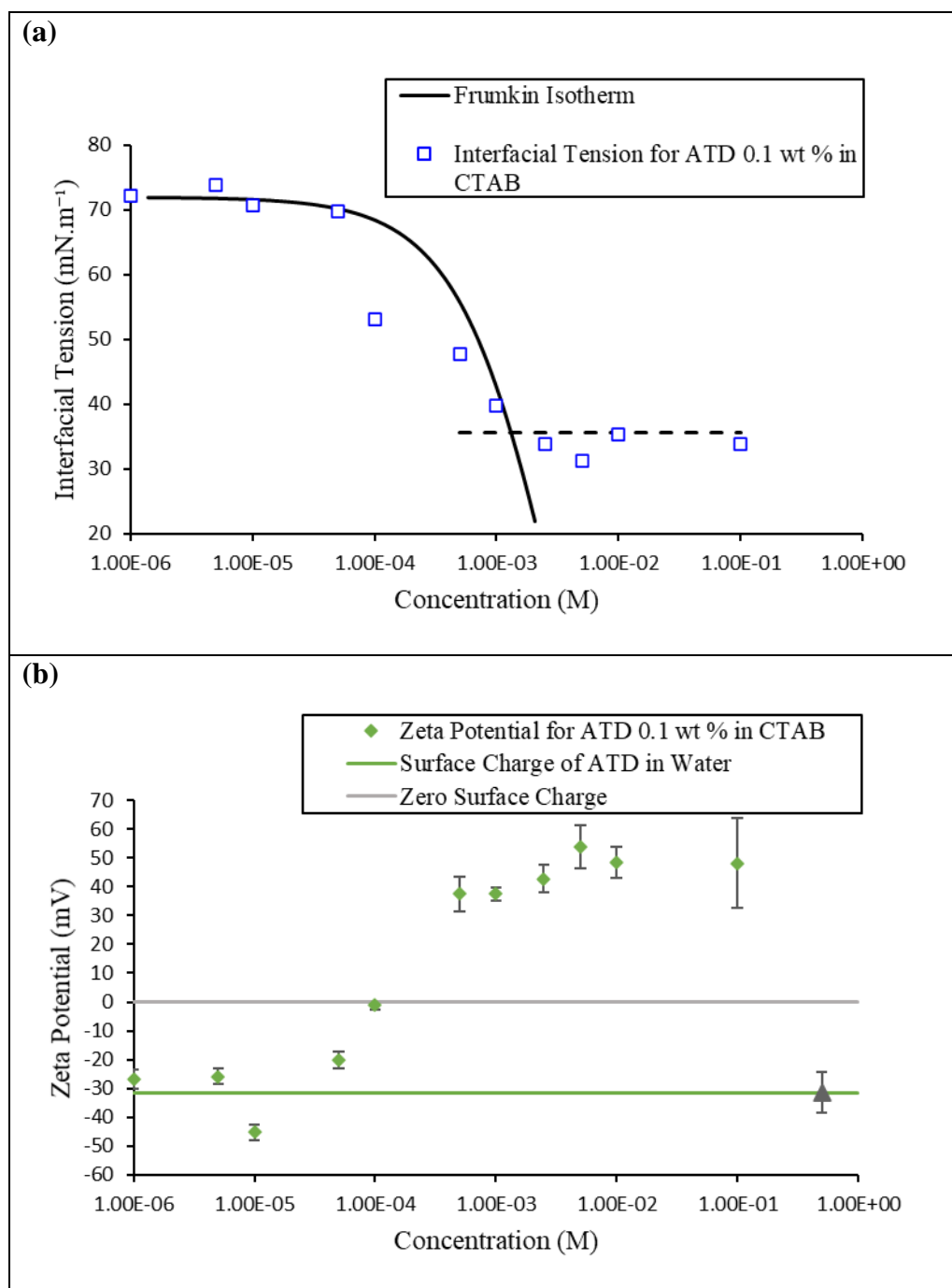


Figure 5.9 Equilibrium interfacial tension (a) and zeta potential (b) of the dispersions of ATD nanoparticles against concentration of the CTAB in aqueous solutions at 25°C. The concentration of ATD nanoparticles is constant and 0.1 wt % in all experiments. The solid line in (a) is the best fitted curve of the Frumkin model for the interfacial tension results for bare surfactant solutions. Dashed line is the representative of reaching CMC point. The green line is the representative of the surface charge of ATD nanoparticles in water. The grey line indicates the zero surface charge.

These two graphs (Figure 5.9 and Figure 5.11) show that the effects of nanoparticles on the interfacial tension of the solution depend on the types of the surfactants. In general, the ATD nanoparticles cause a reduction of interfacial tension of the solutions of CTAB (Figure 5.9) while this effect is reverse in case of SDS because the presence of nanoparticles results in the increase of the value of interfacial tension (Figure 5.11).

The green line in Figure 5.9, b represents the zeta potential of ATD nanoparticles in water which is equal to -31.46 ± 7.11 mV. It means that the ATD nanoparticles are negatively charged. When CTAB is used in the solution, the surface charge is changed due to the interactions between the CTAB molecules and the surface of the nanoparticles. Due to these interactions, the interfacial tension at the air-liquid interface is also affected.

When the concentration of CTAB is increased from 1.00×10^{-6} M to 5.00×10^{-5} M, the interfacial tension of the dispersions of ATD in the surfactant solution is slightly higher than the bare surfactant solutions. At the same range of concentration change, the zeta potential is changed from -26.78 mV to -20.08 mV. It is probable that the ATD nanoparticles are electrostatically interacting with the surfactant molecules. However, as the changes of zeta potential are mostly in the range of that of ATD in water (-31.46 ± 7.11 mV) and the interfacial tension is not changed significantly, the surfactant-nanoparticles interactions are not significant (Figure 5.10, a).

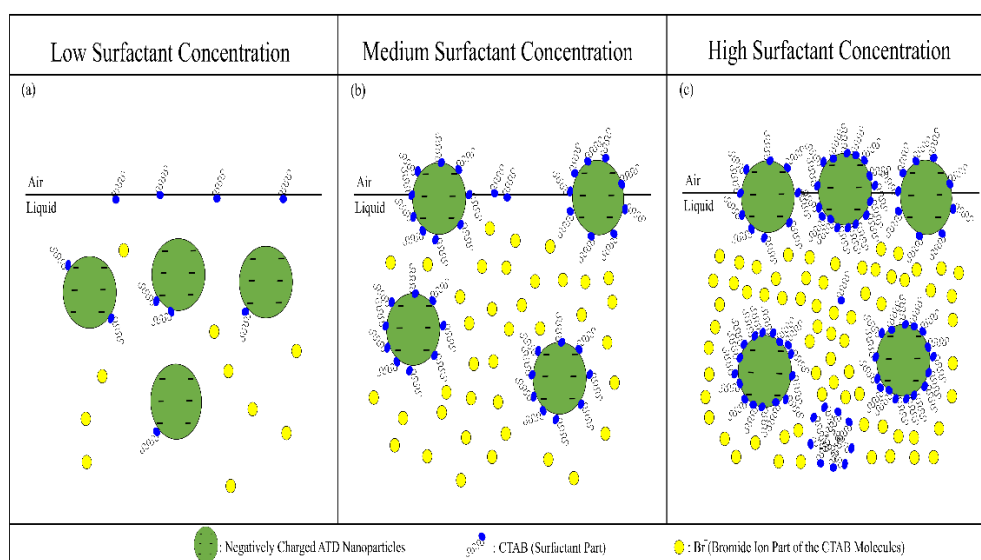


Figure 5.10 Schematic likely mechanism of interactions between ATD nanoparticles and surfactant molecules of CTAB. The bromide ions shown by yellow circles are released into the solution after dissolving CTAB in water.

At the concentration of 1.00×10^{-4} M of CTAB, the zeta potential of the ATD nanoparticles is -1.2 ± 1.46 mV which can be considered very close to the point of zero surface charge. It shows that, at this concentration, the surface of the negatively charged ATD nanoparticles has been slightly covered by the surfactant molecules. In fact, the positively charged heads of the molecules of the CTAB have interacted with the ATD nanoparticles. The surface charge has been reduced to almost zero. This type of interaction will produce hydrophobic ATD nanoparticles because the hydrophilic heads of the surfactant molecules are adsorbed onto their surface and the hydrophobic tails of surfactant molecules are still in the solution. Therefore, these surfactant-decorated nanoparticles are hydrophobic, tending to migrate to the air-liquid interface and acting as surface active agents (Figure 5.10, b). Due to the larger sizes of these nanoparticles in comparisons to surfactant molecules, they decrease the interfacial tension to 53.05 mN.m^{-1} which is below the Frumkin isotherm for the bare surfactant solution at the concentration of 1.00×10^{-4} M (Figure 5.9, a).

This change trend of surface charges continues when the concentration is increased to 5.00×10^{-4} M. At this point and also beyond that, the ATD nanoparticles are adsorbing more surfactant molecules. Therefore, the charge inversion phenomenon happens, the surface charges of nanoparticles become

positive, and increase continuously with increasing the concentration of surfactant. Moreover, the interfacial tension of the nanoparticle dispersions is still less than the interfacial tension of the bare surfactant solution. It means that the ATD nanoparticles adsorb more surfactant molecules, become hydrophilic, and are then adsorbed at the air-liquid interfaces. It can be concluded that, in the case of CTAB solutions in the range of the concentrations used in this study, the probability of formation of bilayers of the surfactant molecules on the surface of nanoparticles is low. Otherwise, the nanoparticles would stay in the bulk of the solution and the interfacial tension would be higher than that of the bare surfactant solutions.

At the highest concentrations, e.g., 1.00×10^{-1} M, the zeta potential is highly positive (48.08 mV), which can also be attributed to the formation of CTAB micelles in the bulk of the solutions. The colloidal structures of micelles show a positive charge. The large standard deviation at this point, i.e., ± 15.59 mV, can be justified by this hypothesis. In fact, at the highest concentration of CTAB, there might be two types of structures in the solution. The first one is the ATD nanoparticles decorated with surfactant molecules with a tendency to go to the interface. The second structure is the micelles of surfactant molecules that show the positive charge and tend to stay in the bulk of the solution (Figure 5.10, c).

Figure 5.11 shows the interfacial tension and zeta potential for the system containing ATD nanoparticles at the fixed concentration of 0.1 wt % and the SDS at different concentrations.

At the lowest concentrations of SDS, i.e., 1.00×10^{-6} M and 5.00×10^{-6} M, the interfacial tension is almost equal to the interfacial tension of the bare surfactant solutions. This means that there is no significant depletion of surfactant molecules from the air-liquid interface. At these two concentrations, the zeta potential of ATD nanoparticles is increasing from -13.28 mV to -3.88 mV. Results show that the ATD nanoparticles, which show negative surface charges in water (-31.46 ± 7.11 mV; green line in Figure 5.11, b), have lost their surface charges. They are also getting close to the zero surface charge point when the concentration of SDS is increased from 1.00×10^{-6} M to 5.00×10^{-6} M.

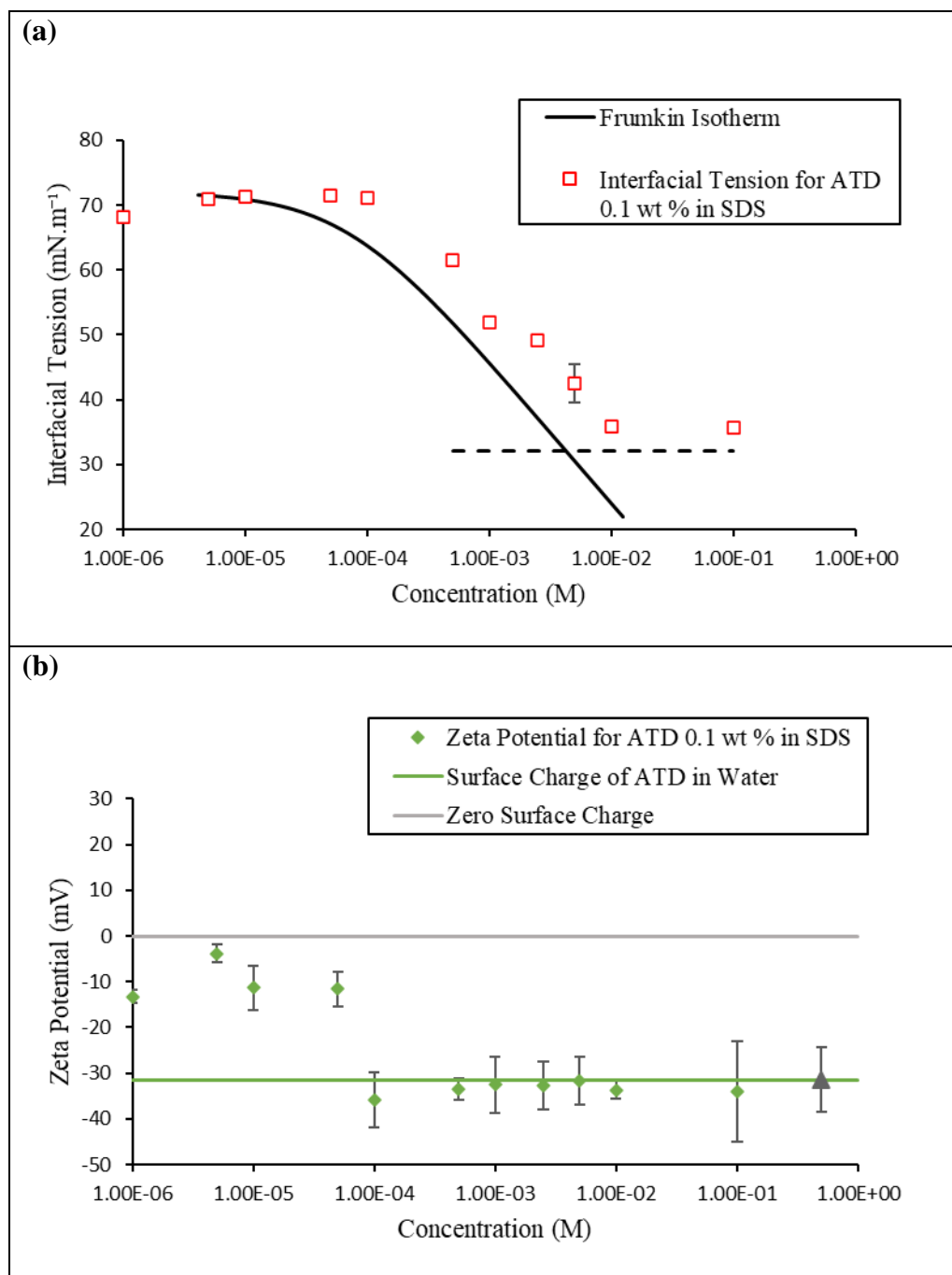


Figure 5.11 Equilibrium interfacial tension (a) and zeta potential (b) of the dispersions of ATD nanoparticles against concentration of the SDS in aqueous solutions at 25°C. The concentration of ATD nanoparticles is constant and 0.1 wt % in all experiments. The solid line in (a) is the best fitted curve of the Frumkin model for the interfacial tension results for bare surfactant solutions. Dashed line is the representative of reaching CMC point. The green line is the representative of the surface charge of ATD nanoparticles in water. The grey line indicates the zero surface charge.

As it has been mentioned above, there are no significant interactions between surfactant molecules and ATD nanoparticles, therefore, this amount of surface charges can be attributed to the interactions of sodium ions (Na^+) with ATD nanoparticles (Figure 5.12, a). The Na^+ ions in the structure of SDS have been released in the solution when the SDS is dissolved in water. The Na^+ ions act as the same function as the salts of sodium chloride in the surfactant solutions [218]. The ions of sodium with positive charges interact with the ATD nanoparticles and cause the reduction of negative charges on the surfaces of ATD nanoparticles. Accordingly, the electrostatic forces between the surfactant molecules and ATD nanoparticles are reduced.

By increasing the concentration of SDS from 5.00×10^{-6} M to 5.00×10^{-5} M, the zeta potential is decreased from -3.88 mV to -11.63 mV. It shows that the negative charges on the surface of nanoparticles are increasing. At the same concentration range, the interfacial tension is increasing. This means that the surfactant molecules are interacting with the ATD nanoparticles. Based on the reduction of electrostatic forces between nanoparticles and surfactant molecules due to the adsorption of Na^+ ions, it can be concluded that the interactions between SDS molecules and ATD nanoparticles are hydrophobic interactions. Therefore, the hydrophobic tail of SDS is adsorbed onto the solid surfaces of the ATD nanoparticles (Figure 5.12, b). Therefore, the hydrophilic heads of SDS will be exposed into aqueous solution. As a result, the nanoparticles will stay in the solution and are not adsorbed onto the air-liquid interfaces.

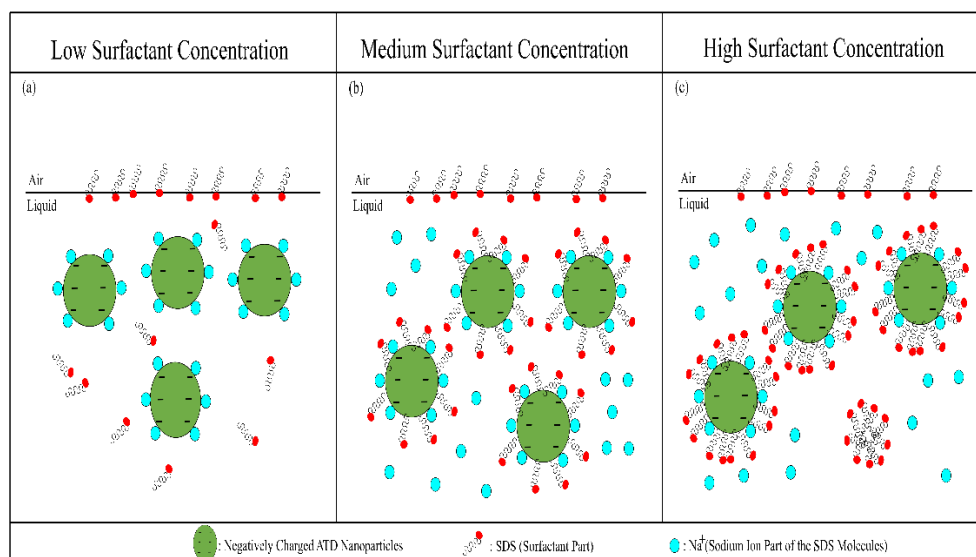


Figure 5.12 Schematic likely mechanism of interactions between ATD nanoparticles and surfactant molecules of SDS. The sodium ions shown by blue circles are released into the solution after dissolving SDS in water.

The zeta potential continues to decrease until reaching a concentration of 1.00×10^{-4} M of SDS. At concentrations higher than this value, the changes in the zeta potentials are not significant and the zeta potential is almost constant. It can be due to the full coverage of the solid surface of ATD nanoparticles with surfactant molecules (Figure 5.12, c). Therefore, the surface charges of particles are not significantly changed. There is also a possibility of the formation of micelles which results in the larger negative values of zeta potentials. The zeta potential measurement is about measuring the surface charge of particles and any colloidal structures in the solution. Therefore, the measuring system treat any sort of structure in the solution as a single particle. The formation of the micelles of SDS in the solution can be one of the origins of larger negative zeta potentials.

5.1.3.2 Foaming Properties

The foam formation or foamability of CTAB (Figure 5.13, a and b) and SDS (Figure 5.14, a and b) solutions without nanoparticles are quite similar.

In the CTAB solutions with the concentration magnitude of 10^{-6} M, no foam and bubbles were formed by manual shaking (method mentioned in Section 3.3). At the concentration of 1.00×10^{-5} M of the CTAB, unstable bubbles were formed and observed in the glass vial (Figure 5.13, a). However, due to the instability of the bubble, they were disappeared upon transferring onto the glass slide. Therefore, it was impossible to observe them under optical microscope.

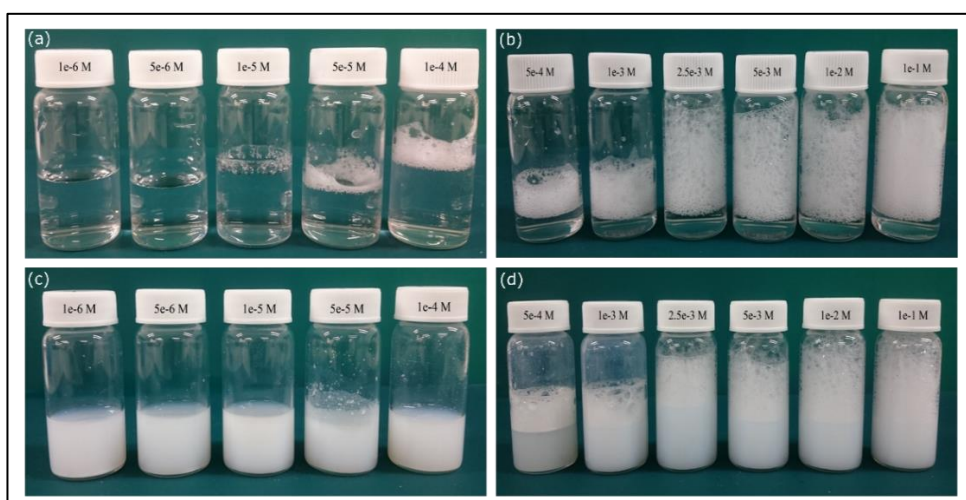


Figure 5.13 Foam formation in CTAB solutions (a, b) and dispersions with a fixed concentration of ATD nanoparticles equal to 0.1 wt % in CTAB (c, d).

At the concentration of 5.00×10^{-5} M, small amount of foam was formed. Some stable foams were observed from the CTAB concentrations of 1.00×10^{-4} M and higher (Figure 5.13, a and b). The larger amount of compressed and stable foams is related to the concentrations of 1.00×10^{-3} M which is very close to the CMC point of CTAB solutions (1.30×10^{-3} M).

In comparison with that of the bare CTAB solutions, the dispersions of 0.1 wt % of ATD nanoparticles were not able to form any foam at the concentrations less than or equal to 1.00×10^{-4} M (Figure 5.13, c). Although the stable foams were produced at the concentration of 5.00×10^{-4} M, the compressed and more stabilised ones were related to the concentration of 2.50×10^{-3} M (Figure 5.13, d) as the closest point to the CMC of CTAB.

Figure 5.14 shows that SDS solutions did not form any foam at the concentrations of 1.00×10^{-5} M and less than it. At the concentration of 5.00×10^{-5}

5×10^{-5} M, an unstable foam was formed. The stability of this foam was as much as it could be transferred onto the glass slide. Above this concentration, foams were formed and the foamability was increased with increasing the concentration of SDS (Figure 5.14, b).

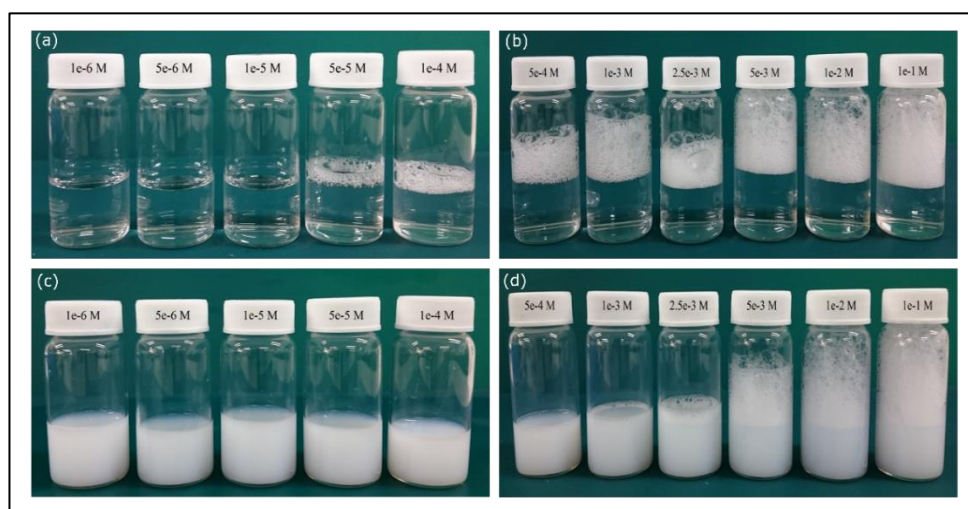


Figure 5.14 Foam formation in SDS solutions (a, b) and dispersions with a fixed concentration of ATD nanoparticles equal to 0.1 wt % in SDS (c, d).

The dispersions of 0.1 wt % of ATD nanoparticles in the SDS did not cause formation of any bubble at the concentrations less than 1.00×10^{-3} M. At this concentration of 1.00×10^{-3} M, foam began to form. The most stable foams were formed at those conditions associated with concentrations equal to 5.00×10^{-3} M and above it (Figure 5.14, c and d). This point is very close to the CMC point of SDS (4.23×10^{-3} M).

In the presence of ATD nanoparticles, there were quite large differences between CTAB and SDS solutions. The visual inspection of the ATD dispersions in the SDS solutions showed that they were more homogeneous than those in the CTAB solutions. This non-homogeneity in the CTAB-contained dispersions was much more apparent in the concentrations of 5.00×10^{-5} M and 1.00×10^{-4} M.

The other noteworthy difference between the foamability of the ATD dispersions in the CTAB and SDS was the foaming concentration. The first foam was formed at a concentration of 5.00×10^{-4} M of CTAB, whereas the first foam

of the ATD dispersion in the SDS solutions was formed at a concentration of 1.00×10^{-3} M of SDS.

Based on the results presented in Figure 5.9 and the proposed mechanism of interactions between ATD nanoparticles and CTAB molecules in Figure 5.10, it can be concluded that the foam formation for CTAB solutions with ATD nanoparticles happened at the concentration of 5.00×10^{-4} M where the surface charges of nanoparticles were positive and zeta potential value was 37.53 mV. At this point, enough numbers of nanoparticles are adsorbed at the air-liquid interface, and they act as the solid surface active agents.

For the dispersions of ATD nanoparticles in the SDS solutions, as the interfacial tension of the dispersions was higher than that of the bare surfactant solutions (Figure 5.11), it was expected that the foams would be formed at higher concentrations of SDS in the ATD dispersions. As the surfactant molecules are hydrophobically interacted with solid nanoparticles (Figure 5.12, b and c), higher concentrations of SDS were required for decreasing the interfacial tension for the foam formation.

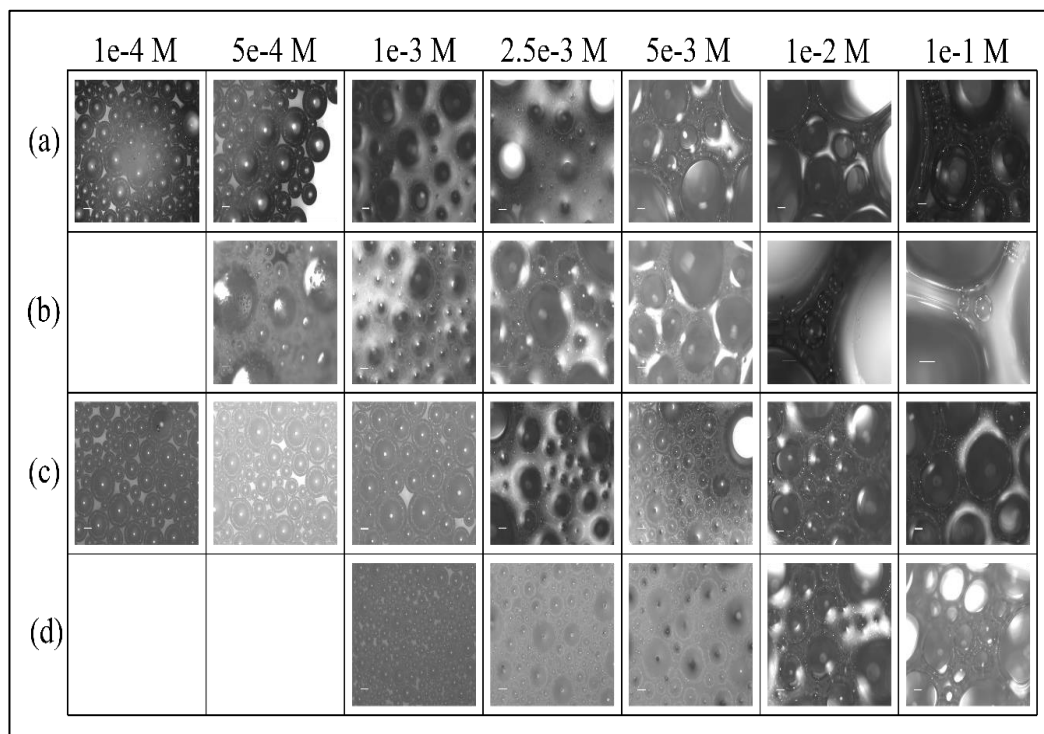


Figure 5.15 The bubbles observed at the initial time after formation at different concentrations of surfactants for (a) CTAB, (b) ATD-CTAB, (c) SDS, and (d) ATD-SDS. All the scale bars are representing a length of 100 μ m. Blank spaces are related to the situations where no foams were formed.

Immediately after the formation of foams by manual shaking, the bubbles of the foams were observed under the optical microscope. Figure 5.15 shows the bubbles of the foams for both the CTAB and SDS with and without ATD nanoparticles. These images were taken immediately after the formation of the bubbles.

Upon analysis of the images using the ImageJ software, the bubble size distributions, in terms of the bubble diameter for each concentration of every solution and dispersion, were analysed, measured, and plotted (Figure 5.16 and Figure 5.17). For the sake of visual considerations, the data range for the horizontal axis also contains the negative values. However, the amounts under zero were not considered in the interpretation of the diameter distribution.

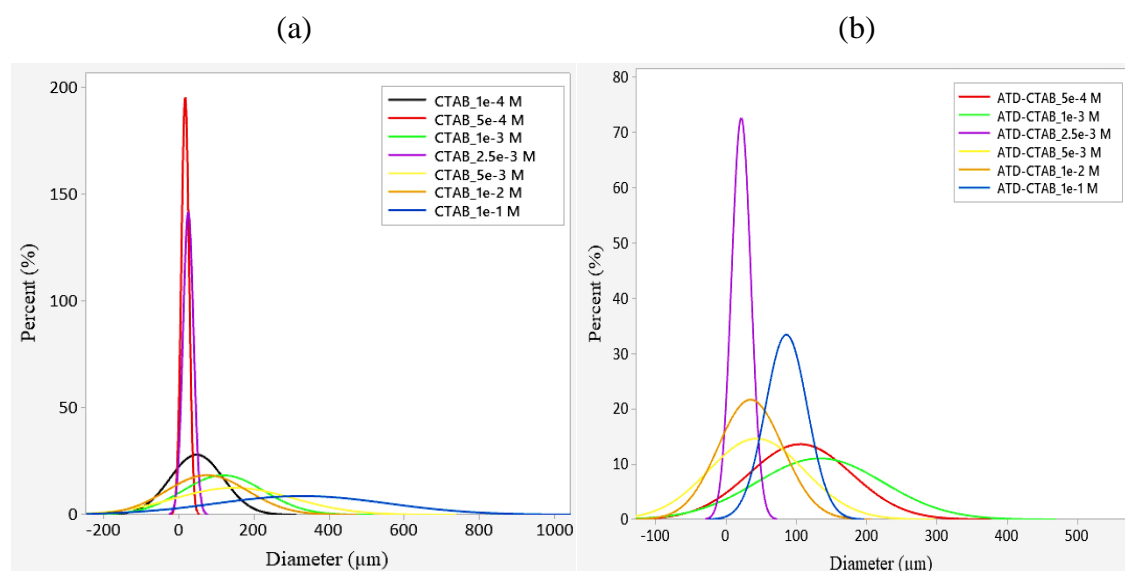


Figure 5.16 Normal distribution of bubble size based on the diameter of the bubbles for (a) CTAB solutions and (b) ATD-CTAB dispersions at different concentrations of CTAB and a fixed concentration of ATD nanoparticles (0.1 wt %).

As shown in Figure 5.16, for both CTAB solutions and ATD-CTAB dispersions, the diameter of the bubbles is generally less than 200 μm. However, the presence of nanoparticles resulted in a wider distribution of sizes even slightly more than 200 μm, especially in both concentrations of 5.00×10^{-4} M and 1.00×10^{-3} M (Figure 5.16, b).

In the cases of SDS solutions and ATD-SDS dispersions, the dimensions of the bubbles were larger than those of CTAB-based solutions. The approximate ranges of diameter were 0 – 600 μm and 0 – 500 μm for SDS solutions and ATD-SDS dispersions, respectively (Figure 5.17). Considering SDS solution, the size distribution became narrower by adding ATD nanoparticles to the system, whereas the size distribution became wider upon adding ATD nanoparticles. Figure 5.17, b shows that, with the SDS concentrations of 1.00×10^{-3} M and 2.50×10^{-3} M, ATD nanoparticles caused more homogeneous size distribution of the bubbles in the system.

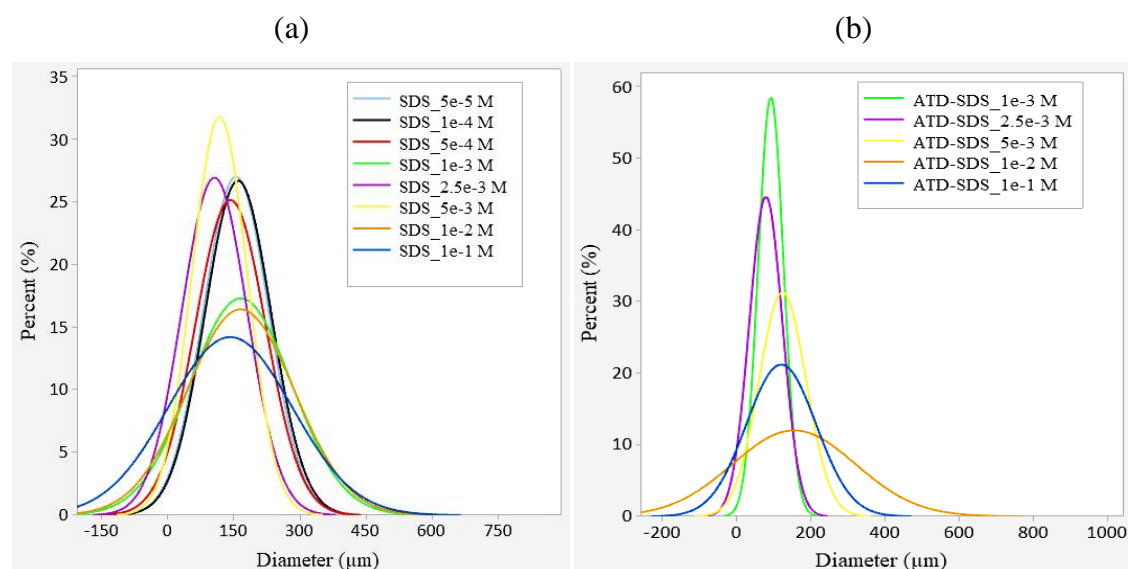


Figure 5.17 Normal distribution of bubble size based on the diameter of the bubbles for (a) SDS solutions and (b) ATD-SDS dispersions at different concentrations of SDS and a fixed concentration of ATD nanoparticles (0.1 wt %).

As the ATD nanoparticles are adsorbed onto the air-liquid interface of bubble in case of CTAB solutions, they would prevent bubbles' coalescence. These hydrophobic solid nanoparticles exist at the air-liquid interface of CTAB solutions, decrease the interfacial tension, and result in formation of foams with smaller bubble sizes in comparison with those of SDS solutions in which nanoparticles have no participation in adsorption process at the air-liquid interfaces [186]. Therefore, it can be concluded that the ATD nanoparticles affect

the size distribution of the bubbles based on their performance both in the bulk solution and at air-liquid interface.

5.2 Summary

In this chapter, the interfacial behaviour of two industrial surfactants, i.e., CTAB and SDS, were investigated. Moreover, the interactions between ATD nanoparticles with these two ionic surfactants were studied.

Firstly, to understand the adsorption behaviour of these surfactants at the air-liquid interface, the Frumkin model as the adsorption isotherm was applied. The Frumkin interaction parameter, adsorption equilibrium constant, and the partial molar area of both surfactants were obtained. For both cases of CTAB and SDS, there were attraction forces among the hydrophobic tails at the air-liquid interface. This means that the molecules of these surfactants are closely packed at the air-liquid interface. At a given concentration of the surfactant, due to the larger molar area, SDS decreases the interfacial tension more than the CTAB does. This can be a key point in selecting the surfactant for different formulations.

Using the tensiometry and adsorption isotherms, the CMC values of both CTAB and SDS were obtained. The CMC of SDS was more than that of CTAB meaning that, for the formulations requiring the micelle formation, using the CTAB could result in the micellar formulations at lower concentrations of surfactant.

Moreover, another potential method based on optical fibre was proposed to measure the CMC of the surfactants. In this method which plots the spectrum width centre, λ_c , against the concentration of surfactant, the point, at which the trend in the behaviour of spectrum width centre suddenly changes, is attributed to the CMC. The results of the CMC for CTAB and SDS using tensiometry were comparable with those of optical fibre technique. This potential method can be optimised in the future studies. This chapter has provided the considerations for the design of the experiments in the future.

The study of the interactions between negatively charged ATD nanoparticles and surfactants resulted in proposing two different mechanisms of the interactions. It was shown that the mechanism of the interaction of ATD with surfactants depends on the characteristics of the surfactant (in terms of the charge of the hydrophilic head) and the surfactant concentration.

The hydrophilic ATD nanoparticles which carry negative charge interact with CTAB molecules due to the electrostatic interactions between the positively charged head group of CTAB and negatively charged surface of the ATD nanoparticles. These interactions decrease the hydrophilicity of the ATD nanoparticles, which in turn, result in their adsorption at the air-liquid interface. In contrast, the interactions between SDS molecules and ATD nanoparticles are mostly hydrophobic interactions. As the hydrophilic heads of SDS molecules adsorbed onto the surface of ATD nanoparticles are exposed into aqueous solution, the nanoparticles remained in the solution are not adsorbed onto the air-liquid interfaces. These results are useful for different applications including the encapsulation of nanoparticles in the formulations and/or controlling the adsorption of nanoparticles at the air-liquid interfaces of foams.

It was also found out, in general, the foam formation depends on the type and concentration of the surfactant. However, the presence of the ATD nanoparticles extremely affects the concentration of surfactants at which the foams are formed. ATD nanoparticles inhibit the formation of the foams in the SDS solution more than CTAB solutions. Moreover, ATD nanoparticles affect the size distribution of the bubbles in the foam. In case of the CTAB solutions containing ATD nanoparticles, the adsorption of the ATD nanoparticles at the air-liquid interface prevents bubbles' coalescence which results in the formation of foams with smaller bubble sizes in comparison with those of SDS solutions. These conclusions about the foaming properties are helpful for the formulations of detergents and also for the industrial processes where the foaming characteristics need to be controlled.

Chapter 6

Interactions of Nano-Pollutants with DPPC in the Bulk of Solution and at the Air-Liquid Interface

In this chapter, the interactions between the single-type nano-pollutants and DPPC in the bulk of the solution have been initially investigated using ^1H NMR analysis. These nanoparticles include anatase form of titanium dioxide (ATD), rutile form of titanium dioxide (RTD), and multi-walled carbon nanotube (CNT). This investigation has been conducted based on the preparation methods of the solutions. As the nanoparticles and DPPC have been mixed, the ^1H NMR analysis of the solution of DPPC with and without nanoparticles can be an indicator of the possible interactions of DPPC molecules with the nanoparticles.

In the next step, the interfacial tension and zeta potential of the solutions of single-type nanoparticles and DPPC have been studied. Based on these results, the possible mechanisms of interactions between the nanoparticles and DPPC molecules have been discussed. Two different shapes of titanium dioxide nanoparticles have been investigated, and the obtained results can be applied as an indicator of effects of shape and surface properties of the nanoparticles on their behaviour in the interfacial system.

Finally, as the most innovative part of this chapter, effects of the mixture of nano-pollutants on the DPPC are investigated using visual inspection, optical microscopy, SEM analysis, and interfacial tension measurements. To our knowledge, this is the first time that the effects of the mixture of nanoparticles on the DPPC in the bulk of the solution and at the air-liquid interface have been studied in a systematic way. This approach in the study of the lung surfactant system is important and has often been overlooked. The interactions among nanoparticles and between nanoparticles and other contaminants extremely

influence the final toxicity effects [132]. Therefore, the physicochemical investigation of these systems is also of a great importance to provide fundamental information about the mechanisms of the interactions of the mixtures of nanoparticles with the lung surfactant. For this part of study, three types of mixtures have been used. Moreover, to simulate the real-life scenarios of the mixing procedure of the nano-pollutants, three different methods of mixing have been used to address the effects of the mixing methods.

6.1 Results and Discussion

6.1.1 Adsorption and Structure of DPPC onto the Surface of Nanoparticles

In this study, the method used in preparing the solutions and dispersions is similar to the first step of ethanol injection method, which is one of the conventional methods of liposome preparation [219]. In the ethanol injection method, the lipid is dissolved in ethanol as the organic solvent. Then, it is diluted by injection into an aqueous solution. Upon injection of the phospholipid dissolved in ethanol into the aqueous phase, the bilayer planar fragments are formed. The middle layer in this bilayer structure is the hydrophobic tails of the phospholipid molecules. In this structure, the hydrophilic heads are directed outwards (Figure 6.1). To form different types of vesicles such as liposomes from the individual bilayer fragments, external energy is required [220], e.g., heating to 60 °C and evaporation of the ethanol have been used to form the liposomes with fusion of those individual bilayer fragments.

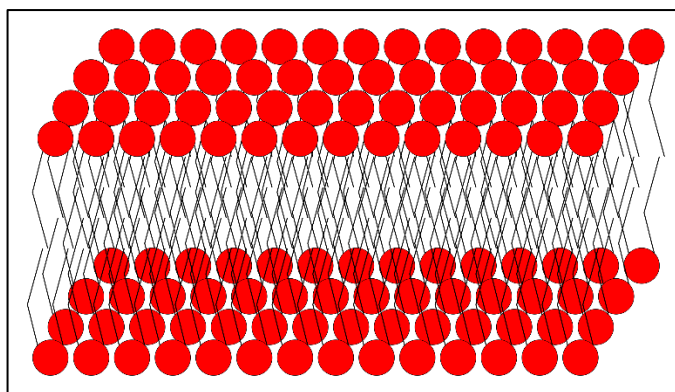


Figure 6.1 Self-assembly of the phospholipid molecules and formation of the bilayer upon using the ethanol injection method.

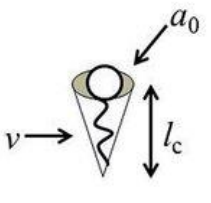
At the operational temperature of this study, i.e., 37 °C, the formation of the vesicles due to heating is less possible. As the sonication is used at different steps, there might be a probability of using it to supply the demanding energy for the formation of some vesicles. For the DPPC molecules with the final concentration of 5.38×10^{-8} M in the solutions and/or dispersions at 37 °C, the formation of the micelles is the most reasonable hypothesis [221].

It should be noted that the micelles of DPPC are not the same as simple spherical ones normally observed in some surfactants such as SDS and CTAB. The shape of the DPPC micelles is cylindrical, and its structure is related to its critical packing parameter (CPP), which is defined as below:

$$CPP = \frac{v}{a_0 l_c} \quad \text{Eq. 6-1}$$

where v , a_0 , and l_c are the volume of hydrocarbon chain, the surface area of the polar headgroup, and the length of hydrocarbon chain, respectively. As shown in Figure 6.2, the shape of the aggregate of lipids depends on the value of CPP [222].

Critical Packing Parameter (v/a_0l_c)	Critical Packing Shape	Structures Formed
$< 1/3$	Cone	Spherical micelles
$1/3 - 1/2$	Truncated cone	Cylindrical micelles
$1/2 - 1$	Truncated cone	Flexible bilayers, vesicles
~ 1	Cylinder	Planar bilayers
> 1	Inverted truncated cone or wedge	Inverted micelles



$$CPP = v/a_0l_c$$

Figure 6.2 The Critical Packing Parameter (CPP) and structure of the aggregates of the surfactant and lipid molecules [222].

For DPPC, the value of the CPP is 0.57. Therefore, DPPC molecules will form cylindrical micelles or flexible bilayers (vesicles) [221, 223, 224]. Figure 6.3 shows two suggested structures, and for both the cases of cylindrical micelles and flexible bilayers, the hydrophobic tails are inside the structure. Moreover, both these structures are potential to induce aggregates with varied sizes inside the solutions.

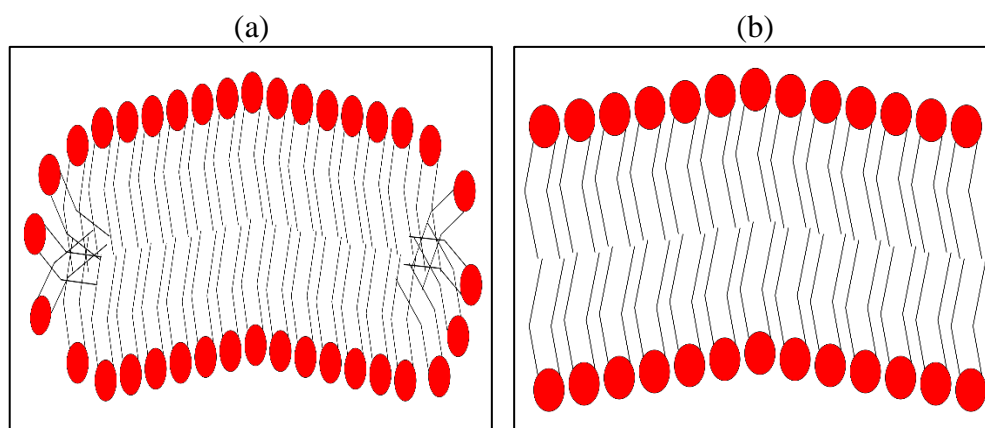


Figure 6.3 Self-assembly of the DPPC molecules into the structure of (a) cylindrical micelle and (b) flexible bilayer.

Based on the discussions about the most probable structure of the DPPC molecules and also the NMR analysis, the status of the DPPC molecules in both those solutions without nanoparticles and dispersions containing nanoparticles can be obtained. It should be noted that, due to the large number of peaks and noises, the spectra related to ^{31}P -NMR analysis were not convincing to be used for data analysis.

Figure 6.4 shows the ^1H NMR spectrum for the aqueous solution of DPPC- d_{62} without nanoparticles. In this case, five main peaks (a, b, c, d, and e) were detected. Peak (a) at 5.03-5.34 ppm is the representative of the singular tertiary proton at the *sn*-2 position on the glycerol backbone [225]. This hydrogen has been labelled as (a) in Figure 6.5. The next peak (b) in Figure 6.4 is between 4.54 ppm and 4.96 ppm, which can be attributed to the water existing in the solution [226]. In Figure 6.4, there are some small peaks between 4.04 ppm and 4.40 ppm labelled as (c), which are related to the protons positioned between the quaternary amine and the phosphate group. These peaks can also be related to the protons at the *sn*-1 and *sn*-3 positions on the glycerol backbone [225]. These hydrogens have been labelled as (c) Figure 6.5.

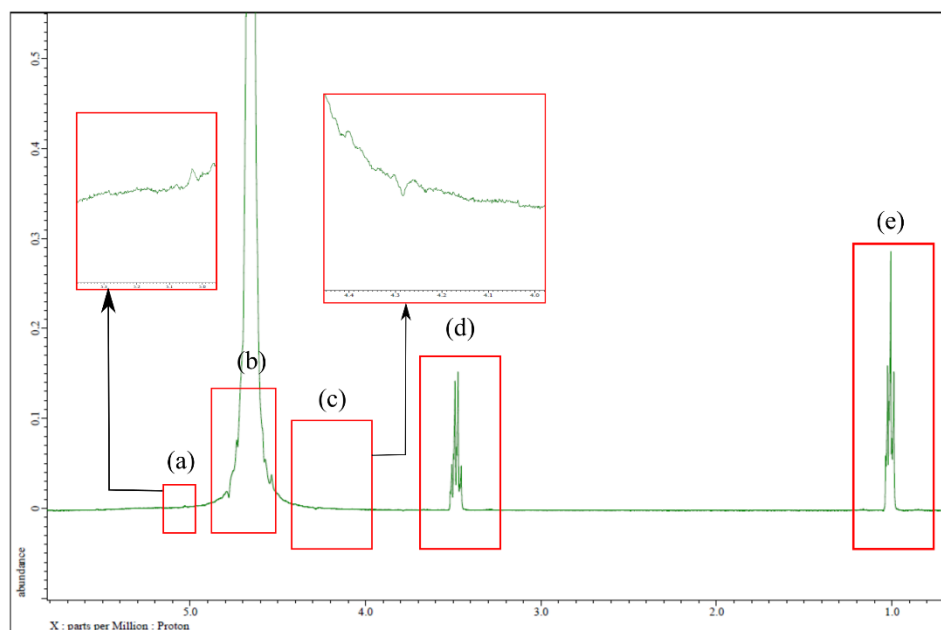


Figure 6.4 ^1H NMR spectrum of aqueous solution of the DPPC-d₆₂ without nanoparticles. The sample was prepared in the laboratory and the ^1H NMR analysis was done on the sample. The labels (a) to (e) on the spectrum are the representative of singular tertiary proton at the *sn*-2 position on the glycerol backbone (a), protons of water (b), protons positioned between the quaternary amine and the phosphate group (c), protons of the three methyl groups in the quaternary amine part of the hydrophilic head of DPPC (d), and protons of the methyl groups at the endpoints of the tail groups in the structure of the DPPC (e), respectively. Due to the size of peaks, the regions of (a) and (c) have been zoomed.

The next identified peaks in the ^1H NMR spectrum of aqueous solution of DPPC-d₆₂ were between 3.45 ppm and 3.52 ppm, as labelled as (d) in Figure 6.4. These peaks correspond to the nine protons of the three methyl groups in the quaternary amine part of the hydrophilic head of DPPC [225]. These hydrogens have been labelled as (d) in Figure 6.5.

The last identified peaks labelled as (e) in Figure 6.4 fall between 0.84 ppm and 1.16 ppm. These peaks represent the methyl groups at the endpoints of the tail groups in the structure of the DPPC. The related hydrogens in the structure have been labelled as (e) in Figure 6.5 [225]. These detected hydrogens in the tails can also be a representative of the presence of either the individual molecules of DPPC in the solution or the open-ended bilayers of the DPPC.

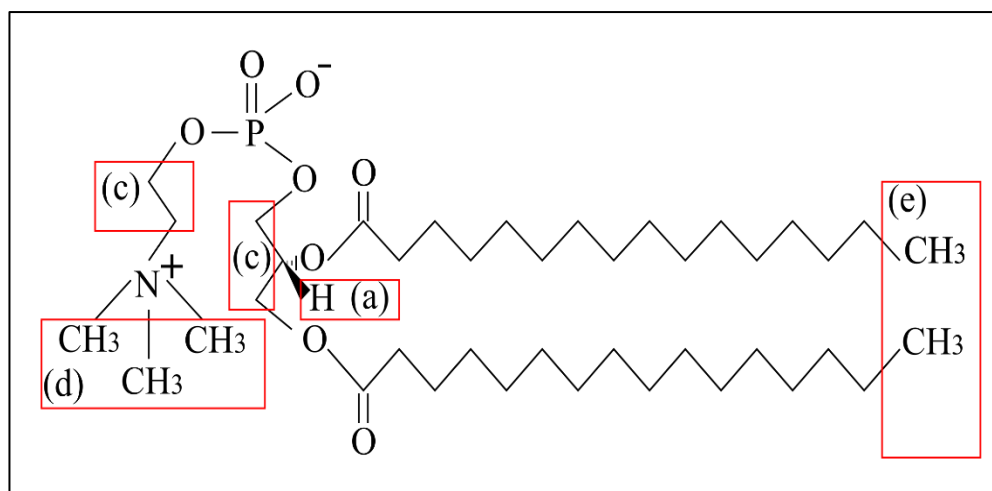


Figure 6.5 The labelled hydrogens in the structure of DPPC.

The detection of these four types of protons (i.e., a, c, d, and e in Figure 6.5) using ^1H NMR analysis of the DPPC solution proves that, at the operational concentration of DPPC, i.e., 5.38×10^{-8} M, the DPPC molecules are in the micellar or bilayer forms. Therefore, it is less likely that the liposomes have also been formed. If the system is a liposomal one, most of the signals related to the DPPC would be disappeared due to the restricted motions of the buried protons in the liposomes. In this case, only the signals related to the three methyl groups of the quaternary amine would be detected [227].

After investigating the ^1H NMR spectrum of the aqueous solution of DPPC- d_{62} without adding nanoparticles, the ^1H NMR spectra of the aqueous solution of DPPC- d_{62} containing the dispersions of individual nanoparticles with different concentrations were also analysed. The results associated to the ATD, RTD, and CNT particles are shown in Figure 6.6, Figure 6.7, and Figure 6.8, respectively.

ATD Nanoparticles

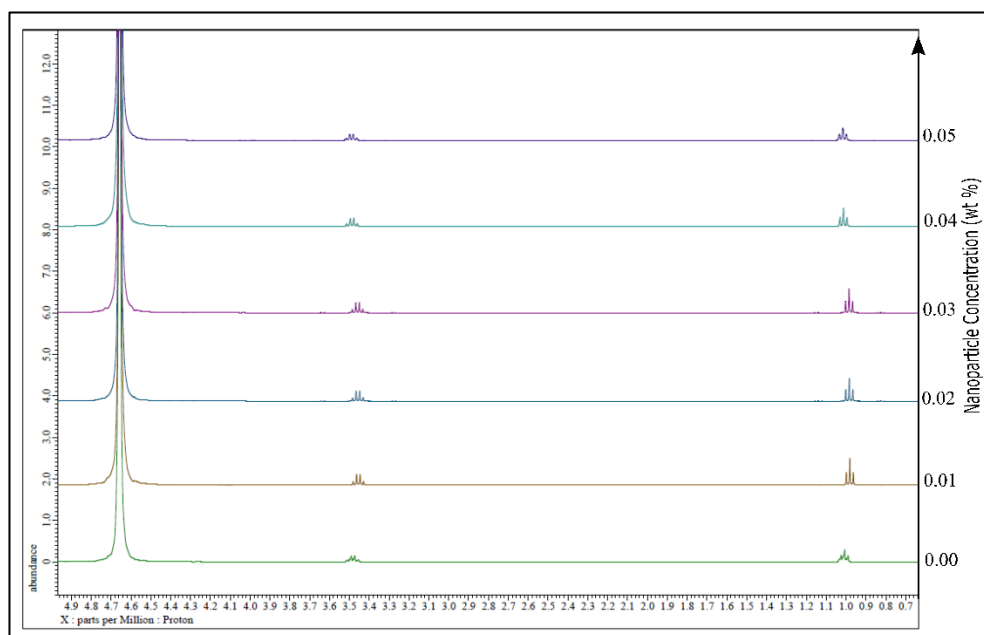


Figure 6.6 ¹H NMR spectra of DPPC-d₆₂ with different concentrations of ATD nanoparticles (right vertical axis). The concentration of the DPPC is constant at 5.38×10^{-8} M in all solutions and dispersions.

The ¹H NMR spectra related to the dispersions of ATD nanoparticles (Figure 6.6) shows that the number of peaks decreases by increasing the concentration of nanoparticles. However, the integration of the spectra for each region of peaks reveals that the number of detected protons related to each functional group of DPPC in presence of nanoparticles is more than that of DPPC solution without nanoparticles. This might be due to the interactions of the bilayers with nanoparticles which results in the local deformation of the bilayers of DPPC, formation of the pores in the structure of the bilayers, leakage in the bilayers, and release of some more individual molecules of DPPC to the solution [228]. These molecules can be either individual molecules in the solution or the molecules interacted with the ATD nanoparticles.

RTD Nanoparticles

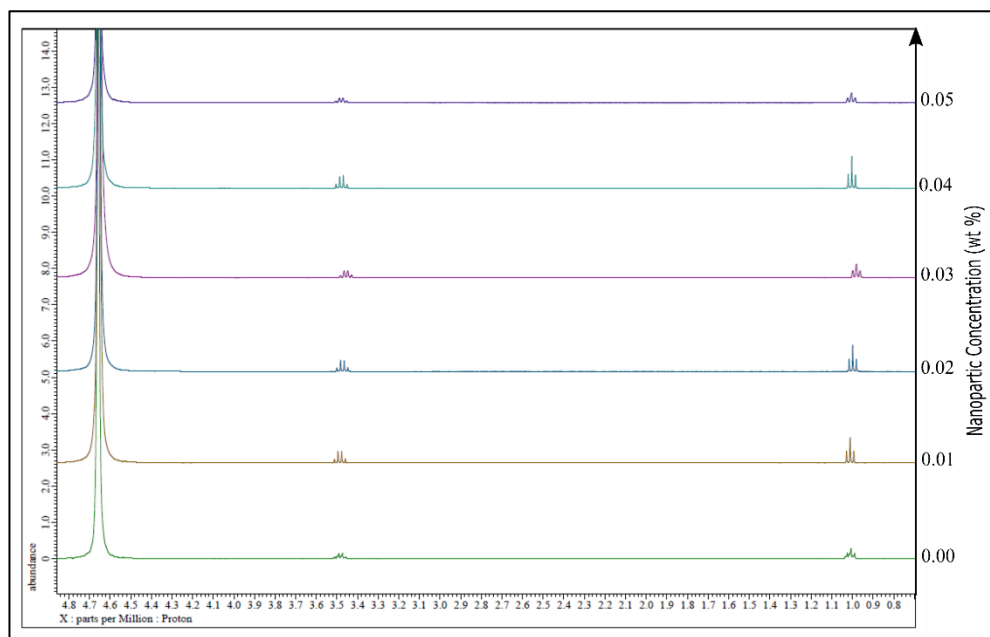


Figure 6.7 ¹H NMR spectra of DPPC-d₆₂ with different concentrations of RTD nanoparticles (right vertical axis). The concentration of the DPPC is constant at 5.38×10^{-8} M in all solutions and dispersions.

The ¹H NMR spectra of the dispersions of RTD nanoparticles (shown in Figure 6.7) were analysed. The obtained results show that the number of peaks decreases by adding the RTD nanoparticles to the system that only contains DPPC. However, the changes in the number of peaks do not have a clear relationship with the concentration of RTD nanoparticles. Integration of the spectra for each region of peaks shows the same results as the ATD nanoparticles. It means that the number of detected protons related to each functional group of DPPC in presence of RTD nanoparticles is more than that of DPPC solution without adding nanoparticles.

However, there are some differences between the cases of ATD and RTD. The integral values related to the methyl groups of the endpoint of the tails in the samples related to RTD nanoparticles are much higher than those of ATD nanoparticles. The only exceptional case is related to the concentration of 0.05 wt % of nanoparticle. At this concentration, the integral value of the peaks related to the methyl groups of the tails for the ATD sample is 5.564 whereas this value is 5.406 for those for the RTD sample (the peaks between 3.45 ppm and 3.52

ppm of the 0.05 wt % in Figure 6.6 and Figure 6.7). In other concentrations, this specific integral value of RTD samples is higher than that of ATD samples, and the difference is in the range of 0.887-14.515. This higher number of protons related to the tails might be due to the higher number of individual DPPC molecules released to the solution because of their interactions with RTD nanoparticles.

CNT Particles

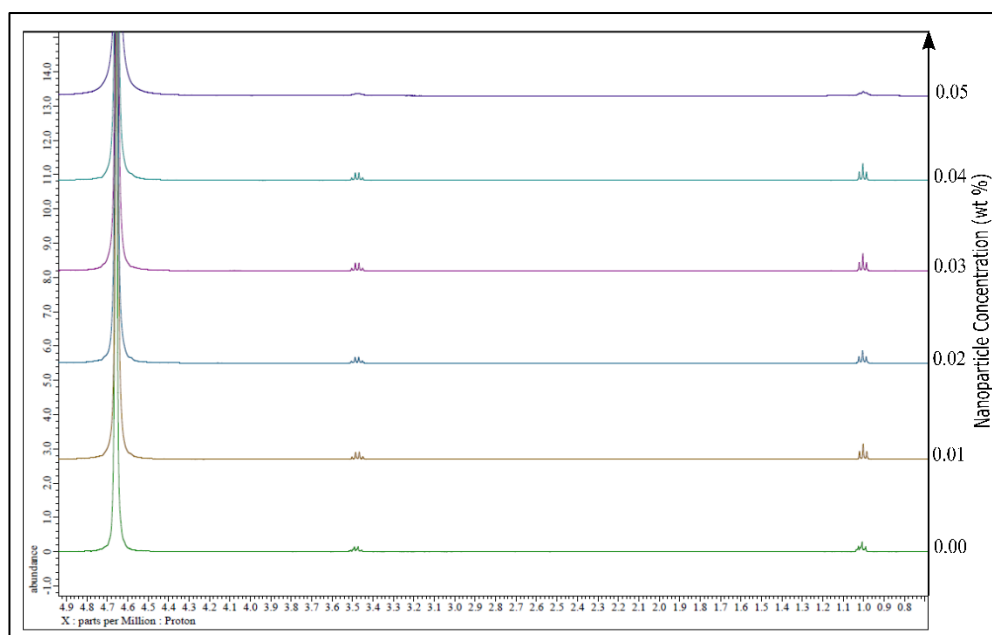


Figure 6.8 ^1H NMR spectra of DPPC-d62 with different concentrations of CNT particles (right vertical axis). The concentration of the DPPC is constant at 5.38×10^{-8} M in all solutions and dispersions.

The ^1H NMR spectra of the dispersions of CNT particles at different concentrations are shown in Figure 6.8. The number of peaks is less than the DPPC systems without nanoparticles and the samples of ATD and RTD nanoparticles described before. Moreover, there is no clear relationship between the concentration of CNT particles and changes of the number of peaks. Similar to those of the ATD and RTD samples, the integral values of the CNT-related spectra show that the number of detected protons related to each individual functional group of DPPC in the presence of CNT nanoparticles is more than

that of DPPC solution without particles. In the case of the CNT samples, the behaviour of the peaks related to the protons between the quaternary amine and the phosphate group and the hydrogens at the *sn*-1 and *sn*-3 positions on the glycerol backbone was different from the samples with ATD and RTD nanoparticles (the peaks between 4.04 ppm and 4.40 ppm in Figure 6.8). At the concentrations of 0.01 wt % and 0.02 wt % of CNT particles, the integral values were 83.162 and 80.019, respectively. However, these large amounts might be due to the signal shift related to the water. For the concentrations of 0.04 wt % and 0.05 wt % of CNT particles, the peaks related to those mentioned protons, i.e., the protons labelled (C) in Figure 6.5, disappeared. It is difficult to make a hypothesis behind this phenomenon. However, the changes in the integral values in case of CNT particles clearly show that there are interactions between CNT particles and the bilayers of DPPC. It should be noted that the mentioned peaks are not clearly visible on the spectrum, but the analysis software, i.e., Delta 6.1.0 can detect those peaks and report them.

The analysis of the integral list and peaks list of Figure 6.6, Figure 6.7, and Figure 6.8 shows that for all three types of nanoparticles, i.e., ATD, RTD, and CNT, the presence of nanoparticles decreases the number of peaks in the DPPC system. These number of peaks were calculated using Delta 6.1.0 software. However, these peaks cannot be recognised on the spectra shown in Figure 6.6, Figure 6.7, and Figure 6.8.

6.1.2 Effects of the Single-Type Nano-Pollutants on the DPPC

The dynamic interfacial tension and zeta potential of the DPPC solution and the dispersions containing DPPC and nanoparticles at different concentrations were measured. For the DPPC solution without nanoparticles, it has been shown that the surface pressure curve (defined as the difference between the current interfacial tension of the systems and the interfacial tension of pure water at a constant temperature) reaches a plateau within 10 min at the surface pressures less than 25 mN.m⁻¹ [145]. However, the time frames of reaching this equilibrium for the DPPC systems is varied based on the method of

measurement. Some studies have started their rheology measurements after 20 min [129]. Another study using a micropipette technique mentioned that the equilibrium interfacial tension has been reached within less than 4 min [229]. In general, the rule of thumb for reaching the equilibrium is when the interfacial tension changes is smaller than or equal to 0.1 mN.m^{-1} within 5 min [136]. In this study, the equilibrium time for the DPPC solution without particles was 2500 s equivalent to 42 min. As the red curve in Figure 6.9 shows, the equilibrium interfacial tension of the DPPC solution without nanoparticles was 65.51 mN.m^{-1} . It should be noted that the zeta potential for the DPPC solution without nanoparticles was also measured and reported as $-0.76 \pm 0.64 \text{ mV}$.

ATD Nanoparticles

Figure 6.9 also represents the dynamic interfacial tension of the dispersions of ATD nanoparticles at different concentrations. These experiments were done three times for each concentration, and the curves shown in Figure 6.9 are the examples for each concentration. The average values of three experiments for each concentration and the related error bars have been shown in Figure 6.10, a. Figure 6.9 shows that the equilibrium interfacial tension values related to the dispersions containing ATD nanoparticles are higher than that of DPPC solution without nanoparticles. This shows that adding the ATD nanoparticles to the system of DPPC causes the depletion of the DPPC from the air-liquid interface.

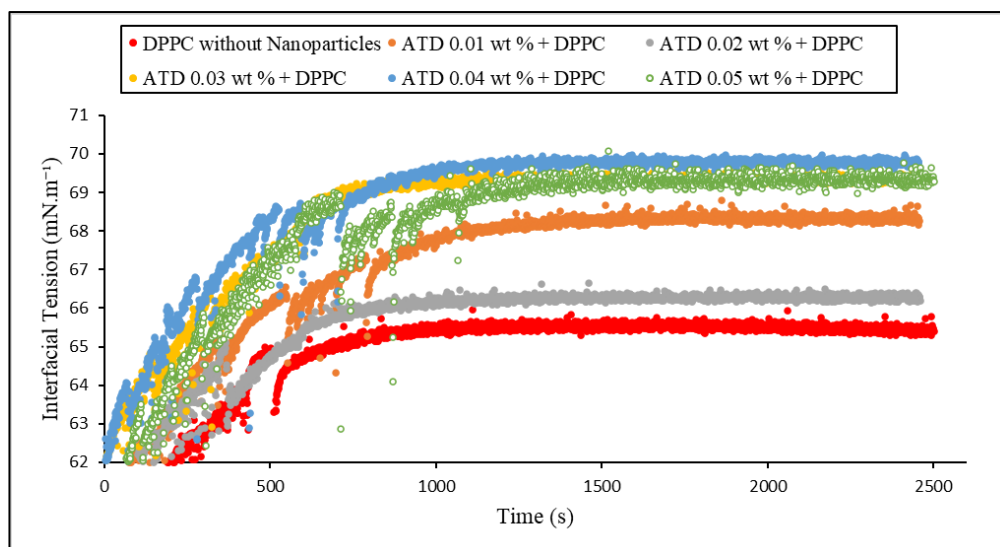


Figure 6.9 Dynamic interfacial tension of the dispersions of ATD nanoparticles with different concentrations in the DPPC solutions at 37°C. The concentration of the DPPC is constant at 5.38×10^{-8} M in all solutions and dispersions. The red dots, as a reference, are related to the DPPC solution without nanoparticles.

To understand the effect of the concentration of ATD nanoparticles and the real mechanism of interactions between ATD nanoparticles and DPPC molecules, the equilibrium interfacial tension and zeta potential of the dispersions of ATD nanoparticles are plotted against the concentration of ATD nanoparticles, and the results are shown in Figure 6.10. It should be reminded that, in this study, the nanoparticles have been in the mixture of DPPC solution before the start of the interfacial tension measurements. Therefore, the monolayer formed at the air-liquid interface of the droplet in the PAT system is the result of the nanoparticle-DPPC interactions and complex formation. In fact, different structures including DPPC molecules, nanoparticles, and/or nanoparticles interacted with the DPPC molecules can be adsorbed at the air-liquid interface.

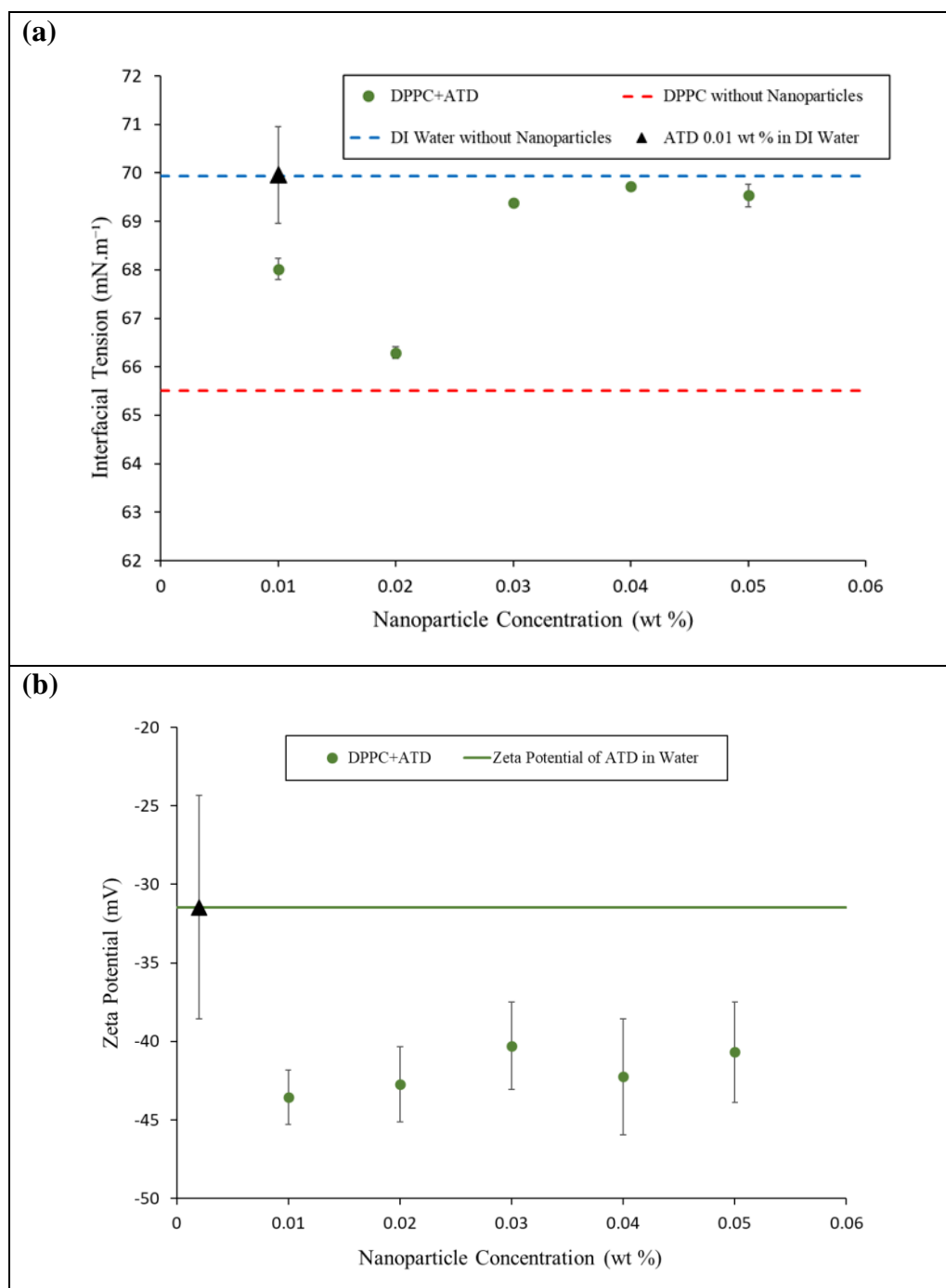


Figure 6.10 Equilibrium interfacial tension (a) and zeta potential (b) of the dispersions of ATD nanoparticles in the DPPC solutions against the concentration of nanoparticles at 37°C. The concentration of the DPPC is constant at 5.38×10^{-8} M in all solutions and dispersions. The blue and red dashed lines in (a) are the representative of the interfacial tension of DI water without DPPC and with DPPC, respectively. The green line and the triangle on it in (b) are the representative of the surface charge of ATD nanoparticles in water.

Figure 6.10, a shows that the interfacial tension of the dispersions containing hydrophilic ATD nanoparticles is higher than that of DPPC solution without nanoparticles (red dashed line). This might be due to the electrostatic interactions between the negatively charged ATD nanoparticles (zeta potential equal to -31.46 mV) and the amine group of the hydrophilic head of the DPPC molecules [74]. Moreover, attractive van der Waals interactions and hydrophobic interactions between the functional groups on the structure of the DPPC and nanoparticles might also be the possible mechanisms of the interactions between DPPC molecules and ATD particles [230].

As shown in Figure 6.10, a, at the concentration of 0.01 wt % of ATD nanoparticles, the interfacial tension is 68.01 mN.m^{-1} . This is higher than the interfacial tension of aqueous solution of DPPC (65.51 mN.m^{-1}) and far less than the interfacial tension of pure DI water (69.93 mN.m^{-1}) at the temperature of 37°C . It indicates that the ATD nanoparticles are interacting with the DPPC molecules and the depletion of surfactant is occurring.

By increasing the concentration of ATD nanoparticles to 0.02 wt %, the interfacial tension is decreased to 66.29 mN.m^{-1} . It might be due to the adsorption of ATD nanoparticles and/or their aggregates at the air-liquid interface, meaning that these particles are acting like surface active agents.

At the concentrations of 0.03, 0.04, and 0.05 wt % of ATD nanoparticles, the interfacial tension values increase to 69.39, 69.72, and 69.54 mN.m^{-1} , respectively. These interfacial tension values are close to that of DI water at the same temperature. It means that the air-liquid interface is similar to the air-water interface without using any surface-active agents. Explaining the precise mechanism behind the interactions of ATD nanoparticles and DPPC molecules needs more characterisation methods including chemical and surface analysis techniques. The interactions in the solution can be complicated. For example, some nanoparticles might penetrate the fragments of the flexible bilayers of DPPC in the bulk, and then accumulated in the bilayer cores. This phenomenon depends on the thickness of the bilayer and the size of the nanoparticles and/or their agglomerates [231, 232]. Some nanoparticles might penetrate across the DPPC bilayers and disrupt it [233, 234].

Regarding the zeta potential of the ATD nanoparticles (Figure 6.10, b), it can be seen that the zeta potential of the ATD nanoparticles (-31.46 mV) has become more negative (between -40.28 mV to -43.54 mV) after interactions with DPP molecules. Within the experimental error, the zeta potential has remained constant for different concentrations of ATD nanoparticles. The larger negative value of zeta potential upon interactions with DPPC molecules means that the repulsion between the particles has become significant. Therefore, the ATD nanoparticles in presence of DPPC molecules form a more stable colloidal dispersion [235].

To explain the reason, the effect of DPPC should be considered. As mentioned before, the zeta potential for the DPPC solution without nanoparticles was -0.76 ± 0.64 mV. The electrostatic interactions between DPPC molecules and ATD nanoparticles might be the reason of negative charge increase of ATD nanoparticles after these interactions. The effect of the aggregation of some of ATD nanoparticles should also be considered. For more in-detail description of the zeta potential changes, the zeta potential data should be coupled with dynamic light scattering (DLS) which determines the size distribution profile in the solution [236].

RTD Nanoparticles

As well as the ATD, the dynamic interfacial tension of the dispersions of RTD nanoparticles at different concentrations were measured three times for each concentration. Figure 6.11 shows the examples for each concentration. The average values of three experiments for each concentration and the related error bars have been shown in Figure 6.12, a. Figure 6.11 shows that the equilibrium interfacial tensions related to the dispersions of RTD nanoparticles are lower and higher than that of DPPC solution without nanoparticles (i.e., the red curve in Figure 6.11). This means that the interfacial behaviour of the system containing RTD nanoparticles is extremely dependent on the concentration of nanoparticle.

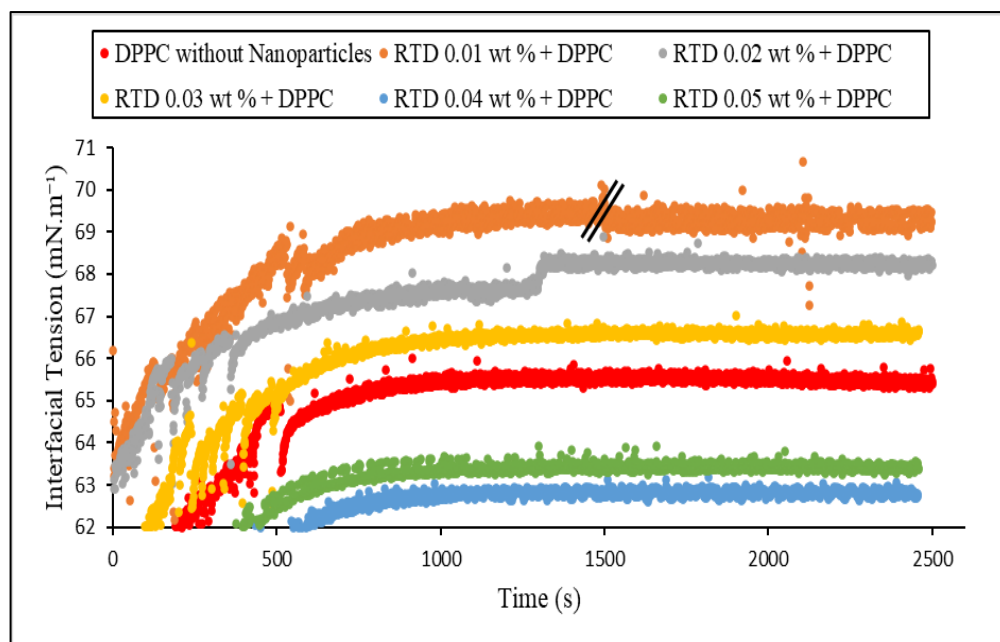


Figure 6.11 Dynamic interfacial tension of the dispersions of RTD nanoparticles with different concentrations in the DPPC solutions at 37°C. The concentration of the DPPC is constant at 5.38×10^{-8} M in all solutions and dispersions. The red dots, as a reference, are related to the DPPC solution without nanoparticles. The scratched part on the graph of RTD 0.01 wt % is because this experiment was done for 4000 s to reach the equilibrium. Therefore, the data of the last 1000 s has been shifted from the interval of 3000-4000 s in the main experiment.

The interfacial tension and zeta potential of the dispersions containing the hydrophilic RTD nanoparticles and DPPC against the concentration of the nanoparticles are shown in Figure 6.12, a and b. At the concentrations between 0.01 wt % and 0.03 wt %, the depletion of the DPPC is obvious because the interfacial tension of the nanoparticle-contained samples is higher than that of DPPC solution without nanoparticles (red dashed line in Figure 6.12, a).

At the concentration of 0.01 wt % of RTD nanoparticles, the interfacial tension is 69.18 mN.m^{-1} (Figure 6.11). This is almost close to the interfacial tension of DI water (69.93 mN.m^{-1}) at the temperature of 37 °C. This can be attributed to the electrostatic interactions of individual DPPC molecules with RTD nanoparticle. The zeta potential of the RTD nanoparticles in DI water was -0.11 ± 0.11 mV. Although this is a very small value of negative charge, it can still be the key reason of electrostatic interactions between the amine part of the headgroup of the DPPC molecules and slightly negatively charged RTD nanoparticles [237, 238].

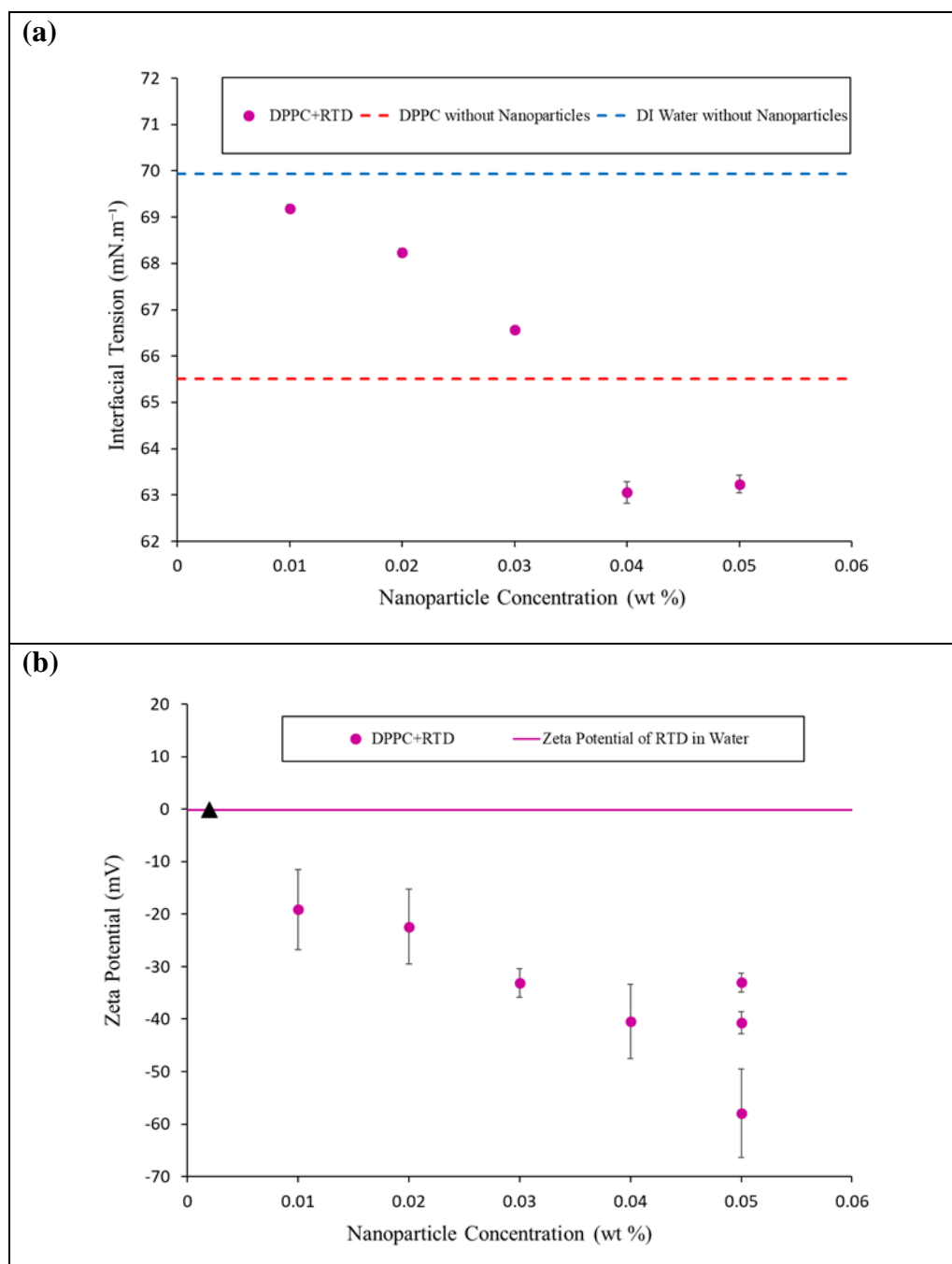


Figure 6.12 Equilibrium interfacial tension (a) and zeta potential (b) of the dispersions of RTD nanoparticles in the DPPC solutions against the concentration of nanoparticles at 37°C. The concentration of the DPPC is constant at 5.38×10^{-8} M in all solutions and dispersions. The blue and red dashed lines in (a) are the representative of the interfacial tension of DI water without DPPC and with DPPC, respectively. The purple line and the triangle on it in (b) are the representative of the surface charge of RTD nanoparticles in water.

By increasing the concentration of RTD nanoparticles to 0.02 wt % and 0.03 wt %, the interfacial tension decreases to 68.23 mN.m⁻¹ and 66.57 mN.m⁻¹, respectively. At these concentrations, the air-liquid interface of the system might be a combination of some DPPC molecules and some RTD nanoparticles.

At the concentrations of 0.04 wt % and 0.05 wt % of the RTD nanoparticles, the interfacial tension values are dramatically decreased to 63.06 mN.m⁻¹ and 63.23 mN.m⁻¹, respectively. Following the mentioned mechanism of interactions between RTD nanoparticles and DPPC bilayers, it is probable that at higher concentrations of nanoparticles, more nanoparticles are adsorbed onto the air-liquid interface causing a decreased interfacial tension in comparison with the situation where only DPPC is existed in the system (i.e., the red dashed line in Figure 6.12, a) [239].

Figure 6.12, b shows the zeta potential of the nanoparticles. As mentioned before, the zeta potential value of the RTD nanoparticles in DI water was -0.11 ± 0.11 mV. In presence of DPPC in the dispersions, the zeta potential becomes more negative from -19.15 mV at the concentration of 0.01 wt % to -57.95 mV at the concentration of 0.05 wt %. It should be noted that, at a concentration of 0.05 wt %, three populations with three major values of the zeta potentials were found as clearly shown in Figure 6.12, b. The values of the zeta potential of the RTD nanoparticles at the concentration of 0.05 wt % are -33.02, -40.69, and -57.95 mV. These three different values of zeta potential show that there are three major populations of RTD particles interacted with DPPC, and these interactions are not necessarily similar for all RTD nanoparticles. Some of these RTD particles have adsorbed more DPPC molecules on their surface and some particles have been decorated with less DPPC molecules. This is because of the constant concentration of the DPPC and the variable concentration of nanoparticles. Therefore, at the concentration of 0.05 wt % of RTD nanoparticles, the number of free DPPC molecules to interact with all RTD nanoparticles in the same way is not enough.

The changes in the zeta potential of the RTD nanoparticles in contact with DPPC further proved the interactions between the nanoparticles and DPPC molecules. It should also be noted that the amount of changes in zeta potential values in case of RTD samples is extremely larger than that of ATD samples.

This can be an indicator of the larger driving force for the RTD-DPPC electrostatic interactions in comparison with ATD-DPPC electrostatic interactions [240]. More detailed explanation on the results of the zeta potential measurement can be done if the DLS results are combined with them (which have not been done in this study).

CNT Particles

Measurements of the interfacial tension of the dispersions of CNT particles containing DPPC were also conducted. Although these measurements were also conducted three times for each concentration of the CNT particles, the results were not reproducible and repeatable. In fact, only about one-thirds of the interfacial tension experiments on the CNT particles resulted in the equilibrium interfacial tension. Even repeating the experiments with a longer equilibrium time, i.e., 4000 s, did not improve the reproducibility of the data. Due to the lack of reproducibility, the data related to CNT particles are not presented in this chapter. However, as a comparative point for any future research on carbon nanoparticles, the access to the current results on CNT particles would be beneficial. Therefore, these results have been shown and explained in **Appendix A**.

After measuring the interfacial tension and zeta potential for the individual nanoparticles and understanding more about the effect of the single-type nano pollutant on the DPPC, effect of the mixture of nano-pollutants on the DPPC was investigated. The experimental methods related to this part have been explained in Section 3.1.4.2. The results related to the mixture of nanoparticles are described in the next section.

6.1.3 Effects of the Mixture of Nano-Pollutants on the DPPC

Effects of the mixture of nanoparticles as the representatives of the nano-pollutants on the DPPC were evaluated due to the importance of this approach in the real life. In fact, when the air is inhaled into the lung, a mixture of

nanoparticles with different physicochemical properties and various amounts enters the respiratory system. The physicochemical properties such as surface charge, size, and shape of these nanoparticles can significantly affect the interparticle interactions with other nanoparticles with different features.

To simulate some of the real-life scenarios for the mixture of nanoparticles reaching the lung surfactant, three different mixing methods were used (Section 3.1.4.2) which are:

- i. Mixing the individual nanoparticles with DPPC and then mixing the DPPC-interacted nanoparticles with each other.
- ii. Mixing the aqueous dispersions of nanoparticles with each other and then adding the DPPC to this mixture.
- iii. Mixing the solid nanoparticles with each other, preparing the aqueous dispersions, and then adding the DPPC to this mixture.

For the sake of time management, all three methods were done on ATD+CNT mixture whereas the RTD+CNT and ATD+RTD+CNT mixtures were prepared only by the first and second methods (summary in Table 3.1). The visual inspection, optical microscopy, and SEM analysis were conducted to collect the most possible data about the stability of the colloids, the size and shape of the agglomerates (Section 6.1.3.1 and section 6.1.3.2). Then, the interfacial tension of the air-liquid interface of these mixtures was measured (Section 6.1.3.3). The results have been presented in the following sections.

6.1.3.1 Visual Inspection and Optical Microscopy

Figure 6.13 shows the colloids and the structures of sediments for the mixtures of ATD+CNT nanoparticles with the concentration of 0.01 wt % in DPPC solution prepared by all three mixing methods. These images have been taken one week after the preparation of the samples. The turbidity can be considered as a preliminary indicator of the stability of the colloids [129]. After checking both side view and bottom view of the vials, the turbidity of the mixture prepared using the second mixing method (Figure 6.13, b) is much more significant than the one prepared using the first method (Figure 6.13, a).

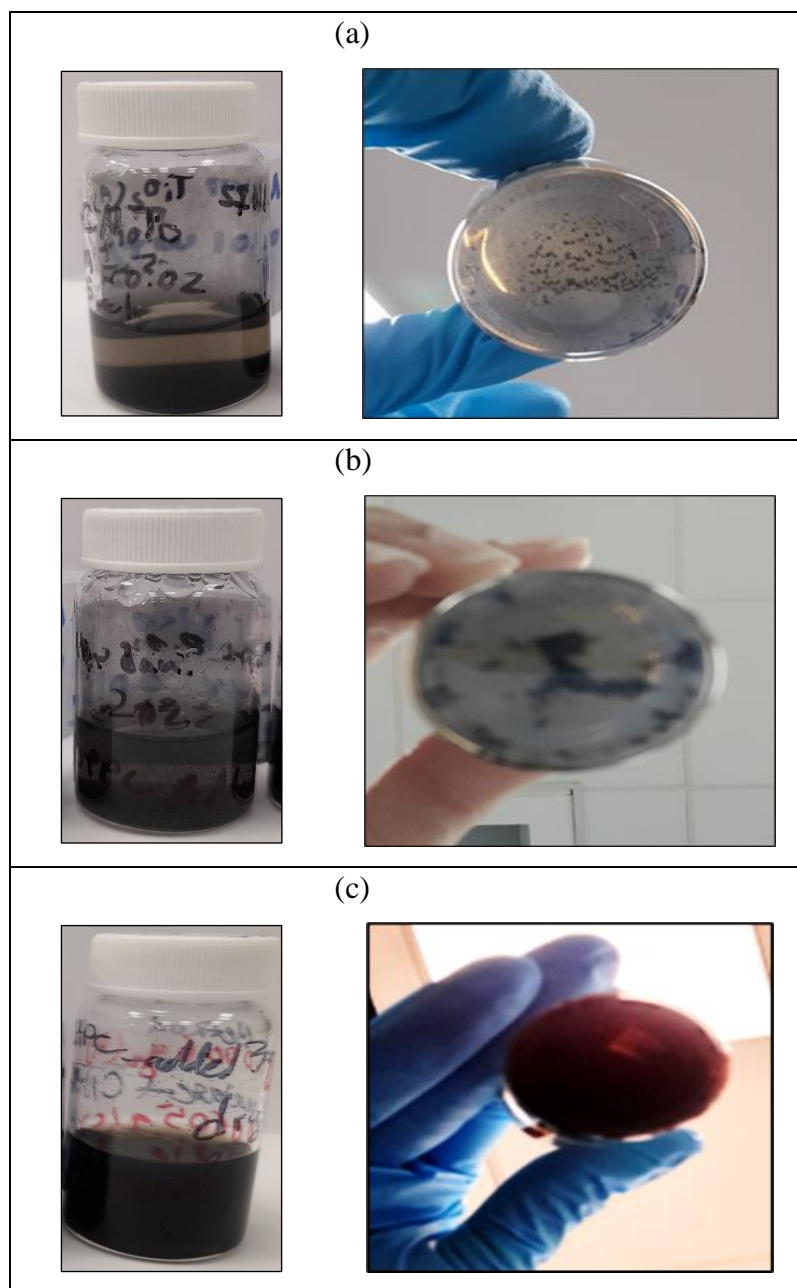


Figure 6.13 Visual inspection of the colloids (side view) and the structure of the sediments (bottom view) for the mixture of ATD+CNT nanoparticles with the concentration of 0.01 wt % in DPPC solution prepared using (a) method i, (b) method ii, and (c) method iii.

Moreover, the side view of the vials indicates that the ATD+CNT mixture prepared using the third method (Figure 6.13, c) shows the highest turbidity. It

can be concluded that the mixture prepared using the third method (Figure 6.13, c) is more stable than the samples prepared using the other two methods (Figure 6.13, a and b). However, it is difficult to compare the stability of the mixture prepared using the first method (Figure 6.13, a) and second one (Figure 6.13, b). The size of the agglomerates for the sediments of the mixture prepared using the first method (Figure 6.13, a) is smaller than that of the mixture prepared using the second method (Figure 6.13, b). On the other hand, the turbidity of the mixture prepared using the second method is higher (Figure 6.13, a and b). Based on the turbidity analysis, the colloid of the second method is more stable, but the size of the sediments of this sample is also larger. This contrast results in difficulties in providing a consolidated conclusion about comparing the stabilities of the mixtures prepared using the first and second methods.

To precisely analyse these colloids, the sizes of the particles in the colloidal phases and the structures of the sediments were observed using the optical microscopy. The results are shown in Figure 6.14.

As it can be seen, the structure of sediments for the sample prepared using the first mixing method (Figure 6.14, a-2) is less dense than that of the second mixing method (Figure 6.14, b-2). There were no apparent solid agglomerates from the sediments of the ATD+CNT mixture prepared using the third method.

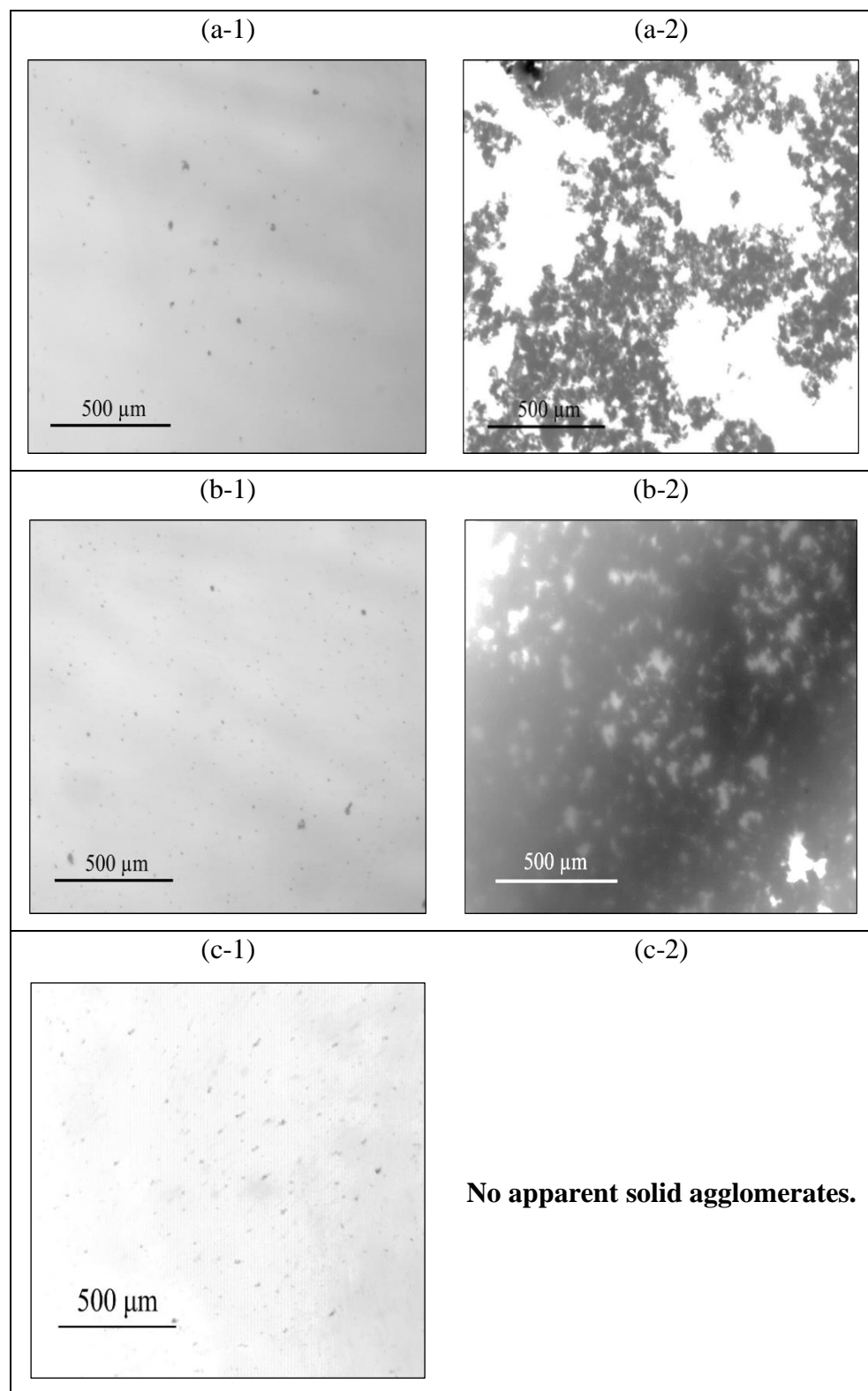


Figure 6.14 Optical microscopy images of the solid agglomerates in the colloid phase (left column including a-1, b-1, and c-1) and the structure of the sediments (right column including a-2, b-2, and c-2) for the mixture of ATD+CNT nanoparticles with the concentration of 0.01 wt % in DPPC solution prepared using (a) method i, (b) method ii, and (c) method iii. There were no visible solid agglomerates in the sediments prepared using mixing method iii under optical microscope.

Based on analysis of the images shown in Figure 6.14 (a-1, b-1, and c-1), the size distribution of the agglomerates in the colloidal phase is plotted in Figure 6.15. For the sake of the better visibility, in Figure 6.15, b, the histogram and normal distribution of the surface area related to the sample prepared by the third method have been added to Figure 6.15, a. These analysis results show that the average size of the particles in the colloidal phase of the ATD+CNT mixture prepared using the first, second, and third methods are ~ 73.67 , ~ 27.87 , and $\sim 26.85 \mu\text{m}^2$, respectively. The sample prepared using the third method has the colloidal phase with the smallest size of the agglomerates or the possibly highest stability. Based on these results, the first mixing method results in the poorest stability of the colloids due the larger size of the agglomerates in the colloidal phase.

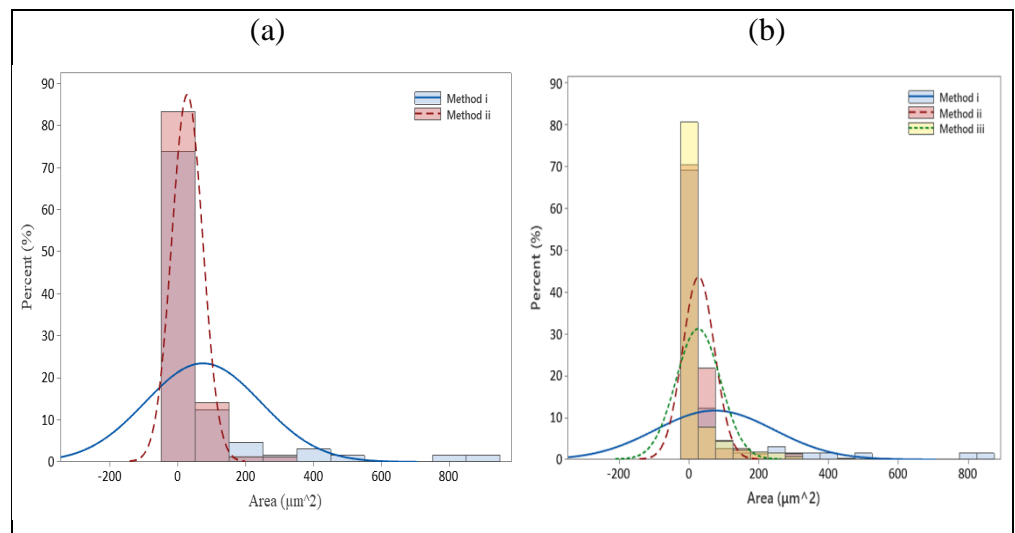


Figure 6.15 Histogram and normal distribution of the surface area of solid agglomerates in the colloid phase for the mixture of ATD+CNT nanoparticles with the concentration of 0.01 wt% in DPPC solution prepared using (a) mixing method i and method ii, and (b) methods i, ii, and iii. The results for method iii have been excluded from part (a) to obtain a better view in the part (b).

Based on the results from Figure 6.13, Figure 6.14, and Figure 6.15 for the mixture of ATD+CNT, it can be concluded that the mixing method directly affects the stability of the agglomerates for the nanoparticles in the colloidal phase. The third method of mixing shows the best stability. This method is

related to the mixing of the dried nanoparticles and then adding the aqueous matrix and DPPC afterwards. This improved stability can be attributed to the negative surface charges of both ATD and CNT particles. There are electrostatic repulsion forces among these particles, which might be the reason for the smaller agglomerates of particles and more stabilised mixtures prepared using this method. For the other two methods, as the nanoparticles have been in contact and are interacted with the DPPC molecules and water molecules in advance, surface properties of these particles have been changed in a way that the repulsive interactions have been apparently decreased among the nanoparticles or among their agglomerates. This could result in the generation of larger sizes of the agglomerates, sedimentation, and thus the less stabilised colloids.

Visual observation and optical microscopy inspections of the colloids containing RTD+CNT nanoparticles were also done and the results are shown in Figure 6.16, Figure 6.17, and Figure 6.18, respectively.

From the side views of the vials in Figure 6.16, the turbidity of the RTD+CNT mixture prepared using the second method (Figure 6.16, b) is more apparent than that of the RTD+CNT mixture prepared using the first method (Figure 6.16, a). However, it is difficult to compare the stability of these two mixtures, by simply comparing their turbidity, as their turbidity differences are not that much significant.

Regarding those sediments at the bottom of the vials for the RTD+CNT mixtures, the visible white spot at the bottom reveals the sedimentation of the RTD nanoparticles and their significant segregation of the CNT particles at the centre of the vial's bottom. This aggregation of RTD nanoparticles can be attributed to the small surface charges of these nanoparticles, i.e., -0.11 ± 0.11 mV.

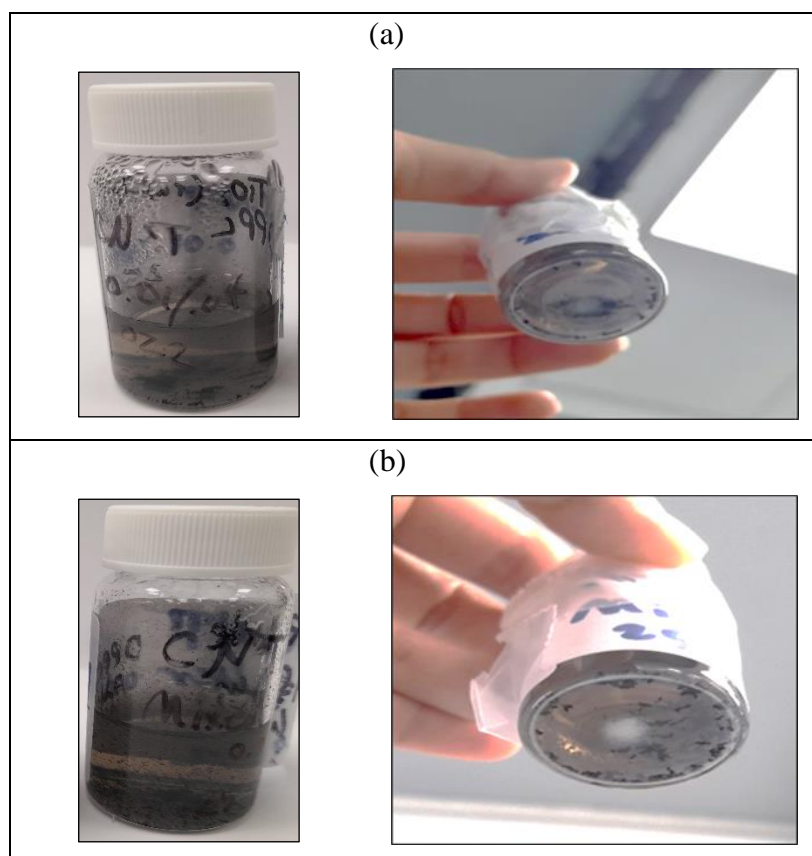


Figure 6.16 Visual inspection of the colloids (side view) and the structure of the sediments (bottom view) for the mixture of RTD+CNT nanoparticles with the concentration of 0.01 wt % in DPPC solution prepared using (a) method i and (b) method ii.

The colloidal phase and the aggregates at the bottom of the vials were observed using the optical microscope. The obtained images are shown in Figure 6.17. The structure of the agglomerates at the bottom of the vials does not show apparent differences (see Figure 6.17, a-2 and b-2). There are no apparent agglomerates of the nanoparticles for the mixture of RTD+CNT prepared using the first mixing method (Figure 6.17, a-1). Therefore, the size distribution analysis and measurements were done only for the colloidal phase of the RTD+CNT mixture prepared using the second method (Figure 6.17, b-1). The obtained results are plotted in Figure 6.18.

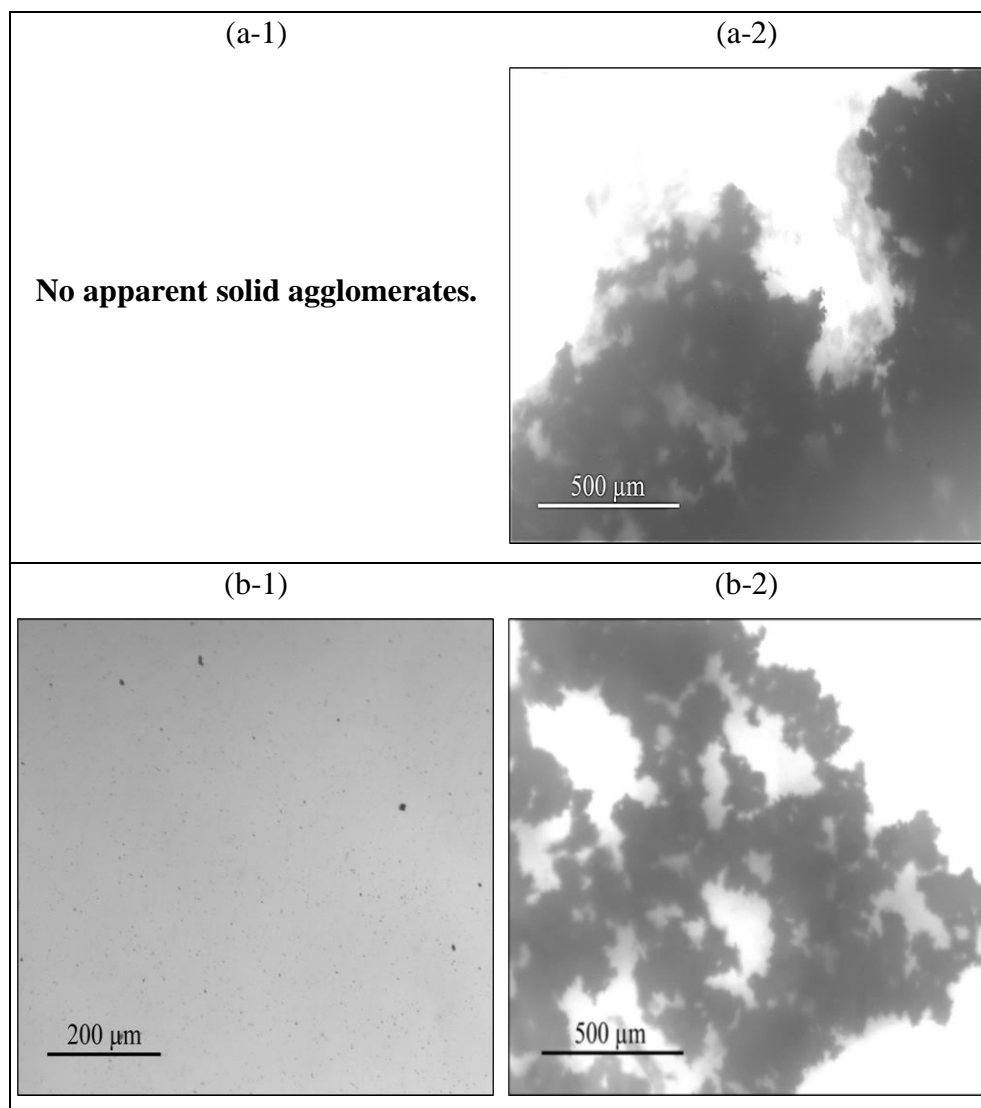


Figure 6.17 Optical microscopy images of the solid agglomerates in the colloid phase (left column including a-1 and b-1) and the structure of the sediments (right column including a-2 and b-2) for the mixture of RTD+CNT nanoparticles with the concentration of 0.01 wt % in DPPC solution prepared using (a) method i and (b) method ii. There were no visible solid agglomerates in the colloid phase prepared using mixing method i under optical microscope.

Data analysis represented in Figure 6.18 shows that the average surface area of the agglomerates in the colloidal phase of the RTD+CNT mixture prepared using the second mixing method is $\sim 5.02 \mu\text{m}^2$. The size of the agglomerates is significantly smaller than that of ATD+CNT mixtures prepared using all three different methods (see Figure 6.15).

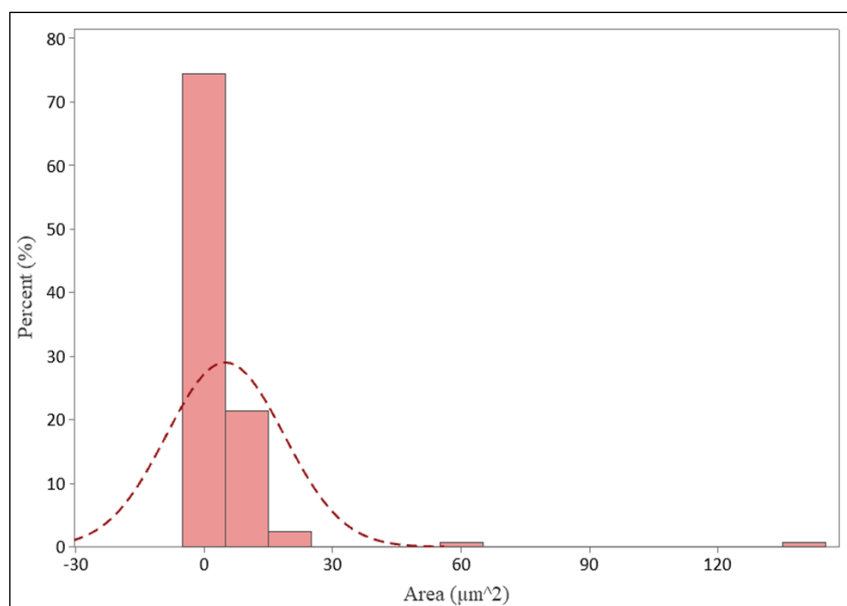


Figure 6.18 Histogram and normal distribution of the surface area of solid agglomerates in the colloid phase for the mixture of RTD+CNT nanoparticles with the concentration of 0.01 wt% in DPPC solution prepared using mixing method ii. There were no visible solid agglomerates in the colloid phase prepared using mixing method i under optical microscope.

The obtained results for the RTD+CNT mixtures prepared using the first and second mixing methods show the significant segregation of the RTD nanoparticles from CNT particles and the sedimentation of RTD nanoparticles. These results can be attributed to the surface charges of these nanoparticles. The surface charges of RTD nanoparticles are very small and they are in a nearly neutral state. Therefore, there is no significant repulsion among these nanoparticles when they move within the colloids. Therefore, they easily form larger agglomerates that can be readily sedimented. On the other hand, there is a significant repulsion force among the CNT particles which carry larger surface charges (-49.02 ± 8.21 mV). Therefore, it is probable that the smaller agglomerates of CNT particles are formed and then remain in the colloidal phase. However, we should address that the stabilities of these colloids prepared using the different mixing methods are difficult to compare and obtain a consolidate conclusion because measuring the particle size distribution using the optical microscope images for the first method was impossible.

The obtained results related to the visual inspection and optical microscopy analysis of the mixtures of ATD+RTD+CNT particles prepared using the first and second mixing methods are shown in Figure 6.19 and Figure 6.20.

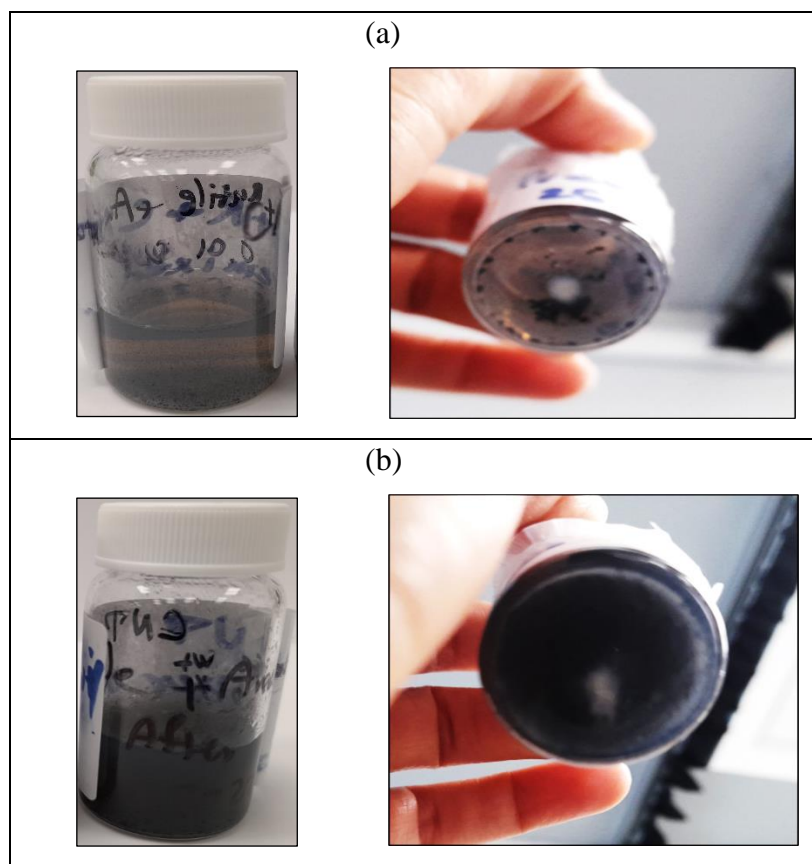


Figure 6.19 Visual inspection of the colloids (side view) and the structure of the sediments (bottom view) for the mixture of ATD+RTD+CNT nanoparticles with the concentration of 0.01 wt % in DPPC solution prepared using (a) method i and (b) method ii.

From both side views of the ATD+RTD+CNT mixtures in Figure 6.19, a and b, the turbidity of the sample prepared using the second method is more apparent than that of the mixture prepared using the first method. This indicates the better stability of the colloid prepared using the second mixing method. From their bottom views, the white spots are visible for both the samples prepared using the first and second methods. These white spots are most probably associated to the aggregated RTD nanoparticles. These white spots were also observed in RTD+CNT mixtures (Figure 6.16). As mentioned before, this type of

agglomeration and sedimentation of RTD nanoparticles is attributed to the small amount of surface charges of these nanoparticles.

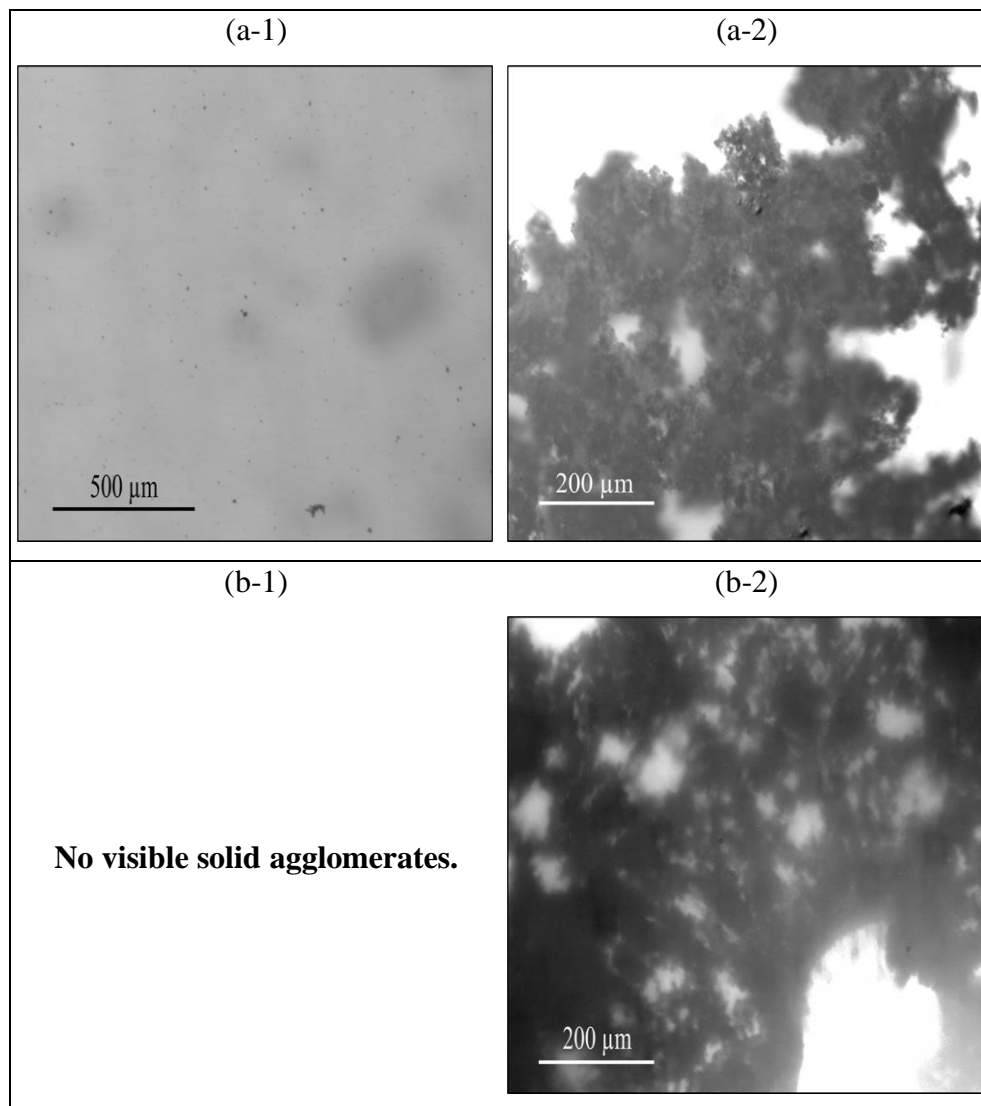


Figure 6.20 Optical microscopy images of the solid agglomerates in the colloid phase (left column including a-1 and b-1) and the structure of the sediments (right column including a-2 and b-2) for the mixture of ATD+RTD+CNT nanoparticles with the concentration of 0.01 wt % in DPPC solution prepared using (a) method i and (b) method ii. There were no visible solid agglomerates in the colloid phase prepared using mixing method ii under optical microscope.

Figure 6.20 shows the optical microscopy images for both the colloidal phases and the sediments of the ATD+RTD+CNT mixtures prepared using the first and second methods. There are not significant differences in the structures of the

sedimented aggregates of the samples prepared using these two methods (Figure 6.20, a-2 and b-2). There are not visible solid agglomerates of ATD+RTD+CNT mixture prepared using the second method. Therefore, only the size distribution of the agglomerates in the colloidal phase of the ATD+RTD+CNT mixture prepared using the first method was analysed and the results are shown in Figure 6.21.

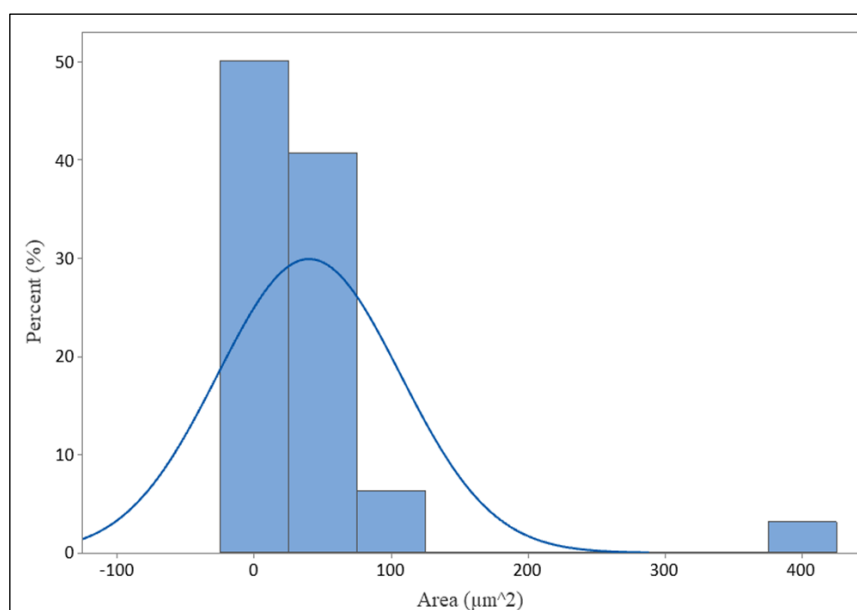


Figure 6.21 Histogram and normal distribution of the surface area of solid agglomerates in the colloid phase for the mixture of ATD+RTD+CNT nanoparticles with the concentration of 0.01 wt% in DPPC solution prepared using mixing method i. There were no visible solid agglomerates in the colloid phase prepared using mixing method ii under optical microscope.

Figure 6.21 shows that the average surface area of the agglomerates of nanoparticles in the colloidal phase of ATD+RTD+CNT mixtures prepared using the first method is $\sim 39.86 \mu\text{m}^2$. As the size distribution measurement for the sample prepared using the second method was impossible, it is thus difficult to conclude which method can result in a better stability of the colloids. However, the significant higher turbidity of the sample prepared using the second method (Figure 6.19) is a reliable reason for the higher stability of this sample. Therefore, it can be concluded that the mixing method affects the stability of the colloids of the ATD+RTD+CNT mixtures.

6.1.3.2 SEM Image Analysis

SEM images of the ATD+CNT mixtures prepared using the first, second, and third mixing methods are shown in Figure 6.22, Figure 6.23, and Figure 6.24, respectively. All these figures show that the ATD nanoparticles have been effectively interacted with CNT particles, causing the agglomeration of ATD+CNT.

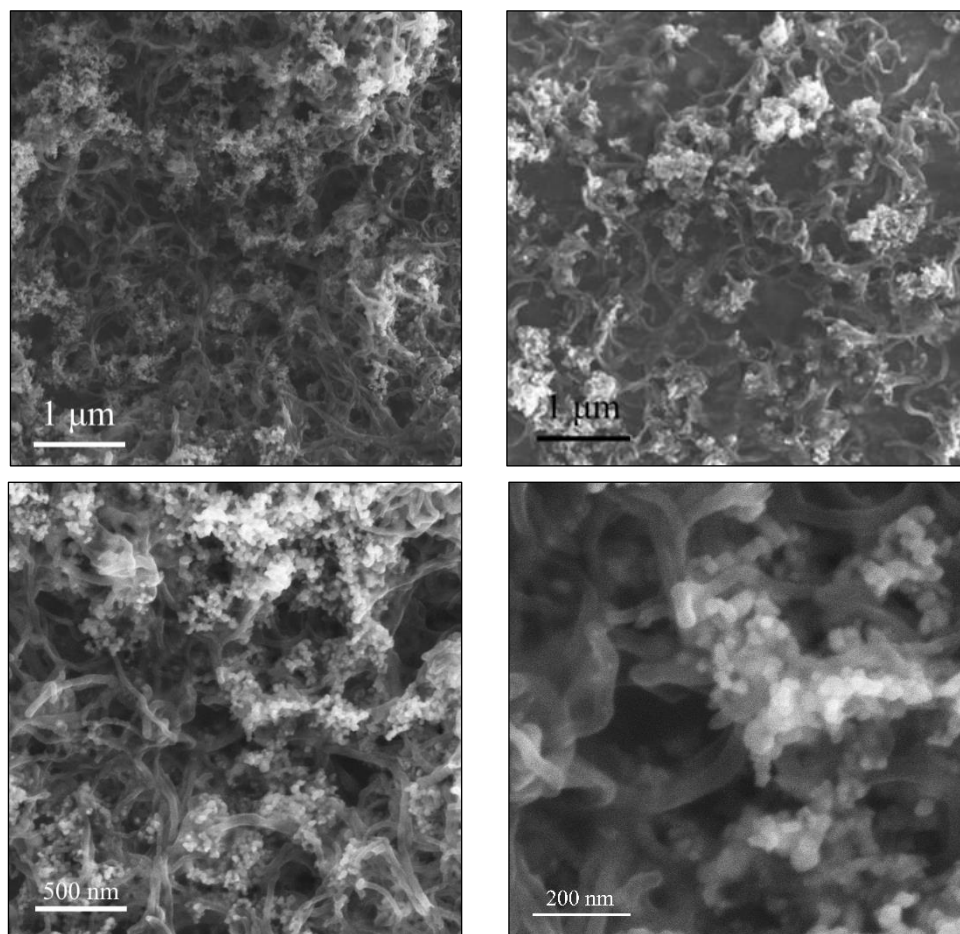


Figure 6.22 SEM images of the droplet of the mixture of ATD+CNT nanoparticles with the concentration of 0.01 wt % in DPPC solution prepared using mixing method i.

Comparisons of Figure 6.22, Figure 6.23, and Figure 6.24 at the scales of both 500 nm and 200 nm do not show strong evidences of structural differences. All these figures show that the ATD nanoparticles have been adsorbed onto the outer surfaces of the CNT particles. Some of the ATD nanoparticles have also been

entrapped inside the porous structures of the CNT agglomerates (see Figure 6.22, Figure 6.23, and Figure 6.24 at the scale of 200 nm).

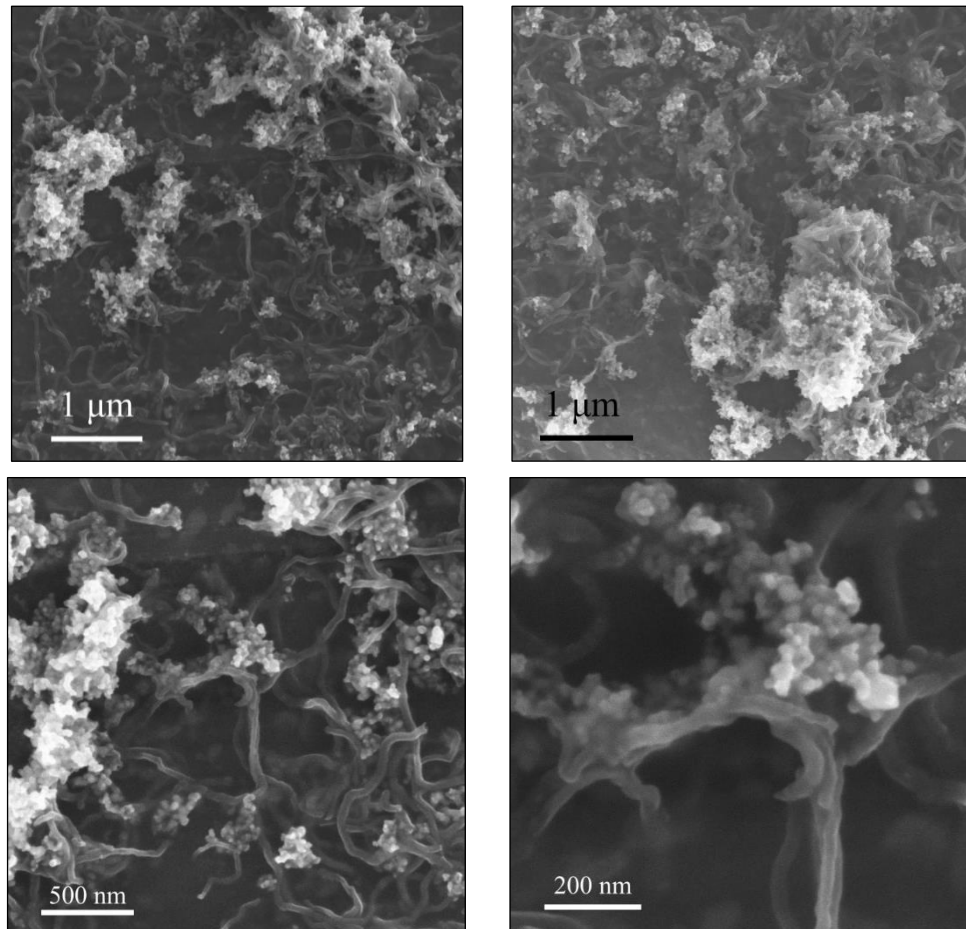


Figure 6.23 SEM images of the droplet of the mixture of ATD+CNT nanoparticles with the concentration of 0.01 wt % in DPPC solution prepared using mixing method ii.

Comparing Figure 6.22, Figure 6.23, and Figure 6.24 at the scale of 1 μm, the ATD nanoparticles appear more evenly distributed and interacted with the CNT particles in the ATD+CNT mixture prepared using the third method (Figure 6.24). This type of evenly distributed ATD nanoparticles on the surface of the CNTs (Figure 6.24 with the scale of 1 μm) might result in enhanced stability of the ATD+CNT colloids prepared using the third mixing method (Figure 6.13, c).

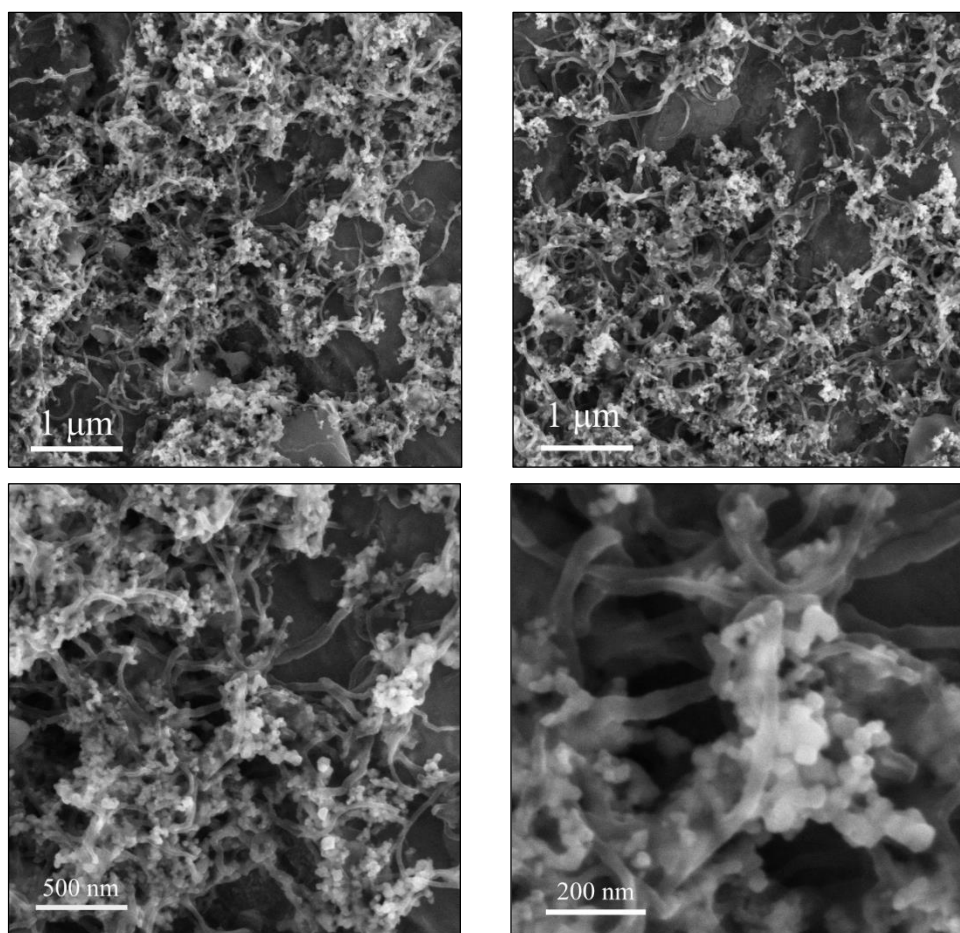


Figure 6.24 SEM images of the droplet of the mixture of ATD+CNT nanoparticles with the concentration of 0.01 wt % in DPPC solution prepared using mixing method iii.

Figure 6.25 and Figure 6.26 show the SEM images of RTD+CNT mixtures prepared using the first and second mixing methods, respectively. Together with ATD+CNT mixtures, the RTD nanoparticles have also been interacted with CNT particles. The evenly distributed RTD nanoparticles on the surfaces of the CNT particles in the RTD+CNT mixture prepared using the second method (see Figure 6.26 with the scale of 1 μm) are quite apparent compared with that of the mixture prepared using the first method (Figure 6.25 with the scale of 1 μm). However, the difference is not significant.

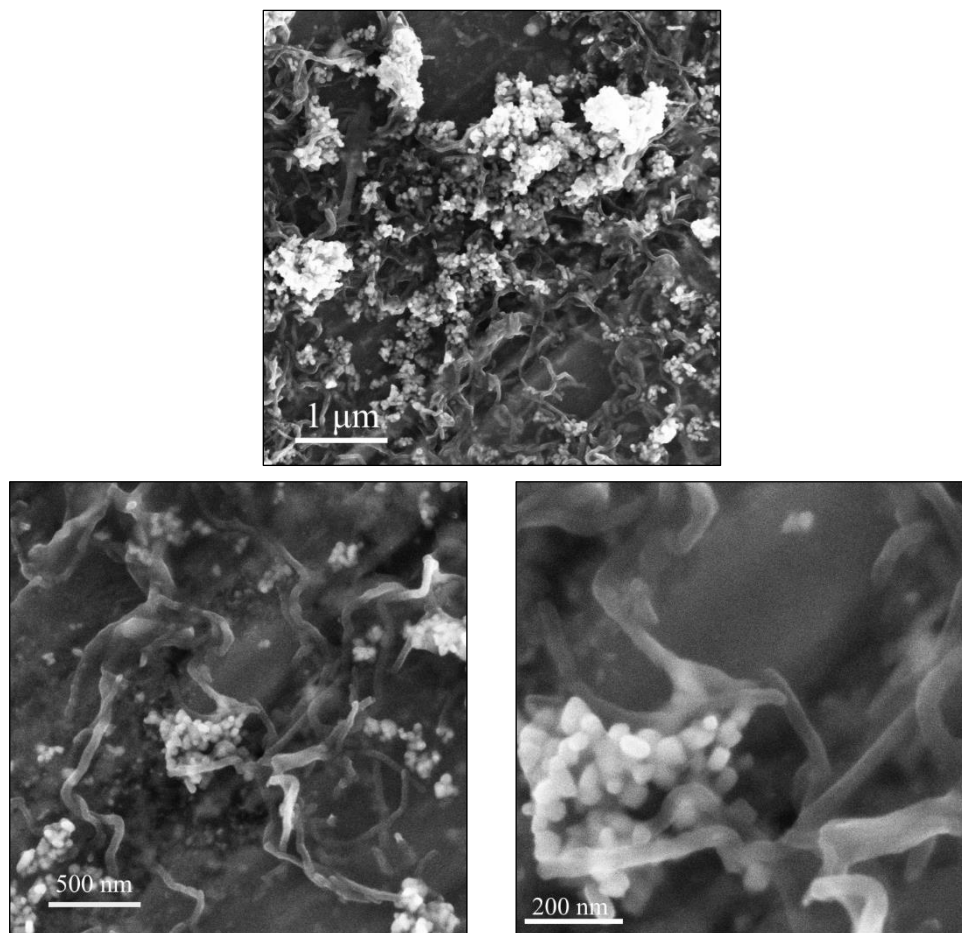


Figure 6.25 SEM images of the droplet of the mixture of RTD+CNT nanoparticles with the concentration of 0.01 wt % in DPPC solution prepared using mixing method i.

Comparing Figure 6.25 and Figure 6.26 (at the two different scales of 500 nm and 200 nm) does not provide any evidence of significant differences between the structures of the RTD+CNT agglomerates prepared using the first and second mixing methods.

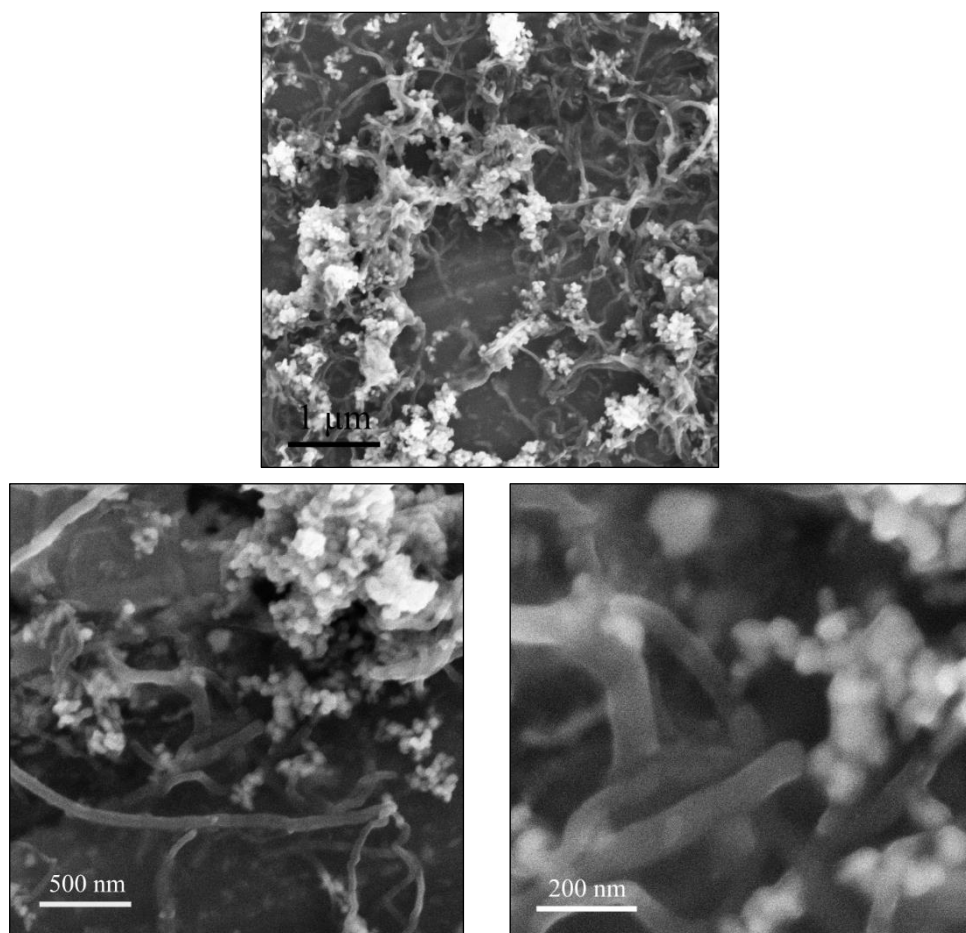


Figure 6.26 SEM images of the droplet of the mixture of RTD+CNT nanoparticles with the concentration of 0.01 wt % in DPPC solution prepared using mixing method ii.

SEM images of the agglomerates of the ATD+RTD+CNT mixtures prepared using the first and second mixing methods are shown in Figure 6.27 and Figure 6.28, respectively. For all the cases with different scales of 200 nm, 500 nm, and 1 μm, there are no significant differences between the samples prepared using the first and second methods. However, these samples show more evenly distributed ATD and/or RTD nanoparticles on the surfaces of the CNTs, in comparison to the ATD+CNT and RTD+CNT mixtures which have been discussed before.

One surprisingly observed phenomenon is that the ATD+RTD+CNT mixtures prepared using both first and second methods show the needle-like structures on the samples (Figure 6.27 and Figure 6.28 with the scale of 10 μm).

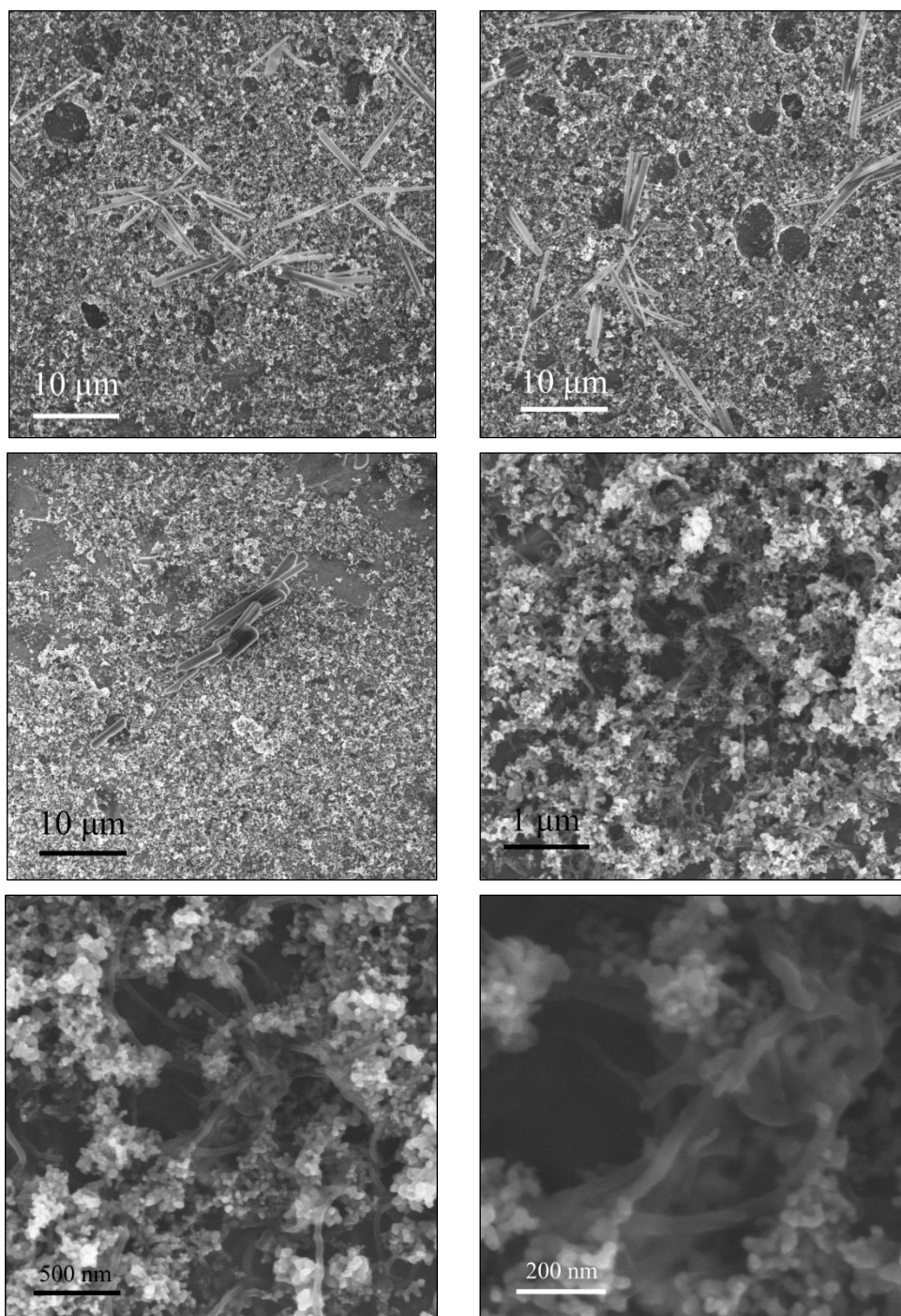


Figure 6.27 SEM images of the droplet of the mixture of ATD+RTD+CNT nanoparticles with the concentration of 0.01 wt % in DPPC solution prepared using mixing method i.

To check whether these structures are random structures generated only at some specifically located areas of the samples or not, different images at

different areas of the sample (e.g., centre, edge, between the centre and edge) were taken. From the obtained results, these structures are visible at all different areas of ATD+RTD+CNT mixture samples prepared using the first and second methods.

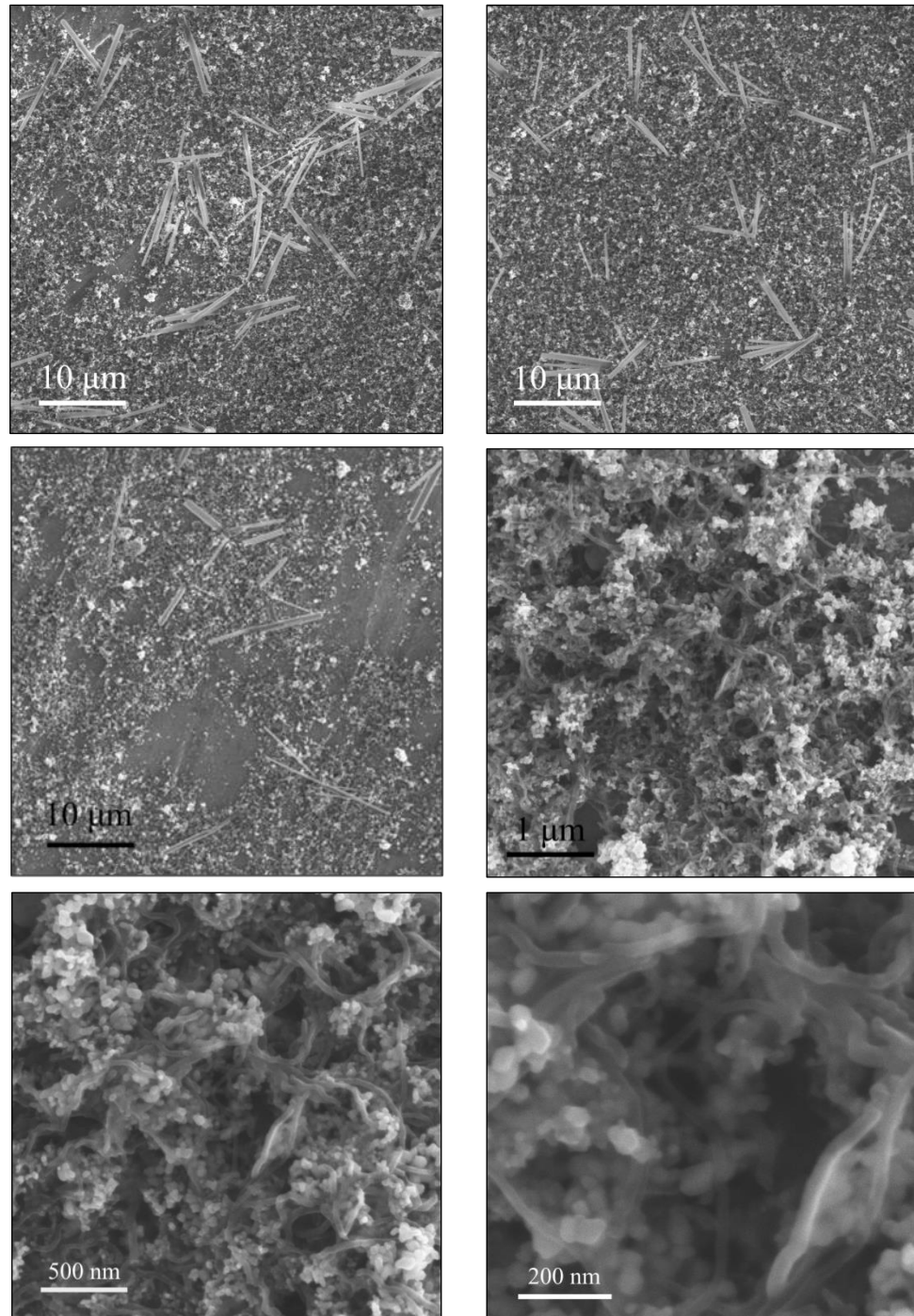


Figure 6.28 SEM images of the droplet of the mixture of ATD+RTD+CNT nanoparticles with the concentration of 0.01 wt % in DPPC solution prepared using mixing method ii.

The types of needle-like structures can be easily attributed to the contamination. If the contamination was due to the storage stage of the samples, it should have happened in the other samples of the mixtures as well, simply because all the samples were stored in the same way. However, the other mixtures did not show needle-like structures. The other potential source of contamination might be the operational procedures conducted to prepare the samples. It should be noted that all the samples of mixtures were prepared using the same procedures and also from the same stock solutions / dispersions of nanoparticles. Therefore, if there was any contamination, it should have been seen in the previous mixtures as well. However, there are no such needle-like structures (as shown in Figure 6.29) observed in the previous mixtures. There might be a possibility of the presence of straight type CNTs among the tangled type CNTs because these structures (Figure 6.29) are similar to the structures of straight type multi-walled CNTs previously observed in the macrophage cytoplasm of rat lungs [241].

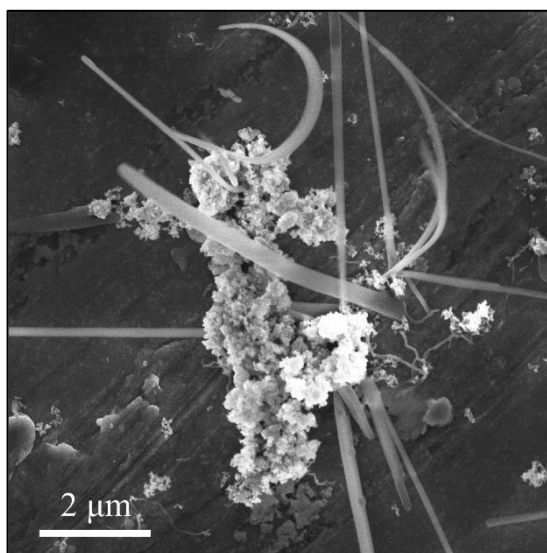


Figure 6.29 SEM image of the needle-shaped structure in the mixture of ATD+RTD+CNT nanoparticles with the concentration of 0.01 wt % in DPPC solution prepared using mixing method i.

To obtain more information about these needle-shaped structures, the Energy Dispersive X-Ray Analysis (EDX) analysis was performed to obtain the

chemical information of those structures. Figure 6.30 shows a typical example of the EDX analysis.

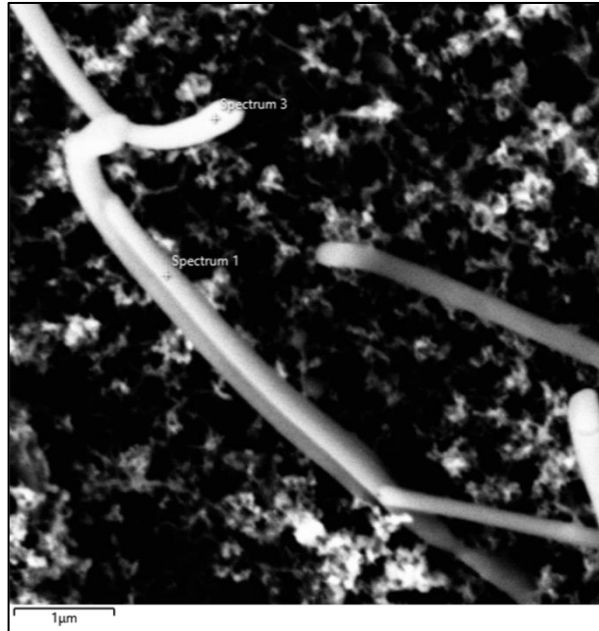


Figure 6.30 SEM image of the needle-shaped structure in the mixture of ATD+RTD+CNT nanoparticles with the concentration of 0.01 wt % in DPPC solution.

The EDX spectra related to those spots on Figure 6.30 are shown in Figure 6.31. The highest peak related to Al is due to the aluminium stub of the SEM. The presence of carbon and oxygen in these structures can be attributed to the CNT particles and the oxygen in the structure of the titanium dioxide (ATD and RTD). The presence of sodium (Na), copper (Cu), and silicon (Si) needs to be discussed carefully.

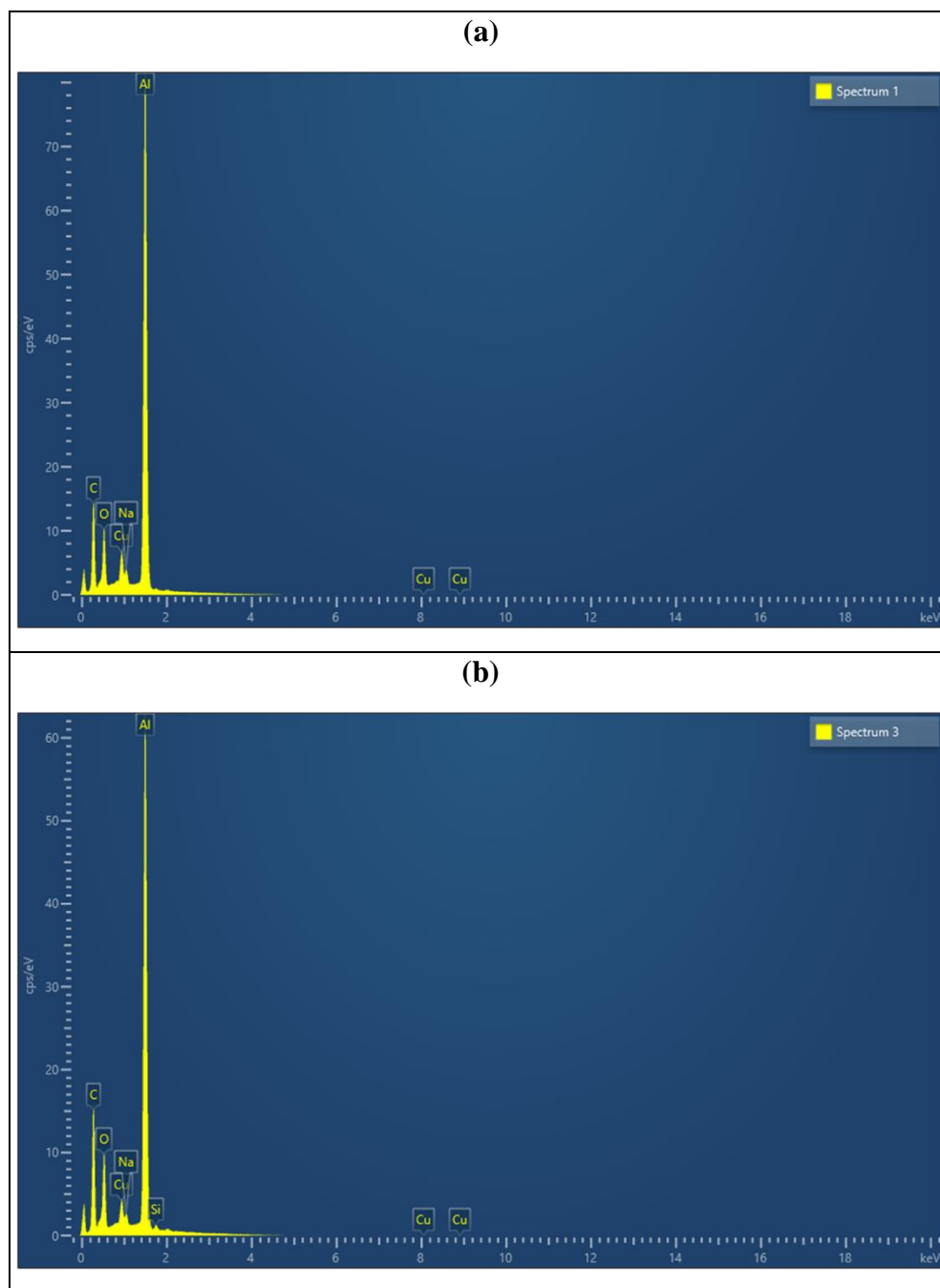


Figure 6.31 EDX analysis of the spectrum 1 (a) and spectrum 3 (b) of the SEM image in Figure 6.30 for the mixture of ATD+RTD+CNT nanoparticles with the concentration of 0.01 wt % in DPPC solution. There were no visible solid agglomerates in the colloid phase prepared using mixing method ii under optical microscope.

Atomic numbers of sodium and silicon are 11 and 14, respectively. As the atomic number of aluminium is 13 and very close to those of sodium and silicon, these two elements might have been read due to the identification error of the software (which is assumed to reasonably occur). The atomic number of copper

is 29 which is not close to aluminium. However, the evidence is not strong enough to trace the source of the copper in these needle-shaped structures which have only occurred in case of ATD+RTD+CNT mixtures. It is better to use the other techniques such as X-ray Photoelectron Spectroscopy (XPS) for analysing the surface chemistry of materials. As we did not have this equipment, it was impossible to do this type of analysis.

6.1.3.3 Interfacial Tension Measurement

The interfacial tension values obtained at the air-liquid interface of all mixtures (including ATD+CNT prepared with three mixing methods, and RTD+CNT and ATD+RTD+CNT mixtures prepared with two mixing methods) were measured and the results are shown in Figure 6.32. As expected, Figure 6.32 clearly depicts that the composition of the mixtures affects the interfacial tension. Moreover, this figure shows that there are differences between two crystal forms of titanium dioxide when they were mixed with CNT particles. For the ATD+CNT mixture prepared using the first method, the interfacial tension is $65.34 \text{ mN}\cdot\text{m}^{-1}$ which is less than that of the DPPC without nanoparticles (red dashed line), DPPC+ATD dispersions (green dashed line), and DPPC+CNT dispersions (grey dashed line). This can be attributed to the adsorption of the agglomerates of ATD+CNT particles at the interface, whereas each of these nanoparticles, at the same concentration, was not being adsorbed at the air-liquid interface when they were in the single-type nanoparticle dispersions. However, the interfacial tension of the RTD+CNT mixture prepared using the first method was $66.26 \text{ mN}\cdot\text{m}^{-1}$ which is higher than the interfacial tension of DPPC without nanoparticles (red dashed line) and DPPC+CNT dispersion (grey dashed line) and is less than the interfacial tension of the DPPC+RTD dispersion (magenta dashed line). This means that mixing the nanoparticle of CNT with RTD using the first method will decrease the interactions of the individual RTD nanoparticles with DPPC molecules in comparison with the situation when there are no CNT particles in the system.

There is also a difference between the behaviours of the ATD+CNT and RTD+CNT mixtures when the second mixing method is used. In this situation, the behaviour is quite opposite compared to those using the first mixing method. This shows that, in cases of ATD+CNT and RTD+CNT mixtures, the mixing method directly affects the interactions of particles among each other and between them and the DPPC molecules. In the second method of mixing, the interfacial tension of ATD+CNT mixture is 66.50 mN.m^{-1} whereas the interfacial tension of RTD+CNT mixture is 65.28 mN.m^{-1} .

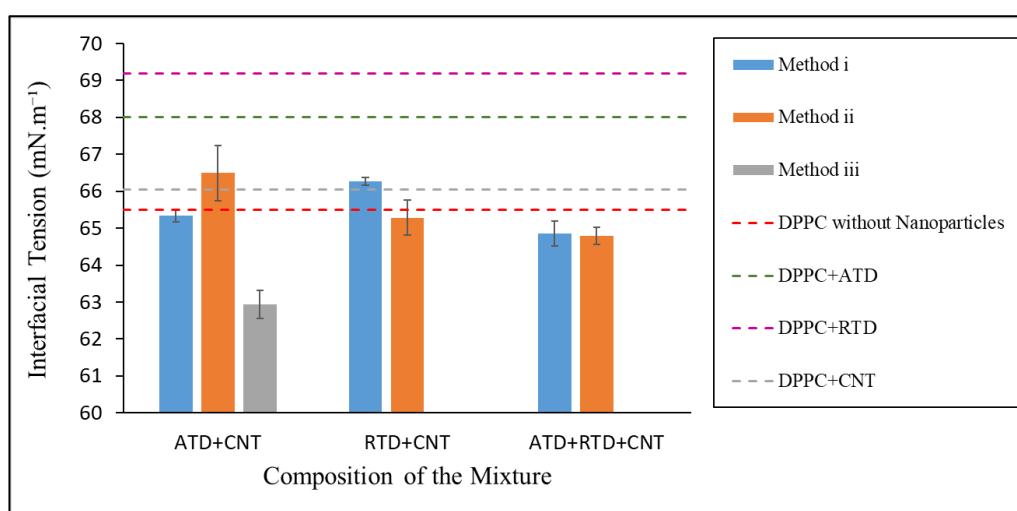


Figure 6.32 Equilibrium interfacial tension for the mixture of nanoparticles with the concentration of 0.01 wt % in DPPC solution using mixing methods i, ii, and iii describes in Section 3.1.4.2. The dashed lines are the representative of the interfacial tension of DPPC solution without nanoparticles and with single-type nanoparticles at $37 \pm 0.2 \text{ }^\circ\text{C}$.

As mentioned above, the mixing method affects the interfacial tension of the mixtures. For the ATD+CNT mixture, an additional third mixing method was used. This method includes the mixing of the dried nanoparticles firstly and then adding of the aqueous matrix and DPPC afterwards. Figure 6.32 shows that the dispersion prepared using this method shows an extremely lower interfacial tension (62.94 mN.m^{-1}), if compared to the other two mixing methods used for preparing ATD+CNT mixture. This means that the agglomerates existed in the mixture of ATD+CNT have been adsorbed onto the air-liquid interface. To make

a more detailed discussion about the status of the agglomerates in all these mixtures and the mechanisms of the actions, the zeta potential and DLS measurements would be very helpful. However, due to the limitations in accessing the related equipment, these measurements were impossible to do on the samples of the mixture.

In case of the mixture of ATD+RTD+CNT, Figure 6.32 shows that the mixing method does not have a significant effect on the interfacial tension. The interfacial tension of the ATD+RTD+CNT mixtures prepared using the first and second methods are 64.86 mN.m^{-1} and 64.79 mN.m^{-1} , respectively. This observation in combination with the previously discussed results for ATD+CNT and RTD+CNT mixtures shows that the mixing method can be an effective factor depending on the composition of the system.

The results from Figure 6.32 clearly show that there are considerable differences between the effects of the individual nanoparticles and mixture of nanoparticles on the interfacial tension of the solutions containing DPPC. This means that the mixed nanoparticles inhaled in real life can affect the lung surfactant in a way which totally differs from single-type inhaled nanoparticles. Only measuring the effect of single-type nanoparticles on the DPPC or lung surfactant could oversimplify the real-life situation. Therefore, it is suggested to combine the data related to the single-type nanoparticles with their mixture. The results can be helpful in many fields including the regulations related to the environmental pollution, and the distance between the industrial plants (factories) emitting nanoparticles into the air. Moreover, the mixture of nanoparticles with different surface properties can also be a potential option for more efficient and controlled drug delivery to the lungs as well.

6.2 Summary

In this chapter, the interactions among the DPPC molecules, single-type nanoparticles and the mixture of nanosized pollutants were investigated to understand the mechanisms of the interactions and effects of the nanomaterials on the DPPC in the bulk of the solution and at the air-liquid interface.

The initial structure of the DPPC molecules in the aqueous solution was established based on the applied method of preparation. In this study, the DPPC molecules in the solutions were in three forms including individual molecules, cylindrical micelles, and open-ended flexible bilayers. These structures induce aggregates with varied sizes inside the aqueous solutions of DPPC which is considered as one of the reasons of the complexity of these systems.

It was experimentally proved that the interactions of nanoparticles with DPPC strongly depends on the surface properties including their shapes and surface charges. Two shapes of titanium dioxide nanoparticle, i.e., ATD and RTD, with different surface charges showed completely different behaviours in interactions with DPPC although both of these nanoparticles were hydrophilic and with the same average size of 20 nm.

Both ATD and RTD nanoparticles interact with individual DPPC molecules and their bilayers, which in turn, cause the depletion of DPPC as the surfactant. However, the types of these interactions are different. Comparing to the DPPC solution without nanoparticles, the negatively charged ATD nanoparticles cause an increase in the interfacial tension at all concentrations whereas RTD nanoparticles decrease the interfacial tension at the concentrations of 0.04 and 0.05 wt %. Although the interfacial behaviour of RTD nanoparticles against their concentrations appeared to follow an order, it was proved that the non-homogeneity of the RTD+DPPC system at the highest concentration, i.e., 0.05 wt %, was increased and the particles and/or their agglomerates were at various states in terms of surface charges.

The predictable behaviours of the ATD and RTD nanoparticles arising from their surface properties can be used as a key solution for designing the nanosized drug delivery carriers for pulmonary drug delivery, when the target is to control the medicine in the bulk and/or at the air-liquid interface of the lung surfactant.

Despite the ordered behaviour of hydrophilic titanium dioxide nanoparticles interacting with DPPC molecules, the CNT particles did not show any reproducibility in terms of the interfacial experiments. This behaviour, which was an obstacle in finding the mechanism of interactions between DPPC molecules and CNTs, indicates the variety of the complex and random structures

of CNT particles at the air-liquid interface. This means that these particles in interactions with the lung surfactant cause unpredictable consequences.

Although it has been proved that CNT particles can be inhaled and might play an important role in the diseases related to air pollution [242], the anthropogenic CNT particles in air are still rare [243]. Therefore, other types of carbon nanoparticles might lead to more reproducible results in interfacial studies.

Investigating effects of the mixture of nano-pollutants on the DPPC was the most innovative part of this chapter which revealed that not only the chemical composition of the mixture of nanoparticles affects the interfacial behaviour of the DPPC solution, but also the method of mixing changes this behaviour. This means that, in the real-life scenarios, the effect of the mixture of nano-sized pollutants on the lung surfactant depends on the type of the pollutants and the way that these nano-pollutants have interacted at the first place.

Chapter 7

Dynamic Responses of DPPC Monolayers to Nano-Pollutants Impact Studied using Interfacial Rheology

In the interfacial systems, such as emulsions, foams, and lung alveoli, the dilatational rheology is focused more than the shear rheology. This is because, in such systems, effect of the dilatational deformation on the liquid motion are more significant [244]. Moreover, the dilatational rheology is beneficial in the DPPC-nanoparticles systems investigated in this study. In this research, the dynamic conditions of the breathing cycle in the respiratory system is simulated, and dilatational rheology is a powerful tool for studying the dynamic properties [245].

In this chapter, firstly the interfacial dilatational rheology of the DPPC solution without particles is investigated using a linear (traditional) approach. The same approach is used for TiO₂ nanoparticles with the least concentration (0.01 wt %) in DPPC solution. After careful investigation of data, the nonlinearity of the mentioned systems (i.e., DPPC solution without particles, ATD 0.01 wt%+DPPC, and RTD 0.01 wt %+DPPC) is proved. Therefore, the interfacial rheology of these systems and the systems containing higher concentrations of nanoparticles is studied using a nonlinear approach. In this approach, the Lissajous plots [20] are used to understand the microstructures of the air-liquid interfaces in the presence and absence of nanoparticles. To our knowledge, it is the first time that the nonlinear surface dilatational rheology approach is used for the DPPC system containing nanoparticles in which the data have been obtained from a PAT equipment.

7.1 Results and Discussion

Rheological experiments or oscillations were conducted after the samples (including DPPC solution without particles, dispersions of DPPC and single-type nanoparticle, and mixture of nanoparticles with DPPC) reached the equilibrium interfacial tension, i.e., after 2500 s. For those samples that did not reach an equilibrium within 2500 s, the oscillation was done after 4000 s when the equilibrium was finally reached. A typical plot of the interfacial tension and surface area as a function of time during oscillation (i.e., after reaching an equilibrium) is shown in Figure 7.1. As this figure shows, the measurements were conducted at four amplitudes (i.e., 1%, 2%, 5%, and 10%). At each amplitude, four frequencies (i.e., 0.1, 0.125, 0.25, and 0.5 Hz) were applied for tests. For every single amplitude at a defined frequency, the number of repeated cycles was five.

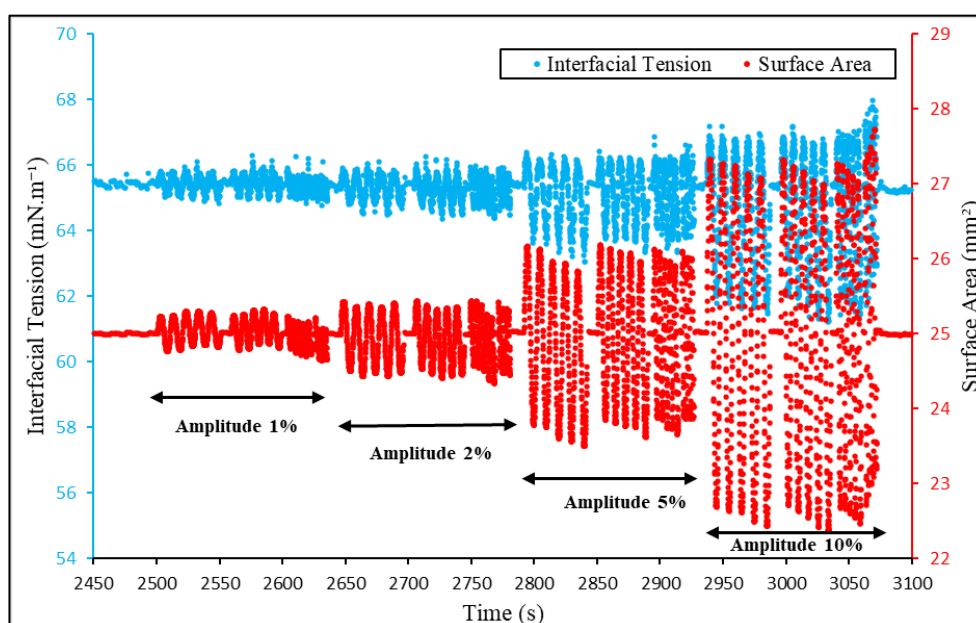


Figure 7.1 A typical plot of the dynamic interfacial tension and surface area vs. time during oscillation. Red and blue dots correspond to the surface area and interfacial tension, respectively. The sample is related to DPPC solution without nanoparticles.

Each oscillation at a defined amplitude and frequency was extracted individually for further analysis using both linear and nonlinear approaches which will be explained in the following sections.

7.1.1 Linear (Traditional) Approach: Fourier Analysis

A linear approach based on the Fourier transform analysis was conducted by using a curve fitting method for the dispersions of titanium dioxide (both anatase and rutile crystal forms) with the least concentration of the nanoparticles in DPPC solutions. The data were extracted from the PAT software in the “.dpa” format and were saved in an Excel format file. Then, this file was used for curve fitting performed using the MATLAB.

The curve fitting toolbox (cftool) in MATLAB was used to measure the complex viscoelastic (dilatational) modulus based on the first harmonic of the Fourier transform, i.e., number of terms were equal to one [246].

An example of the fitted curve for both surface area and interfacial tension is shown in Figure 7.2.

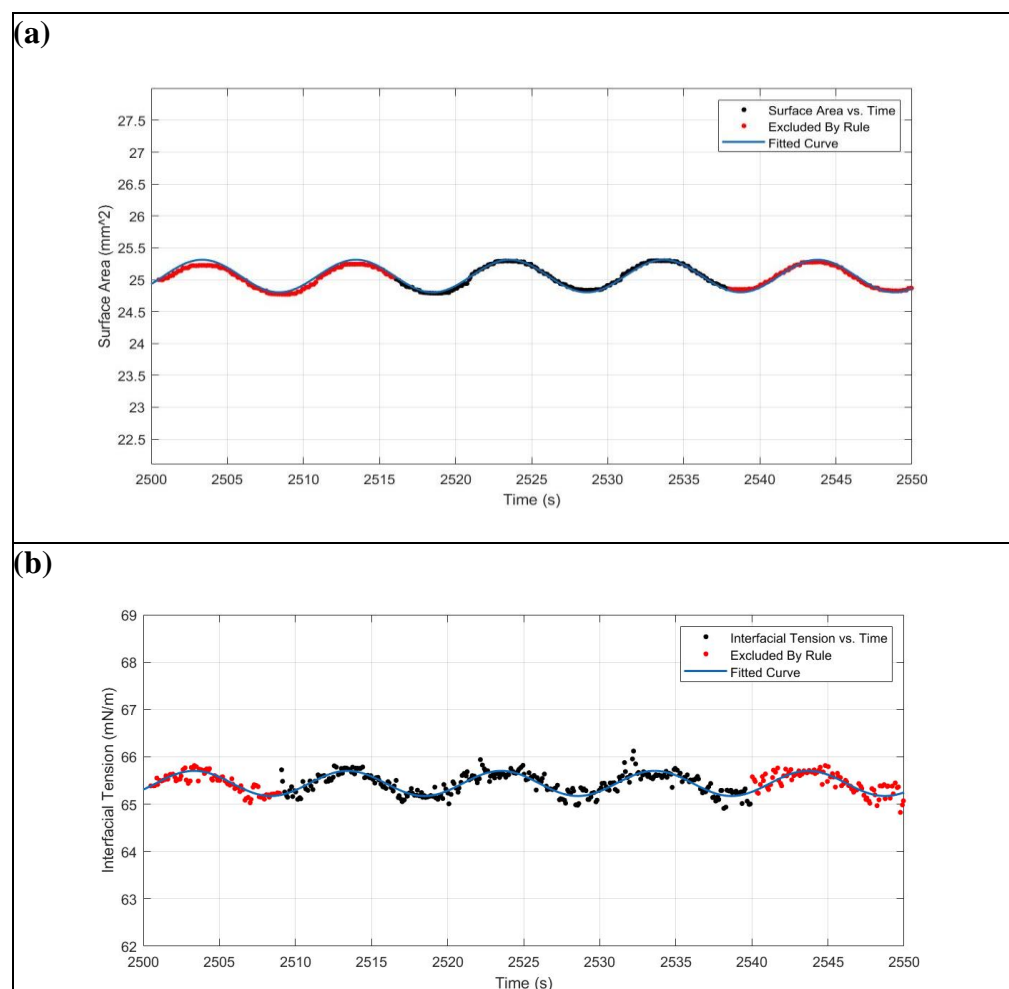


Figure 7.2 An example of the Fourier curve fitting using MATLAB for (a) surface area, and (b) interfacial tension, versus time.

Finding the best fit was not straightforward meaning that it was impossible to choose the Fourier transform in MATLAB and obtain the best fit immediately. In fact, the quality of the fitted curves was not enough for many samples. Therefore, based on the known parameter in the Fourier transform equation, the data exclusion method (i.e., red dots shown in Figure 7.2) was applied to obtain the best possible fit. In this study, the angular frequency, ω , was defined as the known parameter.

The curve fitting method not only is a data analysis technique, but also reveals the suitability of the fitting model and proves the hypotheses behind it by measuring the statistical parameters of the fitted curve. Therefore, the statistical parameters of the fitted curves for each individual sample of DPPC solution without particles, DPPC+ATD, and DPPC+RTD nanoparticles with the concentration of 0.01 wt % of nanoparticles were obtained. The statistical parameters used to assess the standard of the fitting include R-squared, the sum of squares due to error (SSE), and the root mean square error (RMSE). These parameters were used as the first indications of the nonlinearity of the systems. In fact, the higher R-squared (≥ 0.9) and lower SSE / RMSE (closer to zero) values indicate the better fitting.

The R-squared values of these fitted curves for both interfacial tension, $\gamma(t)$, and surface area, $A(t)$, as the functions of time have been summarised and listed in Table 7.1.

Table 7.1 shows that the R-squared values of surface areas as a function of time are ≥ 0.95 for all the samples regardless of the frequencies and amplitudes. This shows the accuracy of the fitted curves. Moreover, it indicates the precision of the input signals, i.e., changes in the surface areas in the PAT set-up. Despite the acceptable R-squared values of the fitted curves on the surface area data, the fitted curves on the interfacial tension shown in Table 7.1 must be considered carefully and case-by-case.

Table 7.1 The R-squared values of the fitted curves of interfacial tension and surface area as functions of time.

Sample	Frequency (Hz)	R-Squared Amplitude = 1%		R-Squared Amplitude = 2%		R-Squared Amplitude = 5%		R-Squared Amplitude = 10%	
		$\gamma(t)$	$A(t)$	$\gamma(t)$	$A(t)$	$\gamma(t)$	$A(t)$	$\gamma(t)$	$A(t)$
DPPC Solution without Particles	0.1	0.707	0.984	0.821	0.995	0.924	0.990	0.950	0.999
	0.125	0.668	0.960	0.836	0.989	0.939	0.996	0.943	0.997
	0.25	0.289	0.986	0.788	0.965	0.961	0.997	0.926	0.998
	0.5	0.486	0.991	0.851	0.994	0.849	0.994	0.812	0.995
ATD 0.01 wt%+DPPC	0.1	0.316	0.983	0.675	0.992	0.860	0.998	0.927	0.996
	0.125	0.205	0.971	0.617	0.994	0.849	0.987	0.929	0.995
	0.25	0.435	0.993	0.453	0.986	0.783	0.991	0.846	0.998
	0.5	0.415	0.990	0.546	0.993	0.632	0.988	0.361	0.992
RTD 0.01 wt%+DPPC	0.1	0.089	0.984	0.259	0.996	0.304	0.986	0.584	0.999
	0.125	0.201	0.954	0.223	0.982	0.269	1.000	0.491	1.000
	0.25	0.137	0.988	0.044	0.994	0.091	0.998	0.396	0.998
	0.5	0.120	0.990	0.103	0.993	0.297	0.994	0.335	0.993

For the DPPC solution without particles, the R-squared values of the interfacial tension, $\gamma(t)$, is less than 0.9 at the lowest amplitudes, i.e., 1% and 2%. By increasing the amplitude to 5% and 10%, the R-squared values of the interfacial tension is increasing meaning that the fitted curve becomes reliable. As mentioned above, the higher R-squared values indicate the better fitting. At these high amplitudes, i.e., 5% and 10%, the lower R-squared values are related to the highest frequency of 0.5 Hz. For example, at the amplitude of 5%, the R-squared value is 0.849, and at the amplitude of 10%, the value of R-squared is 0.812. Overall, in case of DPPC solution without particles, the fitted curves with higher R-squared values are related to higher amplitudes and lower frequencies. It should be noted that the source of the higher R-squared value for the interfacial tension is not necessarily related to the higher accuracy of the fitted curve. It might be due to the data brushing and exclusion of outlier data in the curve fitting technique (i.e., red dots shown in Figure 7.2, b).

Table 7.1 clearly shows that the R-squared values for interfacial tension of ATD 0.01 wt % + DPPC are less than that of DPPC solutions without nanoparticles. This can be seen at all amplitudes and frequencies except the case of the amplitude of 1% and frequency of 0.25 Hz. In this case, the R-squared value of ATD 0.01 wt % + DPPC is 0.435 whereas the R-squared value of DPPC

solution without nanoparticles is 0.289. Similar to the DPPC solution without nanoparticles, it is shown that the R-squared value of ATD 0.01 wt % +DPPC is increasing with the increase of amplitude. The only exception can be observed at the highest frequency. This might be due to the number of data obtained during the experiment at the highest frequency, 0.5 Hz. In the PAT set-up, the number of recorded data points is 12-14 points per second during oscillation. At the highest frequency of 0.5 Hz for 5 cycles, the oscillation takes 10 seconds. Therefore, the number of acquired data points will be 120-140 points which is less than the number of data points used for curve fitting at lower frequencies of 0.1, 0.125, and 0.25 Hz.

Table 7.1 also shows that, in case of the RTD 0.01 wt % +DPPC, the R-squared values of interfacial tension are extremely low at all amplitudes. It can be attributed to the higher nonlinearity of RTD 0.01 wt % +DPPC system in comparison with DPPC without nanoparticles and ATD 0.01 wt % +DPPC systems. This means that, for the RTD +DPPC system, the curve fitting method to measure the first harmonic Fourier moduli will not give realistic results for calculating the viscoelasticity parameters including the viscoelastic modulus and the phase difference between interfacial tension and surface area signals.

In the calculation of R-squared values, both the SSE and the total sum of squares (SST) are considered (Eq. 7-1).

$$R - squared = 1 - \frac{SSE}{SST} \quad \text{Eq. 7-1}$$

The total sum of squares (Eq. 7-2) is defined by the difference between each individual data points, y_i , and the mean value of the data points, \bar{y} . The total number of data is n .

$$SST = \sum_{i=1}^n (y_i - \bar{y})^2 \quad \text{Eq. 7-2}$$

Due to the presence of the mean value of data points in the SST part of R-squared formula, there might be a possibility of misleading R-squared values.

Therefore, it is suggested to calculate one or two other statistical errors to check the suitability of the curve fitting. The advantage of SSE and RMSE is that these two errors show the differences between the predicted data points, \hat{y}_i , and the observed data points, y_i . The predicted data points are the ones obtained by

the suggested model. Eq. 7-3 and Eq. 7-4 show the formula for SSE and RMSE, respectively.

$$SSE = \sum_{i=1}^n (y_i - \hat{y}_i)^2 \quad \text{Eq. 7-3}$$

$$RMSE = \sqrt{\frac{SSE}{n}} \quad \text{Eq. 7-4}$$

Due to the advantage of these errors, SSE and RMSE were all measured in this study (which are listed in Table 7.2 and Table 7.3).

Table 7.2 The SSE values of the fitted curves of interfacial tension and surface area as functions of time.

Sample	Frequency (Hz)	SSE Amplitude = 1%		SSE Amplitude = 2%		SSE Amplitude = 5%		SSE Amplitude = 10%	
		$\gamma(t)$	$A(t)$	$\gamma(t)$	$A(t)$	$\gamma(t)$	$A(t)$	$\gamma(t)$	$A(t)$
DPPC Solution without Particles	0.1	4.162	0.104	9.681	0.160	19.460	2.398	33.320	0.624
	0.125	6.402	0.410	8.898	0.431	12.780	0.739	31.110	2.283
	0.25	2.691	0.034	1.328	0.238	2.102	0.148	22.570	0.449
	0.5	1.305	0.013	1.554	0.049	7.968	0.268	31.150	0.787
ATD 0.01 wt%+DPPC	0.1	2.890	0.126	5.628	0.396	7.529	0.317	15.800	2.933
	0.125	2.599	0.272	4.184	0.212	5.300	2.853	15.770	3.242
	0.25	0.609	0.012	1.283	0.116	2.136	0.579	10.610	0.515
	0.5	0.847	0.022	0.769	0.065	7.062	0.697	38.770	1.774
RTD 0.01 wt%+DPPC	0.1	57.230	0.200	53.450	0.201	144.200	4.488	77.800	1.310
	0.125	11.430	0.595	103.900	0.858	147.200	0.163	131.700	0.456
	0.25	15.370	0.078	26.160	0.073	25.710	0.262	42.590	0.879
	0.5	20.280	0.016	37.170	0.054	40.290	0.379	20.290	1.191

Table 7.2 shows that the SSE values for the surface areas in all systems are in the range of 0-1. There are only some cases that at the higher amplitudes, i.e., 5% and 10%, the SSE values of the surface area are more than 1. The highest SSE of the surface area, 4.488, was reported for the RTD 0.01 wt % + DPPC sample at the amplitude of 5% and the frequency of 0.1 Hz.

Regarding the SSE for the interfacial tension, Table 7.2 shows that the SSE values are very high and deviated from the range of 0-1. These deviations are not

only related to the systems containing ATD and RTD nanoparticles, but they are also obvious in the DPPC solution without nanoparticles. This means that the goodness-of-fit is not enough, which in turn, proves that the Fourier transform does not give the realistic results for these systems. To elaborate the reason why the numbers for SSE are so large, Figure 7.3 has been drawn. When a model such as the Fourier transform one is fitted to the highly scattered data, based on the Eq. 7-3 for SSE, the value of SSE will be very high as the differences between the fitted model and scattered data are quite large. This is quite clear for the case of RTD 0.01 wt % + DPPC as shown in Figure 7.3 where the scattered data have been shown using the double-headed black arrows.

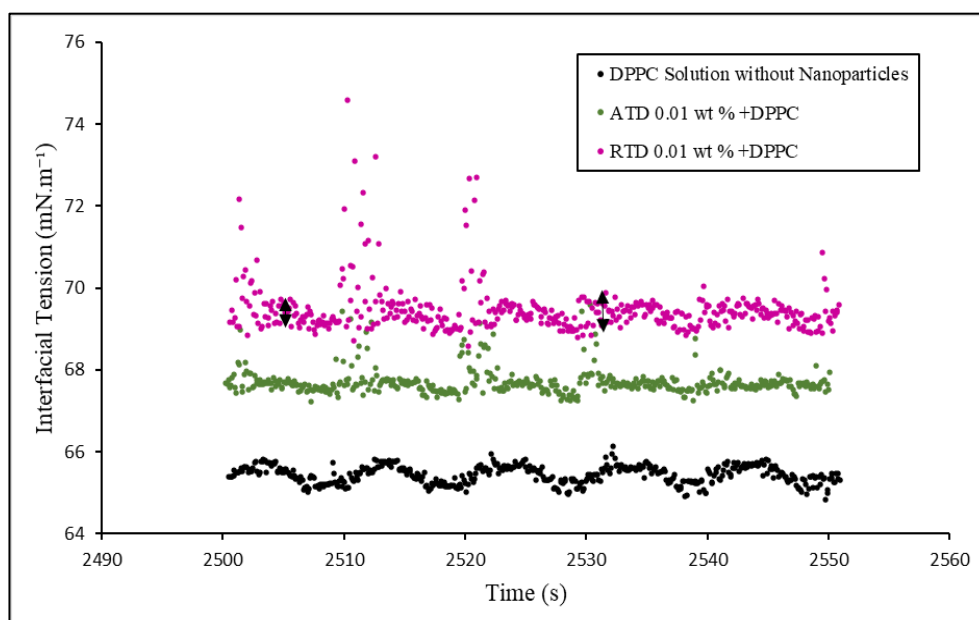


Figure 7.3 The dynamic interfacial tension against time during oscillation at the amplitude of 1% and frequency of 0.1 Hz for DPPC without nanoparticles, ATD 0.01 wt % + DPPC, and RTD 0.01 wt % + DPPC. The double-headed arrows on the data points related to RTD 0.01 wt % + DPPC show the range of data scattering.

The RMSE values of the fitted curves for DPPC solution without particles, ATD 0.01 wt % + DPPC, and RTD 0.01 wt % + DPPC have been summarised in Table 7.3. The values of RMSE for the surface area in all three systems are in the order of 1×10^{-2} order whereas the RMSE values for the interfacial tension

are in the order of 1×10^{-1} . As Eq. 7-3 and Eq. 7-4 show, the RMSE is the square root of SSE divided by the number of data points.

One important point which has been obtained from RMSE values is about the adequacy of the data points at higher frequencies. For examples, in the case of the DPPC solution without nanoparticles, at the amplitude of 10%, the SSE values of the interfacial tension at the frequency of 0.125 Hz and 0.5 Hz are 31.110 and 31.150, respectively (Table 7.2). These values are approximately the same. However, Table 7.3 shows that for this system, at the same amplitude, the RMSE values at the frequency of 0.125 Hz and 0.5 Hz are 0.407 and 0.797. This large difference shows that the number of acquired data points at the frequency of 0.5 Hz is less than the number of data points at the frequency of 0.125 Hz. Therefore, in this case, the higher RMSE at the frequency of 0.5 Hz arise from the number of a smaller number of data points. This is consistent with the low number of acquired data points (i.e., 120-140 points) at the frequency of 0.5 Hz in PAT set-up.

Table 7.3 The RMSE values of the fitted curves of interfacial tension and surface area as functions of time.

Sample	Frequency (Hz)	RMSE Amplitude = 1%		RMSE Amplitude = 2%		RMSE Amplitude = 5%		RMSE Amplitude = 10%	
		$\gamma(t)$	$A(t)$	$\gamma(t)$	$A(t)$	$\gamma(t)$	$A(t)$	$\gamma(t)$	$A(t)$
DPPC Solution without Particles	0.1	0.122	0.023	0.154	0.024	0.241	0.086	0.371	0.052
	0.125	0.147	0.035	0.152	0.034	0.205	0.052	0.407	0.093
	0.25	0.187	0.018	0.131	0.056	0.152	0.040	0.495	0.070
	0.5	0.160	0.014	0.142	0.025	0.322	0.058	0.797	0.127
ATD 0.01 wt%+DPPC	0.1	0.094	0.021	0.120	0.032	0.138	0.034	0.234	0.101
	0.125	0.104	0.033	0.119	0.026	0.134	0.095	0.233	0.112
	0.25	0.100	0.014	0.128	0.039	0.155	0.075	0.338	0.074
	0.5	0.106	0.017	0.124	0.030	0.244	0.094	0.785	0.156
RTD 0.01 wt%+DPPC	0.1	0.432	0.023	0.380	0.023	0.632	0.105	0.496	0.064
	0.125	0.213	0.040	0.594	0.048	0.682	0.020	0.589	0.035
	0.25	0.549	0.019	0.497	0.026	0.717	0.037	0.734	0.071
	0.5	0.637	0.018	0.686	0.029	0.781	0.064	0.960	0.154

After the curve fitting is done using MATLAB, the viscoelastic modulus can be calculated as described in the following section.

7.1.1.1 Viscoelastic Modulus

The complex interfacial dilatational modulus or viscoelastic modulus of the air-liquid interface of each sample at a specific frequency and amplitude were measured using the Fourier transform curve fitting as the standard/traditional method.

Using the curve fitting and Eq. 7-5 (previously mentioned as Eq. 3-20 in Chapter 3), the viscoelastic modulus can be calculated.

$$|\varepsilon| = \frac{\Delta\gamma}{\Delta A/A_0} \quad \text{Eq. 7-5}$$

where ε is the interfacial dilatational modulus or viscoelastic modulus, $\Delta A/A_0$ is the relative area change, and $\Delta\gamma$ is the change of interfacial tension as the response to the change in the surface area.

The plots of the complex viscoelastic modulus of DPPC solution without particles, ATD 0.01 wt % + DPPC, RTD 0.01 wt % + DPPC versus amplitude at different frequencies have been illustrated in Figure 7.4. To avoid any confusion due to the overcrowded plots, the error bars related to the standard deviations have not been shown and the related standard deviation (SD) values have been reported in Table C.1 in **Appendix C**.

Results in Figure 7.4 show that regardless of frequency and amplitude, the complex viscoelastic modulus of the DPPC system decreases when the nanoparticles are added to the system. For the DPPC system without nanoparticles, the viscoelastic modulus is in the range of 34.34 mN.m⁻¹ (amplitude 2%, frequency 0.25 Hz) to 39.82 mN.m⁻¹ (amplitude 1%, frequency 0.125 Hz). For the ATD 0.01 wt % + DPPC, the viscoelastic modulus varies between 6.92 mN.m⁻¹ (amplitude 1%, frequency 0.125 Hz) and 13.70 mN.m⁻¹ (amplitude 10%, frequency 0.25 Hz). This data range for the RTD 0.01 wt % + DPPC is between 7.96 mN.m⁻¹ (amplitude 10%, frequency 0.1 Hz) and 24.11 mN.m⁻¹ (amplitude 1%, frequency 0.25 Hz). The low values of the viscoelastic modulus in the systems containing nanoparticles indicates that, by adding the nanoparticles into the DPPC system, the interfacial tension as the response of the system to the constant deformation is not as much as it should be in the normal situation.

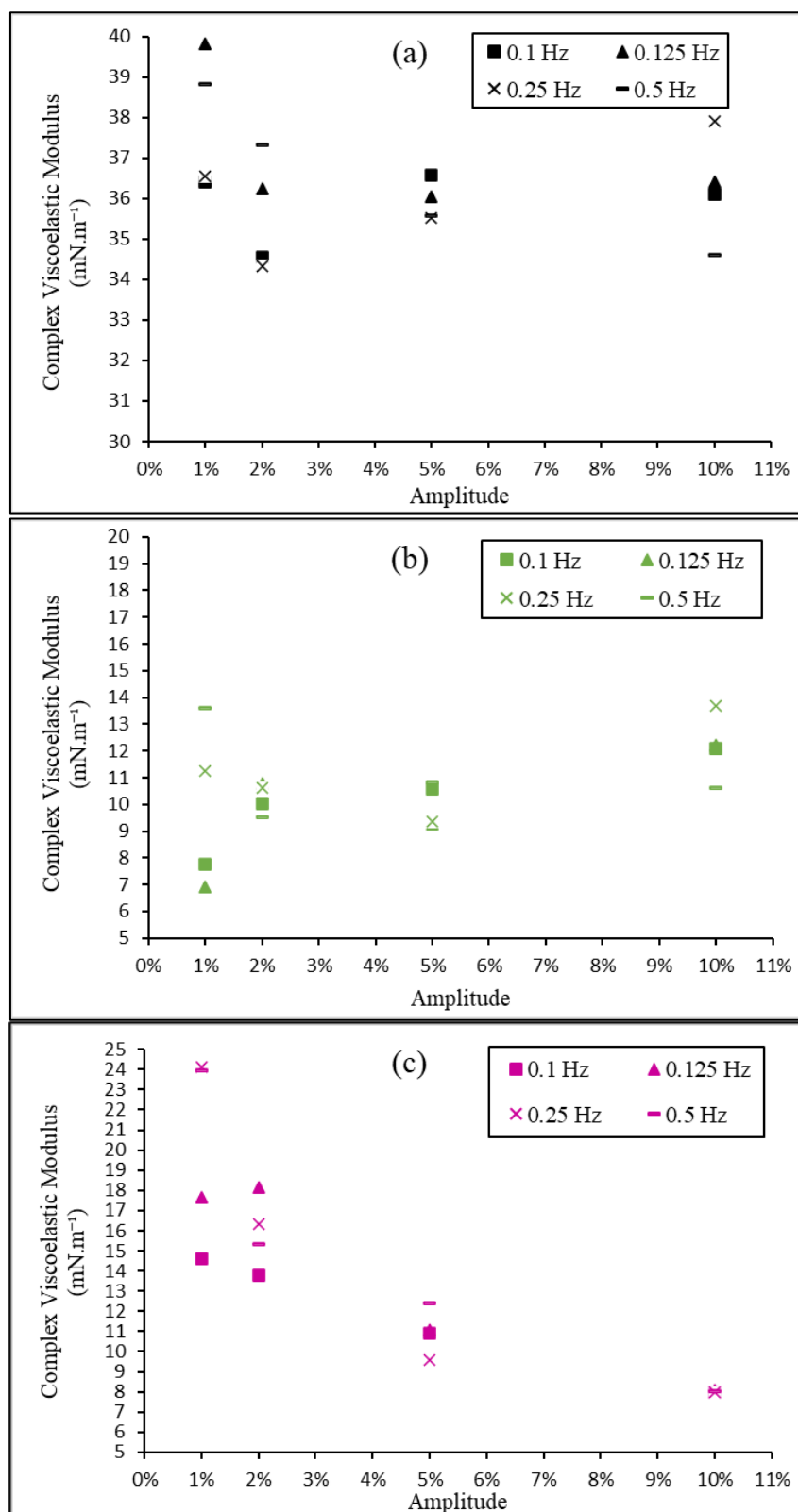


Figure 7.4 Complex viscoelastic (dilatational) modulus of air-liquid interface of (a) DPPC solution without particles, (b) ATD 0.01 wt%+DPPC, and (c) RTD 0.01 wt%+DPPC.

This result can be linked to the physiological conditions of lungs. By breathing the ATD and RTD nanoparticles, the DPPC molecules interact with these particles. The adsorption of these particles at the air-liquid interface of the lung surfactant in the alveoli will result in weak response of interfacial tension to the compression-expansion process of the breathing cycle. This means that the titanium dioxide nanoparticles with the anatase and rutile crystal forms can make the disturbance in mechanical function of the lungs even at the concentrations as low as 0.01 wt %.

To achieve a better understanding of the trend in the behaviour of viscoelastic modulus whilst changing amplitude and frequency, the Analysis of Variance (ANOVA) in Minitab[®] Software was used. After using the General Linear Model, the factorial plots for each system were obtained by introducing the amplitude and frequency as the variable factors and the viscoelastic modulus as the response.

The factorial plots showed that there were no valid interactions between these two factors, i.e., amplitude and frequency, that could be plotted. The main effects plots for the mean of the complex viscoelastic modulus versus each factor were obtained and the results are shown in Figure 7.5. The main effects plot shows the effect of each defined factor on the system's response by measuring the mean value of the responses at the condition where the other factors are maintained as constants. It is noteworthy to mention that the Mixed Effects Model should not be used for this set of data as there is no random factor, and it may mislead the data interpretation.

As shown in Figure 7.5, a and b, the main effects of the amplitude and frequency on the DPPC solution without particles and ATD 0.01 wt % + DPPC are not straightforward. This means that there is no firm and constant qualitative relationship between the effect of frequency or amplitude on the complex viscoelastic modulus for DPPC system without particles and the ATD 0.01 wt % + DPPC system. It can only be assumed that, for the DPPC solution without particles, at the amplitude of 2% and higher, increasing the amplitudes results in the increase of the viscoelastic modulus on an average basis.

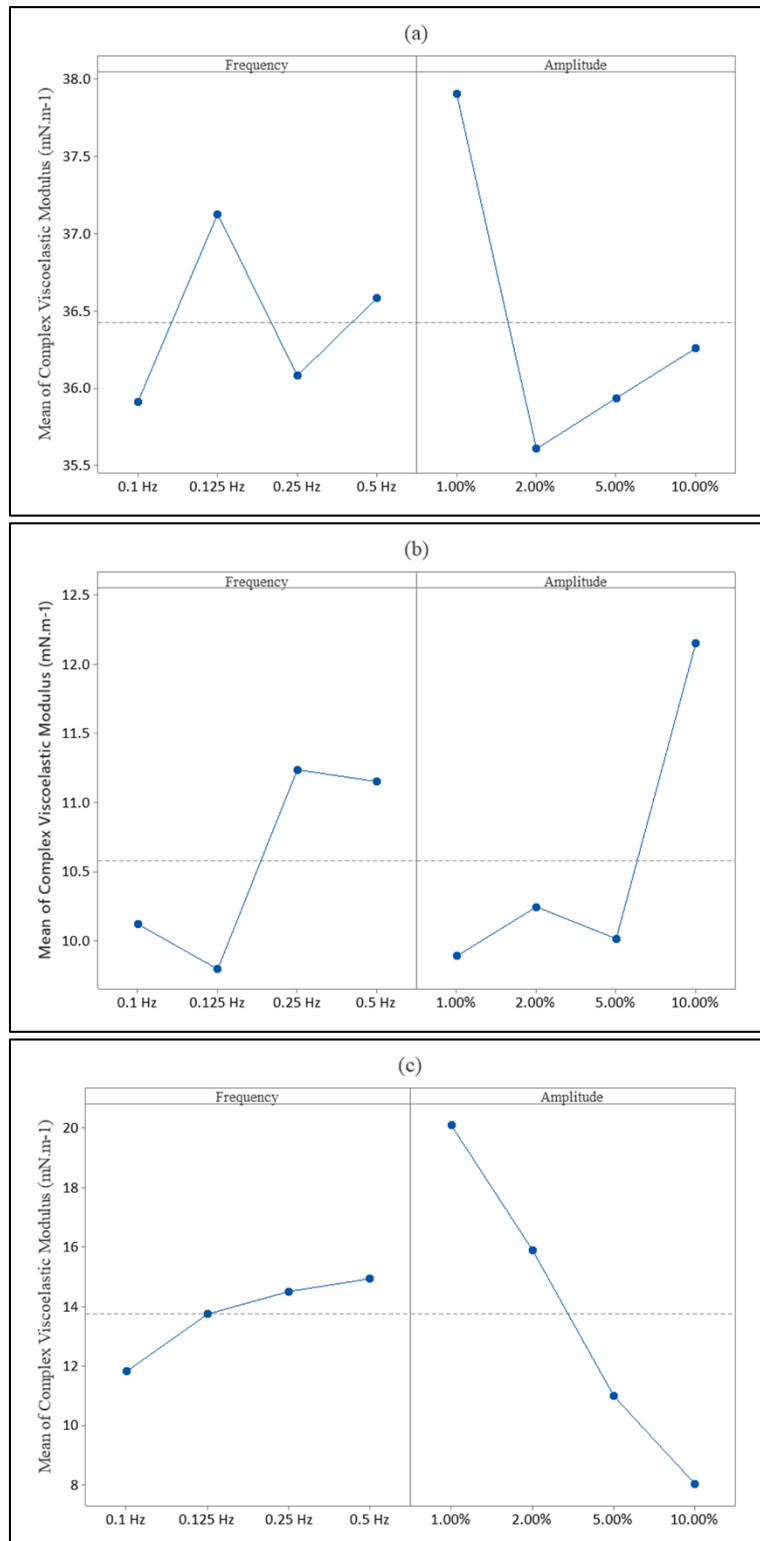


Figure 7.5 The main effects plots for the mean of complex viscoelastic modulus versus frequency and amplitude as the effective factors for (a) DPPC solution without particles, (b) ATD 0.01 wt%+DPPC, and (c) RTD 0.01 wt%+DPPC.

In the case of the RTD 0.01 wt % + DPPC, the main effect plots are showing a meaningful relationship between each factor and response (Figure 7.5, c). It can be concluded that, in the RTD 0.01 wt % + DPPC system, increasing frequency enhances the viscoelastic modulus whereas increasing amplitude decreases the viscoelastic modulus on an average basis. Moreover, the effect of the amplitude is more significant than that of frequency.

7.1.1.2 Phase Difference

Measuring the phase difference in the rheology studies of the lung surfactant during the dynamic conditions of the breathing cycle is advantageous because the phase difference shows the interfacial tension hysteresis in the lung.

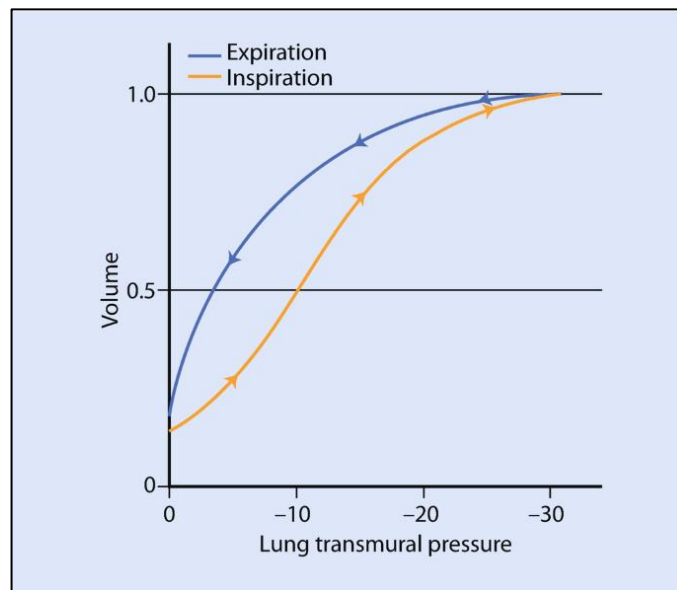


Figure 7.6 The volume versus pressure known as pressure-volume curve of lung during inspiration (expansion) and expiration (compression) in the breathing cycle. Reprinted by permission from Springer Nature Customer Service Centre GmbH: Springer, Cham, Basic Sciences in Anesthesia. © 2018 Springer International Publishing AG [247].

As shown in Figure 7.6, from a physiological point of view, the pressure-volume curves of the inspiration (expansion) and expiration (compression) during the breathing cycle are different. The difference between these two curves

is called hysteresis. In fact, the applied energy of the human body to the lung during its expansion will not be recovered in the compression process. Therefore, there is an energy dissipation called hysteresis in the lung. The hysteresis of the pressure-volume curve in lungs is affected by three factors including tidal re-expansion/collapse, stress relaxation, and the interfacial tension hysteresis due to the presence of the lung surfactant [129, 248, 249].

In the oscillation studies, this hysteresis can be obtained by measuring the phase difference or loss angle which shows the ratio of viscosity to elasticity. In this study, to determine the phase difference between the interfacial tension and surface area signals, a MATLAB function based on Discrete Fourier Transform (DFT) was applied [250-252]. This code provides a highly noise resistive method for the signals in the time domain. The original code entitled Phase Difference Measurement with MATLAB Implementation has been provided in **Appendix B** [250]. In fact, each oscillation with the defined amplitude and frequency was separated. Then, the phase differences between the interfacial tension and surface area signals were obtained. An example of the signals obtained in MATLAB interface has been shown in Figure 7.7.

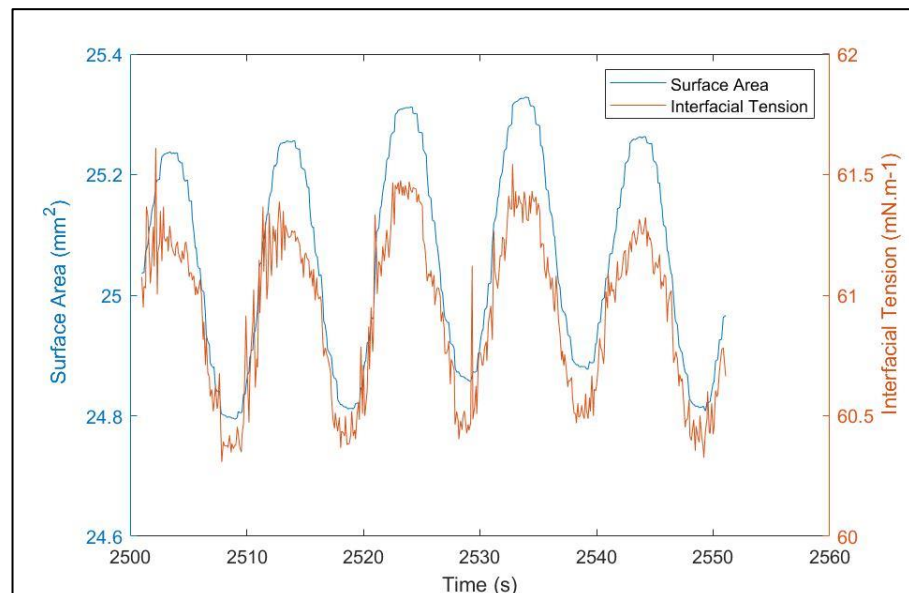


Figure 7.7 The example of the surface area and interfacial tension signals in MATLAB interface during the oscillation at the amplitude of 1% and frequency of 0.1 Hz. The sample is related to the DPPC solution without particle.

Figure 7.8 illustrates the results of the phase differences between interfacial tension and surface area signals. As the values of phase difference are very close to each other at some points, the error bars have not been reported in these plots. The standard deviation values have been reported in Table C.2 in **Appendix C**.

As shown in Figure 7.8, in case of the DPPC solution without adding the particles, the phase difference values are in the range of 0.21-8.20 deg. This range becomes wider when the nanoparticles of ATD and RTD are added to the system. The phase difference values of ATD 0.01 wt % + DPPC are between -15.03 deg and 73.35 deg. There is only one negative phase difference in the ATD 0.01 wt % + DPPC which is related to the amplitude of 10% and the frequency of 0.5 Hz. This number cannot be shown in Figure 7.8 as it is a logarithmic plot. The phase difference values for RTD 0.01 wt % + DPPC system are in the range of 1.63-100.54 deg.

The increase of phase differences or loss angle value upon adding the nanoparticles to the DPPC system shows that the energy dissipation is increased. This effect is more visible at the low amplitudes, i.e., 1% and 2%. For example, for the DPPC solution without particle, the phase difference is 2.98 deg at the amplitude of 1% and the frequency of 0.1 Hz. At the same condition, the phase difference values of ATD 0.01 wt % + DPPC and RTD 0.01 wt % + DPPC are 53.52 deg and 35.56 deg, respectively. Therefore, the presence of titanium dioxide nanoparticles in the DPPC system results in increased loss of energy (deformation energy) at the mentioned amplitude and frequency. This effect of nanoparticles becomes less significant at higher amplitudes as the phase difference values of the nanoparticle-containing systems become closer to those of the DPPC systems without nanoparticles.

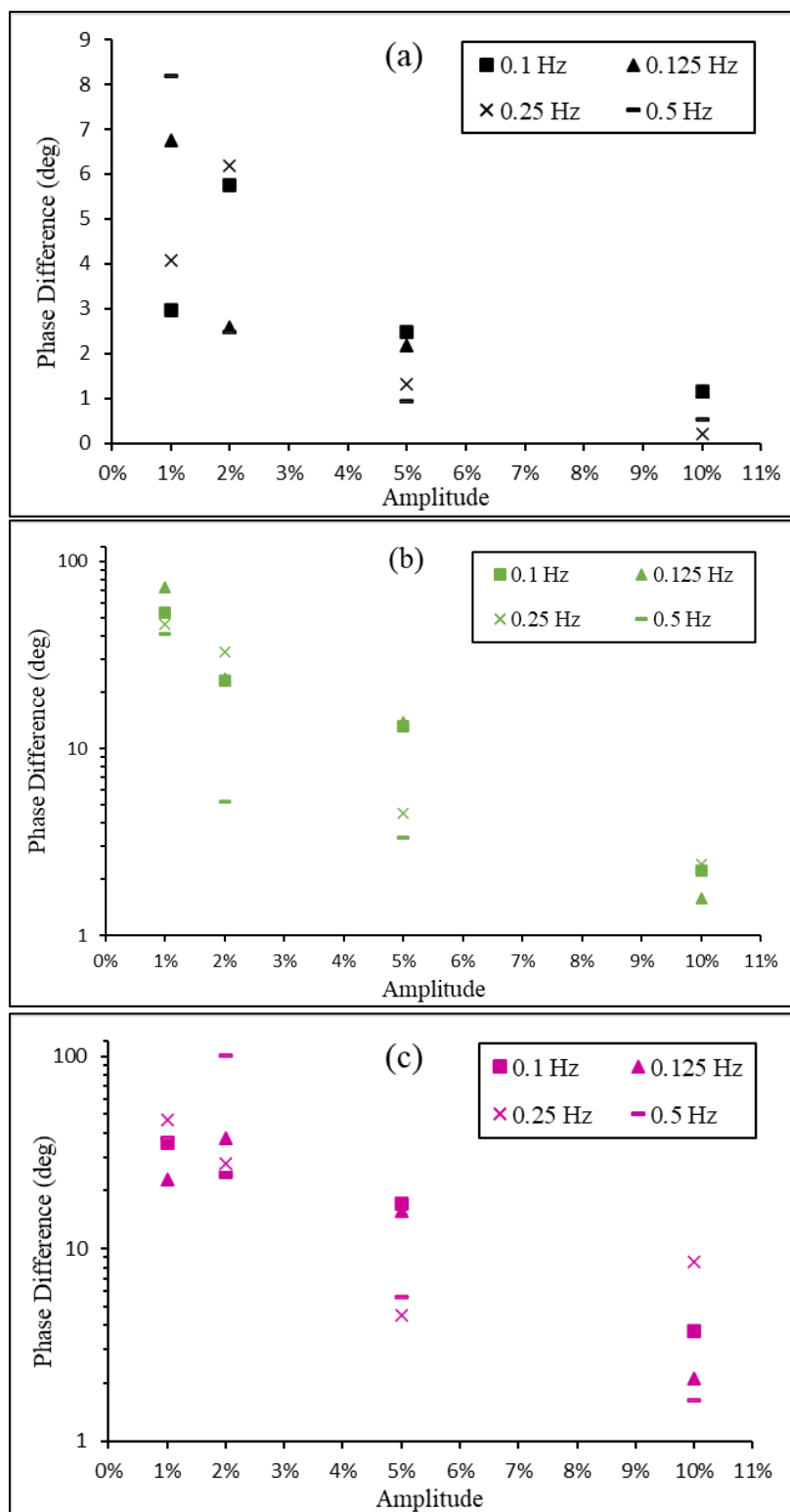


Figure 7.8 Phase difference between interfacial tension and surface area signals for (a) DPPC solution without particles, (b) ATD 0.01 wt%+DPPC, and (c) RTD 0.01 wt%+DPPC.

To further scrutinize the effects of frequency and amplitude on the phase differences, ANOVA and General Linear Models in Minitab® Software were used.

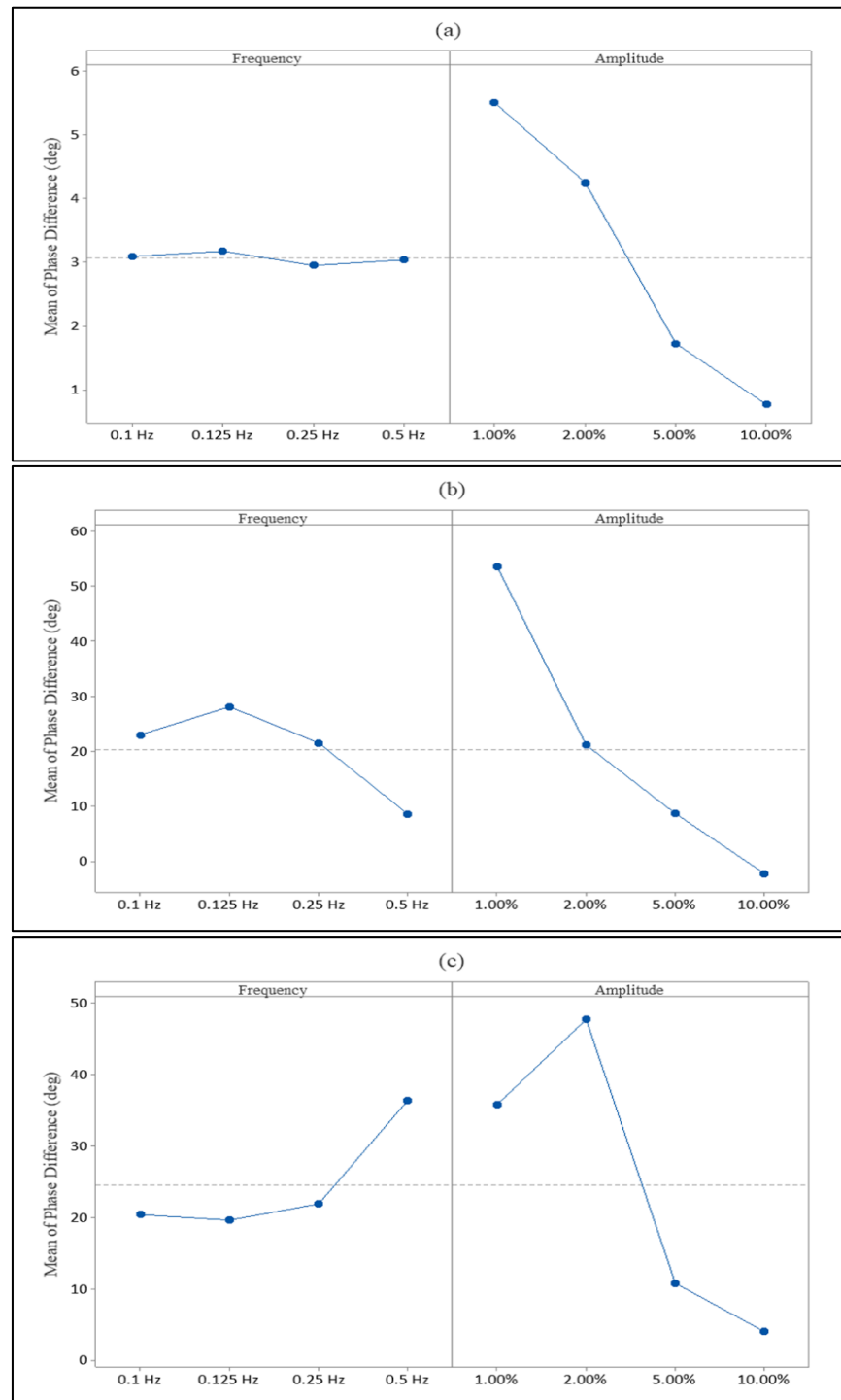


Figure 7.9 The main effects plots for the mean of phase difference versus frequency and amplitude as the effective factors for (a) DPPC solution without particles, (b) ATD 0.01 wt%+DPPC, and (c) RTD 0.01 wt%+DPPC.

The factorial plots are not obtained by the software because there are no valid interactions between the amplitude and frequency as the effective factors on the phase differences. Therefore, only main effects plots for the mean values of the phase differences versus amplitude and frequency were obtained and are shown in Figure 7.9.

As shown in Figure 7.9, effects of the amplitude on the phase differences for samples of DPPC solution without particles, ATD 0.01 wt % + DPPC system, and RTD 0.01 wt % + DPPC are more significant than the effects of frequency. In general, increasing the amplitude results in the decreasing of the mean of the phase difference. Regarding the value of frequency, for the DPPC solution without particles (Figure 7.9, a), all the points are on an approximately horizontal line in the vicinity of the baseline of the mean of the phase difference. These frequency-related points become more scattered in cases of adding ATD and RTD nanoparticles in the system (Figure 7.9, b-c). This means that adding nanoparticles to the DPPC system intensifies the effect of the frequency on the mean of phase difference.

7.1.2 Total Harmonic Distortion (THD) Measurement

To clarify the linearity or nonlinearity of the system, the THD for both surface area and interfacial tension signals was measured using the signal processing toolbox in MATLAB. Based on this MATLAB syntax, six harmonics were used to calculate the THD, thus the response signals were the results of the fundamental oscillation and higher harmonics up to the sixth order. The remainder terms are all considered as noise [253]. Typical outputs of the THD measurements for the surface area signals in MATLAB are shown in Figure 7.10. The THD value can be expressed in both dB unit and percentage. In this example, the THD value is -19.60 dB which is equal to 10.47 %.

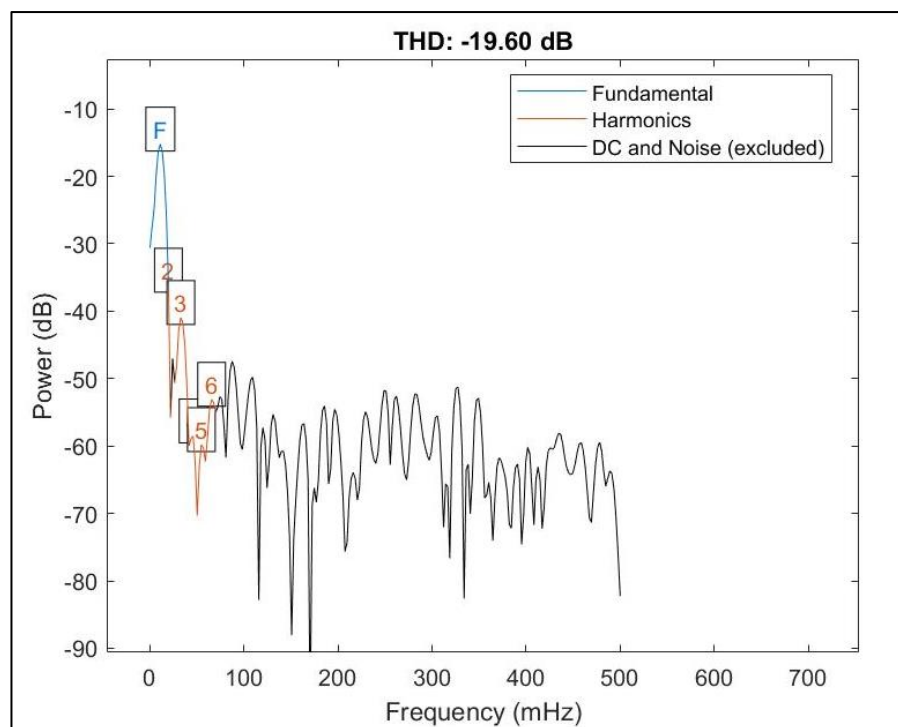


Figure 7.10 The example of the THD measurement for the surface area signal in MATLAB interface. The output of the code is in both dB unit and percentage. This example is related to the oscillation at the amplitude of 1% and frequency of 0.1 Hz. The sample is related to the DPPC solution without particle.

It should be noted that the THD values of both interfacial tension and surface area signals were measured for samples of DPPC solution without particles, ATD 0.01 wt % + DPPC, and RTD 0.01 wt % + DPPC at different frequencies and amplitudes. The results of the THD measurement in percentage are plotted in Figure 7.11.

As shown in Figure 7.11, left column shows that the values of THD percentages of the surface areas are in the ranges of 9.84%-17.71%, 8.15%-18.37%, and 11.11%-17.82%, for DPPC solution without particles, ATD 0.01 wt % + DPPC, RTD 0.01 wt % + DPPC, respectively. These similar ranges of the THD values for the input signals, i.e., surface area, can be applied as an indication of the precision and efficiency of the PAT equipment.

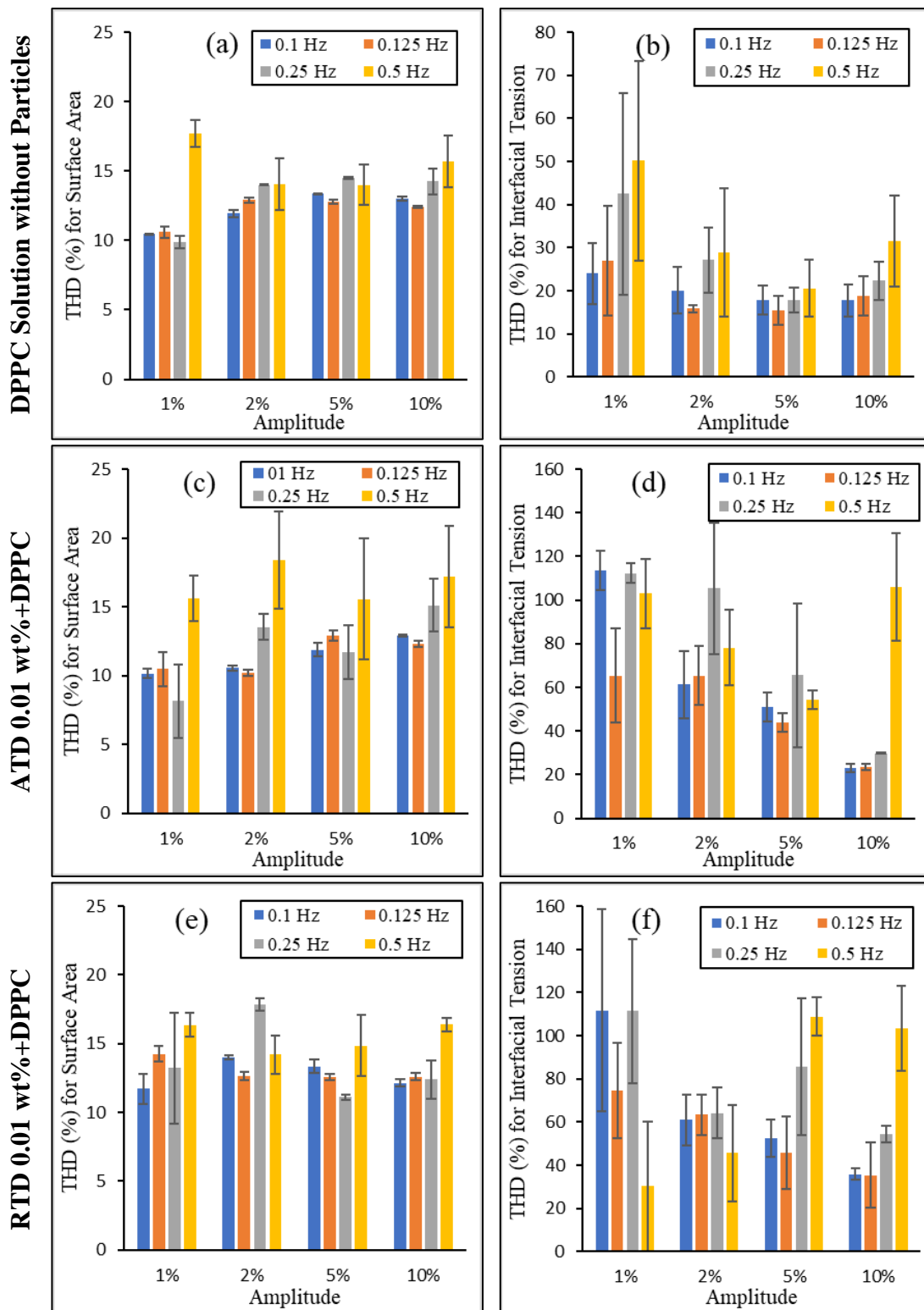


Figure 7.11 THD percentage for surface area (left column) and interfacial tension (right column) for DPPC solution without particles (a-b), ATD 0.01 wt%+DPPC (c-d), and RTD 0.01 wt%+DPPC (e-f).

The THD values for the interfacial tension signals are regarded as the quantitative indicator of the nonlinearity of system. The obtained THD values are shown in the right column of Figure 7.11. The measurement results show that even the DPPC solution without particles is a nonlinear system (Figure 7.11, b) because its THD values at all frequencies and amplitudes are more than 5%, which is considered as the limit of linearity [254]. The range of the THD values for the interfacial tension for DPPC solution without particles was 15.47%-50.20%.

The presence of ATD and RTD nanoparticles in the DPPC system (Figure 7.11, d and f) increases the THD values of the interfacial tension at all frequencies and amplitudes. The THD values for interfacial tension are in the range of 22.99%-113.45% and 30.18%-111.75% for ATD 0.01 wt % + DPPC and RTD 0.01 wt % + DPPC, respectively. These results clearly show that these nanoparticle-containing systems are also nonlinear because they do not fulfil the condition of $THD \leq 5\%$.

Based on the statistical parameters of the curve fitting mentioned in Section 7.1.1 (Table 7.1, Table 7.2, and Table 7.3) and the percentage of THD (more than 5%) for the DPPC solution without particles and the least concentration of the titanium dioxide nanoparticles, i.e., ATD and RTD, in the DPPC solutions, the systems in this study were considered as nonlinear systems. Therefore, the nonlinear approach was applied for these systems as well as higher concentrations of titanium dioxide nanoparticles in the DPPC. The details of the nonlinear approach and the methods of analysis will be provided in the next section.

7.1.3 Interfacial Rheology of Nanoparticles-DPPC Systems: Non-Linear Approach

For the nonlinear interfacial systems, measuring the viscoelastic (dilatational) modulus using only the first harmonic of Fourier transform would not be reliable. In fact, the first harmonic of Fourier transform is not advantageous, and it is incomprehensive to analyse the behaviour of viscoelastic interfacial systems

with nonlinearities. Therefore, other approaches, such as Lissajous plots [20], are used to describe the behaviour of such systems.

The Lissajous plots or Lissajous-Bowditch curves are used to represent the surface pressure (stress) against the deformation (strain) for studying the dilatational rheology, and for this purpose, the surface pressure versus deformation is plotted. The analysis of these plots can show intracycle strain thickening and thinning [20, 21, 255].

The surface pressure, π , of the air-liquid interface is defined as below:

$$\pi = \gamma - \gamma_{eq} \quad \text{Eq. 7-6}$$

where γ and γ_{eq} are interfacial tension as the response of system to the oscillation and equilibrium interfacial tension of the sample before oscillation, respectively.

The deformation of the surface area is defined as below:

$$\text{Deformation} = \Delta A / A_0 \quad \text{Eq. 7-7}$$

where ΔA is the changes of the surface area from the initial surface area during the oscillation, and A_0 is the equilibrium surface area.

This method can be used for higher amplitudes. In this study, the first and the last cycles of each individual oscillation were removed. Then, the Lissajous plots were obtained for the samples including DPPC without nanoparticles and DPPC with the dispersed titanium dioxide nanoparticles (both anatase and rutile crystal forms). The concentrations of nanoparticles were 0.01-0.05 wt %.

In each oscillation at a specific amplitude and frequency, the data related to the expansion (inhalation) and the compression (exhalation) were separated for each cycle. Then, the expansion data for all cycles were combined to obtain the best fitted curve. The same procedure was done for the compression data. An example of the Lissajous plot with the separated data for expansion and compression is shown in Figure 7.12.

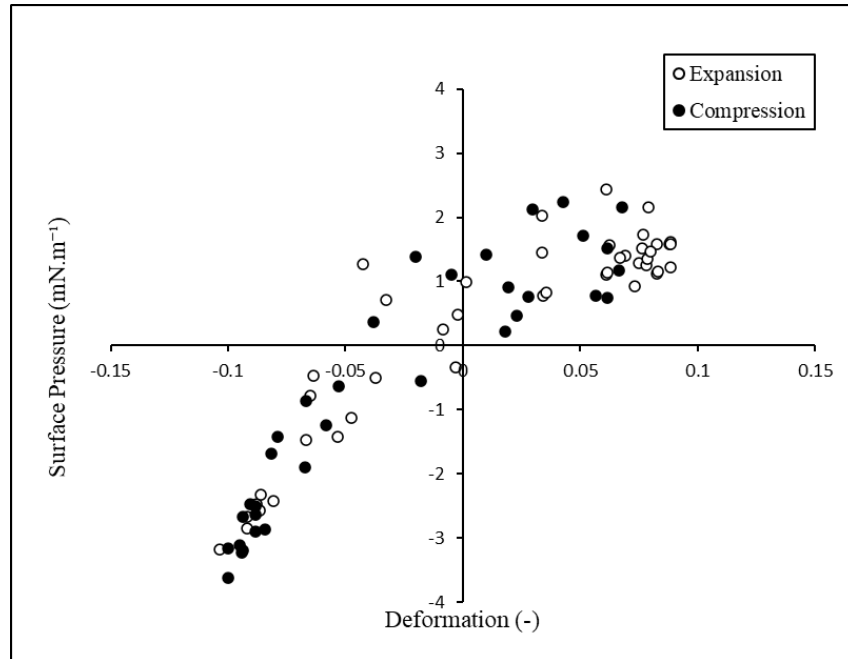


Figure 7.12 An example of the Lissajous plot for DPPC solution without particles at the amplitude of 10% and the frequency of 0.5 Hz. The hollow dots and filled dots are related to the expansion and compression, respectively.

It is noteworthy that there is no special rule about the locations of compression and expansion data around the minor and major axes of the proposed ellipse shape of the Lissajous plot. For example, in the interfaces covered by triterpenoid saponin Escin, the data above the major axis of the ellipse represents the compression and the data under this axis show the expansion [21]. In another system such as interfacial layers containing oligofructose fatty acid esters, the locations of compression and expansion data are in contrast to the previous case, i.e., expansion data are above and compression data are below the major axis [20]. In this study, the general trend was the same as the latter one for the lowest amplitude and frequency. However, the behaviours of the samples at various conditions were quite different from each other.

The raw data shown in Figure 7.12 need more processing for further analysis of the viscoelastic behaviours. To quantify the degree of the nonlinearity of the systems, a dimensionless index called strain-stiffening ratio, S , is defined as below [255]:

$$S \equiv \frac{G_L - G_M}{G_L} \quad \text{Eq. 7-8}$$

where G_L is the large strain modulus and G_M is the minimum strain modulus. It should be noted that, in a Lissajous plot, G_L is calculated as the slope of the secant at the maximum strain. G_M is calculated as the tangent slope at the zero strain [255]. In Eq. 7-8, the case of $S = 0$ represents the linear elastic response, $S > 0$ can be interpreted as intracycle strain stiffening, and $S < 0$ indicates the intracycle strain softening.

To measure the parameters in Eq. 7-8, a curve fitting for the raw data in the Lissajous plot (Figure 7.12) is required. This curve fitting was done for both the expansion and compression data, separately. Using the programme in the Microsoft Excel, a fourth order polynomial regression fit was performed for each expansion and compression part of the cycles. Examples of these fitted curves are shown in Figure 7.13. It should be noted that the fourth order polynomial curves fitted on expansion and compression parts of the cycles are not the representative of a physical or chemical model for the cycle and its viscoelasticity. These fourth order polynomial curves were only used to measure the strain-stiffening ratio which requires the large strain modulus (at the maximum strain at the end point of the curves) and the minimum strain modulus (at the zero-strain point) in each expansion and compression part of the cycle. In fact, the fourth order polynomial curves have been used only as a mathematical tool to measure the secant and tangent at the critical points of the cycle.

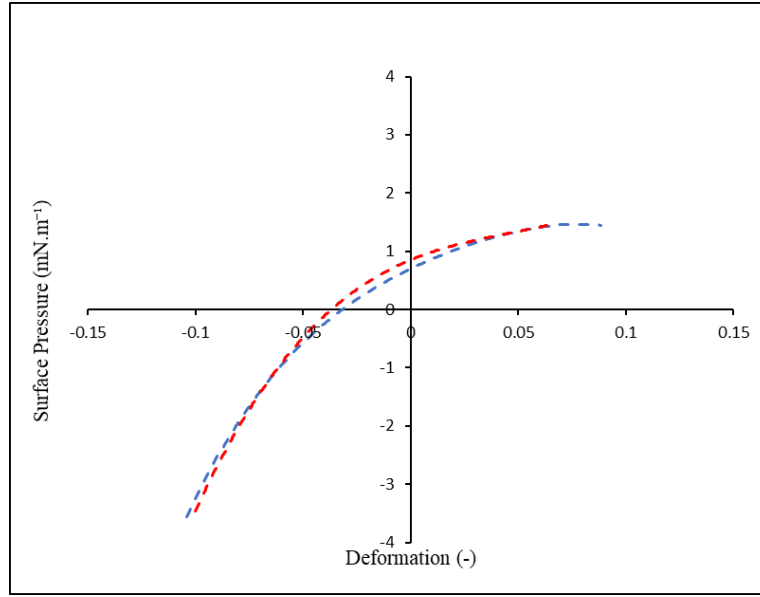


Figure 7.13 The fourth order polynomial curve fitted on the data of Lissajous plots for DPPC solution without particles at the amplitude of 10% and the frequency of 0.5 Hz. The blue and red dashed lines are related to the expansion and compression, respectively.

Using these two curves in Figure 7.13, the parameters in Eq. 7-8 can be calculated.

For the interfacial systems in this study, the expansion and compression responses are different (Figure 7.13). Therefore, two strain-stiffening ratios are defined as below:

$$S_{exp} \equiv \frac{E_{L,E} - E_{M,E}}{E_{L,E}} \quad \text{Eq. 7-9}$$

$$S_{com} \equiv \frac{E_{L,C} - E_{M,C}}{E_{L,C}} \quad \text{Eq. 7-10}$$

where S_{exp} and S_{com} are the strain-stiffening ratios for expansion and compression, respectively. In Eq. 7-9, $E_{L,E}$ is the large strain modulus in expansion and $E_{M,E}$ is the minimum strain modulus in expansion. In Eq. 7-10, $E_{L,C}$ is the large strain modulus in compression and $E_{M,C}$ is the minimum strain modulus in compression. Based on the amount of S_{exp} and S_{com} , the responses of the system during expansion and compression can be quantitatively analysed [20].

In this study, the strain-stiffening ratios of expansion and compression were obtained for the DPPC solutions without particles and with titanium dioxide nanoparticles (both anatase and rutile crystal forms) at different concentrations. The results of the quantitative and qualitative analysis of the interfacial rheology of these systems will be discussed in the next sections.

7.1.4 Interfacial Rheology of DPPC Solution without Nanoparticles

The raw data of the Lissajous plots for the DPPC solution without particles are shown in Figure 7.14 (Part 1 and Part 2). Each row represents a constant amplitude at various frequencies and each column shows a constant frequency at variable amplitudes.

At the lowest amplitudes, i.e., 1% and 2%, the scattered raw data cause some difficulties to strongly conclude the status of the system in terms of the linearity or nonlinearity. However, at higher amplitudes, i.e., 5% and 10%, the asymmetric shape of the data distribution clearly shows significantly nonlinear behaviours of the systems. For example, at the amplitude of 10% and frequency of 0.1 Hz (Figure 7.14, m), when the deformation (x-axis) is changed from -0.098 to 0.094, the surface pressure is changed from -3.148 mN.m^{-1} to 2.418 mN.m^{-1} which is an asymmetric range considering the point of (0, 0) as the centre of symmetry.

Figure 7.14 also shows that at higher amplitudes, i.e., 5% and 10%, the data points become less scattered. This statement cannot be obtained in the highest frequency of 0.5 Hz (Figure 7.14, l and p). As mentioned before, it might be because of lack of enough data points recorded by PAT for 5 cycles at higher frequencies. The raw data presented in Figure 7.14 show that the surface pressure versus deformation data for expansion (hollow dots) and compression (filled dots) become closer and more like each other at higher amplitudes, i.e., 5% and 10%. This confirms the less phase differences at higher amplitudes, as previously mentioned in Figure 7.8, a.

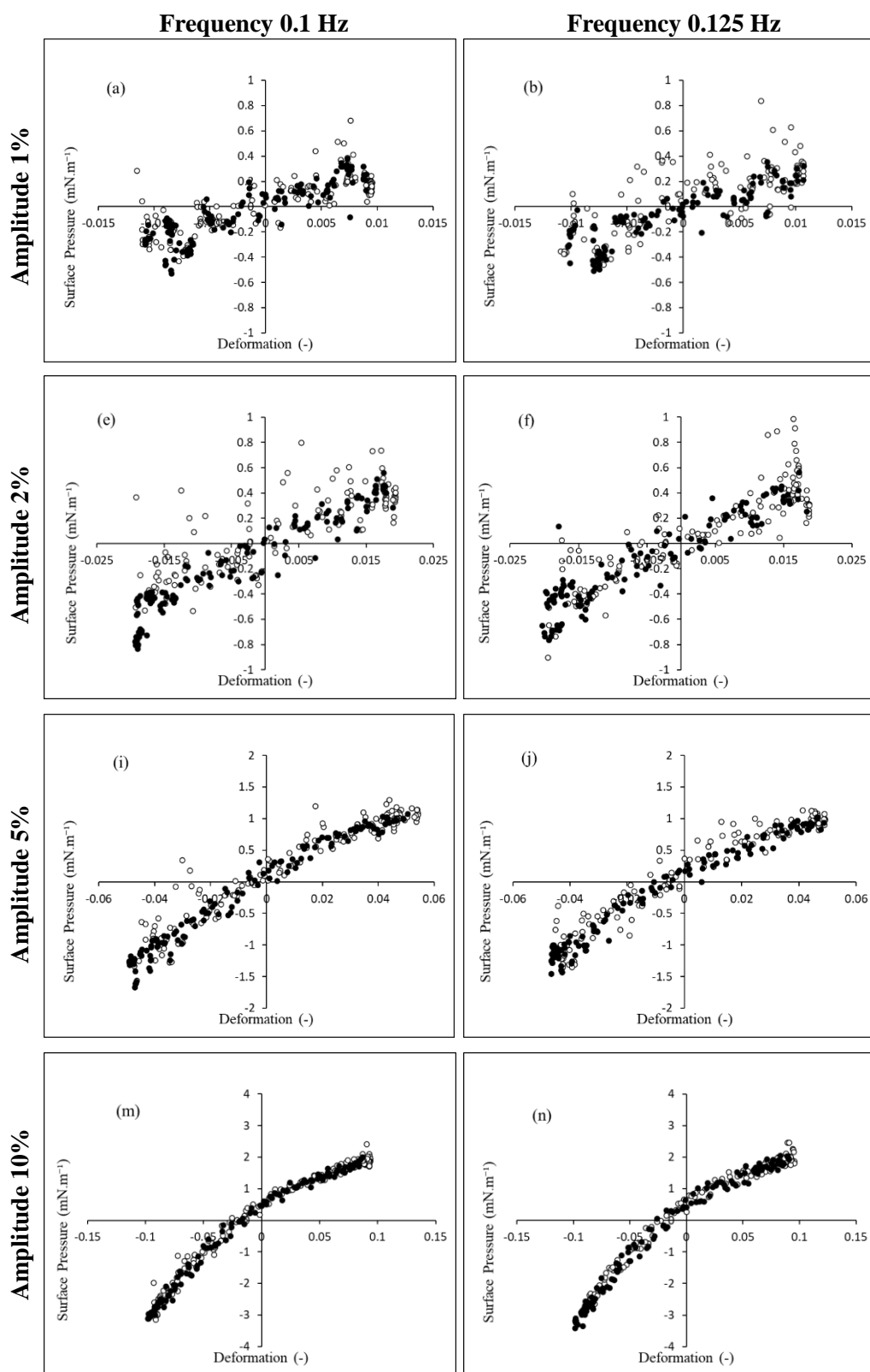


Figure 7.14 Part 1 Lissajous plots for DPPC solution without particles at the amplitudes of 1% (a-b), 2% (e-f), 5% (i-j), and 10% (m-n). The data were obtained for all frequencies including 0.1 Hz (left column) and 0.125 Hz (right column). The hollow dots and filled dots are related to the expansion and compression, respectively.

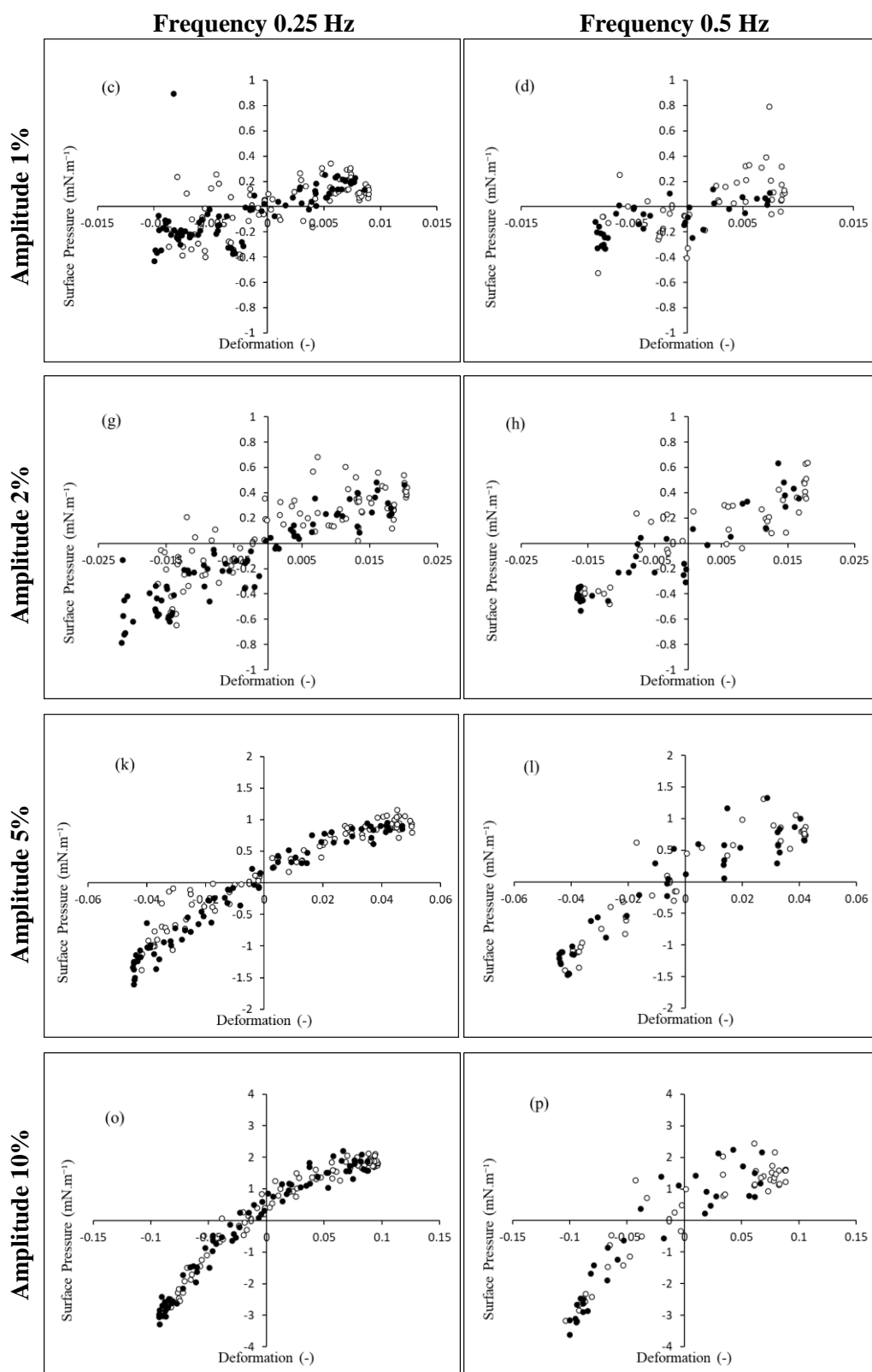


Figure 7.14 Part 2 Lissajous plots for DPPC solution without particles at the amplitudes of 1% (c-d), 2% (g-h), 5% (k-l), and 10% (o-p). The data were obtained for all frequencies including 0.25 Hz (left column) and 0.5 Hz (right column). The hollow dots and filled dots are related to the expansion and compression, respectively.

To measure the strain-stiffening ratio, i.e., S -factor, and to analyse the intracycle behaviour of the DPPC system without particles, the curve fitting of the raw data points was conducted, and the results are shown in Figure 7.15.

In Figure 7.15, the blue and red dashed lines are corresponding to the expansion and compression results, respectively. These fourth order polynomial curves fitted for the raw data of the Lissajous plots for the DPPC solution without particles show the interfacial behaviours of these systems. The values of the R-squared of these fitted curves are all larger than or equal to 0.8 for both expansion and compression cases at most amplitudes and frequencies. The only exceptions are related to the fitted curves for expansion and compression related to the least amplitude, i.e., 1%, in which the R-squared values were in the range of 0.4-0.6.

Figure 7.15 shows that the system becomes more elastic by increasing the amplitude. Figure 7.15 also depicts that the expansion is more sensitive toward frequency sweeps at a constant amplitude because the shape of the expansion curve changes significantly upon changes of frequency (Figure 7.15, a-d and e-h). This frequency dependence behaviour indicates that the migration of the DPPC molecules from the bulk to the interface and vice a versa is not slow, meaning that the system with all its constituents quickly respond to the changes of frequency [20]. This frequency dependence decreases at the higher amplitudes, i.e., 5% and 10% (Figure 7.15, i-l and m-p).

From Figure 7.15, at all amplitudes, the slope of the expansion plots decreases which indicates the strain softening at each specific frequency for the samples of DPPC solution without nanoparticles. There is no clear trend of the intracycle behaviour of the expansion curve at the frequency of 0.5 Hz, especially at the lowest amplitudes, i.e., 1% and 2% (Figure 7.15, d and h). In fact, the slopes of the expansion curve could be increased and decreased at different points which means that the strain softening, and strain stiffening are happening constantly.

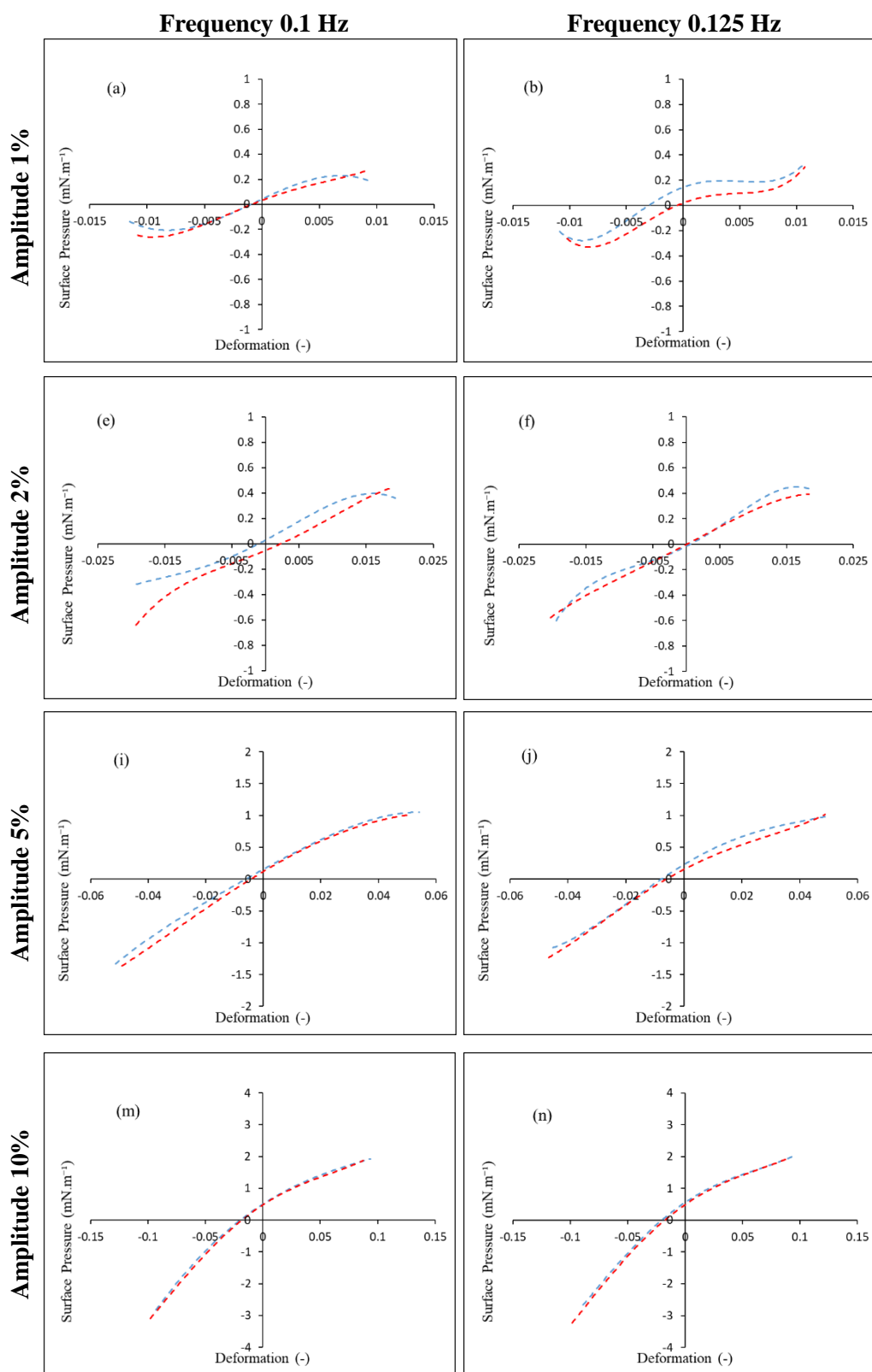


Figure 7.15 Part 1 The fourth order polynomial curve fitted on the data of Lissajous plots for DPPC solution without particles at the amplitudes of 1% (a-b), 2% (e-f), 5% (i-j), and 10% (m-n). The data were obtained for all frequencies including 0.1 Hz (left column) and 0.125 Hz (right column). The blue and red dashed lines are related to the expansion and compression, respectively.

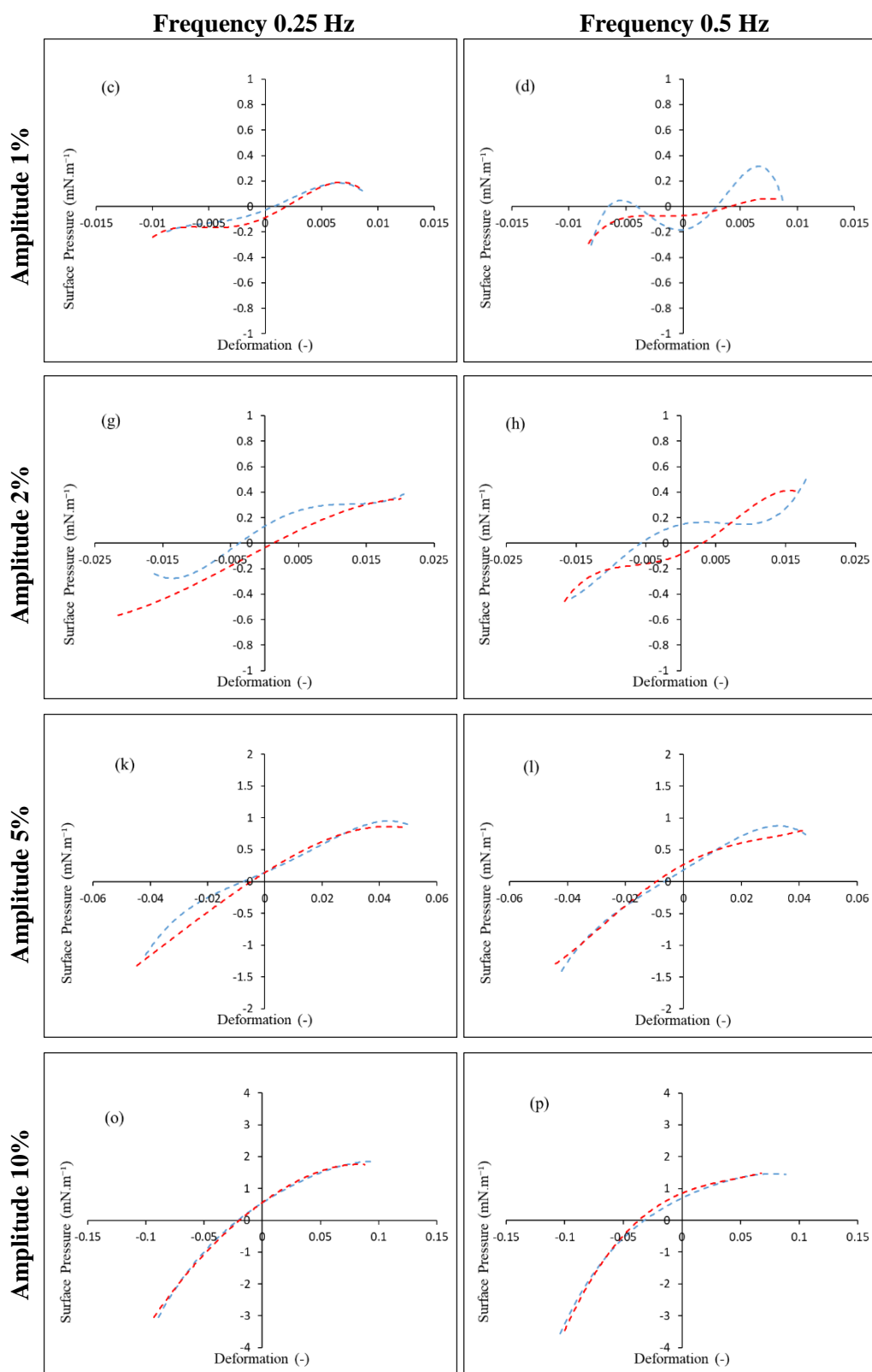


Figure 7.15 Part 2 The fourth order polynomial curve fitted on the data of Lissajous plots for DPPC solution without particles at the amplitudes of 1% (c-d), 2% (g-h), 5% (k-l), and 10% (o-p). The data were obtained for all frequencies including 0.25 Hz (left column) and 0.5 Hz (right column). The blue and red dashed lines are related to the expansion and compression, respectively.

For compression results, the frequency dependence is less apparent than that for the expansion ones. Except for the case for the amplitude of 1% (Figure 7.15, a-d), the compression curves have much weaker frequency dependence. Moreover, in most cases, the slope of the compression curve is increasing meaning that the strain stiffening is happening in each individual amplitude and frequency. The weak frequency dependence and strain stiffening can be attributed to that liquid condensed (LC) domains are formed upon the compression of the DPPC monolayer at the air-liquid interface [127].

In addition to the qualitative descriptions of the fitting curves on the data of Lissajous plots for DPPC solution without particles, the strain-stiffening ratios (or often called S-factor) of this solution at different amplitudes and frequencies were measured, and the results are shown in Figure 7.16. The the S-factor for expansion is mostly negative which indicates that the strain softening occurs, whereas that for the compression case is mostly positive which indicates the strain stiffening occurs.

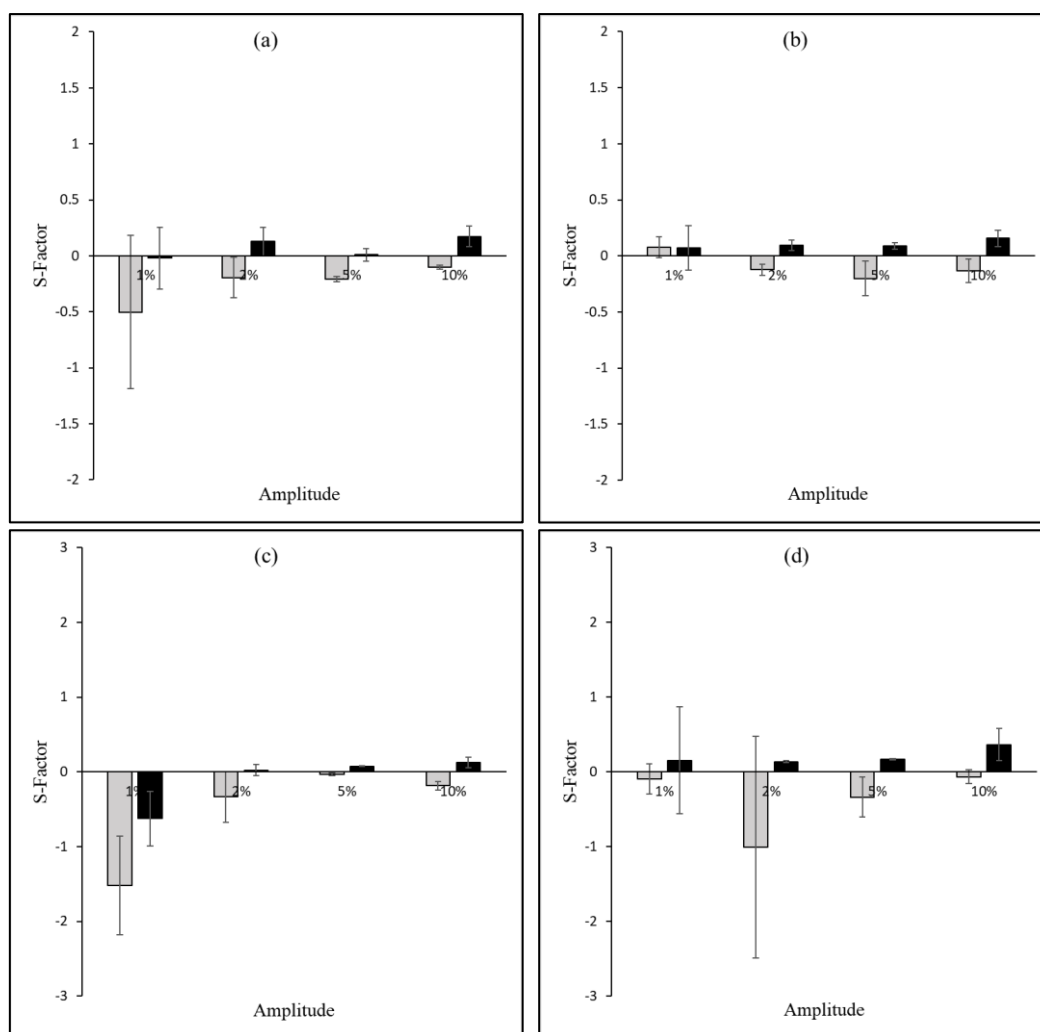


Figure 7.16 The S-factor of Lissajous plots for DPPC solution without particles at various amplitudes for the frequencies of 0.1 Hz (a), 0.125 Hz (b), 0.25 Hz (c), and 0.5 Hz (d). The grey and black colours are related to the expansion and compression, respectively.

After studying the microstructures of the air-liquid interface for the presence of DPPC molecules under oscillation, the same procedure of data analysis was done for DPPC solution with nanoparticles. The results (shown in the next section) will be used to explain the mechanism of the interactions between nanoparticles and DPPC under oscillation.

7.1.5 Mechanism of the Interactions between Nanoparticles and DPPC under Sinusoidal Perturbations

Previous studies have shown that the shape of the pressure-volume loop in the lung can be altered because of the different diseases such as acute respiratory distress syndrome (ARDS), fibrosis, emphysema as one of the chronic obstructive pulmonary diseases (COPD), and asthma [169, 256-258]. The respiratory failures caused by COVID-19 virus can also be considered as ARDS which changes the pressure-volume curves [259]. As shown in Figure 7.17, the hysteresis area for the healthy lungs is different from those of emphysematous and fibrotic lungs.

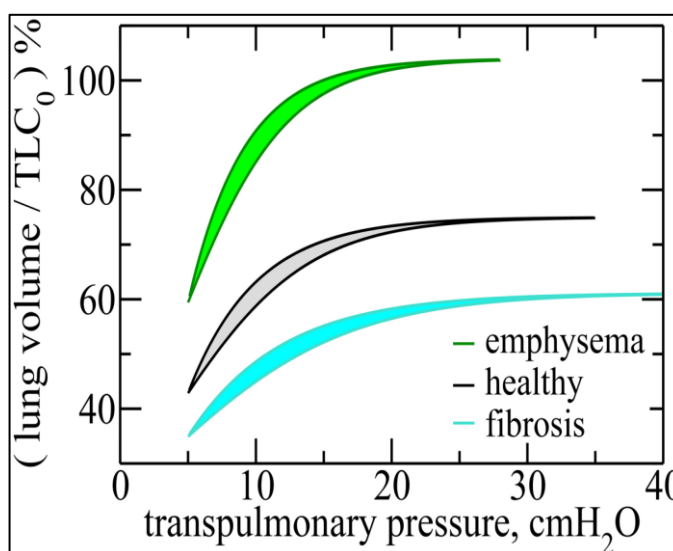


Figure 7.17 Pressure-volume curve for healthy lungs, emphysematous, and fibrotic lungs [257].

Some of the mentioned diseases such as emphysema which cause the change in the pressure-volume hysteresis are developed or worsened by long-term exposure to air pollution and PM_{2.5} [44, 260, 261]. Because of the effects of air pollutants and particulate matter (PM) on the development of these diseases and the impact of these diseases on the hysteresis of pressure-volume curves, it becomes important to study the effects of air pollutants on the hysteresis of the pressure-volume curves. As mentioned in Section 7.1.1.2, one of the factors

affecting the hysteresis of the pressure-volume curve (Figure 7.6) is the interfacial tension hysteresis induced by the lung surfactant. Therefore, the study of the interfacial tension hysteresis of the lung surfactant in presence of air pollutants is of a great importance.

This interfacial tension hysteresis was clearly observed in the Lissajous plots related to the DPPC - one of the most significant components of the lung surfactant - solution without particles (Figure 7.14 and Figure 7.15). To understand the effect of nanosized pollutants, the oscillation experiments were conducted on the dispersions of ATD+DPPC, RTD+DPPC, and CNT+DPPC with five different concentrations. The oscillation experiments were also conducted on the mixtures of nanoparticles at the concentration of 0.01 wt %.

7.1.5.1 Titanium Dioxide Nanoparticles: ATD and RTD

The Lissajous plots and the fitted curves for the samples of ATD+DPPC and RTD+DPPC are presented in **Appendix C**. Due to the presence of nanoparticles in the systems, it was observed that the reproducibility of the curve fitting and, consequently, obtaining the exact values of S-factor, were not simple. Therefore, to define a general method of analysis, the R-squared values of the fitted curves were considered as the criteria of the reliability of the curve fitting. For each individual cycle at a specific amplitude and frequency, the R-squared values of the fitted curves for both expansion and compression cases were measured. Based on the data of the R-squared values, the reliability of the fitted curves was ranked in the form of a colour mapping (as shown in Figure 7.18).

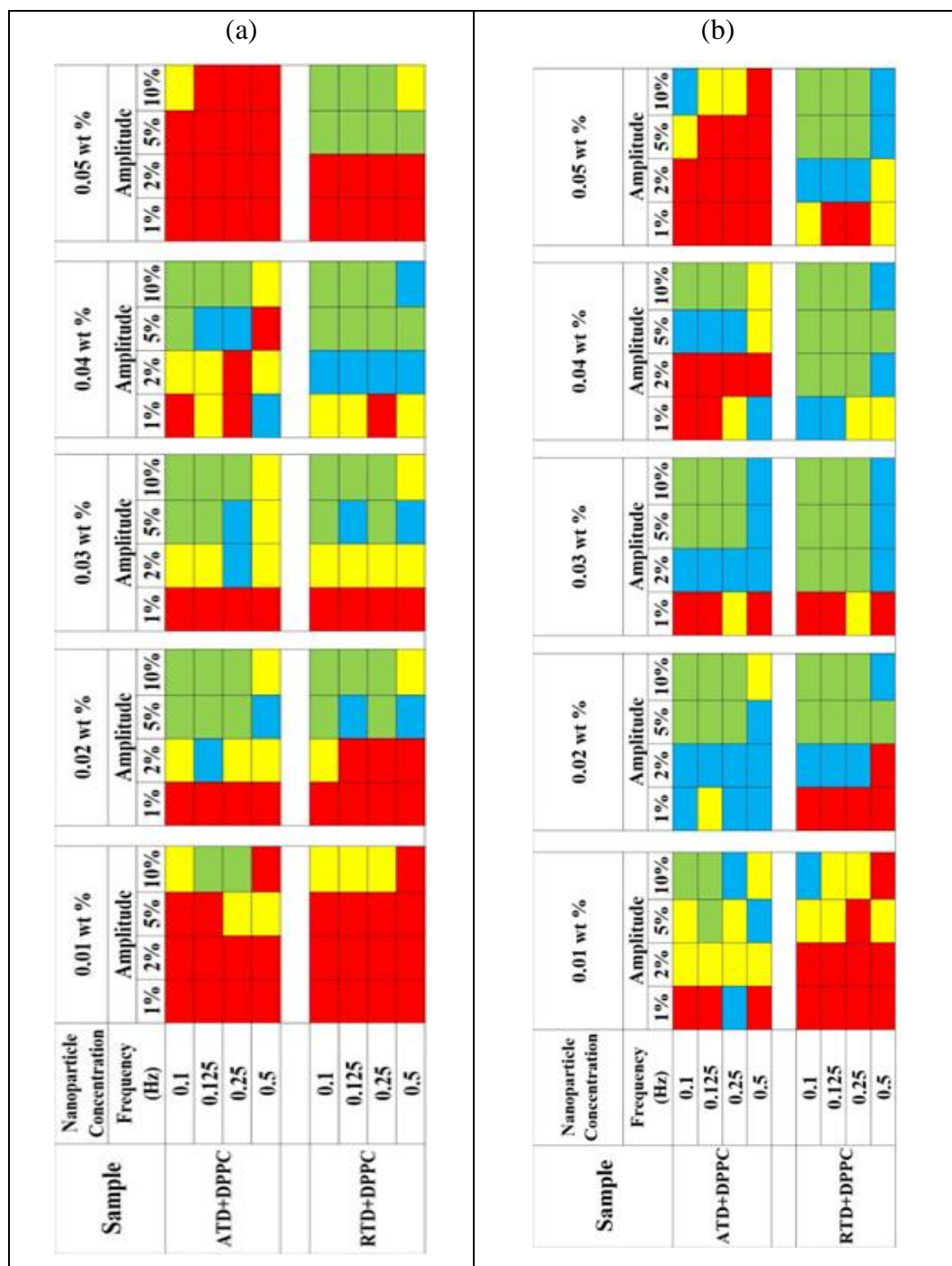


Figure 7.18 Colour maps related to the R-squared values of the fourth order polynomial curve fitted on the data of Lissajous plots for ATD+DPPC and RTD+DPPC with different concentrations during expansion (a) and compression (b). The red, yellow, blue, and green colours are the representative of the R-squared values in the ranges of 0-0.4, 0.4-0.6, 0.6-0.8, and 0.8-1, respectively.

For the R-squared values ≥ 0.8 , the fitted curves were presented as green. For $0.6 \leq R\text{-squared} \leq 0.8$, the assigned colour was blue. For $0.4 \leq R\text{-squared} \leq 0.6$ and $R\text{-squared} \leq 0.4$, the colours were yellow and red, respectively. Figure 7.18

summarises the measured and coded colour for the R-squared values of all the oscillation cycles at different concentrations of nanoparticles in the system.

Figure 7.18 clearly shows that the R-squared values of the fitted curves depend on the operational factors such as amplitude, frequency, and the status of compression or expansion during oscillations. In addition to these operational factors, the composition of the system also affects the R-squared values of the fitted curves. For example, at the same frequency and amplitude, the values of R-squared for the system containing ATD nanoparticles are different from those of RTD nanoparticles. Although both of ATD and RTD nanoparticle are known as the inorganic compounds called titanium dioxide, Figure 7.18 shows that, even at equal concentration of nanoparticles, there are differences between them in the interfacial systems containing DPPC. This is mainly attributed to the differences between these two types of titanium dioxide nanoparticles in the stabilisation of the air-liquid interface.

At the amplitude of 1%, regardless of the frequency values, all the systems show small R-squared values. This might be due to noises and scattered data. In case of ATD+DPPC system, the R-squared values of expansion and compression are almost the same. At the lowest concentration of ATD nanoparticles, i.e., 0.01 wt %, the R-squared values of both expansion and compression cases are very low. With increasing the concentration of nanoparticles by 0.03 wt %, the reliability of the R-squared values for both expansion and compression cases is improved (e.g., showing more green and blue colours). At the concentration of 0.04 wt %, the number of the green colour cells as the indicator of the reliable R-squared values decreases. Reaching the concentration of 0.05 wt %, the ATD+DPPC system shows the worst behaviour in terms of the R-squared values of the fitted curves because all the R-squared values are very small and mostly less than 0.4 (red colour in Figure 7.18).

For the RTD+DPPC system, there are noticeable differences between expansion and compression cases. The R-squared values for fitted curves on the compression data are more reliable (more green and blue cells). Figure 7.18 also shows that, with the increase of the concentration of RTD nanoparticles from 0.02 wt % to 0.04 wt %, the R-squared values are increased. Moreover, for the RTD+DPPC system, the number of reliable R-squared values (higher than 0.6

shown as green and blue colours) at the highest concentration, i.e., 0.05 wt %, is more than that of ATD+DPPC system.

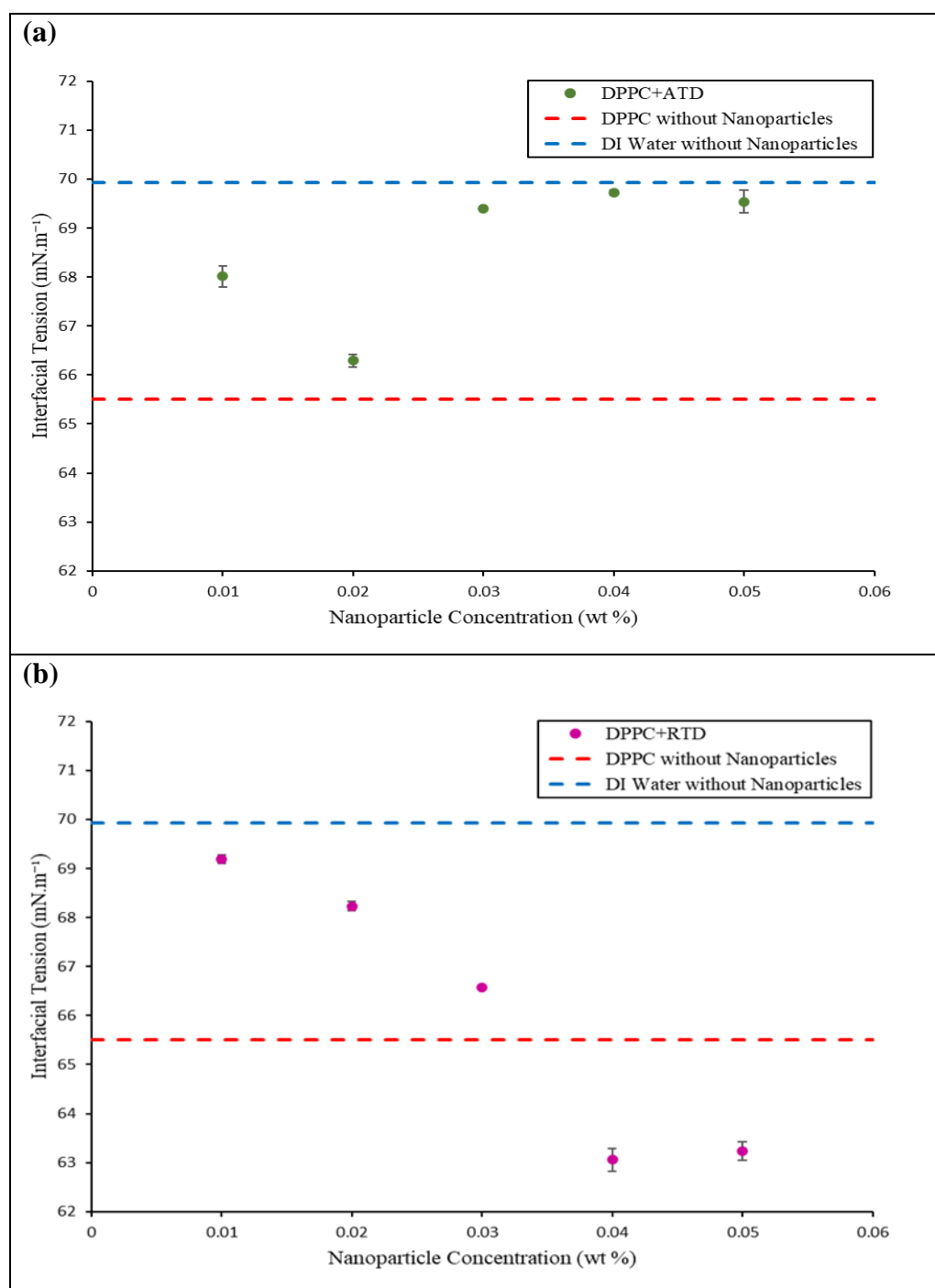


Figure 7.19 Equilibrium interfacial tension of the dispersions of ATD nanoparticles (a) and RTD nanoparticles (b) in the DPPC solutions against the concentration of nanoparticles at 37°C. The concentration of DPPC in the solution is constant. The blue and red dashed lines are the representative of the interfacial tension of DI water without DPPC and with DPPC, respectively.

The different behaviours of the ATD and RTD nanoparticles can be attributed to their different mechanism of interactions with DPPC which, in turn, results in diverse structures of the air-liquid interfaces and different values of equilibrium interfacial tension. Figure 7.19, which is a repeated figure from Chapter 6, has been used here, in order to compare the differences. Based on Figure 7.19, it can be assumed that the RTD nanoparticles are adsorbed at the air-liquid interface and thus decrease the interfacial tension. Therefore, these particles are stabilising the air-liquid interface. This might be the reason why the oscillation data related to RTD+DPPC system show more reliable R-squared values at higher concentrations.

Based on the R-squared values of the fitted curves, the most representative and reliable results related to the systems containing nanoparticles are then compared to those of without using nanoparticles, i.e., the DPPC solution. Figure 7.20 compares the Lissajous plots and fitted curves of the DPPC solution without particles (a-b) with the least concentration (0.01 wt %) of ATD (c-d) and RTD nanoparticles (e-f) at the amplitude of 1% and the frequency of 0.1 Hz. As can be seen from the colour maps shown in Figure 7.18, the curve fitting and S-factor measurement for this concentration of nanoparticles are not correct. However, the data points represent the changes of DPPC system in presence of nanoparticles. As shown in Figure 7.20, c, adding the ATD nanoparticles with a concentration of 0.01 wt % to the DPPC solution significantly affects the expansion part of the cycle as the expansion data are becoming more scattered. However, the RTD nanoparticles affect both expansion and compression parts. Although the shape of the system disturbance is not reproducible, this data scattering phenomenon clearly shows that the normal interfacial hysteresis of the DPPC system (Figure 7.20, b) is changed when the nanoparticles are present in the system (Figure 7.20, d and f). In the presence of nanoparticles, the loss angle or the phase difference is increasing which indicates that the interfacial system becomes more viscous. This means that the system with nanoparticles becomes more dissipative and irreversible during the oscillation which simulates the breathing cycle [129].

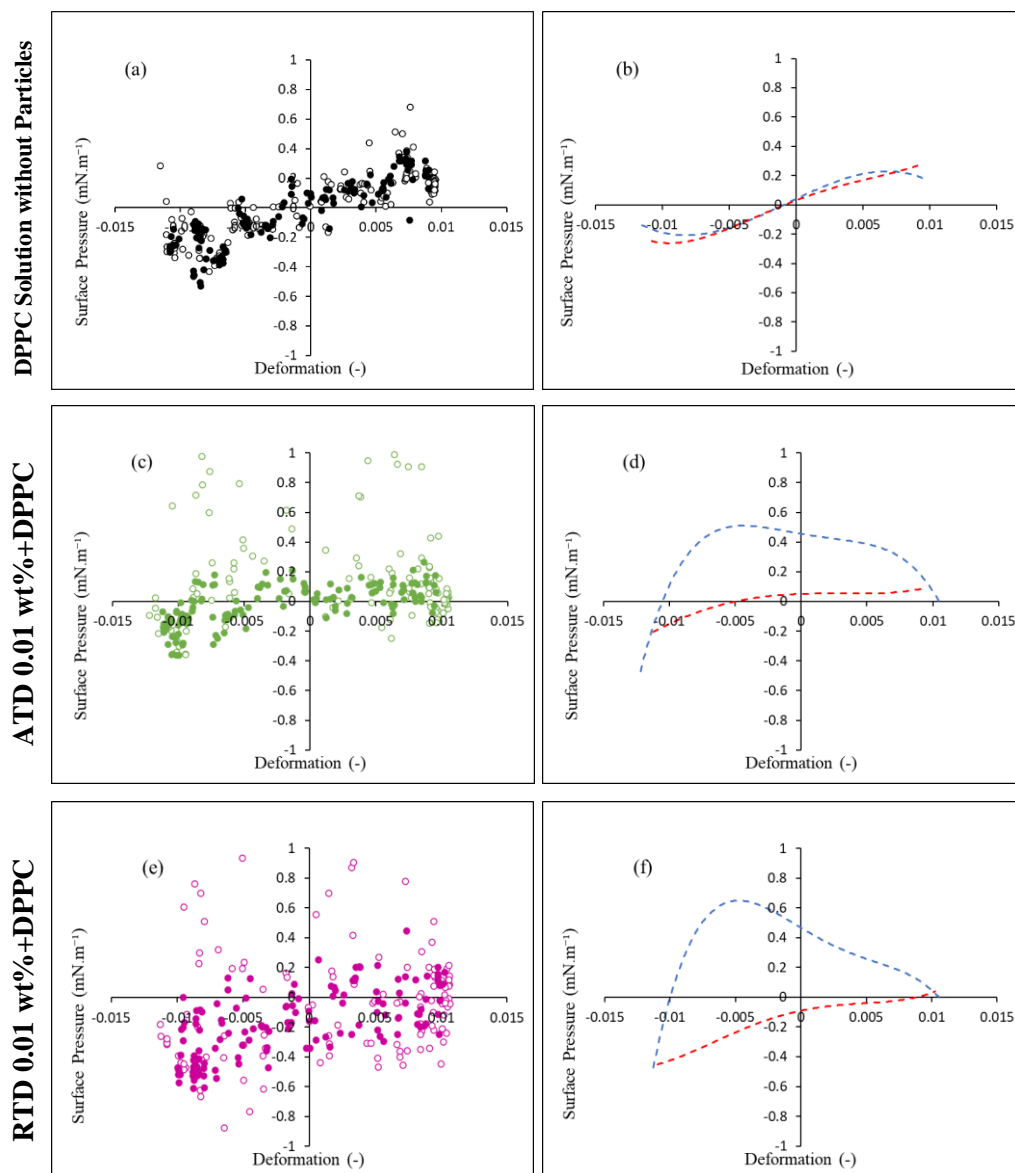


Figure 7.20 Lissajous plots and the fourth order polynomial curve fitted on the data of Lissajous plots for DPPC solution without particles (a-b), ATD 0.01 wt%+DPPC (c-d), and RTD 0.01 wt%+DPPC (e-f) at the amplitude of 1% and the frequency of 0.1 Hz. The hollow dots and filled dots are related to the expansion and compression, respectively. The blue and red dashed lines are related to the expansion and compression, respectively.

At the concentration of 0.01 wt % of nanoparticles, the values of S-factor are not reliable due to the low values of R-squared of the fitted curves. For the ATD and RTD samples with concentrations of 0.02, 0.03, and 0.04 wt %, only the S-factors related to the amplitudes of 5% and 10% are compared because the R-squared values of the fitted curves are considered acceptable at these amplitudes (i.e., the blue and green cells in Figure 7.18). The results of the S-factor

measurements for both the ATD+DPPC and RTD+DPPC systems at the three different concentrations are shown in Figure 7.21 and Figure 7.22, respectively.

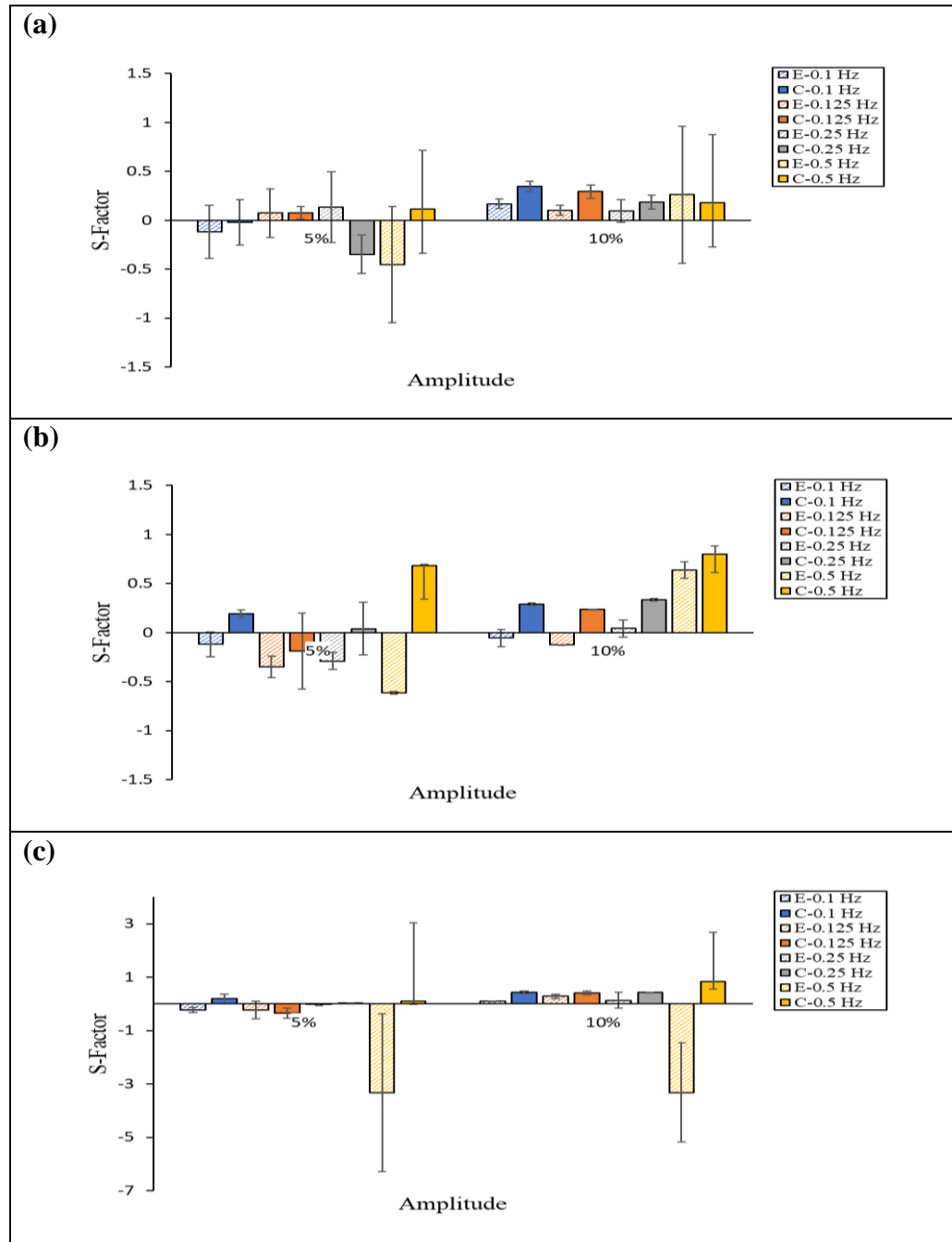


Figure 7.21 The S-factor of Lissajous plots for ATD+DPPC dispersion with the nanoparticle concentrations of (a) 0.02 wt%, (b) 0.03 wt%, and (c) 0.04 wt% at various amplitudes. Blue, orange, grey, and yellow colours represent the frequencies of 0.1, 0.125, 0.25, and 0.5 Hz, respectively. The patterned and non-patterned columns are related to the expansion and compression at each frequency, respectively.

As shown in Figure 7.21, the S-factor related to the expansion at the amplitude of 5% is mainly negative except for the concentration of 0.03 wt % of the nanoparticles at the frequencies of 0.125 Hz and 0.25 Hz. A general conclusion is that, for the ATD+DPPC dispersions with the concentration of nanoparticles between 0.02 wt % and 0.04 wt %, the strain softening occurs during the expansion case at the amplitude of 5%. At the same amplitude, the S-factors for the compression cases are mainly positive, although there are some exceptions such as the frequency of 0.125 Hz for both ATD 0.03 wt % and ATD 0.04 wt %. These positive values of the S-factors indicate the strain stiffening occurred during the compression.

The values of the S-factor at the amplitude of 10% are mainly positive for both expansion and compression cases. This means that the strain stiffening occurs during both expansion and compression parts of the oscillation. This might be due to the higher gradient of concentration caused by larger changes of surface areas during the oscillation at the amplitude of 10%. Due to this larger gradient (based on the Fick's First Law of diffusion), the diffusion flux of the nanoparticles to different areas such as air-liquid interface may increase. This results in the accumulation of the particles at the interface, thus causing the rigidity and stiffening.

It should be noted that the Lissajous plots of these medium concentrations of ATD nanoparticles also show that these systems are more viscous than the DPPC solution without particles. This means that these systems are dissipative and irreversible in terms of the energy. Moreover, regardless of amplitude and frequency, the domains of stress or surface pressure of the systems containing ATD nanoparticles are much less than those of DPPC solutions without nanoparticles (See figures of Lissajous plots and fitted curves in **Appendix C**). Moreover, this more viscous behaviour of the system of ATD+DPPC can be attributed to the DPPC depletion in the systems containing ATD nanoparticles at the concentrations of 0.02 wt %, 0.03 wt %, and 0.04 wt %, which was previously explained in Chapter 6 and shown in Figure 7.19, a.

Figure 7.22 shows the S-factor measurements for RTD+DPPC systems at the concentrations of 0.02 wt %, 0.03 wt %, and 0.04 wt %.

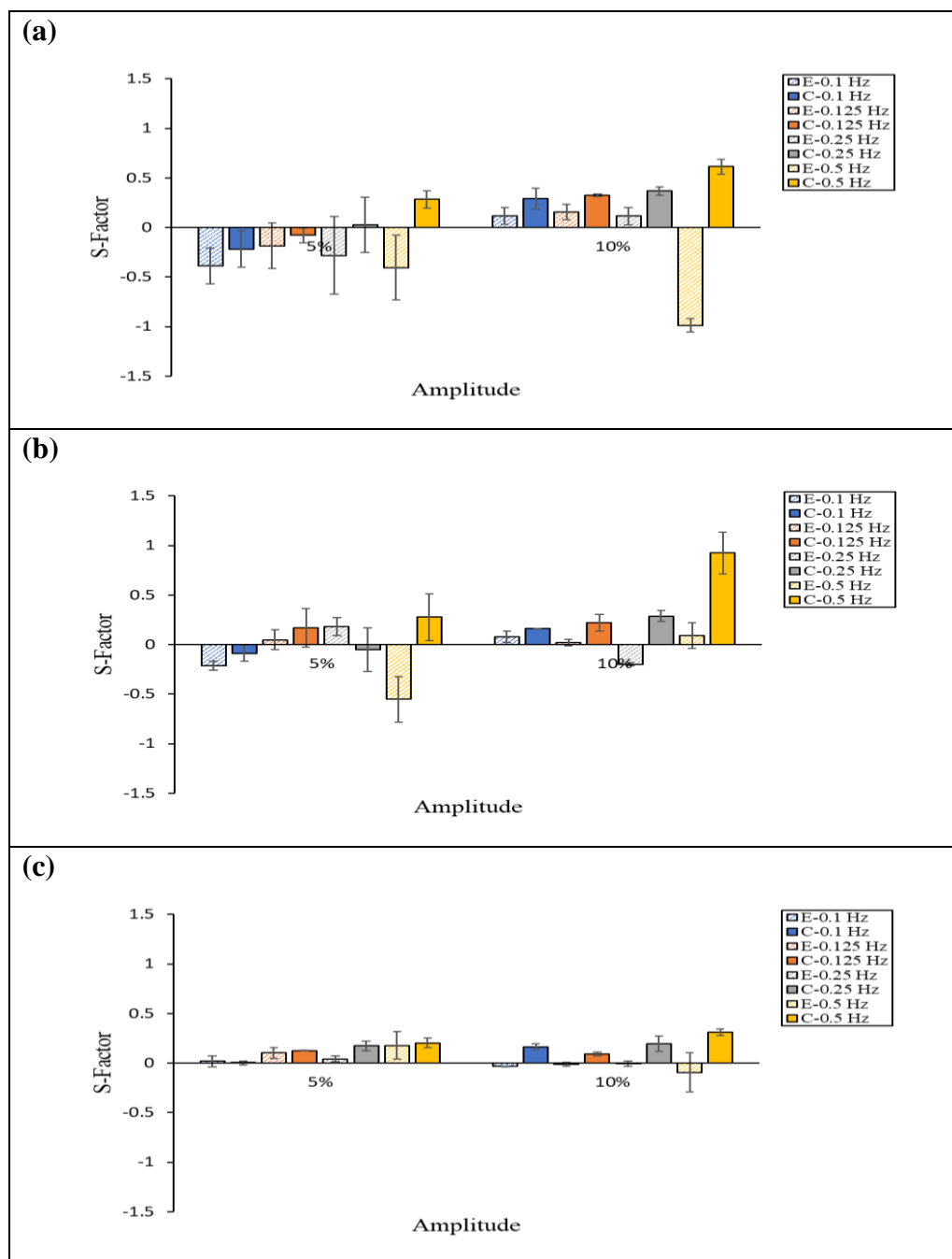


Figure 7.22 The S-factor of Lissajous plots for RTD+DPPC dispersion with the nanoparticle concentrations of (a) 0.02 wt%, (b) 0.03 wt%, and (c) 0.04 wt% at various amplitudes. Blue, orange, grey, and yellow colours represent the frequencies of 0.1, 0.125, 0.25, and 0.5 Hz, respectively. The patterned and non-patterned columns are related to the expansion and compression at each frequency, respectively.

The results of the S-factors for RTD+DPPC system with the concentrations of 0.02 wt % (Figure 7.22, a) and 0.03 wt % (Figure 7.22, b) are approximately similar to those of ATD+DPPC (Figure 7.21, a and b). At the amplitude of 5%,

the S-factor values of expansion stage are mainly negative showing the strain softening effect, whereas the S-factor values for compression are normally positive indicating the strain stiffening effect. However, there are some exceptions such as positive S-factor of expansion at the frequencies of 0.125 Hz and 0.25 Hz at the concentration of 0.03 wt %, or negative S-factor of compression at the frequency of 0.125 Hz for the concentration of 0.02 wt %.

For the concentrations of 0.02 wt % and 0.03 wt %, the S-factor of the RTD+DPPC at the amplitude of 10% is similar to that of ATD+DPPC system. As shown in Figure 7.22, a and b, the S-factor values for both expansion and compression are mostly positive showing the strain stiffening occurred. This can also be attributed to the large gradient of the concentration of nanoparticles between the bulk and the air-liquid interface at higher amplitudes. There is a flux of particles from the bulk to the interface which causes the accumulation of nanoparticles at the interface and thus its stiffening effects during both expansion and compression stages.

At the concentration of 0.04 wt % of RTD nanoparticles, the situation is totally different. At this concentration and the amplitude of 5%, all the S-factor values related to expansion and compression stages are positive which indicates the occurrence of strain stiffening. Comparing with Figure 7.19, the equilibrium interfacial tension of the RTD 0.04 wt %+DPPC shows that the nanoparticles previously interacted with DPPC molecules are being adsorbed onto the air-liquid interface. Therefore, the strain stiffening is attributed to the presence of solid RTD nanoparticles decorated with DPPC at the air-liquid interface.

At the amplitude of 10%, the S-factor during the expansion of RTD 0.04 wt %+DPPC system is slightly negative. These small negative values can either be considered as an indication of linear system or attributed to the flux of those previously adsorbed nanoparticles at the air-liquid interface to the bulk during the expansion.

The Lissajous plots of the RTD 0.04 wt %+DPPC also shows that this system is as elastic as DPPC system at the amplitude of 10% as shown in Figures C.17 and C.18 in **Appendix C**. Moreover, the loss angle of the RTD 0.04 wt %+DPPC system at the amplitude of 5% is less than that of DPPC solution at the same amplitude which means that the air-liquid interface stabilised by RTD

nanoparticles (previously interacted with DPPC) is more elastic than the air-liquid interface covered only by DPPC molecules. However, the domain of the stress or surface pressure for the RTD 0.04 wt % +DPPC systems is still less than DPPC solution without nanoparticles.

Combining the results from Figure 7.21 and Figure 7.22, as well as the equilibrium interfacial tension of the related systems (Figure 7.19), it can be concluded that the configuration of the air-liquid interface affects the surface oscillation responses. In fact, the air-liquid interfaces stabilised by nanoparticles show a completely different behaviour of the air-liquid interfaces without nanoparticles where only DPPC molecules are present in the system. These results are all related to one inorganic compound, TiO_2 , with two different crystal forms, i.e., anatase and rutile. This also indicates that different shapes and surface characteristics of nanoparticles lead to diverse effects on the DPPC solution at dynamic conditions of oscillation. Both types of TiO_2 nanoparticles cause disturbances in the normal performance of DPPC system. They change the loss angle which means that interfacial tension hysteresis is changed. The change of the interfacial tension hysteresis pattern in human lung is one of the signs attributed to different diseases such as emphysema and fibrotic lungs (Figure 7.17). Therefore, presence of TiO_2 nanoparticles in the system containing the lung surfactant under the dynamic conditions of breathing cycle have the similar effects as lung diseases. More *in vivo* and *in vitro* studies are required to conclude which crystal forms of TiO_2 nanoparticles are more dangerous.

7.1.5.2 Carbon Nanotubes

The oscillation experiments for the CNT 0.01 wt % +DPPC were not successful. Figure 7.23 shows that the collapse of the surface area occurs immediately when the oscillation starts at the time of 2500 s. At higher amplitudes, the PAT system is still not able to cope with the proper compression as the lower limit of surface area does not reach the correct lower limit in the oscillation.

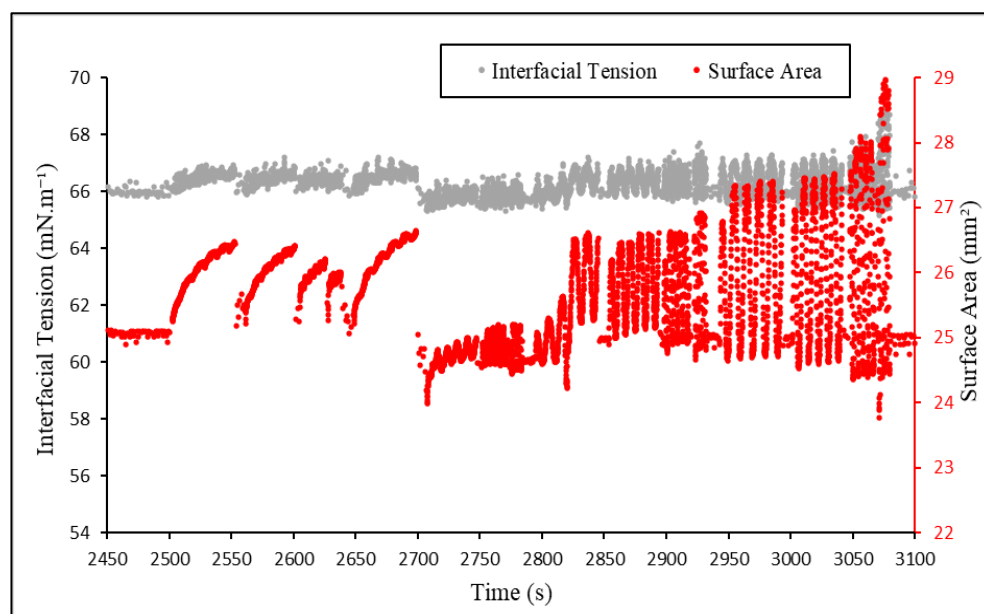


Figure 7.23 The dynamic interfacial tension and surface area vs. time for CNT 0.01 wt%+DPPC during oscillation. Red and grey dots correspond to the surface area and interfacial tension, respectively.

In the data recorder with PAT, it was seen that the total injection of the CNT 0.01 wt % +DPPC from the syringe of the equipment becomes more negative until the value of the total injection reaches -471 mm^3 by the start of oscillation. This might be due to the weight of nanoparticle and their agglomerates which results in their accumulation at the interface and also a constant change of the profile of the system. Moreover, these agglomerates of particles are carried with the liquid due to their partial wettability and porous structure. This can also change the profile of the system. Therefore, to avoid any change in the surface area before oscillation, the system was operated in negative injection condition (based on the recorded data from the PAT equipment). These negative injection values do not show any problem during equilibrium. However, this negative injection causes the failure of PAT system, especially during compression stage. It should be noted that the average profile error of this system (recorded by the PAT equipment's software) during the whole duration of measurement was 3.18 microns whereas the average of this error was 1.72 microns and 1.46 microns for ATD 0.01 wt % +DPPC and RTD 0.01 wt % +DPPC systems, respectively.

According to this unusual behaviour of the system for CNT 0.01 wt % +DPPC, the analysis of the Lissajous plots was not conducted for this system as the results could not be interpreted correctly.

At higher concentrations of CNT particles, i.e., 0.02-0.05 wt %, this error of the surface area change was not observed. However, as mentioned in Chapter 6, the results were not reproducible, and only one out of three repeats of the experiments could reach the equilibrium.

7.1.5.3 Mixture of Nanoparticles

In case of the mixture of nanoparticles with the concentration of 0.01 wt % of nanoparticles in the DPPC solutions, the behaviour of the systems was similar to that of CNT 0.01 wt % +DPPC. In fact, for all mixtures, regardless of composition and mixing method, the total injection before the oscillation (4000 s) becomes highly negative, and it affects the proper oscillation and deformation of the system.

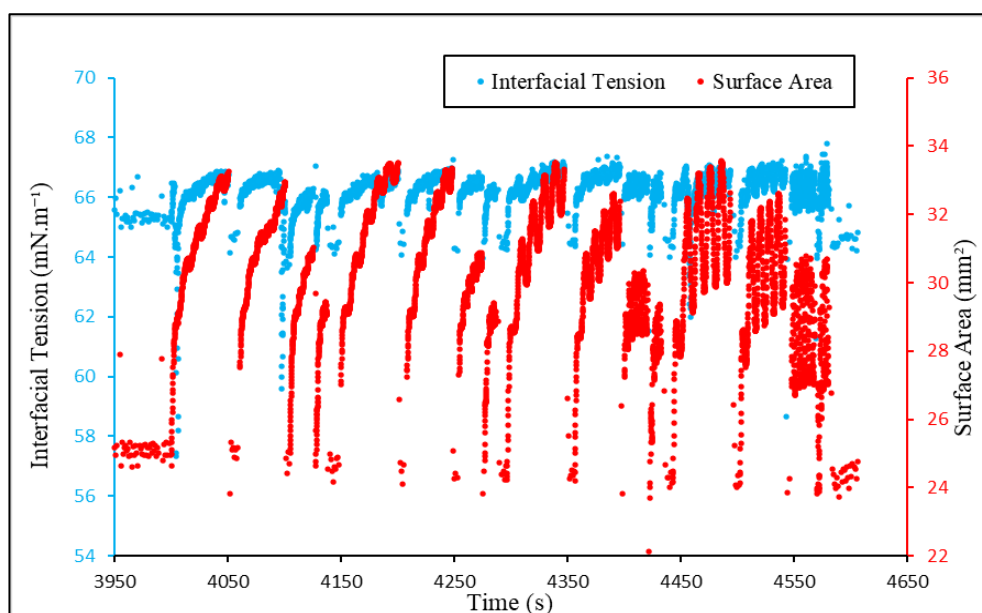


Figure 7.24 The dynamic interfacial tension and surface area vs. time for ATD+RTD+CNT 0.01 wt%+DPPC (mixing method i) during oscillation. Red and blue dots correspond to the surface area and interfacial tension, respectively.

An example of the failure of the proper oscillation is shown in Figure 7.24, which is associated to the mixture of ATD+RTD+CNT 0.01 wt % +DPPC prepared by the first method of mixing.

As shown in Figure 7.24, the oscillation and deformation of the surface areas are not satisfied to derive the Lissajous plots from the raw data because the system inputs (surface area signals) do not show any proper oscillation. This means that the oscillation option in PAT is not essentially suitable for all interfacial systems. Based on the observations and results in this study, the presence of the hydrophobic carbon nanotubes, either individually or in combination with other nanoparticles, causes the high degrees of disturbances in the system.

7.2 Summary

In this chapter, interfacial rheology was applied to investigate the interactions of DPPC monolayers with nano-sized pollutants under dynamic conditions which simulate the dynamic circumstances during the breathing cycles in human lungs.

It was proved that the DPPC systems without nanoparticles and DPPC solutions containing titanium dioxide nanoparticles (either anatase or rutile forms) with concentration as low as 0.01 wt % cannot be treated as linear systems for measuring their interfacial rheology parameters. In fact, the principles of the linear approach based on Fourier transform cannot cover the characteristics of these systems. The data related to the oscillation experiments were not fitted perfectly on the model based on Fourier transform. Moreover, the total harmonic distortion values of these systems were higher than 5% which means that these systems were working in a nonlinear regime. These observations and calculations prove that the linear approach cannot be applied for the rheology studies of all interfacial systems without limitations. Therefore, careful considerations must be taken to understand the linearity and nonlinearity of the interfacial systems.

DPPC solutions without nanoparticles are nonlinear interfacial systems. It was confirmed that increasing the amplitudes of the oscillation (deformation of the surface area) makes this system more elastic. At lower amplitudes, the expansion part of the cycle in DPPC solution is more dependent on frequency, if compared to the compression part of the cycle. During expansion and compression, strain softening and strain stiffening occurred, respectively.

For the DPPC systems containing ATD and RTD nanoparticles with concentrations between 0.01 wt % and 0.05 wt %, nonlinear approach and Lissajous plots result in valuable qualitative conclusions about the microstructures of the air-liquid interfaces. Both the ATD and RTD particles affect the normal interfacial behaviour of DPPC solution under dynamic conditions, meaning that these nanosized pollutants affect the interfacial tension hysteresis and normal operating procedures in human lungs. In the presence of ATD and RTD nanoparticles, interfacial system becomes more viscous, meaning that the DPPC system with nanoparticles becomes more dissipative and irreversible during the oscillation which simulated the breathing cycle. These results can be combined with toxicity and pressure-volume curve studies in the lungs.

At equal concentrations of ATD and RTD nanoparticles in DPPC solutions, there are differences between these two types of titanium dioxides in the interfacial systems under dynamic conditions because these particles behave differently in the stabilisation of the air-liquid interfaces. At the least concentration, i.e., 0.01 wt %, the ATD nanoparticles significantly affected the expansion part of the cycle, whereas RTD nanoparticles affected both expansion and compression parts of the cycle. For the RTD+DPPC systems, the adsorption of the RTD nanoparticles at the air-liquid interface results in stabilisation of the interface. In case of ATD nanoparticles, these particles are mostly in the bulk of the solution. This difference in the location of the nanoparticles in the system results in different gradient of the concentration of nanoparticles during oscillation, which causes different strain softening and stiffening behaviours between ATD and RTD nanoparticles, especially at higher concentrations.

The oscillation experiments for the CNT+DPPC were not successful. Moreover, the behaviour of the mixture of nanoparticles containing CNTs was

similar to that of CNT+DPPC, meaning that CNT particles could predominantly affect the interfacial characteristics of the DPPC systems containing CNT and titanium dioxide nanoparticles even with the equal concentrations.

Chapter 8

Conclusions and Future Work

8.1 Conclusions

This research has investigated the interactions between the surfactants and nanosized materials at the air-liquid interface to address the challenges faced in both industrial applications and human pulmonary system. Therefore, three main topics have been studied based on:

- Investigating the interactions of single-type nanoparticles with the industrial surfactants and a model of pulmonary surfactant by designing the experiments in accordance with the applications of each type of surfactant.
- Establishing and developing a robust systematic method for measuring the physicochemical effects of the mixtures of nanoparticles on the DPPC as a model of pulmonary surfactant.
- Applying a nonlinear interfacial rheology approach for the DPPC systems with and without nanoparticles under the dynamic conditions simulating the breathing cycles in the human lungs.

The novelty and distinctiveness of this research include:

- Using a robust systematic way to understand the effects of the mixture of nanoparticles and using the method of the mixing on the DPPC to address the important challenge of simulating the real conditions of nanosized pollutants reaching the lung surfactant.
- Investigating the interfacial rheology of the DPPC-nanoparticle systems using the nonlinear approach.
- Introducing a potential method based on the optical fibre for measuring the critical micelle concentration of surfactant.

These experimental studies which have put the real conditions of the case studies have led to the following conclusions:

- The structure and porosity of the agglomerates of nanoparticles at the air-liquid interface strongly depended on their surface properties including size, shape, and surface charges. These surface properties also affected the configuration of the agglomerates of nanoparticles at the air-liquid interfaces. The higher surface charge of nanoparticles with the similar size range resulted in more porous and less dense structures of the agglomerates. CNTs formed complicated configurations at the air-liquid interface. These structures obtained using GTT, are one of the sources of complexity of CNT particles in the interfacial systems.
- The interfacial behaviours of two industrial surfactants, i.e., CTAB and SDS, without nanoparticles provided useful results for industrial formulations and processes. At a given concentration of the surfactant, SDS reduced the interfacial tension more than CTAB. This is a key point in selecting the surfactant for different formulations and in cost-effectiveness studies. The CMC of SDS is more than that of CTAB. Therefore, using CTAB for the formulations requiring the micelle formation will result in the micellar formulations at lower concentrations of surfactant. The summary of the experimental results and main conclusions related to CTAB and SDS interacting with ATD nanoparticles have been shown in Table 8.1.

Table 8.1 Summary of experimental results, findings and conclusions related to CTAB and SDS interacting with ATD nanoparticles.

Surfactant	Surfactant Characterisation					Surfactant Concentration (M)	ATD Nanoparticles with Surfactant		Findings/ Conclusions
	ω ($\text{m}^2 \cdot \text{mol}^{-1}$)	a	b ($\text{m}^3 \cdot \text{mol}^{-1}$)	CMC by Tensiometry (M)	CMC by Optical Fibre (M)		Interfacial Tension ($\text{mN} \cdot \text{m}^{-1}$)	Zeta Potential (mV)	
CTAB	$1.00 \times 10^{+5}$	3.00×10^{-1}	7.35×10^{-1}	1.30×10^{-3}	1.60×10^{-3}	1×10^{-6}	72.12 ± 0.05	-26.78 ± 3.43	CTAB as a cationic surfactant interact with negatively charged ATD nanoparticles through electrostatic interactions. At medium and higher concentrations of CTAB, the ATD nanoparticles are probably adsorbed onto the air-liquid interface.
						5×10^{-6}	73.81 ± 0.12	-25.84 ± 2.78	
						1×10^{-5}	70.68 ± 0.05	-45.25 ± 2.73	
						5×10^{-5}	69.78 ± 0.12	-20.08 ± 2.97	
						1×10^{-4}	53.05 ± 0.80	-1.20 ± 1.46	
						5×10^{-4}	47.65 ± 0.85	37.53 ± 5.97	
						1×10^{-3}	39.74 ± 0.70	37.57 ± 2.30	
						2.5×10^{-3}	33.80 ± 0.11	42.70 ± 4.71	
						5×10^{-3}	31.31 ± 0.03	53.70 ± 7.56	
						1×10^{-2}	35.40 ± 0.09	48.36 ± 5.33	
1×10^{-1}	33.92 ± 0.08	48.08 ± 15.59							
SDS	$5.00 \times 10^{+5}$	1.00×10^{-1}	1.26×10^{-1}	4.23×10^{-3}	6.50×10^{-3}	1×10^{-6}	68.16 ± 0.20	-13.28 ± 1.43	SDS as an anionic surfactant interact with sodium ions and negatively charged ATD nanoparticles through hydrophobic interactions. At medium and higher concentrations of SDS, the probability of the adsorption of ATD nanoparticles at the air-liquid interface is low. At a given concentration of surfactant without particles, SDS decreases the interfacial tension more than the CTAB does
						5×10^{-6}	70.84 ± 0.06	-3.88 ± 1.95	
						1×10^{-5}	71.29 ± 0.04	-11.37 ± 4.75	
						5×10^{-5}	71.40 ± 0.17	-11.63 ± 3.81	
						1×10^{-4}	71.11 ± 0.19	-35.85 ± 6.08	
						5×10^{-4}	61.57 ± 0.28	-33.47 ± 2.41	
						1×10^{-3}	51.92 ± 0.15	-32.47 ± 6.15	
						2.5×10^{-3}	49.20 ± 0.74	-32.60 ± 5.24	
						5×10^{-3}	42.48 ± 3.00	-31.70 ± 5.16	
						1×10^{-2}	35.90 ± 0.74	-33.62 ± 2.05	
1×10^{-1}	35.71 ± 0.02	-34.00 ± 10.89							

- A potential method based on optical fibre has been developed to measure the CMC of surfactants. The calculated results from the optical fibre method were comparable with those of traditional method based on tensiometry and adsorption isotherms. The considerations and suggestions for the design of the experiments in the future to develop CMC measurement sensors based on optical fibre were provided. The sensors based on the optical fibre will be helpful for in-situ measurement of the CMC in the industries which require the CMC measurement during the manufacturing process or need the CMC of the samples with small size.
- The mechanism of the interaction of ATD nanoparticles (as one of the widely used nanoparticles in various industries) with ionic surfactants and the foaming properties of these systems depended on the type of the surfactant and its concentration. The hydrophilic ATD nanoparticles with negative charge interact with CTAB molecules due to the electrostatic interactions. In contrast, the interactions between SDS molecules and ATD nanoparticles are the most probably hydrophobic interactions. Because of different mechanisms of interactions, the ATD nanoparticles were adsorbed at the air-liquid interface in case of the CTAB solution, whereas the ATD nanoparticles remain in the solution of the SDS and are not adsorbed onto the interface. These results are important in designing and optimising new formulations and industrial processes such as wastewater treatment and enhanced oil recovery. The interfacial systems such as foams and emulsions comprehensively used in industries are required to be fully controlled to achieve the most stable products and efficient processes. For these applications, understanding the physical chemistry principles behind the interactions of nanoparticles with the industrial surfactants is a key.
- The interactions of nanosized materials with DPPC depends on the surface properties including shape and surface charges of nanoparticles. Two shapes of titanium dioxide nanoparticle, i.e., ATD and RTD, with

the same size and different surface charges showed completely different behaviours in interactions with DPPC. Both ATD and RTD nanoparticles caused the depletion of DPPC due to their interactions with individual DPPC molecules and DPPC bilayers. However, there is a possibility that at higher concentrations of nanoparticles, RTD nanoparticles are adsorbed onto the air-liquid interface whereas ATD nanoparticles remained in the bulk of the solution. At the highest concentrations of RTD nanoparticles, i.e., 0.05 wt %, different types of particles with various surface charges resulted in a higher non-homogeneity of the system. This means that the higher concentration of nanoparticles such as RTD in the lung (i.e., long-term exposure to air pollution) causes different populations of nanoparticles in the lungs. As well as the environmental concept, the proposed mechanism of the interactions between DPPC and ATD/RTD nanoparticles is an important finding for designing the nanosized drug delivery carriers for pulmonary drug delivery. The summary of the experimental results and most important findings about the interactions of DPPC molecules and single-type nanoparticles including ATD, RTD, and CNT have been shown in Table 8.2.

Table 8.2 Summary of experimental results, findings and conclusions related to DPPC interacting with ATD, RTD, and CNT nanoparticles.

Nanoparticle	Nanoparticle Characterisation				Nanoparticle Concentration (wt %)	Nanoparticles with DPPC without Sinusoidal Perturbations		Findings/ Conclusions
	Interfacial Tension of Dispersion of 0.01 wt % of Nanoparticle in DI Water (mN.m^{-1})	Zeta potential in DI Water (mV)	Size of the Agglomerates after IPA Evaporation (nm)	Size of the Agglomerates using GTT (nm)		Interfacial Tension (mN.m^{-1})	Zeta Potential (mV)	
Anatase form of TiO_2 (ATD)	69.96 \pm 0.005	-31.46 \pm 7.11	38-68	99-509	0.01	68.01 \pm 0.22	-43.54 \pm 1.74	Negatively charged and hydrophilic ATD nanoparticles interact with DPPC molecules and cause the depletion of surfactant molecules at the interface at all concentrations.
					0.02	66.29 \pm 0.12	-42.73 \pm 2.41	
					0.03	69.39 \pm 0.03	-40.28 \pm 2.79	
					0.04	69.72 \pm 0.05	-42.25 \pm 3.68	
					0.05	69.54 \pm 0.23	-40.68 \pm 3.19	
Rutile form of TiO_2 (RTD)	69.91 \pm 0.03	-0.11 \pm 0.11	40-73	69-512	0.01	69.18 \pm 0.09	-19.15 \pm 7.66	Negatively charged and hydrophilic RTD nanoparticles interact with DPPC molecules and cause the depletion of surfactant molecules at the interface. At the higher concentrations of RTD, there is a possibility of the adsorption of RTD nanoparticles at the air-liquid interface.
					0.02	68.23 \pm 0.10	-22.39 \pm 7.15	
					0.03	66.57 \pm 0.00	-33.15 \pm 2.75	
					0.04	63.06 \pm 0.23	-40.42 \pm 7.06	
					0.05	63.23 \pm 0.19	-33.02 \pm 1.8	
Carbon Nanotube (CNT)	70.66 \pm 0.06	-49.02 \pm 8.21	OD: 45-103	OD: 44-64	0.01	66.05 \pm 0.20	-46.00 \pm 5.93	The interfacial tension results are not reproducible due to the different possible configurations of CNT particles at the air-liquid interface. The complex structure of carbon nanotubes and the variations in the structure and functional groups of the tubes might be the other cause of lack of reproducibility of results.
					0.02	65.72 \pm 0.23	-46.46 \pm 6.86	
					0.03	68.69 \pm 0.21	-47.88 \pm 3.17	
					0.04	65.68 \pm 0.20	-48.79 \pm 4.61	
					0.05	69.32 \pm 0.14	-24.52 \pm 12.78 -109.39 \pm 28.01 -255.62 \pm 36.75	

- The study on the mixture of nanoparticles in contact with the DPPC in both colloidal phase and air-liquid interface showed that not only the chemical composition of the mixture of nanoparticles affects the interfacial behaviour of the DPPC solution, but also the mixing method significantly changes this behaviour. It was concluded that the effects of the mixture of nano-pollutants on the lung surfactant depends on the nanomaterials and the way that these nano-sized pollutants have interacted at the first place. The samples of the mixtures in this study were not random samples of nanosized pollutants. Instead, these samples were prepared in the laboratory to understand the effect of the dominant nanoparticles. These results can be helpful in revising the environmental and health regulations dealing with the nanosized pollutants. Moreover, these results and findings about the physical chemistry of these interfaces can have a broader application in the field of controlled drug delivery to the lungs.
- The interfacial rheology was applied to investigate the DPPC monolayers interacting with nano-pollutants under dynamic conditions which simulated the dynamic circumstances during the breathing cycles. The DPPC systems without nanoparticles and DPPC solutions containing ATD, RTD, and CNT particles cannot be treated as linear systems for measuring the interfacial rheology parameters.
- Both ATD and RTD particles affected the normal interfacial behaviour of DPPC solution under dynamic conditions. This means that nanosized pollutants affect the interfacial tension hysteresis in human lungs, increase the rigidity of the system and cause anomalies in the mechanics of breathing. In the presence of ATD and RTD nanoparticles, interfacial system becomes more viscous, dissipative, and irreversible during the oscillation and dynamic conditions. Combining these results with toxicity and pressure-volume curve studies in the lungs is useful.
- Although both ATD and RTD are the crystal forms of the same chemical substance, i.e., titanium dioxide, there were differences between ATD and RTD nanoparticles in the interfacial systems under dynamic conditions because these particles are interacting with DPPC molecules and at the

air-liquid interfaces differently. At the least concentration, i.e., 0.01 wt %, RTD nanoparticles affected both expansion and compression parts of the cycle whereas ATD nanoparticles significantly affected the expansion part of the cycle. At higher concentrations of nanoparticles, strain softening and stiffening behaviours between ATD and RTD are different because ATD nanoparticles are mostly located in the bulk of solution whereas RTD nanoparticles stabilise the air-liquid interface by being adsorbed at this interface.

- The interfacial tension measurements for CNT+DPPC dispersions did not provide reproducible results. In fact, the configuration of the CNTs at the air-liquid interface can be extremely changing. Therefore, results of each experiment differ from the other one. Moreover, the oscillation experiments for the CNT+DPPC and the mixture of nanoparticles containing CNTs were not successful. It can be concluded that CNT particles can predominantly affect the dynamic interfacial characteristics of the DPPC systems containing CNT, ATD, and RTD nanoparticles even with the equal concentrations. This shows how different breaths with various composition of the inhaled nanosized pollutants will result in extreme disturbance in the structure of the air-liquid interface of the pulmonary surfactant and its interfacial behaviour under dynamic conditions. Table 8.3 summarises the findings and conclusions about the behaviour of the systems containing DPPC and nanoparticles (including single-type and mixtures) under dynamic conditions or sinusoidal perturbations.

Table 8.3 Summary of findings and conclusions related to DPPC interacting with nanoparticles and their mixtures under dynamic conditions.

Nanoparticle	Findings / Conclusions for Nanoparticles with DPPC under Sinusoidal Perturbations
Anatase Form of TiO₂ (ATD)	<p>ATD nanoparticles affect the normal interfacial behaviour of DPPC solution under dynamic conditions.</p> <p>In the presence of ATD nanoparticles, interfacial system becomes more viscous during the oscillation which simulated the breathing cycle.</p> <p>At the least concentration, i.e., 0.01 wt %, the ATD nanoparticles significantly affect the expansion part of the cycle.</p>
Rutile Form of TiO₂ (RTD)	<p>RTD nanoparticles affect the normal interfacial behaviour of DPPC solution under dynamic conditions.</p> <p>In the presence of RTD nanoparticles, interfacial system becomes more viscous during the oscillation.</p> <p>At the least concentration, i.e., 0.01 wt %, RTD nanoparticles affect both expansion and compression parts of the cycle.</p> <p>At higher concentration of RTD nanoparticles, the air-liquid interface in presence of RTD nanoparticles is more stabilised during the oscillation.</p>
Carbon Nanotube (CNT)	<p>The oscillation experiments using PAT did not result in reliable data for CNT+DPP samples.</p>
Mixture of Nanoparticles	<p>The behaviour of the mixtures with the concentration of 0.01 wt % was similar to that of CNT 0.01 wt % + DPPC.</p>

8.2 Future Work

To advance what has been investigated in this research, the following future studies are suggested:

- This research has investigated the mechanism of the interactions of titanium dioxide with two different ionic surfactants. The presence of the titanium dioxide as a photocatalyst and the surfactant as a cleaning agent gives a dual property to the solutions and dispersions fully characterised in terms of interfacial and foaming properties. Therefore, it is suggested to study the photoactivity of these solutions and dispersions. The results

can be coupled with the results from this research to develop and control the most efficient formulations for the remediation of chemical wastes.

- The preliminary results for the measurement of critical micelle concentration of surfactants using optical fibre have been studied in this research. This method can be further developed to design a sensor device for in situ measurement of the CMC of surfactants.
- In this research, for the health and safety issues related to the application of nanoparticles, it was required to use the nanoparticles in the solutions. As the method of the deposition of the nanoparticles on the air-liquid interface of lung surfactant is important and can affect the results, it is suggested to study the deposition of nanoparticles using a dry powder insufflator. This method simulates the realistic conditions of the inhalation process in a better way. Using a constrained drop surfactometer provides both benefits of drop profile analysis and mimicking the real-life conditions.
- This research has used the DPPC as the single-component model of the lung surfactant to provide the fundamental principles of the physical chemistry behind the interactions of nanoparticles with this model. The future studies should be built up on these types of fundamental studies by adding other components of pulmonary surfactant such as cholesterol and other phospholipids step by step.
- In the next step, as the advanced step closer to the real pulmonary surfactant, clinical lung surfactants (such as CurosurfTM, InfasurfTM, and SurvantaTM) can be used to measure the effects of nanoparticles.
- This research has focused on the interfacial rheology of the DPPC and DPPC-nanoparticle systems using both linear and nonlinear approaches. It is suggested that in future, these data related to the interfacial rheology of DPPC system are used to develop a viscoelastic model for this system. Then, using the data related to the DPPC-nanoparticle systems, the model's parameters mostly affected by the presence of nanoparticles can be found. This research can be very helpful in drug delivery to the lungs and control of the drug substances at the air-liquid interface of lung surfactant.

- It is suggested to simulate the interactions of the nanoparticles with DPPC bilayers using Molecular Dynamic Simulations and software such as GROMACS and LAMMPS. These types of simulations can help to understand the mechanism of interactions in more details.

References

1. *Health matters: air pollution*. 2018; Available from: <https://www.gov.uk/government/publications/health-matters-air-pollution/health-matters-air-pollution>.
2. *Chemical Hazards and Poisons Report: Reducing health harms associated with air pollution*, U.H.S. Agency, Editor. 2022.
3. *Air pollution*. Available from: https://www.who.int/health-topics/air-pollution#tab=tab_2.
4. Roser, M. *Data Review: How many people die from air pollution?* 2021; Available from: <https://ourworldindata.org/data-review-air-pollution-deaths>.
5. Hajirasouliha, F. and D. Zabiegaj, *Effects of Environmental Emissions on the Respiratory System: Secrets and Consequences*, in *Environmental Emissions*. 2020, IntechOpen.
6. Rönkkö, T. and H. Timonen, *Overview of sources and characteristics of nanoparticles in urban traffic-influenced areas*. *Journal of Alzheimer's Disease*, 2019. **72**(1): p. 15-28.
7. Naghdi, M., et al., *Instrumental approach toward understanding nano-pollutants*. *Nanotechnology for Environmental Engineering*, 2017. **2**(1): p. 1-17.
8. Jan, N., et al., *Nano-pollution: Why it should worry us*. *Chemosphere*, 2022: p. 134746.
9. Arick, D.Q., et al., *Effects of nanoparticles on the mechanical functioning of the lung*. *Advances in Colloid and Interface Science*, 2015. **225**: p. 218-228.
10. Xu, Y., et al., *Perturbation of the pulmonary surfactant monolayer by single-walled carbon nanotubes: a molecular dynamics study*. *Nanoscale*, 2017. **9**(29): p. 10193-10204.
11. Keller, J., et al., *Time course of lung retention and toxicity of inhaled particles: short-term exposure to nano-Ceria*. *Archives of toxicology*, 2014. **88**(11): p. 2033-2059.
12. Huang, Z., et al., *Relationship between particle size and lung retention time of intact solid lipid nanoparticle suspensions after pulmonary delivery*. *Journal of Controlled Release*, 2020. **325**: p. 206-222.

13. Habybabady, R.H., et al., *Effects of dust exposure on the respiratory health symptoms and pulmonary functions of street sweepers*. The Malaysian journal of medical sciences: MJMS, 2018. **25**(6): p. 76.
14. Matsuzaki, H., et al., *Asbestos-induced cellular and molecular alteration of immunocompetent cells and their relationship with chronic inflammation and carcinogenesis*. Journal of Biomedicine and Biotechnology, 2012. **2012**.
15. West, J.B., *Respiratory physiology: the essentials*. 2012: Lippincott Williams & Wilkins.
16. Hidalgo, A., A. Cruz, and J. Pérez-Gil, *Barrier or carrier? Pulmonary surfactant and drug delivery*. European Journal of Pharmaceutics and Biopharmaceutics, 2015. **95**: p. 117-127.
17. Ravera, F., et al., *Effect of nanoparticles on the interfacial properties of liquid/liquid and liquid/air surface layers*. The Journal of Physical Chemistry B, 2006. **110**(39): p. 19543-19551.
18. Wu, M., et al., *Interactions of model airborne particulate matter with dipalmitoyl phosphatidylcholine and a clinical surfactant Calsurf*. Journal of Colloid and Interface Science, 2022. **607**: p. 1993-2009.
19. Geng, Y., et al., *Potential hazards associated with interactions between diesel exhaust particulate matter and pulmonary surfactant*. Science of The Total Environment, 2022. **807**: p. 151031.
20. van Kempen, S.E., et al., *Non-linear surface dilatational rheology as a tool for understanding microstructures of air/water interfaces stabilized by oligofructose fatty acid esters*. Soft Matter, 2013. **9**(40): p. 9579-9592.
21. Giménez-Ribes, G., M. Habibi, and L.M. Sagis, *Interfacial rheology and relaxation behavior of adsorption layers of the triterpenoid saponin Escin*. Journal of colloid and interface science, 2020. **563**: p. 281-290.
22. Chen, Z., et al., *Determination of rheology and surface tension of airway surface liquid: a review of clinical relevance and measurement techniques*. Respiratory Research, 2019. **20**(1): p. 1-14.
23. Kukutschová, J., et al., *On airborne nano/micro-sized wear particles released from low-metallic automotive brakes*. Environmental Pollution, 2011. **159**(4): p. 998-1006.

24. Malachova, K., et al., *Toxicity and mutagenicity of low-metallic automotive brake pad materials*. *Ecotoxicology and environmental safety*, 2016. **131**: p. 37-44.
25. Perrino, C., et al., *Air quality characterization at three industrial areas in southern Italy*. *Frontiers in Environmental Science*, 2020: p. 196.
26. Kampa, M. and E. Castanas, *Human health effects of air pollution*. *Environmental pollution*, 2008. **151**(2): p. 362-367.
27. *Particulate Matter in the United Kingdom*. 2005; Available from: <http://www.defra.gov.uk/environment/airquality/>.
28. Muhlfield, C., et al., *Interactions of nanoparticles with pulmonary structures and cellular responses*. *American Journal of Physiology-Lung Cellular and Molecular Physiology*, 2008. **294**(5): p. L817-L829.
29. Oberdörster, G., E. Oberdörster, and J. Oberdörster, *Nanotoxicology: an emerging discipline evolving from studies of ultrafine particles*. *Environmental health perspectives*, 2005. **113**(7): p. 823-839.
30. Babadjouni, R.M., et al., *Clinical effects of air pollution on the central nervous system; a review*. *Journal of Clinical Neuroscience*, 2017. **43**: p. 16-24.
31. Rajagopalan, S., S.G. Al-Kindi, and R.D. Brook, *Air pollution and cardiovascular disease: JACC state-of-the-art review*. *Journal of the American College of Cardiology*, 2018. **72**(17): p. 2054-2070.
32. Guo, Y., et al., *The association between lung cancer incidence and ambient air pollution in China: A spatiotemporal analysis*. *Environmental research*, 2016. **144**: p. 60-65.
33. Drakaki, E., C. Dessinioti, and C.V. Antoniou, *Air pollution and the skin*. *Frontiers in Environmental Science*, 2014. **2**: p. 11.
34. Araviiskaia, E., et al., *The impact of airborne pollution on skin*. *Journal of the European Academy of Dermatology and Venereology*, 2019. **33**(8): p. 1496-1505.
35. Cohen, A.J., et al., *Estimates and 25-year trends of the global burden of disease attributable to ambient air pollution: an analysis of data from the Global Burden of Diseases Study 2015*. *The Lancet*, 2017. **389**(10082): p. 1907-1918.
36. Fiordelisi, A., et al., *The mechanisms of air pollution and particulate matter in cardiovascular diseases*. *Heart failure reviews*, 2017. **22**(3): p. 337-347.

37. Sram, R.J., et al., *The impact of air pollution to central nervous system in children and adults*. Neuroendocrinology Letters, 2017. **38**(6): p. 389-396.
38. *Neurological Disorders: Public Health Challenges*. 2006; Available from: <https://www.who.int/publications/i/item/9789241563369>.
39. *Cardiovascular diseases (CVDs)*. 2021; Available from: [https://www.who.int/news-room/fact-sheets/detail/cardiovascular-diseases-\(cvds\)](https://www.who.int/news-room/fact-sheets/detail/cardiovascular-diseases-(cvds)).
40. Graber, M., et al., *Air pollution and stroke. A new modifiable risk factor is in the air*. Revue neurologique, 2019. **175**(10): p. 619-624.
41. Béjot, Y., et al., *A review of epidemiological research on stroke and dementia and exposure to air pollution*. International journal of stroke, 2018. **13**(7): p. 687-695.
42. Čabanová, K., et al., *Detection of micron and submicron particles in human bronchogenic carcinomas*. Journal of Nanoscience and Nanotechnology, 2019. **19**(5): p. 2460-2466.
43. Jacquemin, B., et al., *Ambient air pollution and adult asthma incidence in six European cohorts (ESCAPE)*. Environmental health perspectives, 2015. **123**(6): p. 613-621.
44. Tung, N.T., et al., *Association between air pollution and lung lobar emphysema in COPD*. Frontiers in medicine, 2021. **8**.
45. Čabanová, K., et al., *Identification of the phase composition of solid microparticles in the nasal mucosa of patients with chronic hypertrophic rhinitis using Raman microspectroscopy*. Scientific reports, 2021. **11**(1): p. 1-8.
46. Ehsanifar, M., S.S. Banihashemian, and F. Farokhmanesh, *Exposure To urban air pollution nanoparticles and CNS disease*. Autism, 2021. **25**: p. 28.
47. Ehsanifar, M., S. Banihashemian, and M. Ehsanifar, *Exposure to air pollution nanoparticles: Oxidative stress and neuroinflammation*. Journal ISSN, 2021. **2766**: p. 2276.
48. Lu, R.X.Z. and M. Radisic, *Organ-on-a-chip platforms for evaluation of environmental nanoparticle toxicity*. Bioactive Materials, 2021. **6**(9): p. 2801-2819.
49. Liu, S., et al., *Development of Human Lung Induction Models for Air Pollutants' Toxicity Assessment*. Environmental Science & Technology, 2021. **55**(4): p. 2440-2451.

50. Timmons, B. and R. Ley, *Behavioral and Psychological Approaches to Breathing Disorders*. PsycCritiques. Vol. 40. 1995, New York: Springer Science + Business Media New York. 321.
51. *Respiratory system*. Available from:
https://en.wikipedia.org/wiki/Respiratory_system.
52. Feher, J.J., *Quantitative human physiology: an introduction*. 2017: Academic press. 1007.
53. Rembiesa, J., et al., *The impact of pollution on skin and proper efficacy testing for anti-pollution claims*. *Cosmetics*, 2018. **5**(1): p. 4.
54. Miller, F.J., et al., *Improvements and additions to the multiple path particle dosimetry model*. *Journal of Aerosol Science*, 2016. **99**: p. 14-26.
55. Knudsen, L. and M. Ochs, *The micromechanics of lung alveoli: structure and function of surfactant and tissue components*. *Histochemistry and cell biology*, 2018. **150**(6): p. 661-676.
56. Nova, Z., H. Skovierova, and A. Calkovska, *Alveolar-capillary membrane-related pulmonary cells as a target in endotoxin-induced acute lung injury*. *International journal of molecular sciences*, 2019. **20**(4): p. 831.
57. Holm, B.A., et al., *Content of dipalmitoyl phosphatidylcholine in lung surfactant: ramifications for surface activity*. *Pediatric research*, 1996. **39**(5): p. 805-811.
58. Dobrowolska, K., et al., *Interactions of insoluble micro-and nanoparticles with the air-liquid interface of the model pulmonary fluids*. *Physicochemical Problems of Mineral Processing*, 2018. **54**.
59. Gerber, P.J., et al., *Wetting and spreading of a surfactant film on solid particles: influence of sharp edges and surface irregularities*. *Langmuir*, 2006. **22**(12): p. 5273-5281.
60. Farnoud, A.M. and J. Fiegel, *Low concentrations of negatively charged sub-micron particles alter the microstructure of DPPC at the air-water interface*. *Colloids and Surfaces A: Physicochemical and Engineering Aspects*, 2012. **415**: p. 320-327.
61. Guzmán, E., et al., *Influence of silica nanoparticles on phase behavior and structural properties of DPPC—Palmitic acid Langmuir monolayers*. *Colloids*

- and Surfaces A: Physicochemical and Engineering Aspects, 2012. **413**: p. 280-287.
62. Ratoi, M., et al., *Impact of lung surfactant on wettability and cytotoxicity of nanoparticles*. RSC Advances, 2014. **4**(39): p. 20573-20581.
63. Ye, X., et al., *Influence of modified silica nanoparticles on phase behavior and structure properties of DPPC monolayers*. Colloids and Surfaces B: Biointerfaces, 2018. **172**: p. 480-486.
64. Bernhard, W., *Lung surfactant: Function and composition in the context of development and respiratory physiology*. Annals of Anatomy-Anatomischer Anzeiger, 2016. **208**: p. 146-150.
65. Kandasamy, S.K. and R.G. Larson, *Molecular dynamics study of the lung surfactant peptide SP-B1-25 with DPPC monolayers: insights into interactions and peptide position and orientation*. Biophysical journal, 2005. **88**(3): p. 1577-1592.
66. Hirota, K. and H. Terada, *Particle-manufacturing technology-based inhalation therapy for pulmonary diseases*, in *Colloid and interface science in pharmaceutical research and development*. 2014, Elsevier. p. 103-119.
67. Park, K., *Biomaterials for cancer therapeutics: diagnosis, prevention and therapy*. 2013: Elsevier.
68. Tiple, A.D., et al., *A review on Nanotoxicology: Aquatic environment and biological system*. Materials Today: Proceedings, 2020. **29**: p. 1246-1250.
69. Bantz, C., et al., *The surface properties of nanoparticles determine the agglomeration state and the size of the particles under physiological conditions*. Beilstein journal of nanotechnology, 2014. **5**(1): p. 1774-1786.
70. Lundqvist, M., et al., *Nanoparticle size and surface properties determine the protein corona with possible implications for biological impacts*. Proceedings of the National Academy of Sciences, 2008. **105**(38): p. 14265-14270.
71. Li, S., et al., *Surface properties of nanoparticles dictate their toxicity by regulating adsorption of humic acid molecules*. ACS Sustainable Chemistry & Engineering, 2021. **9**(41): p. 13705-13716.
72. Surette, M.C. and J.A. Nason, *Nanoparticle aggregation in a freshwater river: the role of engineered surface coatings*. Environmental Science: Nano, 2019. **6**(2): p. 540-553.

73. Silina, Y.E., et al., *Interactions between DPPC as a component of lung surfactant and amorphous silica nanoparticles investigated by HILIC-ESI-MS*. Journal of Chromatography B, 2016. **1029**: p. 222-229.
74. Guzmán, E., et al., *Effect of hydrophilic and hydrophobic nanoparticles on the surface pressure response of DPPC monolayers*. The Journal of Physical Chemistry C, 2011. **115**(44): p. 21715-21722.
75. Sun, L., et al., *Recent advances of surfactant-stabilized N₂/CO₂ foams in enhanced oil recovery*. Fuel, 2019. **241**: p. 83-93.
76. Singh, R., et al., *Multistimuli-responsive foams using an anionic surfactant*. Langmuir, 2018. **34**(37): p. 11010-11020.
77. Houtz, E., M. Wang, and J.-S. Park, *Identification and fate of aqueous film forming foam derived per- and polyfluoroalkyl substances in a wastewater treatment plant*. Environmental Science & Technology, 2018. **52**(22): p. 13212-13221.
78. Collivignarelli, M.C., et al., *Foams in Wastewater Treatment Plants: From Causes to Control Methods*. Applied Sciences, 2020. **10**(8): p. 2716.
79. Gonzalez, P.J. and P.M. Sørensen, *Characterization of saponin foam from Saponaria officinalis for food applications*. Food Hydrocolloids, 2020. **101**: p. 105541.
80. Lee, S., et al., *Synthesis of environment friendly biosurfactants and characterization of interfacial properties for cosmetic and household products formulations*. Colloids and Surfaces A: Physicochemical and Engineering Aspects, 2018. **536**: p. 224-233.
81. Starov, V., *Foam in pharmaceutical and medical applications* Maryam Parsa, Anna Trybala, Danish Javed Malik and. Current Opinion in Colloid & Interface Science, 2019. **44**: p. 153-167.
82. Guo, F. and S. Aryana, *An experimental investigation of nanoparticle-stabilized CO₂ foam used in enhanced oil recovery*. Fuel, 2016. **186**: p. 430-442.
83. Emrani, A.S. and H.A. Nasr-El-Din, *An experimental study of nanoparticle-polymer-stabilized CO₂ foam*. Colloids and Surfaces A: Physicochemical and Engineering Aspects, 2017. **524**: p. 17-27.

84. Peng, D., et al., *Foaming and surface properties of gliadin nanoparticles: Influence of pH and heating temperature*. Food Hydrocolloids, 2018. **77**: p. 107-116.
85. Nazari, N., J.-S. Tsau, and R. Barati, *CO₂ foam stability improvement using polyelectrolyte complex nanoparticles prepared in produced water*. Energies, 2017. **10**(4): p. 516.
86. Yekeen, N., et al., *Bulk and bubble-scale experimental studies of influence of nanoparticles on foam stability*. Chinese Journal of Chemical Engineering, 2017. **25**(3): p. 347-357.
87. Sun, Q., et al., *Aqueous foam stabilized by partially hydrophobic nanoparticles in the presence of surfactant*. Colloids and Surfaces A: Physicochemical and Engineering Aspects, 2015. **471**: p. 54-64.
88. Srivastava, A., et al., *Effects of silica nanoparticles and polymers on foam stability with sodium dodecylbenzene sulfonate in water–liquid paraffin oil emulsions at high temperatures*. Journal of Molecular Liquids, 2017. **241**: p. 1069-1078.
89. AlYousef, Z., M. Almobarky, and D. Schechter, *Enhancing the Stability of Foam by the Use of Nanoparticles*. Energy & Fuels, 2017. **31**(10): p. 10620-10627.
90. Wu, Y., et al., *Stability mechanism of nitrogen foam in porous media with silica nanoparticles modified by cationic surfactants*. Langmuir, 2018. **34**(27): p. 8015-8023.
91. AlYousef, Z.A., M.A. Almobarky, and D.S. Schechter, *The effect of nanoparticle aggregation on surfactant foam stability*. Journal of colloid and interface science, 2018. **511**: p. 365-373.
92. Li, S., et al., *Properties of carbon dioxide foam stabilized by hydrophilic nanoparticles and hexadecyltrimethylammonium bromide*. Energy & Fuels, 2017. **31**(2): p. 1478-1488.
93. Kim, I., et al., *Size-dependent properties of silica nanoparticles for Pickering stabilization of emulsions and foams*. Journal of Nanoparticle Research, 2016. **18**(4): p. 82.

94. Zhu, Y., et al., *Responsive aqueous foams stabilized by silica nanoparticles hydrophobized in situ with a conventional surfactant*. *Langmuir*, 2015. **31**(47): p. 12937-12943.
95. Wang, S., et al., *Enhancing foam stability in porous media by applying nanoparticles*. *Journal of Dispersion Science and Technology*, 2018. **39**(5): p. 734-743.
96. Petkova, B., et al., *Foamability of aqueous solutions: Role of surfactant type and concentration*. *Advances in Colloid and Interface Science*, 2020. **276**: p. 102084.
97. Vatanparast, H., et al., *Surface behavior of hydrophilic silica nanoparticle-SDS surfactant solutions: I. Effect of nanoparticle concentration on foamability and foam stability*. *Colloids and Surfaces A: Physicochemical and Engineering Aspects*, 2017. **513**: p. 430-441.
98. Zhu, J., et al., *Experimental study on the microscopic characteristics of foams stabilized by viscoelastic surfactant and nanoparticles*. *Colloids and Surfaces A: Physicochemical and Engineering Aspects*, 2019. **572**: p. 88-96.
99. Yoon, I.-H., et al., *A highly efficient decontamination foam stabilized by well-dispersed mesoporous silica nanoparticles*. *Colloids and Surfaces A: Physicochemical and Engineering Aspects*, 2019. **560**: p. 164-170.
100. Yoon, I.-H., et al., *Structure and stability of decontamination foam in concentrated nitric acid and silica nanoparticles by image analysis*. *Annals of Nuclear Energy*, 2016. **95**: p. 102-108.
101. Ravera, F., et al., *Liquid–liquid interfacial properties of mixed nanoparticle–surfactant systems*. *Colloids and Surfaces A: Physicochemical and Engineering Aspects*, 2008. **323**(1-3): p. 99-108.
102. Harishchandra, R.K., M. Saleem, and H.-J. Galla, *Nanoparticle interaction with model lung surfactant monolayers*. *Journal of the Royal Society Interface*, 2009. **7**(suppl_1): p. S15-S26.
103. Dwivedi, M.V., et al., *Size influences the effect of hydrophobic nanoparticles on lung surfactant model systems*. *Biophysical journal*, 2014. **106**(1): p. 289-298.

104. Mousseau, F. and J.-F. Berret, *The role of surface charge in the interaction of nanoparticles with model pulmonary surfactants*. *Soft matter*, 2018. **14**(28): p. 5764-5774.
105. Hu, G., et al., *Physicochemical properties of nanoparticles regulate translocation across pulmonary surfactant monolayer and formation of lipoprotein corona*. *ACS nano*, 2013. **7**(12): p. 10525-10533.
106. Munteanu, B., et al., *Charged particles interacting with a mixed supported lipid bilayer as a biomimetic pulmonary surfactant*. *The European Physical Journal E*, 2014. **37**(8): p. 1-8.
107. Li, Y. and N. Gu, *Thermodynamics of charged nanoparticle adsorption on charge-neutral membranes: a simulation study*. *The Journal of Physical Chemistry B*, 2010. **114**(8): p. 2749-2754.
108. Chen, P., et al., *Effect of the surface charge density of nanoparticles on their translocation across pulmonary surfactant monolayer: A molecular dynamics simulation*. *Molecular Simulation*, 2018. **44**(2): p. 85-93.
109. Maestro, A., et al., *Wettability of silica nanoparticle–surfactant nanocomposite interfacial layers*. *Soft Matter*, 2012. **8**(3): p. 837-843.
110. Valle, R.P., et al., *Increasing hydrophobicity of nanoparticles intensifies lung surfactant film inhibition and particle retention*. *ACS Sustainable Chemistry & Engineering*, 2014. **2**(7): p. 1574-1580.
111. Kodama, A.T., et al., *Investigating the effect of particle size on pulmonary surfactant phase behavior*. *Biophysical Journal*, 2014. **107**(7): p. 1573-1581.
112. Lin, X., et al., *Promote potential applications of nanoparticles as respiratory drug carrier: insights from molecular dynamics simulations*. *Nanoscale*, 2014. **6**(5): p. 2759-2767.
113. Lin, X., Y.Y. Zuo, and N. Gu, *Shape affects the interactions of nanoparticles with pulmonary surfactant*. *Science China Materials*, 2015. **58**(1): p. 28-37.
114. Luo, Z., et al., *The role of nanoparticle shape in translocation across the pulmonary surfactant layer revealed by molecular dynamics simulations*. *Environmental Science: Nano*, 2018. **5**(8): p. 1921-1932.

115. Yang, K. and Y.-Q. Ma, *Computer simulation of the translocation of nanoparticles with different shapes across a lipid bilayer*. *Nature nanotechnology*, 2010. **5**(8): p. 579-583.
116. Schüer, J.J., et al., *Establishment of a synthetic in vitro lung surfactant model for particle interaction studies on a Langmuir film balance*. *Langmuir*, 2020. **36**(17): p. 4808-4819.
117. Cañadas, O., et al., *Polyhydroxyalkanoate nanoparticles for pulmonary drug delivery: Interaction with lung surfactant*. *Nanomaterials*, 2021. **11**(6): p. 1482.
118. Bykov, A., et al., *Dynamic properties and relaxation processes in surface layer of pulmonary surfactant solutions*. *Colloids and Surfaces A: Physicochemical and Engineering Aspects*, 2019. **573**: p. 14-21.
119. Rogachev, A., et al., *Permeation of Nanoparticles into Pulmonary Surfactant Monolayer: In Situ X-ray Standing Wave Studies*. *Langmuir*, 2022. **38**(12): p. 3630-3640.
120. Ravera, F., et al., *Methods and models to investigate the physicochemical functionality of pulmonary surfactant*. *Current Opinion in Colloid & Interface Science*, 2021. **55**: p. 101467.
121. Zasadzinski, J.A., et al., *Overcoming rapid inactivation of lung surfactant: analogies between competitive adsorption and colloid stability*. *Biochimica et Biophysica Acta (BBA)-Biomembranes*, 2010. **1798**(4): p. 801-828.
122. Smith, E.C., et al., *Metastability of a supercompressed fluid monolayer*. *Biophysical journal*, 2003. **85**(5): p. 3048-3057.
123. *Surface age*. Available from: <https://www.kruss-scientific.com/en/know-how/glossary/surface-age>.
124. Franses, E.I., O.A. Basaran, and C.-H. Chang, *Techniques to measure dynamic surface tension*. *Current Opinion in Colloid & Interface Science*, 1996. **1**(2): p. 296-303.
125. Guzmán, E., et al., *DPPC–DOPC Langmuir monolayers modified by hydrophilic silica nanoparticles: Phase behaviour, structure and rheology*. *Colloids and Surfaces A: Physicochemical and Engineering Aspects*, 2012. **413**: p. 174-183.

126. Bykov, A., et al., *Influence of temperature on dynamic surface properties of spread DPPC monolayers in a broad range of surface pressures*. Chemistry and physics of lipids, 2019. **225**: p. 104812.
127. Williams, I., J.A. Zasadzinski, and T.M. Squires, *Interfacial rheology and direct imaging reveal domain-templated network formation in phospholipid monolayers penetrated by fibrinogen*. Soft Matter, 2019. **15**(44): p. 9076-9084.
128. Rojewska, M., et al., *Langmuir Monolayer Techniques for the Investigation of Model Bacterial Membranes and Antibiotic Biodegradation Mechanisms*. Membranes, 2021. **11**(9): p. 707.
129. Kondej, D. and T.R. Sosnowski, *Interactions of Carbon Nanotubes and Carbon Nanohorns with a Model Membrane Layer and Lung Surfactant In Vitro*. Journal of Nanomaterials, 2019. **2019**: p. 9457683.
130. Bykov, A., et al., *Impact of Polymer Nanoparticles on DPPC Monolayer Properties*. Colloids and Interfaces, 2022. **6**(2): p. 28.
131. Diez, M.M., et al., *The method of depositing CeO₂ nanoparticles onto a DPPC monolayer affects surface tension behaviour*. NanoImpact, 2019. **16**: p. 100186.
132. Forest, V., *Combined effects of nanoparticles and other environmental contaminants on human health-an issue often overlooked*. NanoImpact, 2021. **23**: p. 100344.
133. Miller, R. and L. Liggieri, *Bubble and drop interfaces*. Vol. 2. 2011: CRC Press.
134. Miller, R. and L. Liggieri, *Interfacial rheology*. Vol. 1. 2009: CRC Press.
135. Vrânceanu, M., et al., *Surface rheology of monolayers of phospholipids and cholesterol measured with axisymmetric drop shape analysis*. Colloids and Surfaces A: Physicochemical and Engineering Aspects, 2007. **311**(1-3): p. 140-153.
136. Vrânceanu, M., et al., *Surface rheology and phase transitions of monolayers of phospholipid/cholesterol mixtures*. Biophysical journal, 2008. **94**(10): p. 3924-3934.

137. Chakravarty, A., et al., *Pulmonary drug delivery and retention: A computational study to identify plausible parameters based on a coupled airway-mucus flow model*. PLOS Computational Biology, 2022. **18**(6): p. e1010143.
138. Kondej, D. and T.R. Sosnowski, *Interfacial rheology for the assessment of potential health effects of inhaled carbon nanomaterials at variable breathing conditions*. Scientific Reports, 2020. **10**(1): p. 1-10.
139. Guzmán, E., et al., *Influence of silica nanoparticles on dilational rheology of DPPC–palmitic acid Langmuir monolayers*. Soft Matter, 2012. **8**(14): p. 3938-3948.
140. Li, P., et al., *Heterostructure of anatase-rutile aggregates boosting the photoreduction of U (VI)*. Applied Surface Science, 2019. **483**: p. 670-676.
141. Marsh, D., *Handbook of lipid bilayers*. 2013: CRC press.
142. Sheridan, A.J., et al., *Changes to DPPC domain structure in the presence of carbon nanoparticles*. Langmuir, 2017. **33**(39): p. 10374-10384.
143. Melbourne, J., et al., *An investigation of the carbon nanotube–Lipid interface and its impact upon pulmonary surfactant lipid function*. Biomaterials, 2015. **55**: p. 24-32.
144. Muñoz-López, R., et al., *Influence of Carbon Nanosheets on the Behavior of 1, 2-Dipalmitoyl-sn-glycerol-3-phosphocholine Langmuir Monolayers*. Processes, 2020. **8**(1): p. 94.
145. Wüstneck, R., et al., *Stress relaxation behaviour of dipalmitoyl phosphatidylcholine monolayers spread on the surface of a pendant drop*. Colloids and Surfaces B: Biointerfaces, 1999. **15**(3-4): p. 275-288.
146. Zhao, Q., et al., *Influence of volatile organic compounds (VOCs) on pulmonary surfactant monolayers at air-water interface: Implication for the pulmonary health*. Colloids and Surfaces A: Physicochemical and Engineering Aspects, 2019. **562**: p. 402-408.
147. Rasband, W.S., *ImageJ*. 1997-2018, U. S. National Institutes of Health, Bethesda, Maryland, USA, <https://imagej.nih.gov/ij/>.
148. Maestro, A., et al., *Contact angle of micro-and nanoparticles at fluid interfaces*. Current opinion in colloid & interface science, 2014. **19**(4): p. 355-367.

149. Paunov, V.N., *Novel method for determining the three-phase contact angle of colloid particles adsorbed at air– water and oil– water interfaces*. *Langmuir*, 2003. **19**(19): p. 7970-7976.
150. Cayre, O.J. and V.N. Paunov, *Contact angles of colloid silica and gold particles at air– water and oil– water interfaces determined with the gel trapping technique*. *Langmuir*, 2004. **20**(22): p. 9594-9599.
151. Arnaudov, L.N., et al., *Measuring the three-phase contact angle of nanoparticles at fluid interfaces*. *Physical Chemistry Chemical Physics*, 2010. **12**(2): p. 328-331.
152. Babay, P.A., et al., *Kinetics and mechanisms of EDTA photocatalytic degradation with TiO₂ under different experimental conditions*. *International Journal of Photoenergy*, 2001. **3**(4): p. 193-199.
153. Cayre, O.J. and V.N. Paunov, *Fabrication of microlens arrays by gel trapping of self-assembled particle monolayers at the decane–water interface*. *Journal of Materials Chemistry*, 2004. **14**(22): p. 3300-3302.
154. *16:0 PC-d62*. Available from: <https://avantilipids.com/product/860355>.
155. Brisebois, P.P., et al., *Comparative study of the interaction of fullereneol nanoparticles with eukaryotic and bacterial model membranes using solid-state NMR and FTIR spectroscopy*. *European Biophysics Journal*, 2012. **41**(6): p. 535-544.
156. *Delta 6.1.0*. JEOL.
157. Javadi, A., et al., *Interfacial dynamics methods*, in *Encyclopedia of Colloid and Interface Science*. 2013, Wiley-VCH. p. 637-676.
158. Zholob, S., et al., *Optimisation of calculation methods for determination of surface tensions by drop profile analysis tensiometry*. *Advances in colloid and interface science*, 2007. **134**: p. 322-329.
159. Javadi, A., et al., *Characterization methods for liquid interfacial layers*. *The European Physical Journal Special Topics*, 2013. **222**(1): p. 7-29.
160. Foxman, E.F., et al., *Temperature-dependent innate defense against the common cold virus limits viral replication at warm temperature in mouse airway cells*. *Proceedings of the National Academy of Sciences*, 2015. **112**(3): p. 827-832.

161. Vargaftik, N., B. Volkov, and L. Voljak, *International tables of the surface tension of water*. Journal of Physical and Chemical Reference Data, 1983. **12**(3): p. 817-820.
162. *Minitab 18 Statistical Software*. 2017: State College, PA, www.minitab.com.
163. *IsoFit(Old)*. Available from: <http://www.thomascat.info/Scientific/AdSo/AdSo.htm>.
164. Wu, Q., et al., *High sensitivity SMS fiber structure based refractometer—analysis and experiment*. Optics Express, 2011. **19**(9): p. 7937-7944.
165. Zholob, S., et al., *Determination of the dilational elasticity and viscosity from the surface tension response to harmonic area perturbations*, in *Interfacial rheology*. 2009. p. 77-102.
166. *Profile Analysis Tensiometer PATIM*. Available from: http://www.sinterface.com/products/measurement/tensiometry/profile_analysis_tensiometer_pat1m/index.html.
167. Sturm, R., *Bioaerosols in the lungs of subjects with different ages-part 1: deposition modeling*. Annals of translational medicine, 2016. **4**(11).
168. Ragnarsdóttir, M. and E.K. Kristinsdóttir, *Breathing movements and breathing patterns among healthy men and women 20–69 years of age*. Respiration, 2006. **73**(1): p. 48-54.
169. Lutfi, M.F., *The physiological basis and clinical significance of lung volume measurements*. Multidisciplinary respiratory medicine, 2017. **12**(1): p. 1-12.
170. Tu, J., K. Inthavong, and G. Ahmadi, *The human respiratory system, in Computational fluid and particle dynamics in the human respiratory system*. 2013, Springer. p. 19-44.
171. Seipenbusch, M., et al. *Interparticle forces in nanoparticle agglomerates*. in *Austria, Salzburg: Proceedings of European Aerosol Conference*. 2007.
172. Toor, A., T. Feng, and T.P. Russell, *Self-assembly of nanomaterials at fluid interfaces*. The European Physical Journal E, 2016. **39**(5): p. 1-13.

173. Sun, L., *Chapter 13-Asphalt mix homogeneity*. Structural Behavior of Asphalt Pavements, LBT-SB of AP Sun, Ed. Butterworth-Heinemann, 2016: p. 821-921.
174. Atif, R. and F. Inam, *Reasons and remedies for the agglomeration of multilayered graphene and carbon nanotubes in polymers*. Beilstein journal of nanotechnology, 2016. **7**(1): p. 1174-1196.
175. Norizan, M.N., et al., *Carbon nanotubes: Functionalisation and their application in chemical sensors*. RSC advances, 2020. **10**(71): p. 43704-43732.
176. Paunov, V.N. and O.J. Cayre, *Supraparticles and "Janus" particles fabricated by replication of particle monolayers at liquid surfaces using a gel trapping technique*. Advanced materials, 2004. **16**(9-10): p. 788-791.
177. Sharp, E.L., et al., *Adsorption of shape-anisotropic and porous particles at the air–water and the decane–water interface studied by the gel trapping technique*. RSC advances, 2014. **4**(5): p. 2205-2213.
178. Adamson, A.W. and A.P. Gast, *Physical chemistry of surfaces*. Vol. 15. 1967: Interscience publishers New York.
179. Rosen, M.J. and J.T. Kunjappu, *Surfactants and interfacial phenomena*. 2012: John Wiley & Sons.
180. Kumal, R.R., T.E. Karam, and L.H. Haber, *Determination of the surface charge density of colloidal gold nanoparticles using second harmonic generation*. The Journal of Physical Chemistry C, 2015. **119**(28): p. 16200-16207.
181. Ge, Z. and Y. Wang, *Estimation of nanodiamond surface charge density from zeta potential and molecular dynamics simulations*. The Journal of Physical Chemistry B, 2017. **121**(15): p. 3394-3402.
182. Yakin, F.E., M. Barisik, and T. Sen, *Pore size and porosity dependent zeta potentials of mesoporous silica nanoparticles*. The Journal of Physical Chemistry C, 2020. **124**(36): p. 19579-19587.
183. Harikrishnan, A., et al., *Effects of interplay of nanoparticles, surfactants and base fluid on the surface tension of nanocolloids*. The European Physical Journal E, 2017. **40**(5): p. 1-14.
184. Jamali, V., et al., *Enhanced ordering in length-polydisperse carbon nanotube solutions at high concentrations as revealed by small angle X-ray scattering*. Soft Matter, 2021. **17**(20): p. 5122-5130.

185. Shima, H., *Buckling of carbon nanotubes: a state of the art review*. Materials, 2011. **5**(1): p. 47-84.
186. J.J., B., *Foams*. 1973, Berlin.Heidelberg.New York: Springer-Verlag New York Inc.
187. Faezian, A., S. Yeganehzad, and H.A. Tighchi, *A simplified model to describe drainage of egg white powder foam containing additives*. Chemical Engineering Science, 2019. **195**: p. 631-641.
188. Weir, A., et al., *Titanium dioxide nanoparticles in food and personal care products*. Environmental science & technology, 2012. **46**(4): p. 2242-2250.
189. Vidmar, J., et al., *Optimization of the procedure for efficient dispersion of titanium dioxide nanoparticles in aqueous samples*. Analytical Methods, 2016. **8**(5): p. 1194-1201.
190. Manan, M., et al., *Effects of nanoparticle types on carbon dioxide foam flooding in enhanced oil recovery*. Petroleum Science and Technology, 2015. **33**(12): p. 1286-1294.
191. Almahfood, M. and B. Bai, *The synergistic effects of nanoparticle-surfactant nanofluids in EOR applications*. Journal of Petroleum Science and Engineering, 2018. **171**: p. 196-210.
192. Ms, D.P., *A pore-scale study on improving CTAB foam stability in heavy crude oil– water system using TiO₂ nanoparticles*. Journal of Petroleum Science and Engineering, 2019. **183**: p. 106411.
193. Razali, N., et al. *Nano-Sized Particle as Foam Stabiliser Designed for Application at High Temperature and Light Crude Oil Condition for Enhanced Oil Recovery-A Fluid-Fluid Case Study*. in *Offshore Technology Conference Asia*. 2018. Offshore Technology Conference.
194. Jami, M., et al., *Photoactivity of titanium dioxide foams*. International Journal of Photoenergy, 2018. **2018**.
195. Llamas, S., et al., *Surface properties of binary TiO₂-SiO₂ nanoparticle dispersions relevant for foams stabilization*. Colloids and Surfaces A: Physicochemical and Engineering Aspects, 2019. **575**: p. 299-309.
196. Arabatzis, I.M. and P. Falaras, *Synthesis of porous nanocrystalline TiO₂ foam*. Nano letters, 2003. **3**(2): p. 249-251.

197. Cao, H., et al., *Synergistic action of TiO₂ particles and surfactants on the foamability and stabilization of aqueous foams*. RSC advances, 2017. **7**(71): p. 44972-44978.
198. Li, H., et al., *Influence factors on the critical micelle concentration determination using pyrene as a probe and a simple method of preparing samples*. Royal Society open science, 2020. **7**(3): p. 192092.
199. Bolis, V., et al., *Hydrophilic/hydrophobic features of TiO₂ nanoparticles as a function of crystal phase, surface area and coating, in relation to their potential toxicity in peripheral nervous system*. Journal of colloid and interface science, 2012. **369**(1): p. 28-39.
200. Hua, X., J. Frechette, and M.A. Bevan, *Nanoparticle adsorption dynamics at fluid interfaces*. Soft matter, 2018. **14**(19): p. 3818-3828.
201. Frumkin, A., *Die Kapillarkurve der höheren Fettsäuren und die Zustandsgleichung der Oberflächenschicht*. Zeitschrift für Physikalische Chemie, 1925. **116**(1): p. 466-484.
202. Fainerman, V. and R. Miller, 2. *Thermodynamics of adsorption of surfactants at the fluid interfaces*, in *Studies in Interface Science*. 2001, Elsevier. p. 99-188.
203. Miller, R., E. Aksenenko, and V. Fainerman, *Dynamic interfacial tension of surfactant solutions*. Advances in colloid and interface science, 2017. **247**: p. 115-129.
204. Vitasari, D., P. Grassia, and P. Martin, *Simulation of dynamics of adsorption of mixed protein-surfactant on a bubble surface*. Colloids and Surfaces A: Physicochemical and Engineering Aspects, 2013. **438**: p. 63-76.
205. Cheng, C. and S.-Y. Ran, *Interaction between DNA and trimethyl-ammonium bromides with different alkyl chain lengths*. The Scientific World Journal, 2014. **2014**.
206. Cases, J., et al., *Long chain ionic surfactants: the understanding of adsorption mechanisms from the resolution of adsorption isotherms*. Colloids and Surfaces A: Physicochemical and Engineering Aspects, 2002. **205**(1-2): p. 85-99.
207. Wu, S., et al., *Determining the critical micelle concentration of surfactants by a simple and fast titration method*. Analytical chemistry, 2019. **92**(6): p. 4259-4265.

208. Nesměrák, K. and I. Němcová, *Determination of critical micelle concentration by electrochemical means*. Analytical letters, 2006. **39**(6): p. 1023-1040.
209. Addanki, S., I.S. Amiri, and P. Yupapin, *Review of optical fibers-introduction and applications in fiber lasers*. Results in Physics, 2018. **10**: p. 743-750.
210. Jee, Y., et al., *Plasmonic conducting metal oxide-based optical fiber sensors for chemical and intermediate temperature-sensing applications*. ACS applied materials & interfaces, 2018. **10**(49): p. 42552-42563.
211. Tan, C.H., Z.J. Huang, and X.G. Huang, *Rapid determination of surfactant critical micelle concentration in aqueous solutions using fiber-optic refractive index sensing*. Analytical biochemistry, 2010. **401**(1): p. 144-147.
212. Hajirasouliha, F., et al., *Can optical fiber compete with profile analysis tensiometry in critical micelle concentration measurement?* Zeitschrift für Physikalische Chemie, 2021. **235**(12): p. 1767-1775.
213. *AQ6370D Optical Spectrum Analyzer*. 2021, YKOGAWA Test and Measurement Corporation.
214. Isobe, H., et al., *Measurements of critical micelle concentration (CMC) using optical fiber covered with porous sol-gel cladding*. Applied surface science, 2005. **244**(1-4): p. 199-202.
215. Ogita, M., et al., *Application of the adsorption effect of optical fibres for the determination of critical micelle concentration*. Sensors and Actuators B: Chemical, 2000. **64**(1-3): p. 147-151.
216. Singh, C. and M. Ogita, *Detection of critical micelle concentration (CMC) using uniform and U-shaped optical fiber in sensing region*. Applied Physics B, 2004. **79**(1): p. 103-105.
217. Ogita, M., et al. *Mechanism and application of critical micelle concentration (CMC) detection using multimode optical fiber*. in *IEEE 2002 28th Annual Conference of the Industrial Electronics Society. IECON 02*. 2002. IEEE.
218. Vatanparast, H., et al., *The role of electrostatic repulsion on increasing surface activity of anionic surfactants in the presence of hydrophilic silica nanoparticles*. Scientific reports, 2018. **8**(1): p. 1-11.

219. Lombardo, D. and M.A. Kiselev, *Methods of Liposomes Preparation: Formation and Control Factors of Versatile Nanocarriers for Biomedical and Nanomedicine Application*. Pharmaceutics, 2022. **14**(3): p. 543.
220. Gouda, A., et al., *Ethanol injection technique for liposomes formulation: An insight into development, influencing factors, challenges and applications*. Journal of Drug Delivery Science and Technology, 2021. **61**: p. 102174.
221. Arai, N., et al., *Self-assembly behaviours of primitive and modern lipid membrane solutions: a coarse-grained molecular simulation study*. Physical Chemistry Chemical Physics, 2016. **18**(28): p. 19426-19432.
222. Salim, M., et al., *Amphiphilic designer nano-carriers for controlled release: from drug delivery to diagnostics*. MedChemComm, 2014. **5**(11): p. 1602-1618.
223. Jurak, M., R. Mroczka, and R. Łopucki, *Properties of artificial phospholipid membranes containing lauryl gallate or cholesterol*. The Journal of Membrane Biology, 2018. **251**(2): p. 277-294.
224. Mkam Tsengam, I.K., et al., *Transformation of Lipid Vesicles into Micelles by Adding Nonionic Surfactants: Elucidating the Structural Pathway and the Intermediate Structures*. The Journal of Physical Chemistry B, 2022. **126**(11): p. 2208-2216.
225. Stevens, M.M., A.R. Honerkamp-Smith, and S.L. Keller, *Solubility limits of cholesterol, lanosterol, ergosterol, stigmaterol, and β -sitosterol in electroformed lipid vesicles*. Soft matter, 2010. **6**(23): p. 5882-5890.
226. Willey, J.D., et al., *Rainwater as a source of Fe (II)-stabilizing ligands to seawater*. Limnology and Oceanography, 2008. **53**(4): p. 1678-1684.
227. Odeh, F., et al., *PFG-NMR Investigation of liposome systems containing hydrotrope*. Journal of dispersion science and technology, 2006. **27**(5): p. 665-669.
228. Chen, K.L. and G.D. Bothun, *Nanoparticles meet cell membranes: probing nonspecific interactions using model membranes*. 2014, ACS Publications.
229. Needham, D., K. Kinoshita, and A. Utoft, *Micro-surface and interfacial tensions measured using the micropipette technique: applications in*

- ultrasound-microbubbles, oil-recovery, lung-surfactants, nanoprecipitation, and microfluidics*. *Micromachines*, 2019. **10**(2): p. 105.
230. Sommer, P., *Interaction between cobalt nanoparticles and DPPC at pulmonary conditions*. 2021.
231. Schulz, M., A. Olubummo, and W.H. Binder, *Beyond the lipid-bilayer: interaction of polymers and nanoparticles with membranes*. *Soft Matter*, 2012. **8**(18): p. 4849-4864.
232. Daniel, M., et al., *Clustering and separation of hydrophobic nanoparticles in lipid bilayer explained by membrane mechanics*. *Scientific reports*, 2018. **8**(1): p. 1-7.
233. Nakamura, H., et al., *Direct translocation of nanoparticles across a model cell membrane by nanoparticle-induced local enhancement of membrane potential*. *Physical Chemistry Chemical Physics*, 2019. **21**(35): p. 18830-18838.
234. Wang, S., et al., *Penetration of nanoparticles across a lipid bilayer: effects of particle stiffness and surface hydrophobicity*. *Nanoscale*, 2019. **11**(9): p. 4025-4034.
235. Mady, M.M. and M.M. Darwish, *Effect of chitosan coating on the characteristics of DPPC liposomes*. *Journal of Advanced Research*, 2010. **1**(3): p. 187-191.
236. Wang, W., et al., *Zeta-potential data reliability of gold nanoparticle biomolecular conjugates and its application in sensitive quantification of surface absorbed protein*. *Colloids and Surfaces B: Biointerfaces*, 2016. **148**: p. 541-548.
237. Binks, B.P., L. Isa, and A.T. Tyowua, *Direct measurement of contact angles of silica particles in relation to double inversion of pickering emulsions*. *Langmuir*, 2013. **29**(16): p. 4923-4927.
238. Maestro, A., et al., *Particle and particle-surfactant mixtures at fluid interfaces: assembly, morphology, and rheological description*. *Advances in Condensed Matter Physics*, 2015. **2015**.
239. Garbin, V., J.C. Crocker, and K.J. Stebe, *Nanoparticles at fluid interfaces: Exploiting capping ligands to control adsorption, stability and dynamics*. *Journal of colloid and interface science*, 2012. **387**(1): p. 1-11.

240. Bornemann, S., M. Herzog, and R. Winter, *Impact of Y³⁺-ions on the structure and phase behavior of phospholipid model membranes*. Physical Chemistry Chemical Physics, 2019. **21**(10): p. 5730-5743.
241. Saleh, D.M., et al., *Comparative carcinogenicity study of a thick, straight-type and a thin, tangled-type multi-walled carbon nanotube administered by intra-tracheal instillation in the rat*. Particle and fibre toxicology, 2020. **17**(1): p. 1-14.
242. Lam, C.-w., et al., *A review of carbon nanotube toxicity and assessment of potential occupational and environmental health risks*. Critical reviews in toxicology, 2006. **36**(3): p. 189-217.
243. Kolosnjaj-Tabi, J., H. Szwarc, and F. Moussa, *Carbon nanotubes: Culprit or witness of air pollution?* Nano Today, 2017. **15**: p. 11-14.
244. Lucassen-Reynders, E. and J. Lucassen, *Surface dilational rheology: past and present*. Interfacial Rheology; Miller, R., Liggieri, L., Eds, 2009.
245. Ravera, F., G. Loglio, and V.I. Kovalchuk, *Interfacial dilational rheology by oscillating bubble/drop methods*. Current Opinion in Colloid & Interface Science, 2010. **15**(4): p. 217-228.
246. MATLAB, *Curve Fitting Toolbox*. 2020.
247. Dugar, S.P., M. Latifi, and E. Mireles-Cabodevila, *Respiratory System Physiology*, in *Basic Sciences in Anesthesia*, E. Farag, et al., Editors. 2018, Springer International Publishing: Cham. p. 329-354.
248. Chiumello, D., et al., *Hysteresis and lung recruitment in acute respiratory distress syndrome patients: a CT scan study*. Critical care medicine, 2020. **48**(10): p. 1494-1502.
249. Zhou, C., et al., *A Nonlinear Hysteretic Model for Automated Prediction of Lung Mechanics during Mechanical Ventilation*. Ifac-papersonline, 2020. **53**(5): p. 817-822.
250. Zhivomirov, H., *Phase Difference Measurement with Matlab*. 2022, MATLAB Central File Exchange. Retrieved May 2022.
251. Sedlacek, M. and M. Krumpholc, *Digital measurement of phase difference-a comparative study of DSP algorithms*. Metrology and Measurement Systems, 2005. **12**(4): p. 427-448.

252. Sedláček, M. *Digital measurement of phase difference of LF signals—A comparison of DSP algorithms*. in *Proceedings of IMEKO XVII World Congress (CD), Dubrovnik, Croatia*. 2003.
253. MATLAB, *Signal Processing Toolbox*.
254. Loglio, G., et al., *Perturbation–response relationship in liquid interfacial systems: non-linearity assessment by frequency–domain analysis*. *Colloids and Surfaces A: Physicochemical and Engineering Aspects*, 2005. **261**(1-3): p. 57-63.
255. Ewoldt, R.H., A. Hosoi, and G.H. McKinley, *New measures for characterizing nonlinear viscoelasticity in large amplitude oscillatory shear*. *Journal of Rheology*, 2008. **52**(6): p. 1427-1458.
256. Markhorst, D.G., H.R. van Genderingen, and A.J. van Vught, *Static pressure-volume curve characteristics are moderate estimators of optimal airway pressures in a mathematical model of (primary/pulmonary) acute respiratory distress syndrome*. *Intensive care medicine*, 2004. **30**(11): p. 2086-2093.
257. Oliveira, C.L., et al., *Entropy production and the pressure–volume curve of the lung*. *Frontiers in Physiology*, 2016. **7**: p. 73.
258. Papandrinopoulou, D., V. Tzouda, and G. Tsoukalas, *Lung compliance and chronic obstructive pulmonary disease*. *Pulmonary medicine*, 2012. **2012**.
259. Grieco, D.L., et al., *Respiratory physiology of COVID-19-induced respiratory failure compared to ARDS of other etiologies*. *Critical Care*, 2020. **24**(1): p. 1-11.
260. *Study finds link between long-term exposure to air pollution and emphysema*. 2019; Available from: <https://www.nih.gov/news-events/news-releases/study-finds-link-between-long-term-exposure-air-pollution-emphysema#:~:text=Long%2Dterm%20exposure%20to%20air%20pollution%20was%20linked%20to%20increases,the%20National%20Institutes%20of%20Health>.
261. Wang, M., et al., *Association between long-term exposure to ambient air pollution and change in quantitatively assessed emphysema and lung function*. *Jama*, 2019. **322**(6): p. 546-556.

Appendix A: Data related to Chapter 6

Figure A.1 shows the dynamic interfacial tension of those samples of CNT+DPPC in which the equilibrium and plateau were reached. As Figure A.1 shows, the interfacial tension of the CNT+DPPC dispersions is more than that of DPPC solution without particles. It means that the depletion of the DPPC is happening.

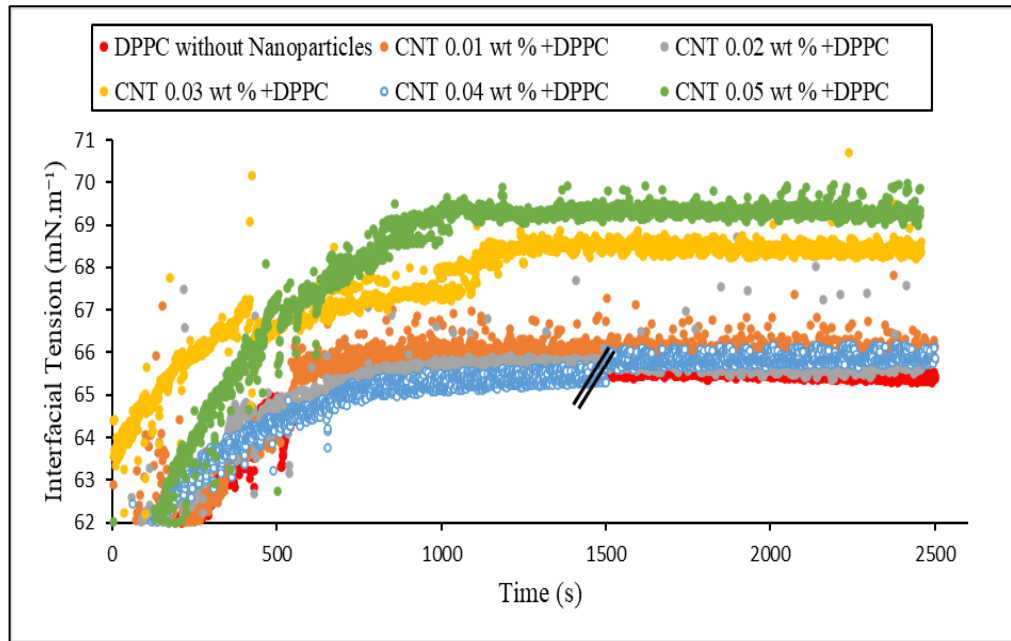


Figure A.1 Dynamic interfacial tension of the dispersions of CNT particles with different concentrations in the DPPC solutions at 37°C. The concentration of the DPPC is constant at 5.38×10^{-8} M in all solutions and dispersions. The red dots, as a reference, are related to the DPPC solution without nanoparticles. The scratched part on the graph of CNT 0.04 wt % is because this experiment was done for 4000 s to reach the equilibrium. Therefore, the data of the last 1000 s has been shifted from the interval of 3000-4000 s in the main experiment.

Figure A.2 (a) and (b) represent the equilibrium interfacial tension values of the CNT+DPPC dispersions vs. different concentrations of CNT particles. It should be noted that the source of the standard deviation in the data related to interfacial tension is the fluctuations of the data points in a single acceptable experiment, but not the average values of three experiments.

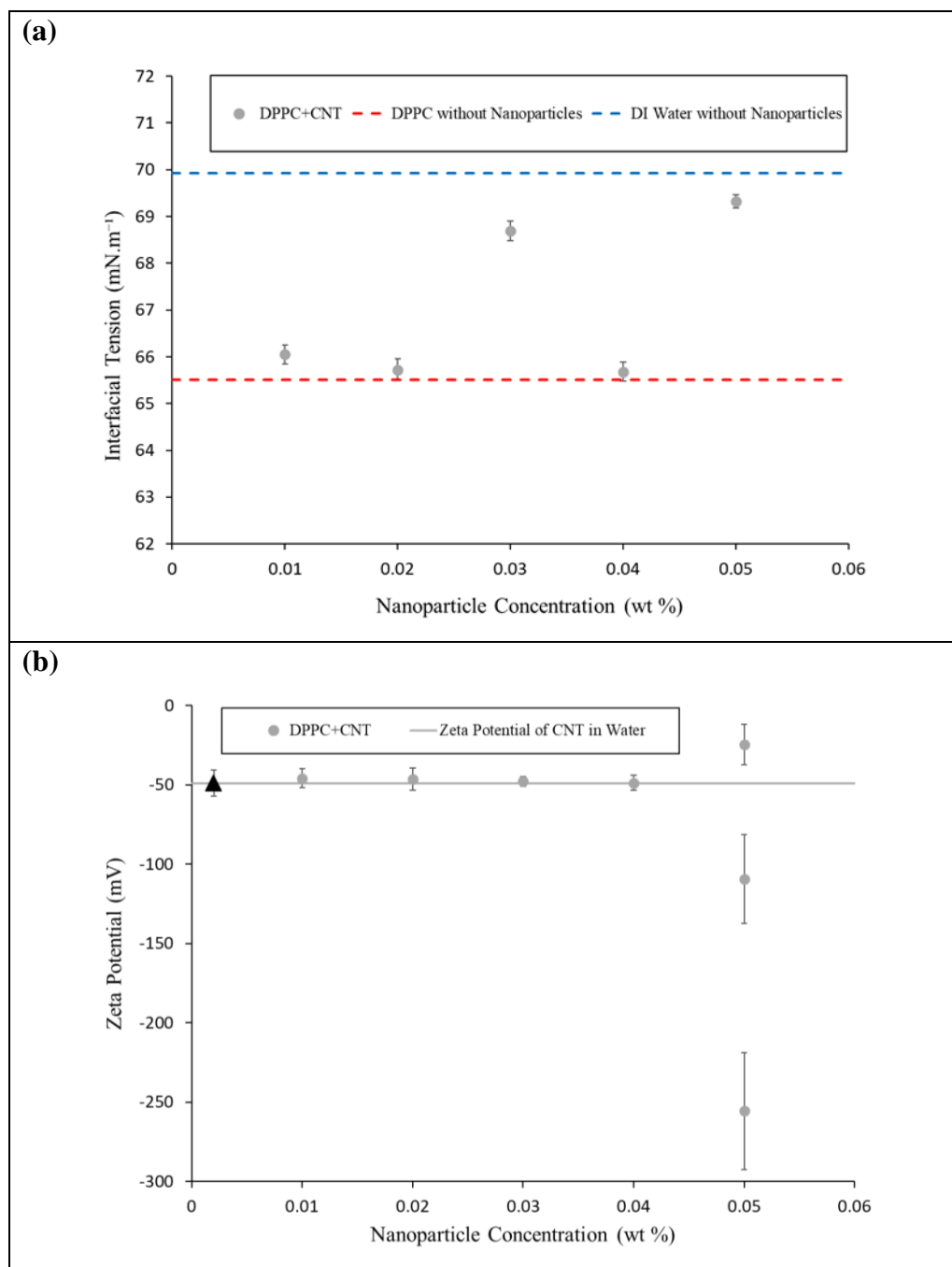


Figure A.2 Equilibrium interfacial tension (a) and zeta potential (b) of the dispersions of CNT particles in the DPPC solutions against the concentration of nanoparticles at 37°C. The concentration of the DPPC is constant at 5.38×10^{-8} M in all solutions and dispersions. The blue and red dashed lines in (a) are the representative of the interfacial tension of DI water without DPPC and with DPPC, respectively. The grey line and the triangle on it in (b) are the representative of the surface charge of CNT particles in water.

Although it is expected that the interactions between the CNT particles and DPPC molecules are controlled by the hydrophobicity of the CNT particles and

the hydrophobic tail (hydrocarbon chains) of the DPPC molecules [74], the lack of the reproducibility of the interfacial tension data is an obstacle in suggesting the most possible mechanism of interactions between CNT particles and DPPC molecules.

Despite the challenge of the reproducibility of the interfacial tension data, the data related to the zeta potential values were quite consistent. The zeta potential values of the CNT+DPPC dispersions at the concentrations of 0.01 wt % to 0.04 wt % are between -46 mV and -48.79 mV. These values are very close to the zeta potential of the CNT particles in DI water (-49.02 ± 8.21 mV). This might be an indication of the limited interactions of the CNT particles and DPPC molecules. This can happen due to the aggregation of CNT particles which results in the reduction of the surface area of the interactions with DPPC molecules [129]. The interfacial tension values of the concentrations of 0.01, 0.02, and 0.04 wt % (Figure A.2, a) also show these limited interactions as the values of interfacial tension are very close to that of DPPC solution without particles (i.e., the red dashed line). However, this is an ambitious expectation to predict the mechanism of the interactions of DPPC molecules and CNT particles, only based on one acceptable interfacial tension experiment.

It should also be noted that, at the highest concentration of 0.05 wt % of CNT particles, three different populations of particles with three different values of zeta potential were observed. As shown in Figure A.2, b, the values of the zeta potential at this unique concentration of 0.05 wt % were -24.52 mV, -109.39 mV, and -255.62 mV. These three different values of zeta potential show that there are three major populations of CNT particles interacted with DPPC. These interactions are not necessarily similar for all CNT particles. Therefore, different populations of CNT particles with various surface charges are identified. As mentioned before, the complementary data of DLS can help in interpreting the zeta potential data in a better way.

Appendix B: MATLAB Codes

Phase Difference Measurement with MATLAB Implementation

Author: M.Sc. Eng. Hristo Zhivomirov [250]

```
% function: PhDiff = phdiffmeasure(x, y)
%
% Input:
% x - first signal in the time domain
% y - second signal in the time domain
%
% Output:
% PhDiff - phase difference Y -> X, rad
function PhDiff = phdiffmeasure(x, y)
% represent the signals as column-vectors
x = x(:);
y = y(:);
% remove the DC component of the signals
x = x - mean(x);
y = y - mean(y);
% signals length calculation
xlen = length(x);
ylen = length(y);
% windows generation
xwin = hanning(xlen, 'periodic');
ywin = hanning(ylen, 'periodic');
% perform fft on the signals
X = fft(x.*xwin);
Y = fft(y.*ywin);
% fundamental frequency detection
[~, indx] = max(abs(X));
[~, indy] = max(abs(Y));
% phase difference estimation
PhDiff = angle(Y(indy)) - angle(X(indx));
end
```

Appendix C: Data related to Chapter 7

Table C.1 The standard deviation (SD) values of the complex viscoelastic modulus obtained for DPPC solution without particles, ATD 0.01 wt % + DPPC, and RTD 0.01 wt % + DPPC.

Sample	Frequency (Hz)	SD Amplitude = 1%	SD Amplitude = 2%	SD Amplitude = 5%	SD Amplitude = 10%
DPPC Solution without Particles	0.1	10.408	10.754	11.266	11.401
	0.125	9.719	9.585	11.473	11.227
	0.25	17.155	12.375	11.153	10.476
	0.5	13.399	10.961	11.282	11.025
ATD 0.01 wt%+DPPC	0.1	2.131	1.871	0.299	0.258
	0.125	0.283	0.196	0.141	0.495
	0.25	2.202	1.259	0.025	1.403
	0.5	0.887	0.384	1.153	1.896
RTD 0.01 wt%+DPPC	0.1	4.290	1.986	0.766	0.529
	0.125	3.556	4.465	0.596	0.148
	0.25	6.218	8.654	3.178	0.467
	0.5	10.643	1.866	2.571	1.270

Table C.2 The standard deviation (SD) values of the phase difference obtained for DPPC solution without particles, ATD 0.01 wt % + DPPC, and RTD 0.01 wt % + DPPC.

Sample	Frequency (Hz)	SD Amplitude = 1%	SD Amplitude = 2%	SD Amplitude = 5%	SD Amplitude = 10%
DPPC Solution without Particles	0.1	0.571	3.148	0.187	0.028
	0.125	4.036	0.090	0.129	0.054
	0.25	0.421	3.300	0.621	0.060
	0.5	6.479	0.971	0.313	0.044
ATD 0.01 wt%+DPPC	0.1	9.162	6.778	5.875	0.216
	0.125	18.415	9.632	4.194	0.861
	0.25	25.416	17.735	3.747	0.126
	0.5	11.597	8.733	6.087	1.228
RTD 0.01 wt%+DPPC	0.1	22.215	7.331	4.807	1.413
	0.125	6.832	1.603	11.251	0.369
	0.25	12.935	13.387	5.322	0.734
	0.5	85.098	94.644	8.911	1.005

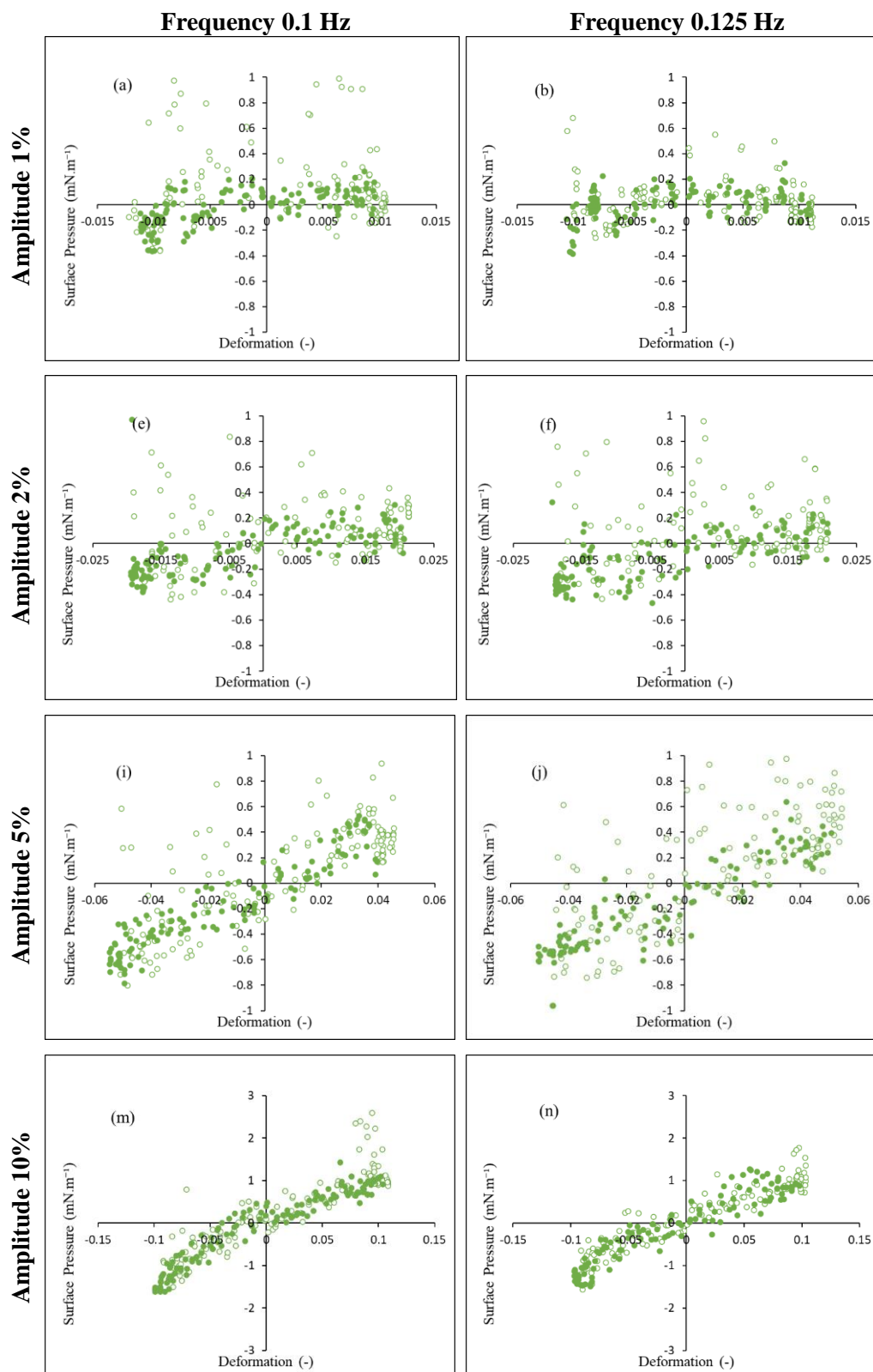


Figure C.1 Part 1 Lissajous plots for ATD 0.01 wt%+DPPC at the amplitudes of 1% (a-b), 2% (e-f), 5% (i-j), and 10% (m-n). The data were obtained for all frequencies including 0.1 Hz (left column) and 0.125 Hz (right column). The hollow dots and filled dots are related to the expansion and compression, respectively.

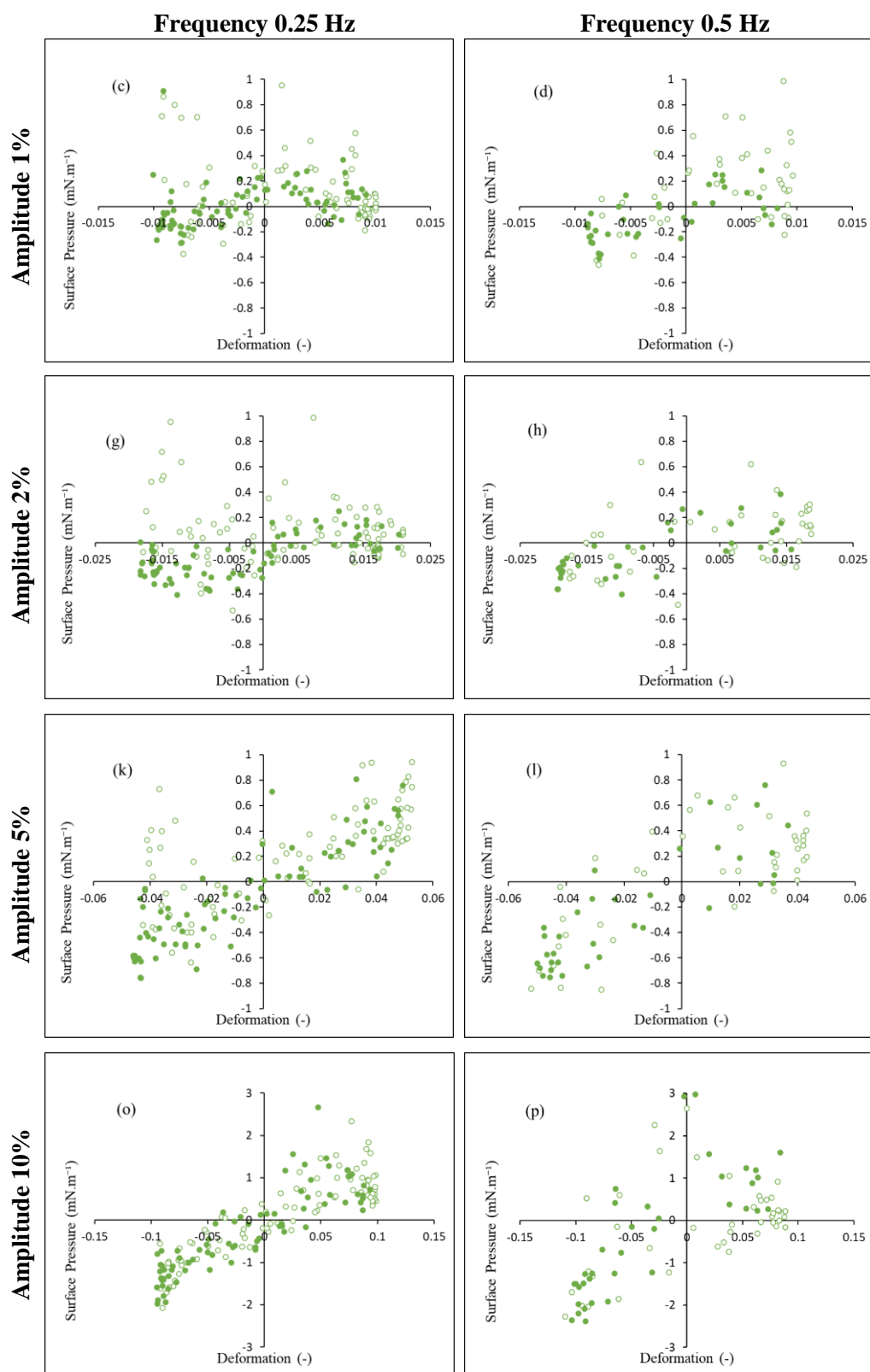


Figure C.1_Part 2 Lissajous plots for ATD 0.01 wt%+DPPC at the amplitudes of 1% (c-d), 2% (g-h), 5% (k-l), and 10% (o-p). The data were obtained for all frequencies including 0.25 Hz (left column) and 0.5 Hz (right column). The hollow dots and filled dots are related to the expansion and compression, respectively.

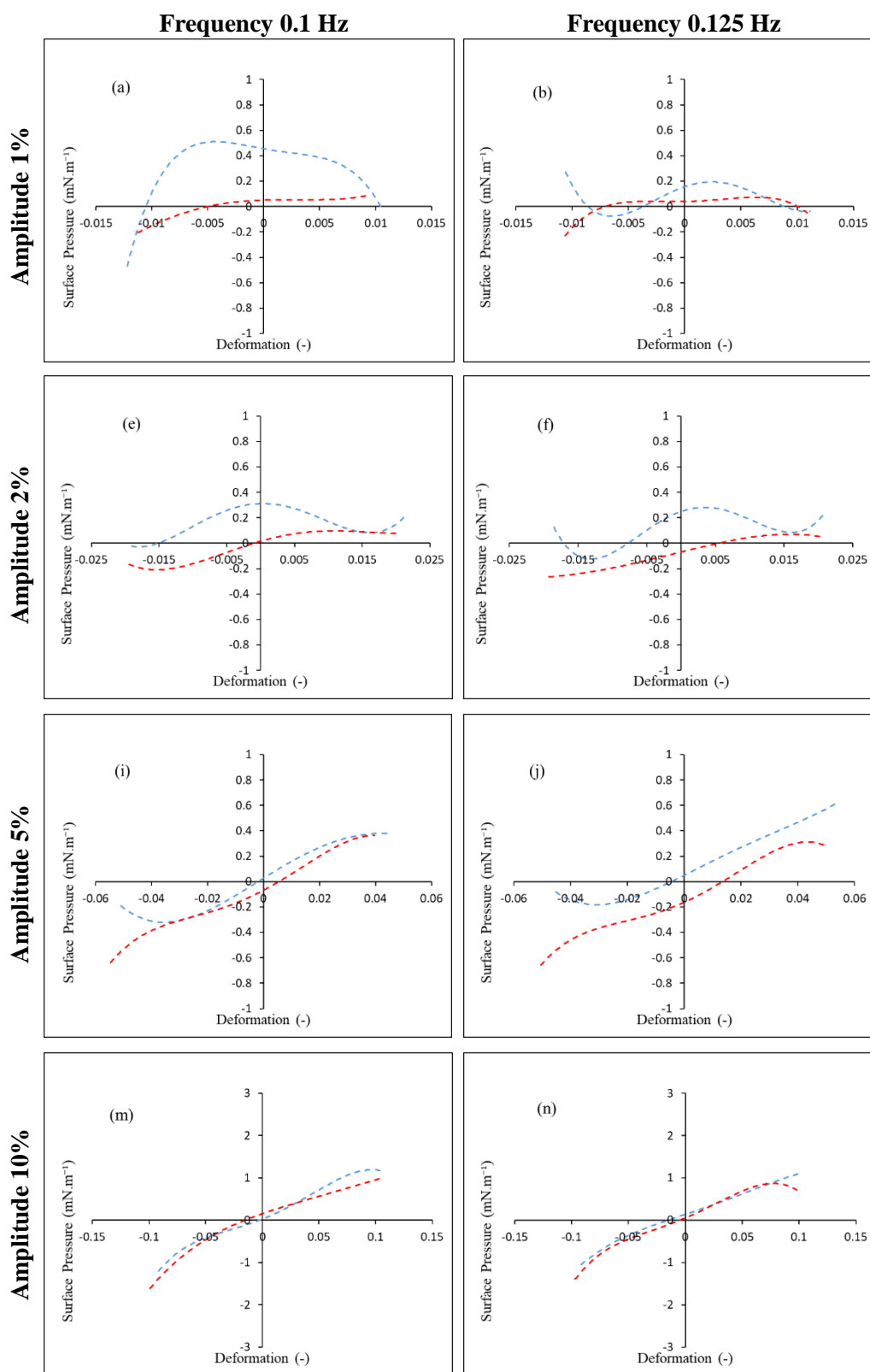


Figure C.2 Part 1 The fourth order polynomial curve fitted on the data of Lissajous plots for ATD 0.01 wt%+DPPC at the amplitudes of 1% (a-b), 2% (e-f), 5% (i-j), and 10% (m-n). The data were obtained for all frequencies including 0.1 Hz (left column) and 0.125 Hz (right column). The blue and red dashed lines are related to the expansion and compression, respectively.

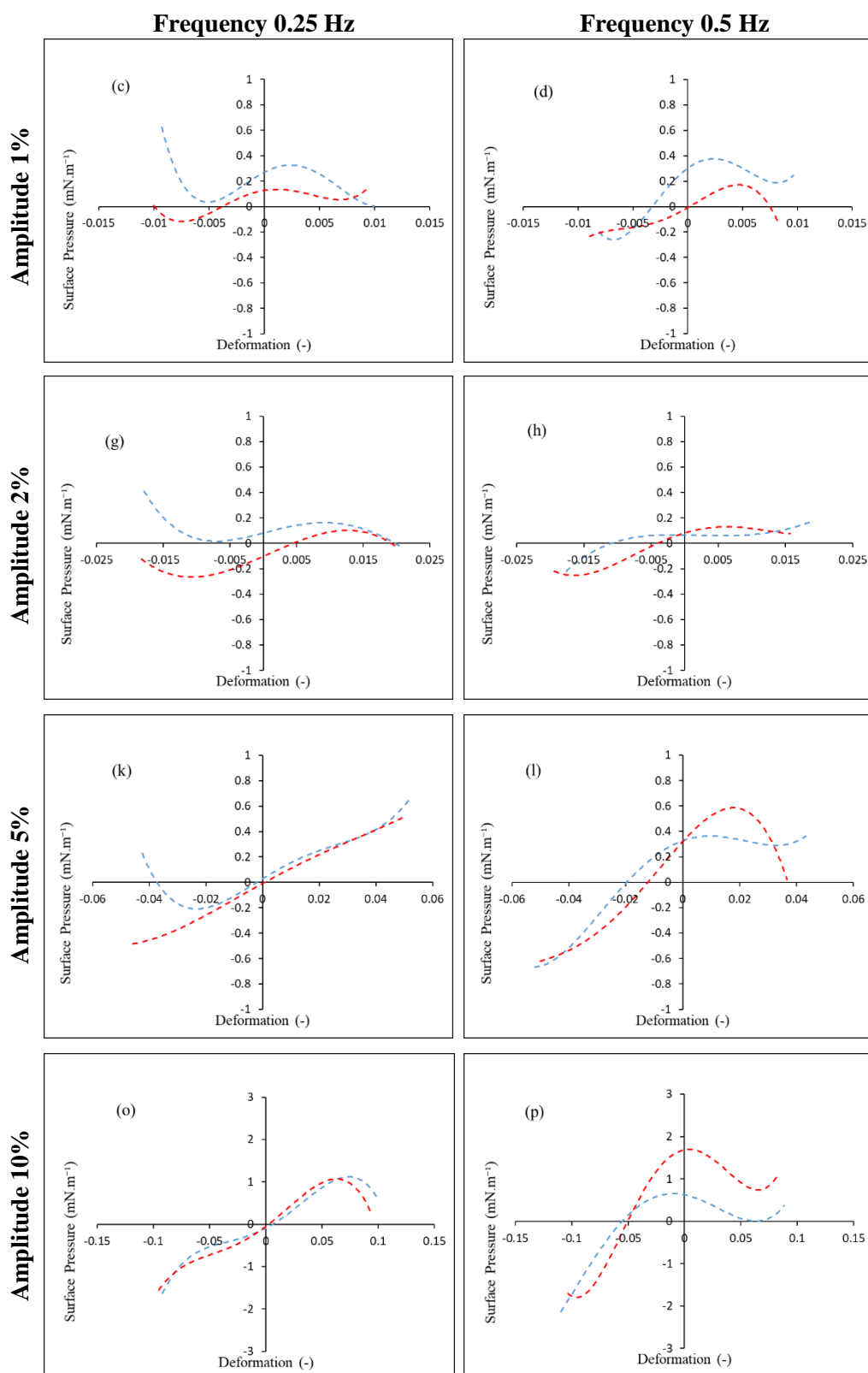


Figure C.2 Part 2 The fourth order polynomial curve fitted on the data of Lissajous plots for ATD 0.01 wt%+DPPC at the amplitudes of 1% (c-d), 2% (g-h), 5% (k-l), and 10% (o-p). The data were obtained for all frequencies including 0.25 Hz (left column) and 0.5 Hz (right column). The blue and red dashed lines are related to the expansion and compression, respectively.

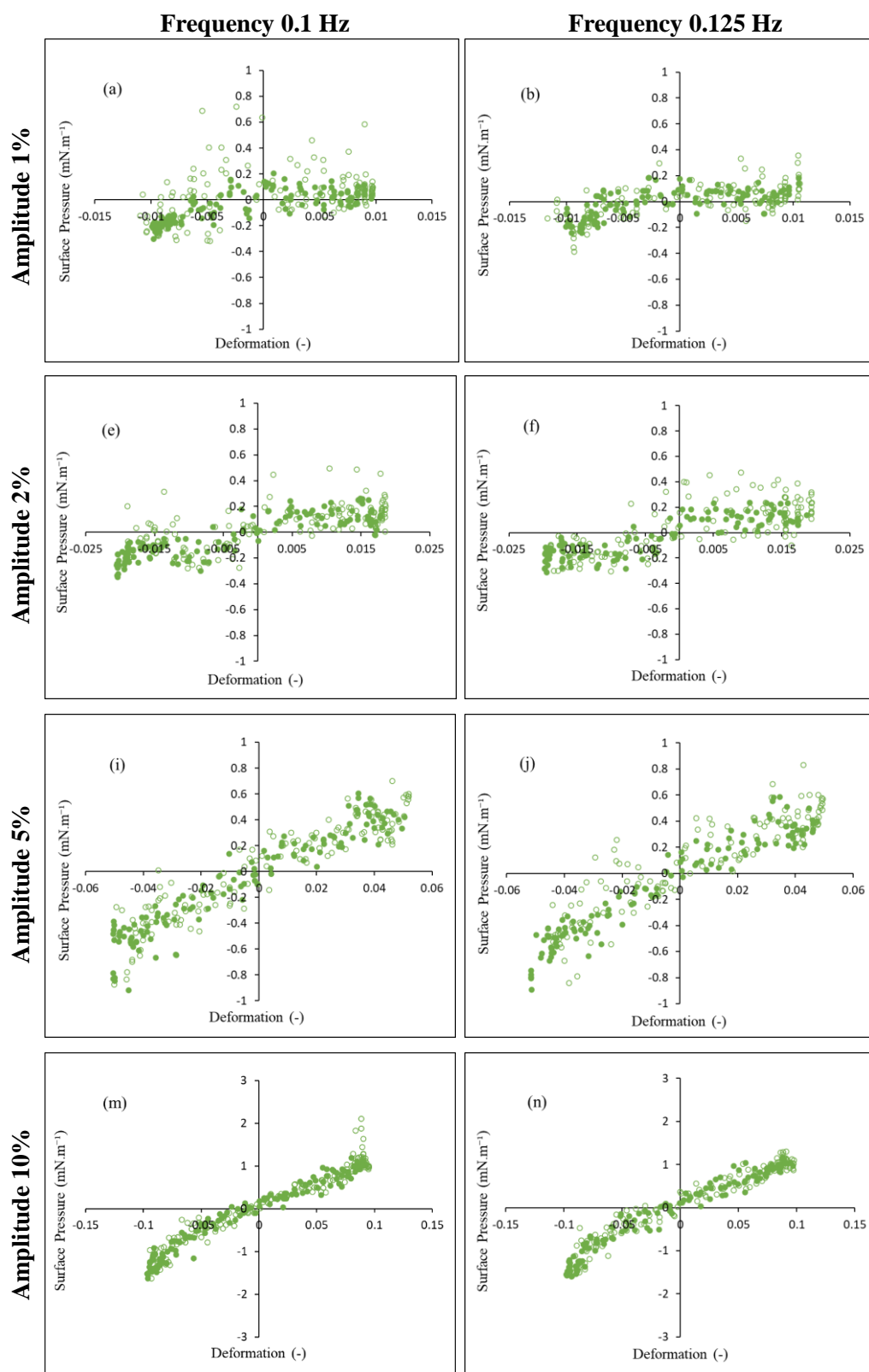


Figure C.3_Part 1 Lissajous plots for ATD 0.02 wt%+DPPC at the amplitudes of 1% (a-b), 2% (e-f), 5% (i-j), and 10% (m-n). The data were obtained for all frequencies including 0.1 Hz (left column) and 0.125 Hz (right column). The hollow dots and filled dots are related to the expansion and compression, respectively.

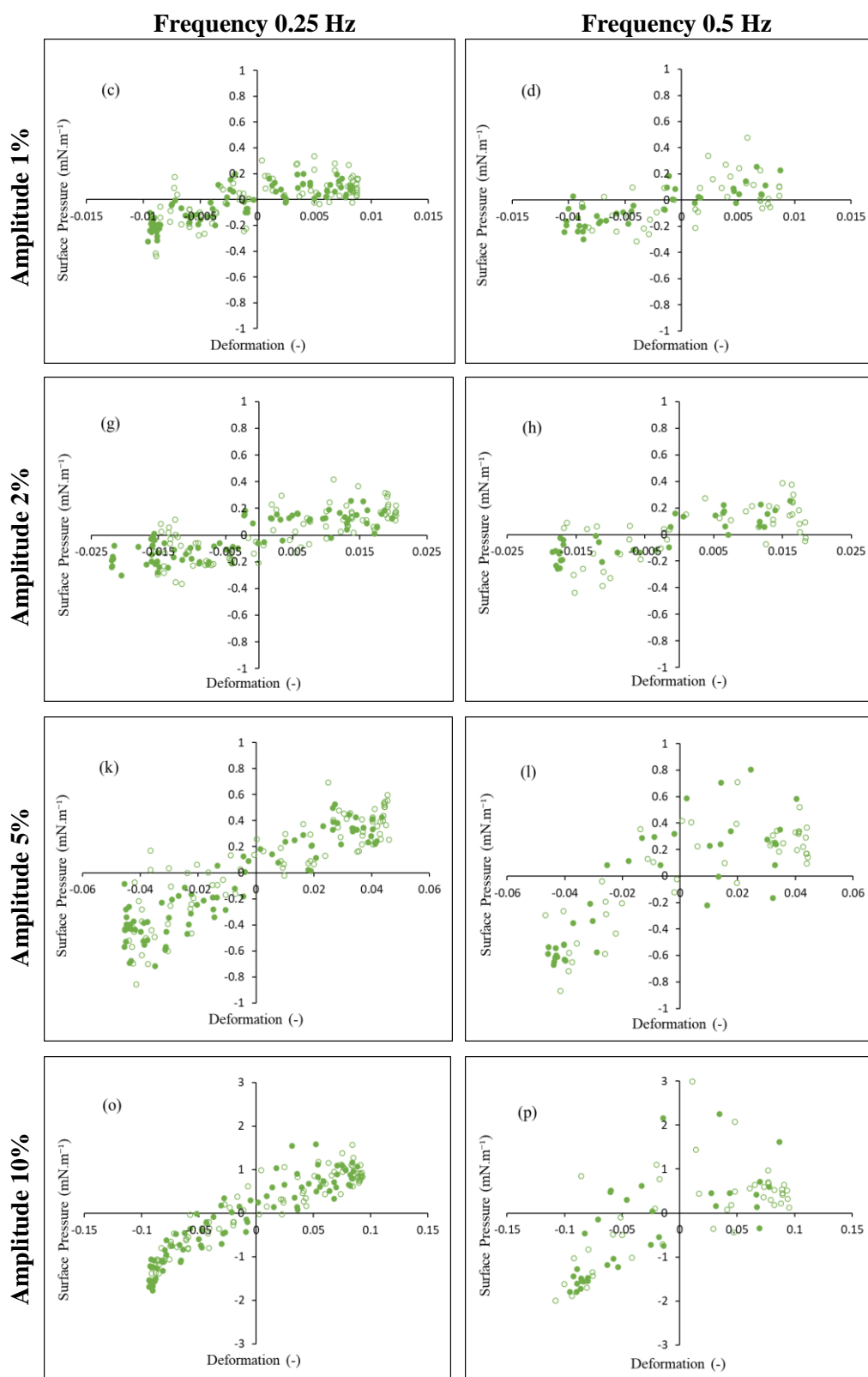


Figure C.3_Part 2 Lissajous plots for ATD 0.02 wt%+DPPC at the amplitudes of 1% (c-d), 2% (g-h), 5% (k-l), and 10% (o-p). The data were obtained for all frequencies including 0.25 Hz (left column) and 0.5 Hz (right column). The hollow dots and filled dots are related to the expansion and compression, respectively.

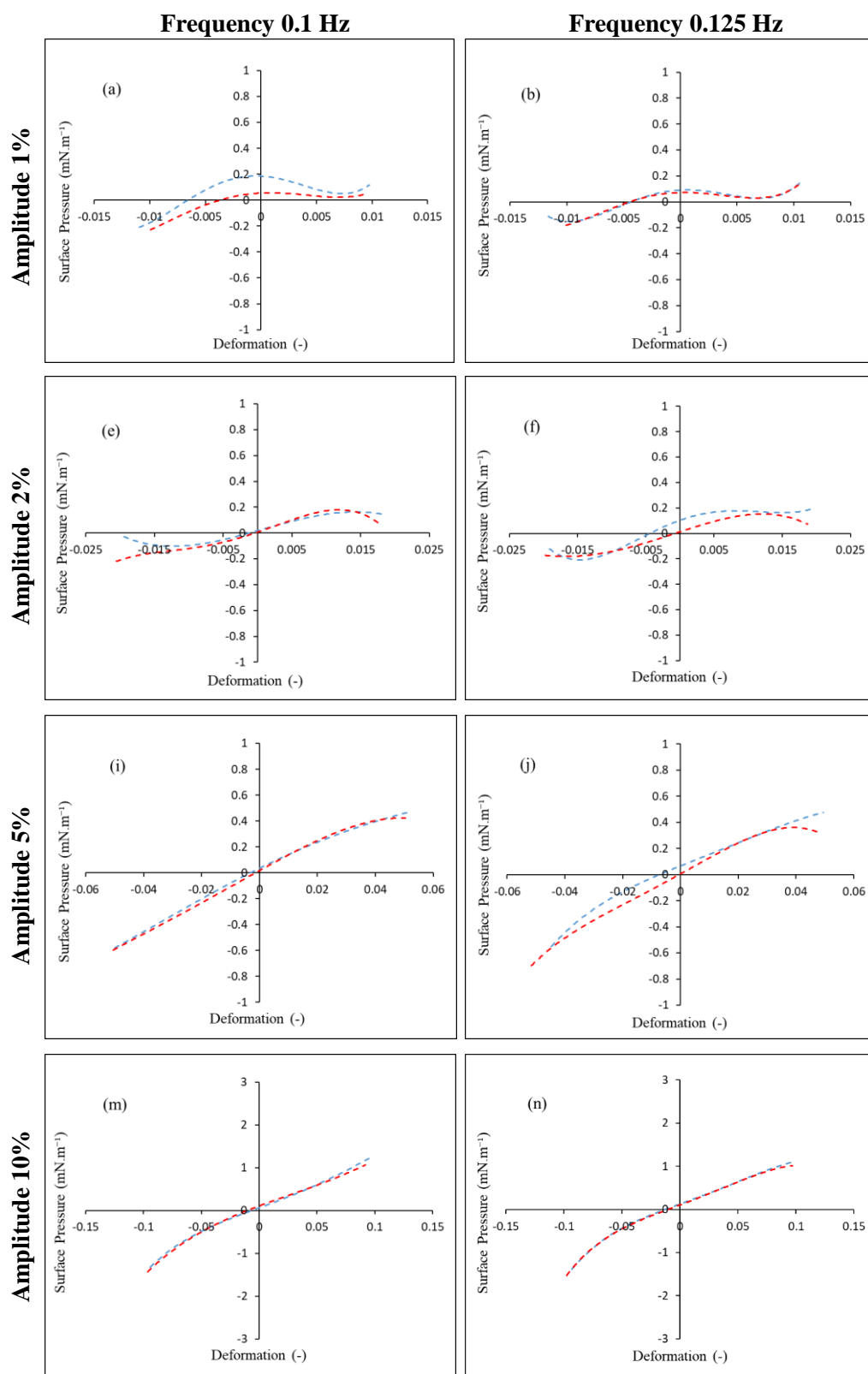


Figure C.4 Part 1 The fourth order polynomial curve fitted on the data of Lissajous plots for ATD 0.02 wt%+DPPC at the amplitudes of 1% (a-b), 2% (e-f), 5% (i-j), and 10% (m-n). The data were obtained for all frequencies including 0.1 Hz (left column) and 0.125 Hz (right column). The blue and red dashed lines are related to the expansion and compression, respectively.

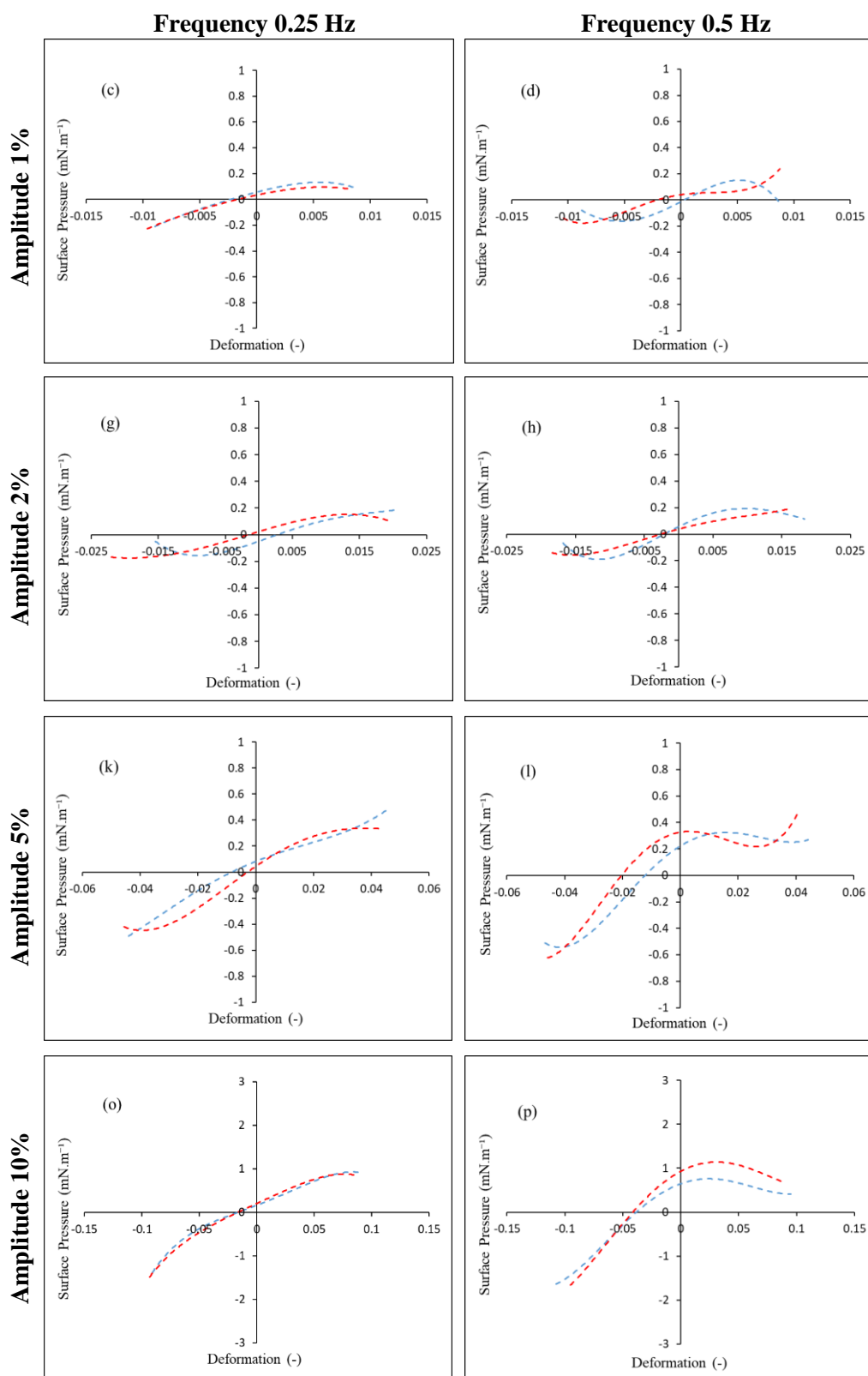


Figure C.4 Part 2 The fourth order polynomial curve fitted on the data of Lissajous plots for ATD 0.02 wt%+DPPC at the amplitudes of 1% (c-d), 2% (g-h), 5% (k-l), and 10% (o-p). The data were obtained for all frequencies including 0.25 Hz (left column) and 0.5 Hz (right column). The blue and red dashed lines are related to the expansion and compression, respectively.

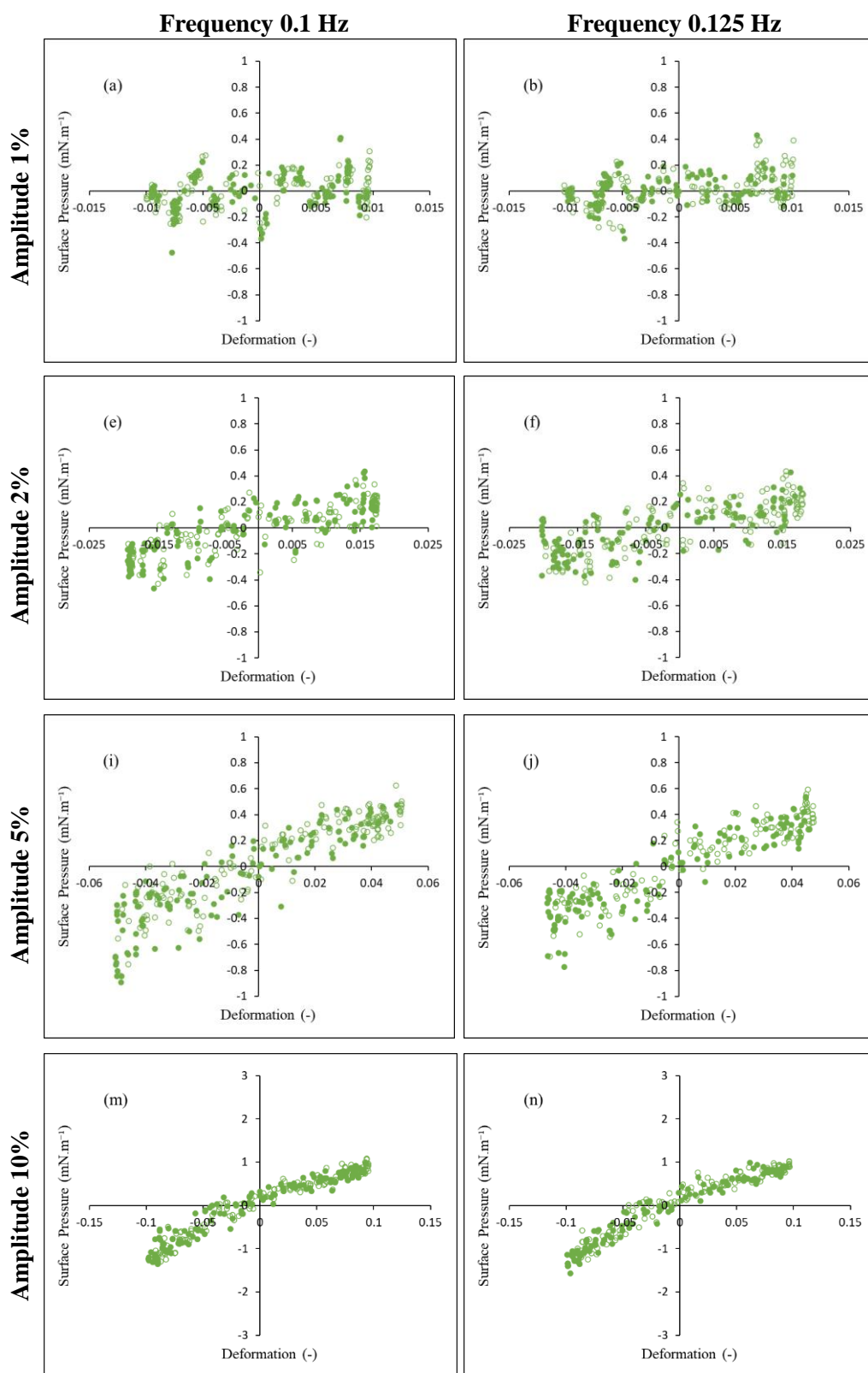


Figure C.5_Part 1 Lissajous plots for ATD 0.03 wt%+DPPC at the amplitudes of 1% (a-b), 2% (e-f), 5% (i-j), and 10% (m-n). The data were obtained for all frequencies including 0.1 Hz (left column) and 0.125 Hz (right column). The hollow dots and filled dots are related to the expansion and compression, respectively.

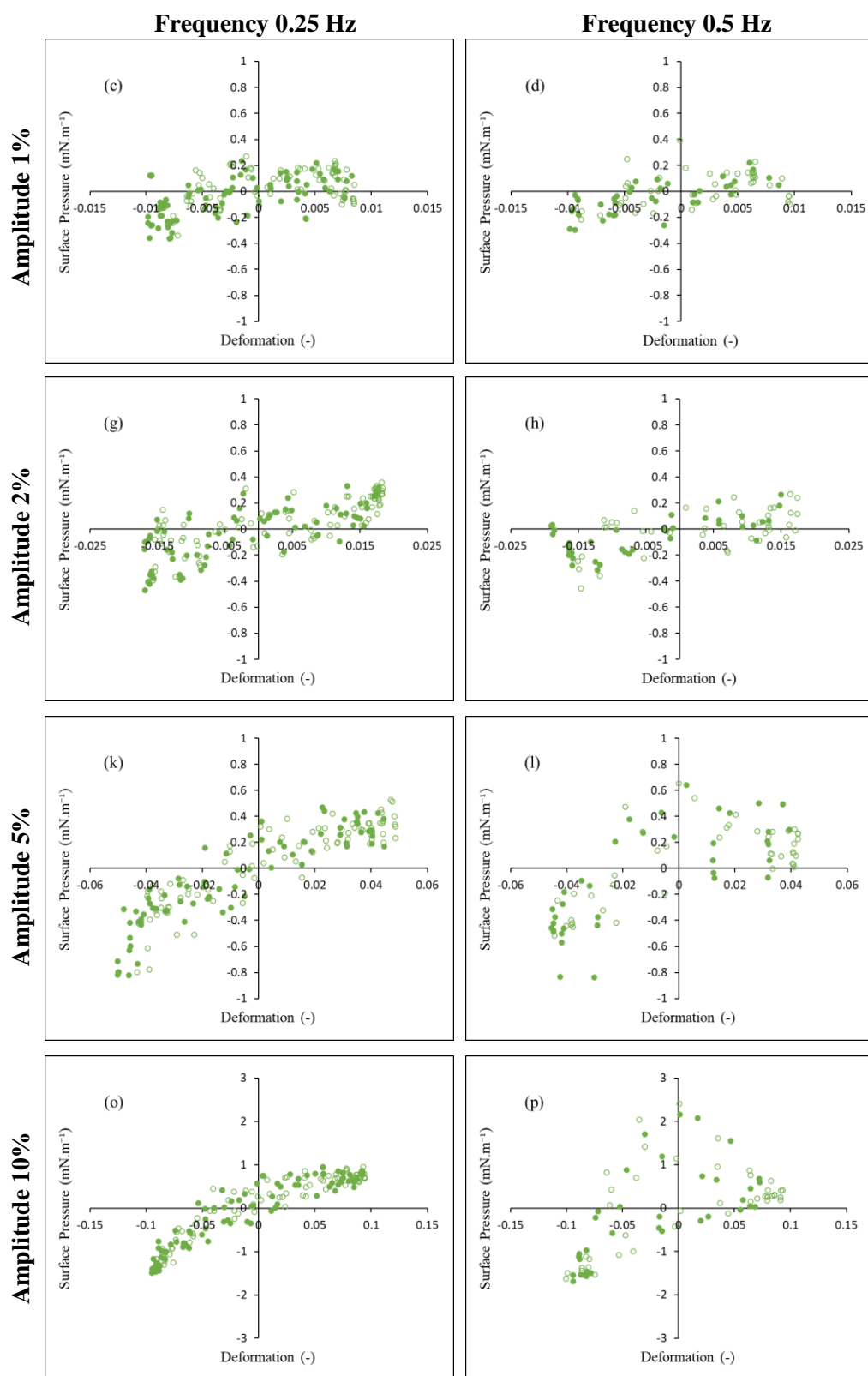


Figure C.5_Part 2 Lissajous plots for ATD 0.03 wt%+DPPC at the amplitudes of 1% (c-d), 2% (g-h), 5% (k-l), and 10% (o-p). The data were obtained for all frequencies including 0.25 Hz (left column) and 0.5 Hz (right column). The hollow dots and filled dots are related to the expansion and compression, respectively.

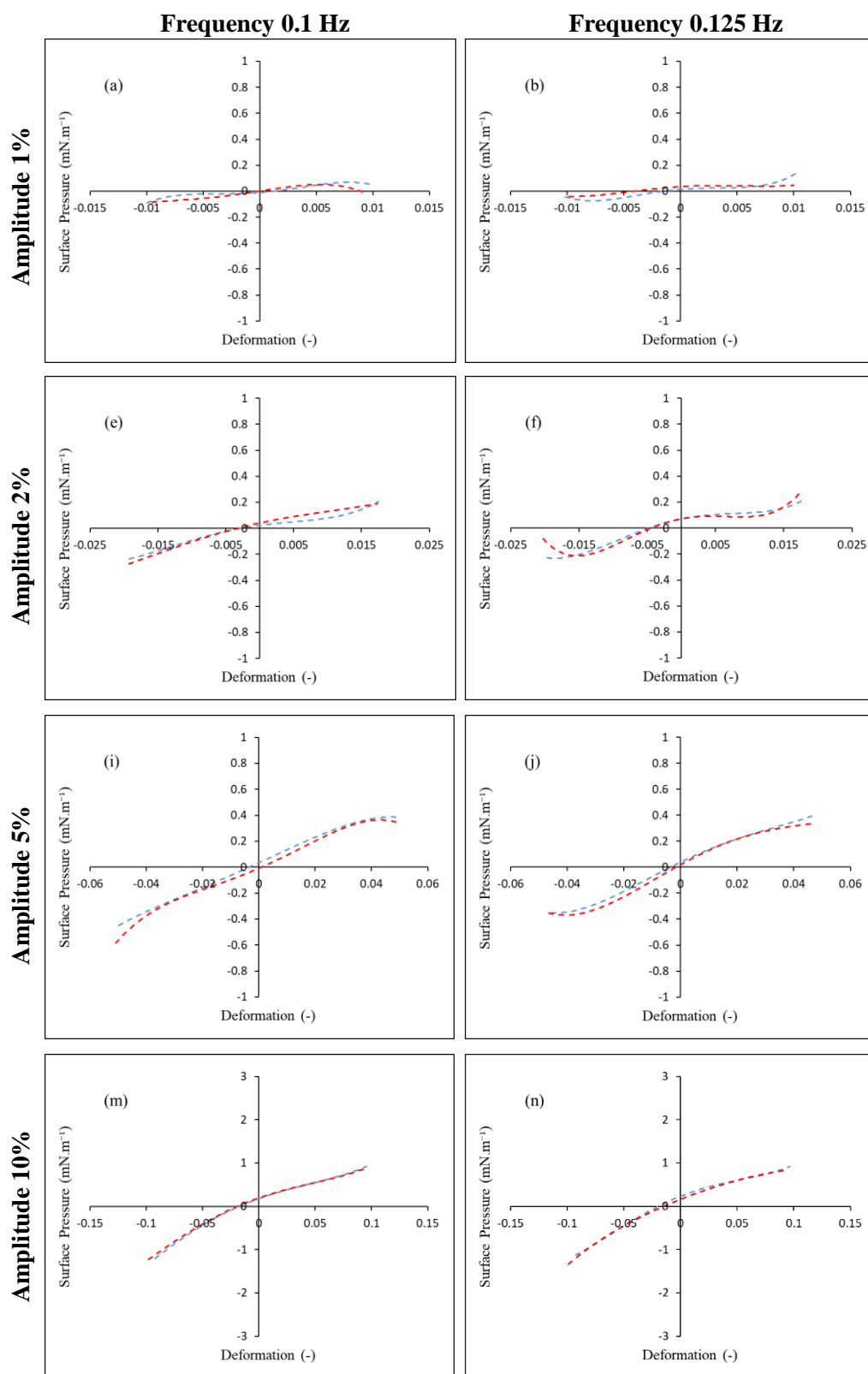


Figure C.6 Part 1 The fourth order polynomial curve fitted on the data of Lissajous plots for ATD 0.03 wt%+DPPC at the amplitudes of 1% (a-b), 2% (e-f), 5% (i-j), and 10% (m-n). The data were obtained for all frequencies including 0.1 Hz (left column) and 0.125 Hz (right column). The blue and red dashed lines are related to the expansion and compression, respectively.

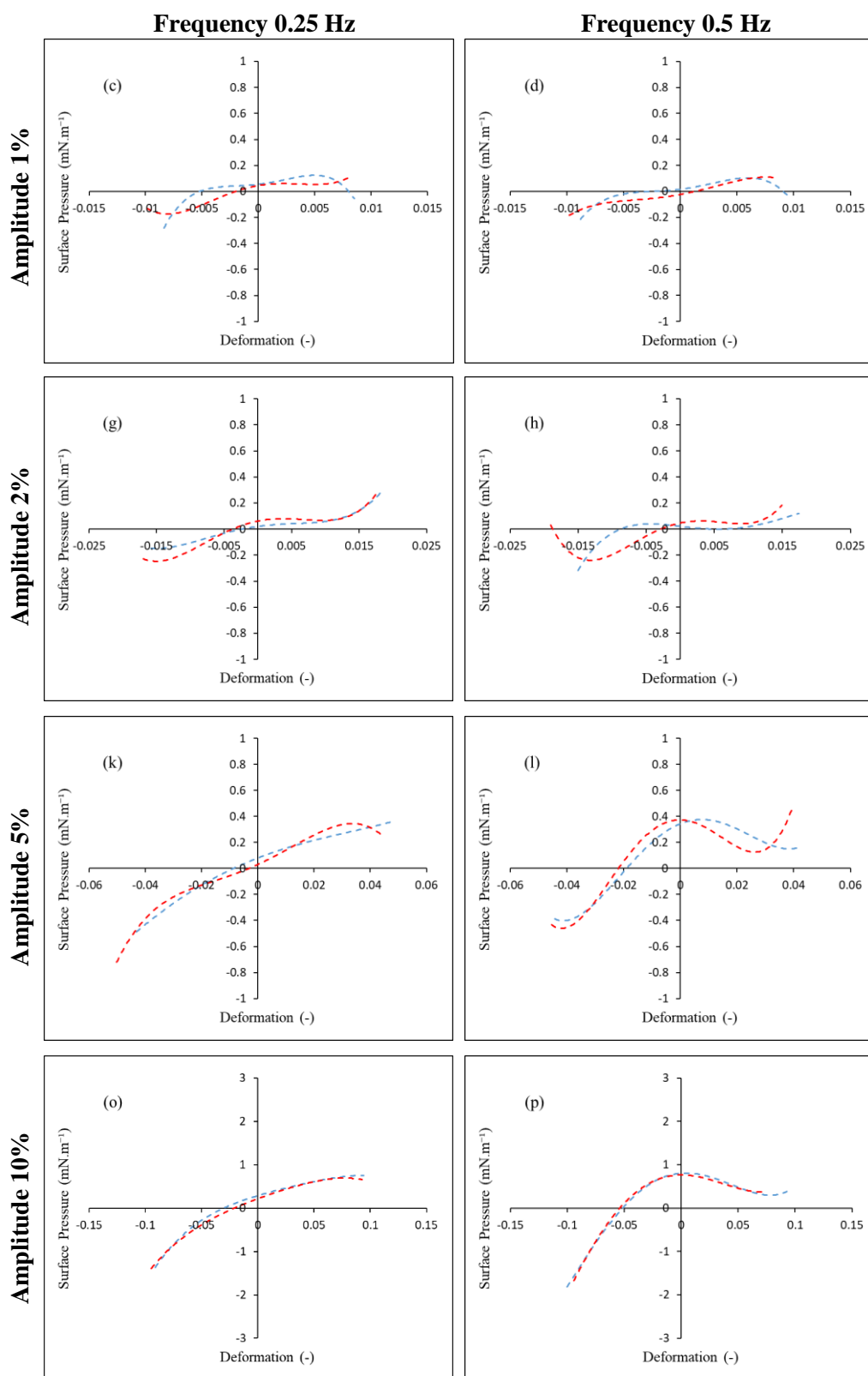


Figure C.6 Part 2 The fourth order polynomial curve fitted on the data of Lissajous plots for ATD 0.03 wt%+DPPC at the amplitudes of 1% (c-d), 2% (g-h), 5% (k-l), and 10% (o-p). The data were obtained for all frequencies including 0.25 Hz (left column) and 0.5 Hz (right column). The blue and red dashed lines are related to the expansion and compression, respectively.

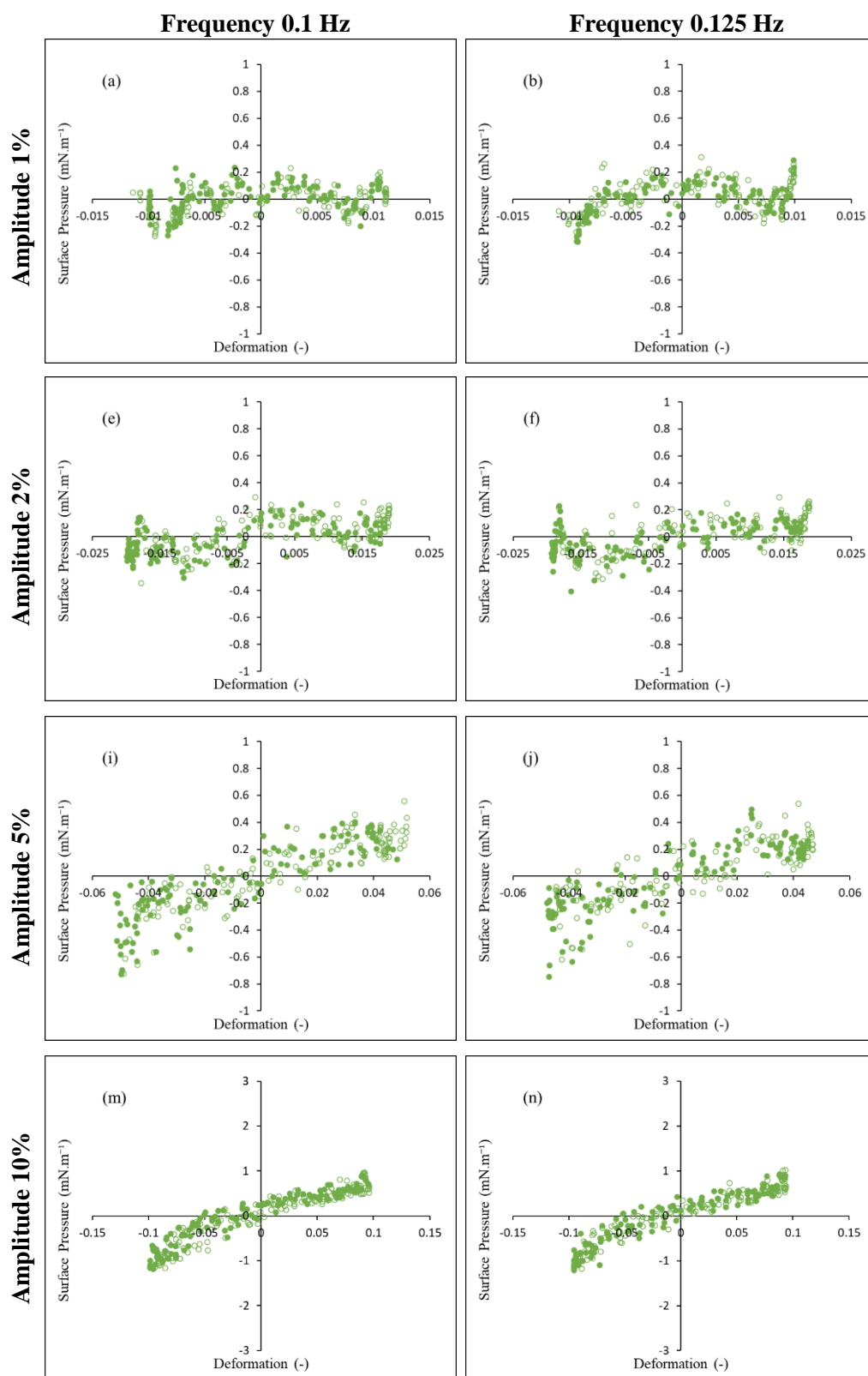


Figure C.7_Part 1 Lissajous plots for ATD 0.04 wt%+DPPC at the amplitudes of 1% (a-b), 2% (e-f), 5% (i-j), and 10% (m-n). The data were obtained for all frequencies including 0.1 Hz (left column) and 0.125 Hz (right column). The hollow dots and filled dots are related to the expansion and compression, respectively.

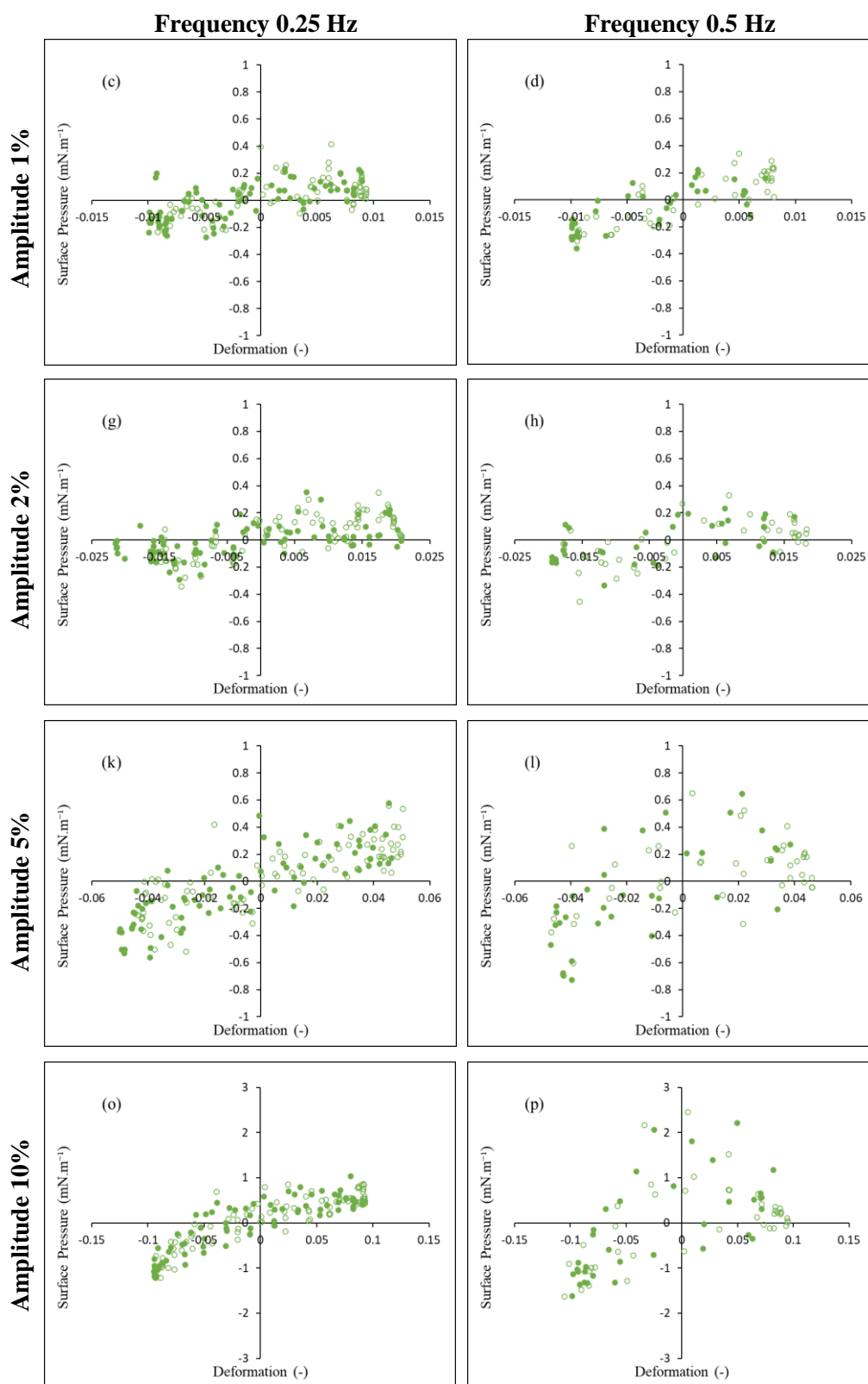


Figure C.7_Part 2 Lissajous plots for ATD 0.04 wt%+DPPC at the amplitudes of 1% (c-d), 2% (g-h), 5% (k-l), and 10% (o-p). The data were obtained for all frequencies including 0.25 Hz (left column) and 0.5 Hz (right column). The hollow dots and filled dots are related to the expansion and compression, respectively.

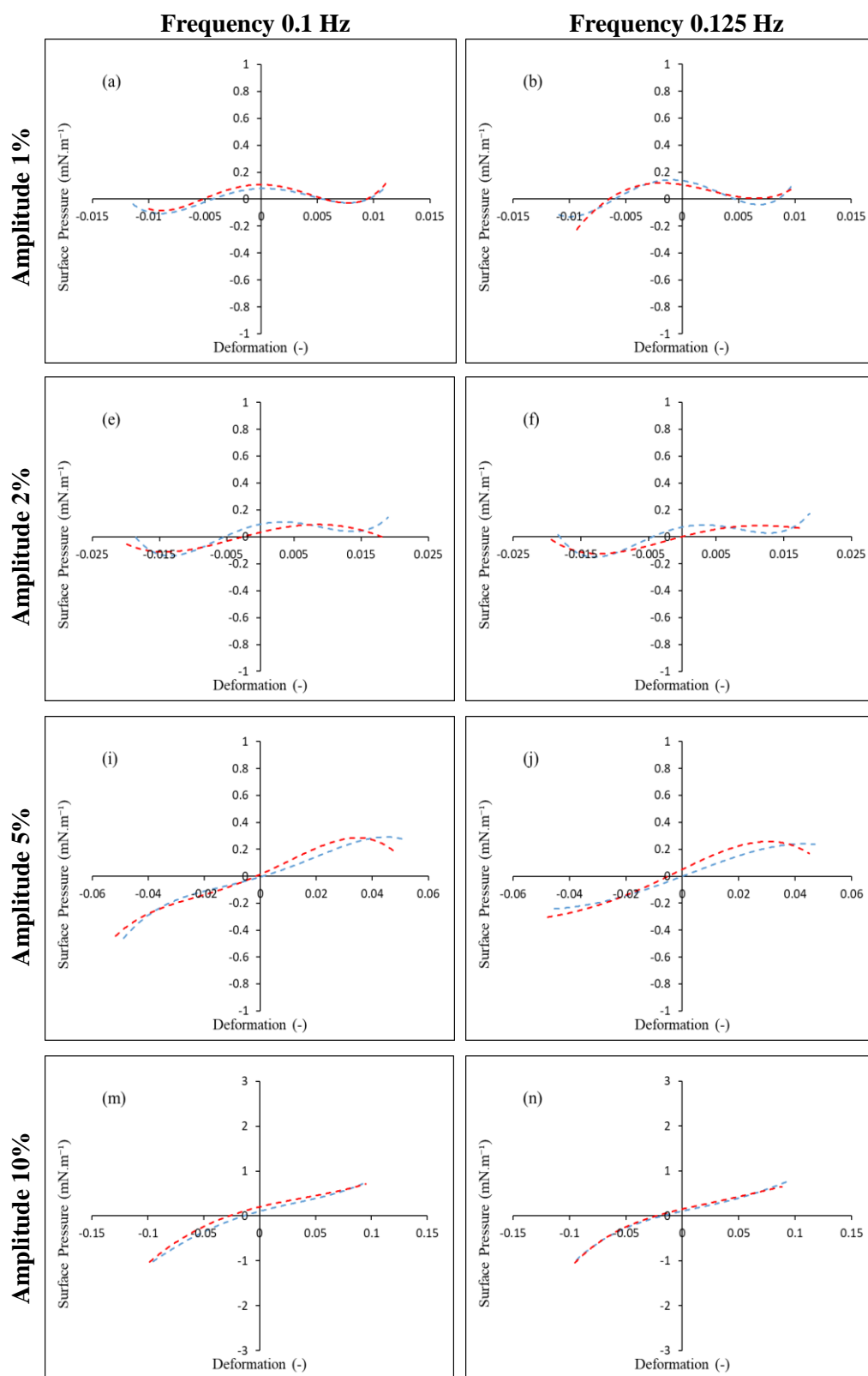


Figure C.8_Part 1 The fourth order polynomial curve fitted on the data of Lissajous plots for ATD 0.04 wt%+DPPC at the amplitudes of 1% (a-b), 2% (e-f), 5% (i-j), and 10% (m-n). The data were obtained for all frequencies including 0.1 Hz (left column) and 0.125 Hz (right column). The blue and red dashed lines are related to the expansion and compression, respectively.

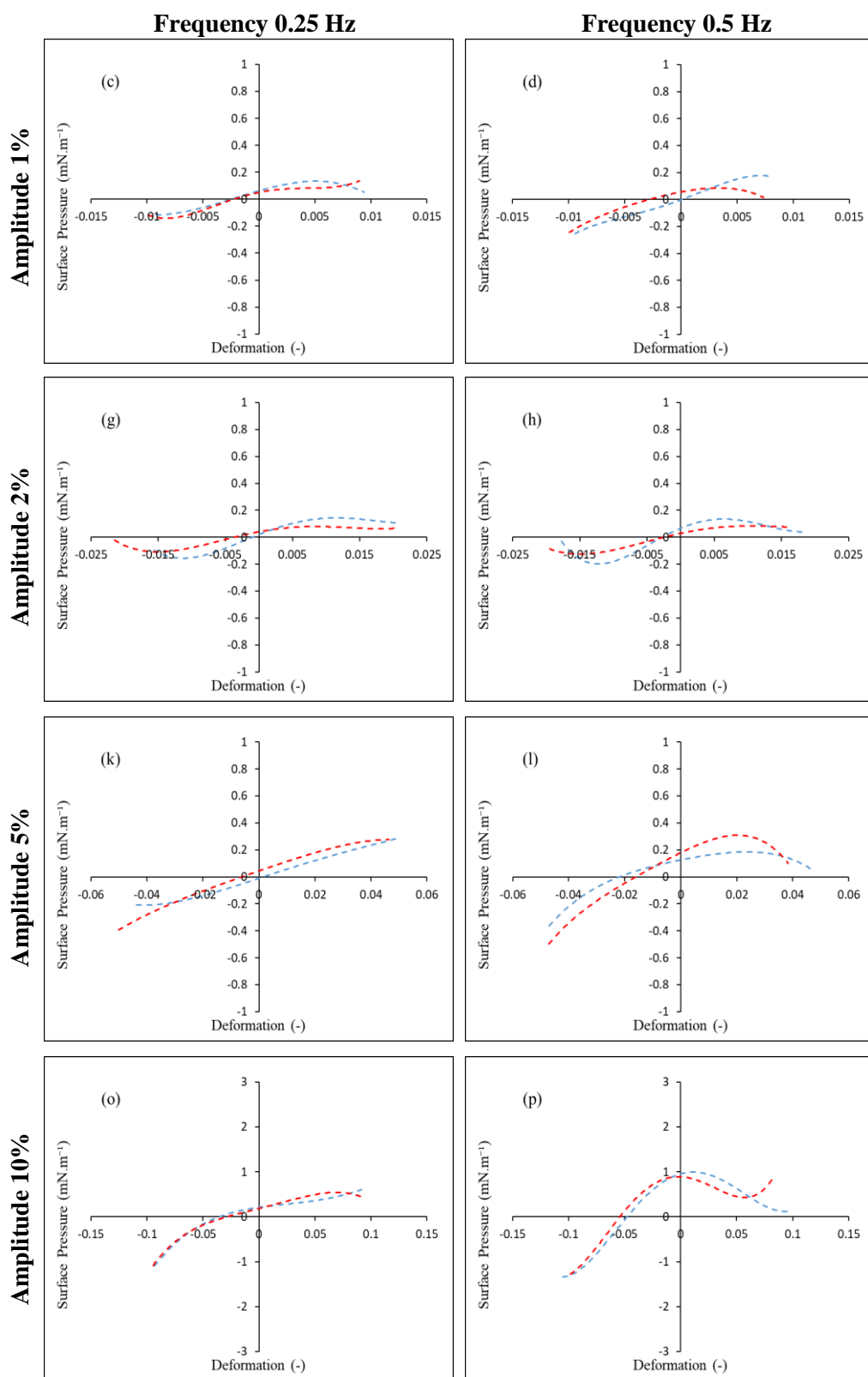


Figure C.8_Part 2 The fourth order polynomial curve fitted on the data of Lissajous plots for ATD 0.04 wt%+DPPC at the amplitudes of 1% (c-d), 2% (g-h), 5% (k-l), and 10% (o-p). The data were obtained for all frequencies including 0.25 Hz (left column) and 0.5 Hz (right column). The blue and red dashed lines are related to the expansion and compression, respectively.

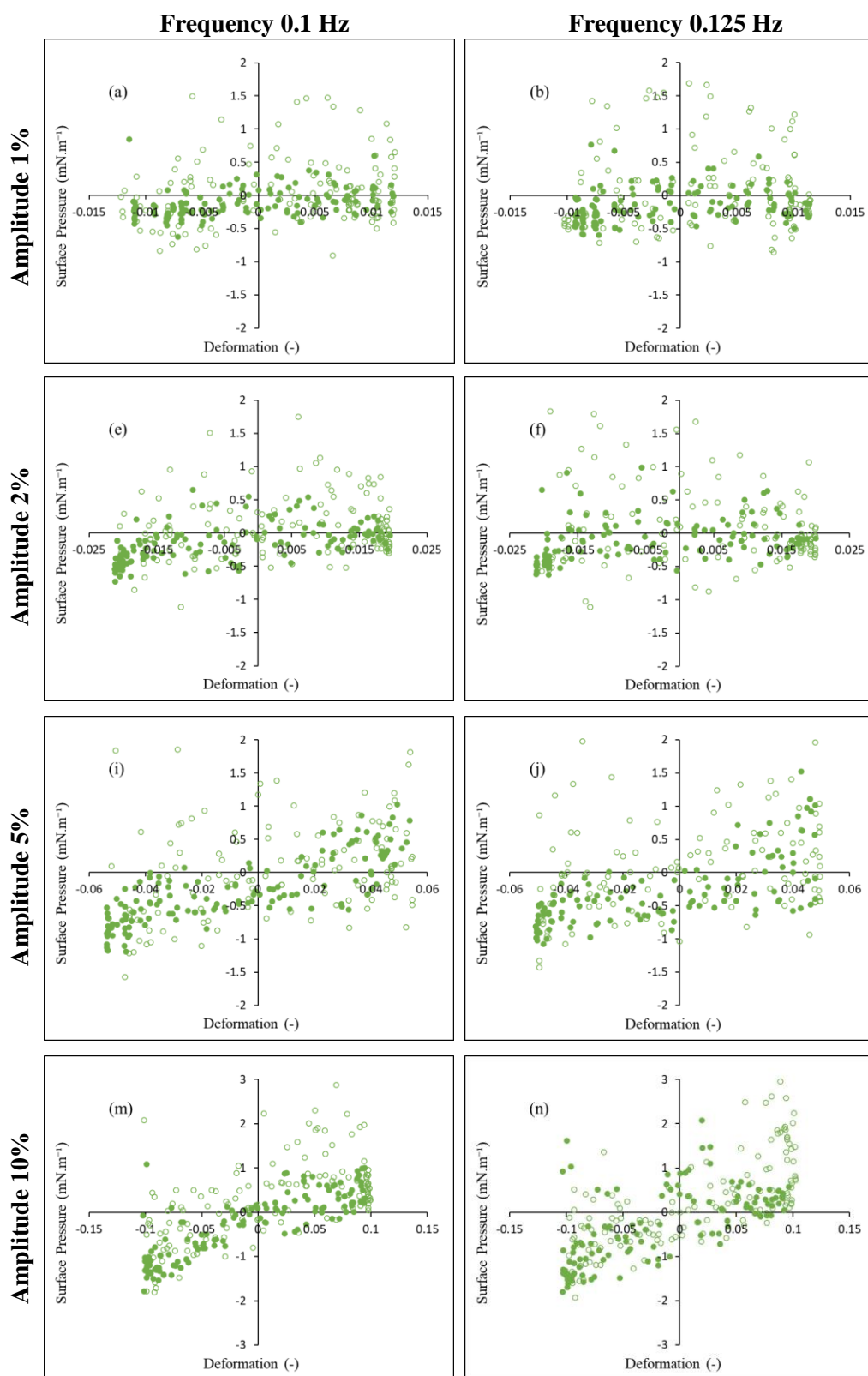


Figure C.9_Part 1 Lissajous plots for ATD 0.05 wt%+DPPC at the amplitudes of 1% (a-b), 2% (e-f), 5% (i-j), and 10% (m-n). The data were obtained for all frequencies including 0.1 Hz (left column) and 0.125 Hz (right column). The hollow dots and filled dots are related to the expansion and compression, respectively.

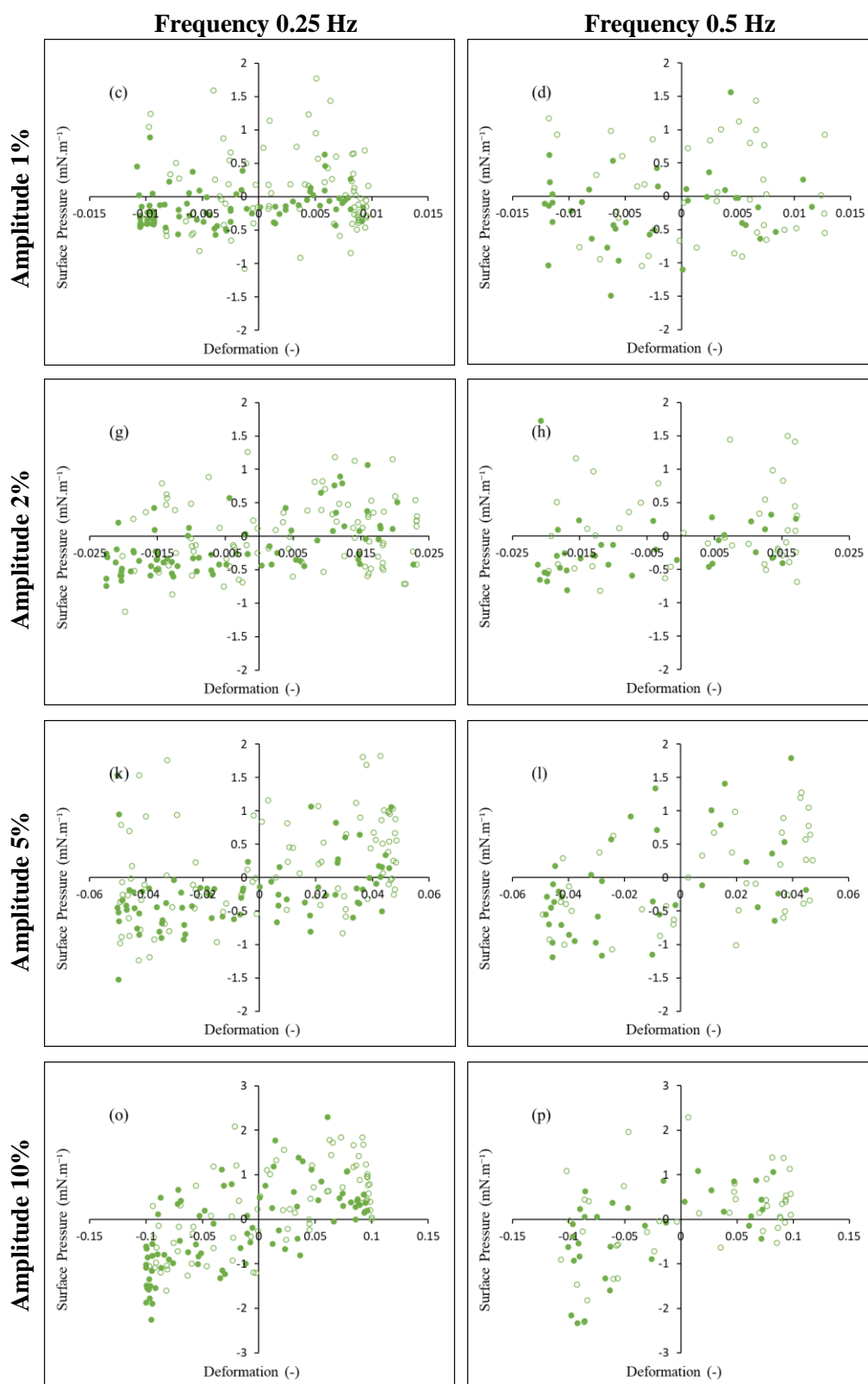


Figure C.9_Part 2 Lissajous plots for ATD 0.05 wt%+DPPC at the amplitudes of 1% (c-d), 2% (g-h), 5% (k-l), and 10% (o-p). The data were obtained for all frequencies including 0.25 Hz (left column) and 0.5 Hz (right column). The hollow dots and filled dots are related to the expansion and compression, respectively.

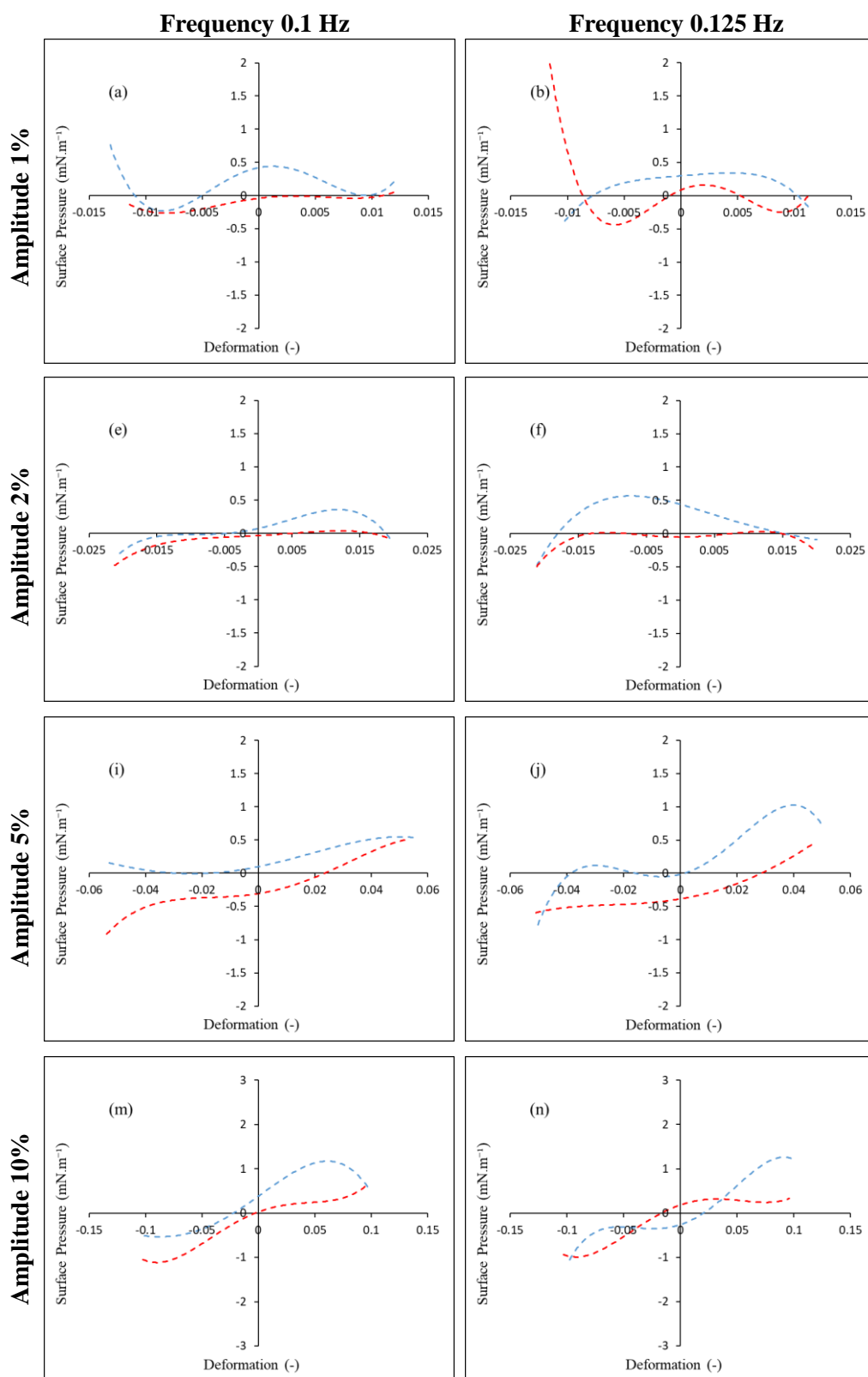


Figure C.10_Part 1 The fourth order polynomial curve fitted on the data of Lissajous plots for ATD 0.05 wt%+DPPC at the amplitudes of 1% (a-b), 2% (e-f), 5% (i-j), and 10% (m-n). The data were obtained for all frequencies including 0.1 Hz (left column) and 0.125 Hz (right column). The blue and red dashed lines are related to the expansion and compression, respectively.

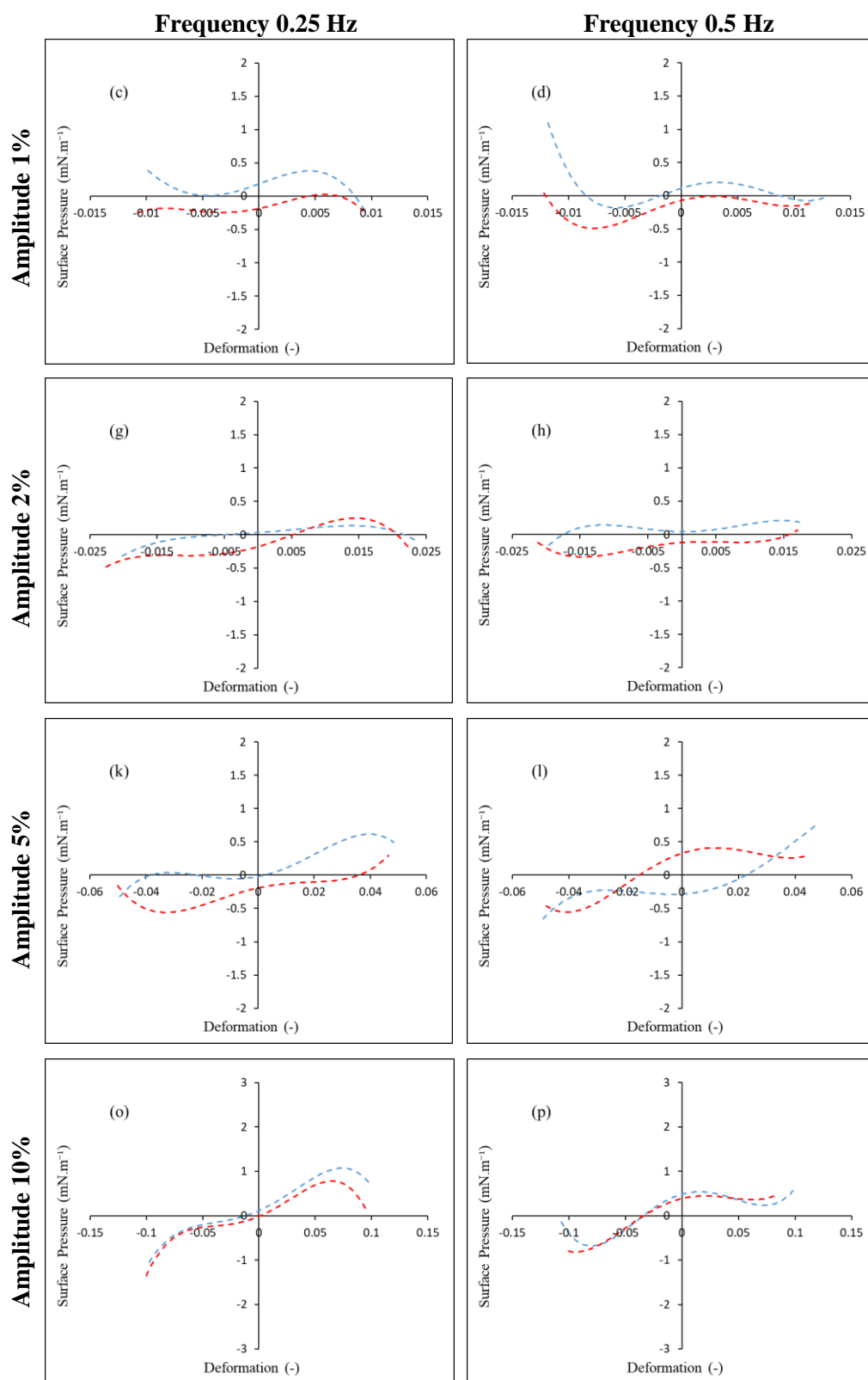


Figure C.10_Part 2 The fourth order polynomial curve fitted on the data of Lissajous plots for ATD 0.05 wt%+DPPC at the amplitudes of 1% (c-d), 2% (g-h), 5% (k-l), and 10% (o-p). The data were obtained for all frequencies including 0.25 Hz (left column) and 0.5 Hz (right column). The blue and red dashed lines are related to the expansion and compression, respectively.

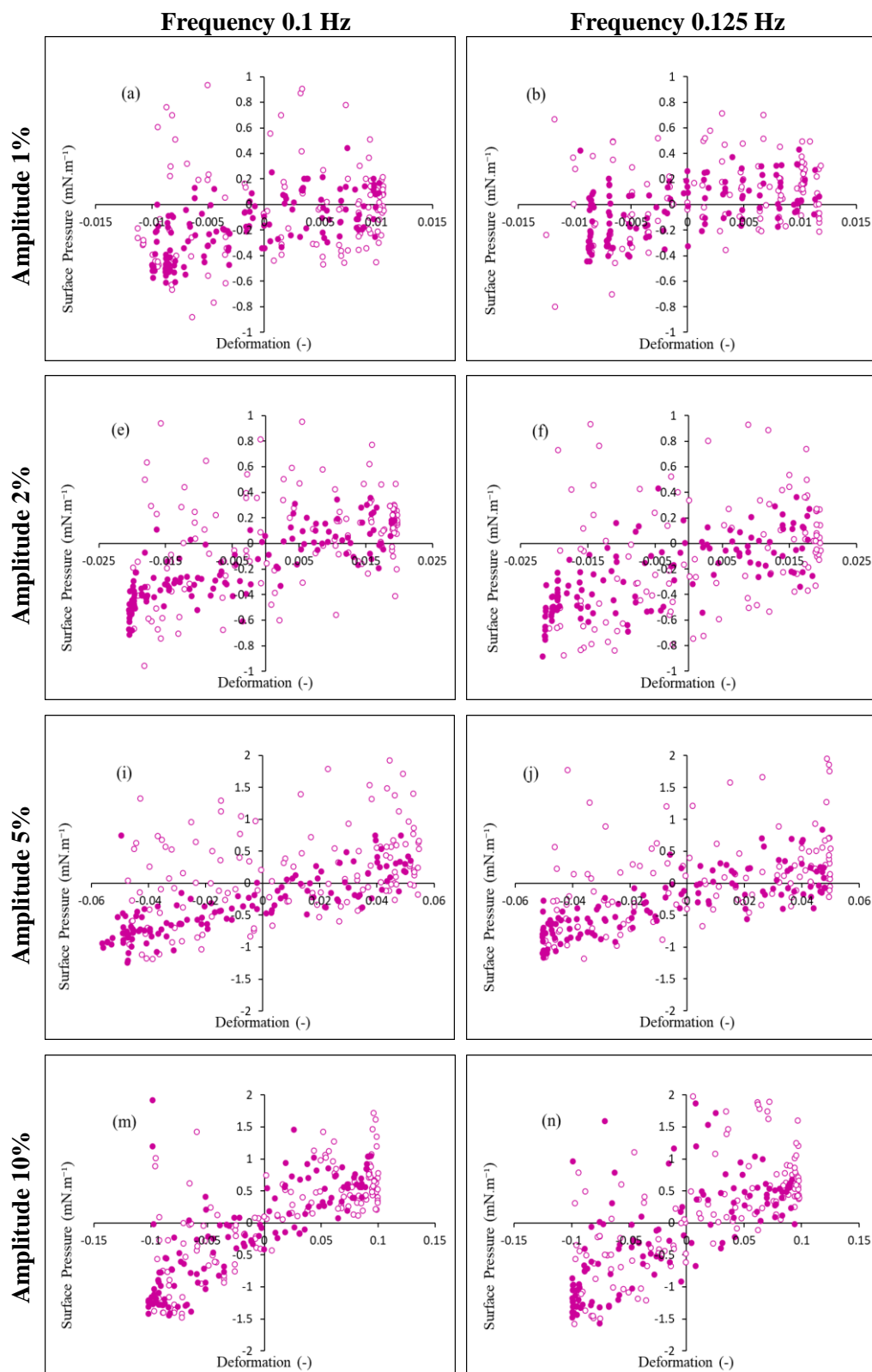


Figure C.11_Part 1 Lissajous plots for RTD 0.01 wt%+DPPC at the amplitudes of 1% (a-b), 2% (e-f), 5% (i-j), and 10% (m-n). The data were obtained for all frequencies including 0.1 Hz (left column) and 0.125 Hz (right column). The hollow dots and filled dots are related to the expansion and compression, respectively.

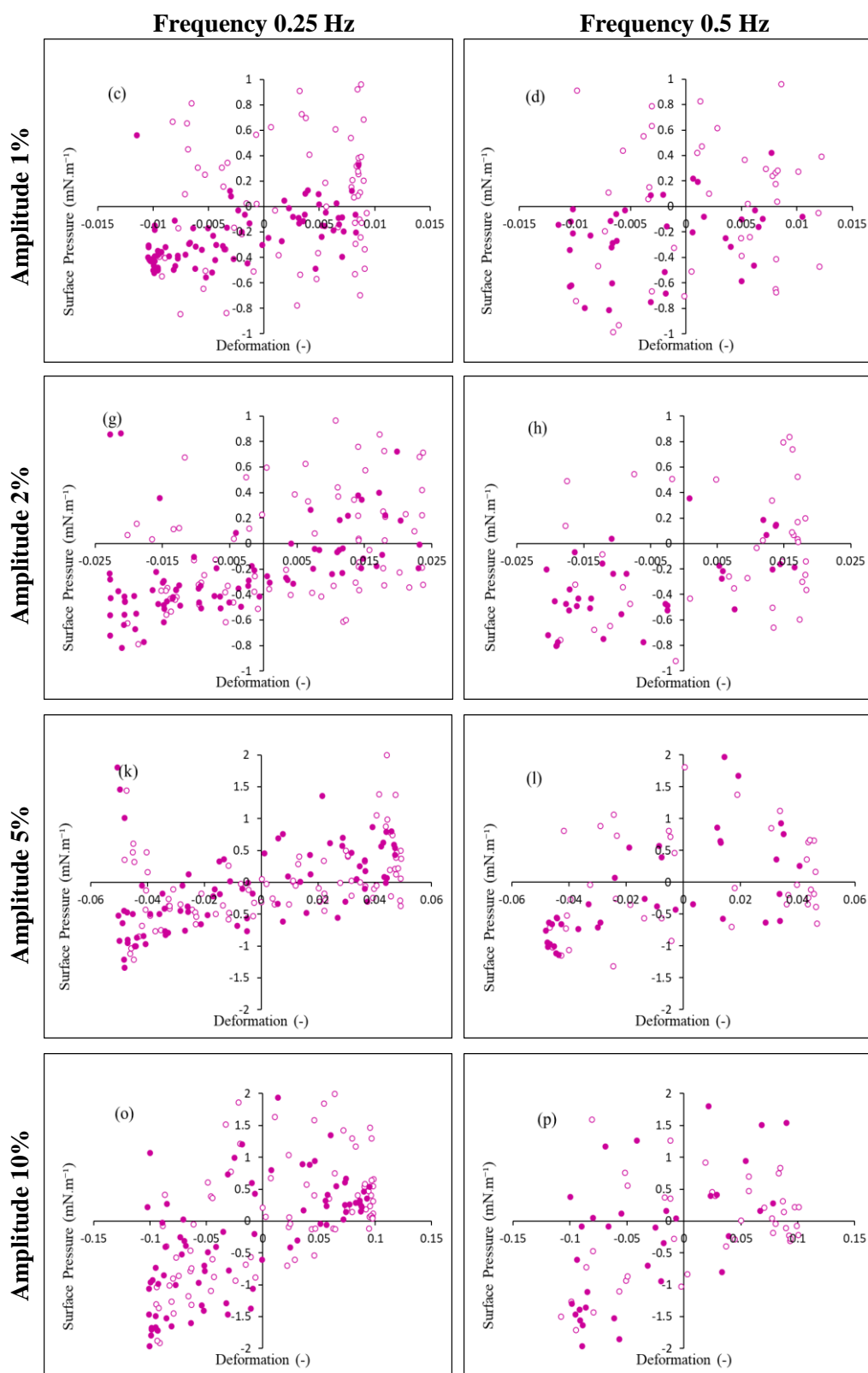


Figure C.11_Part 2 Lissajous plots for RTD 0.01 wt%+DPPC at the amplitudes of 1% (c-d), 2% (g-h), 5% (k-l), and 10% (o-p). The data were obtained for all frequencies including 0.25 Hz (left column) and 0.5 Hz (right column). The hollow dots and filled dots are related to the expansion and compression, respectively.

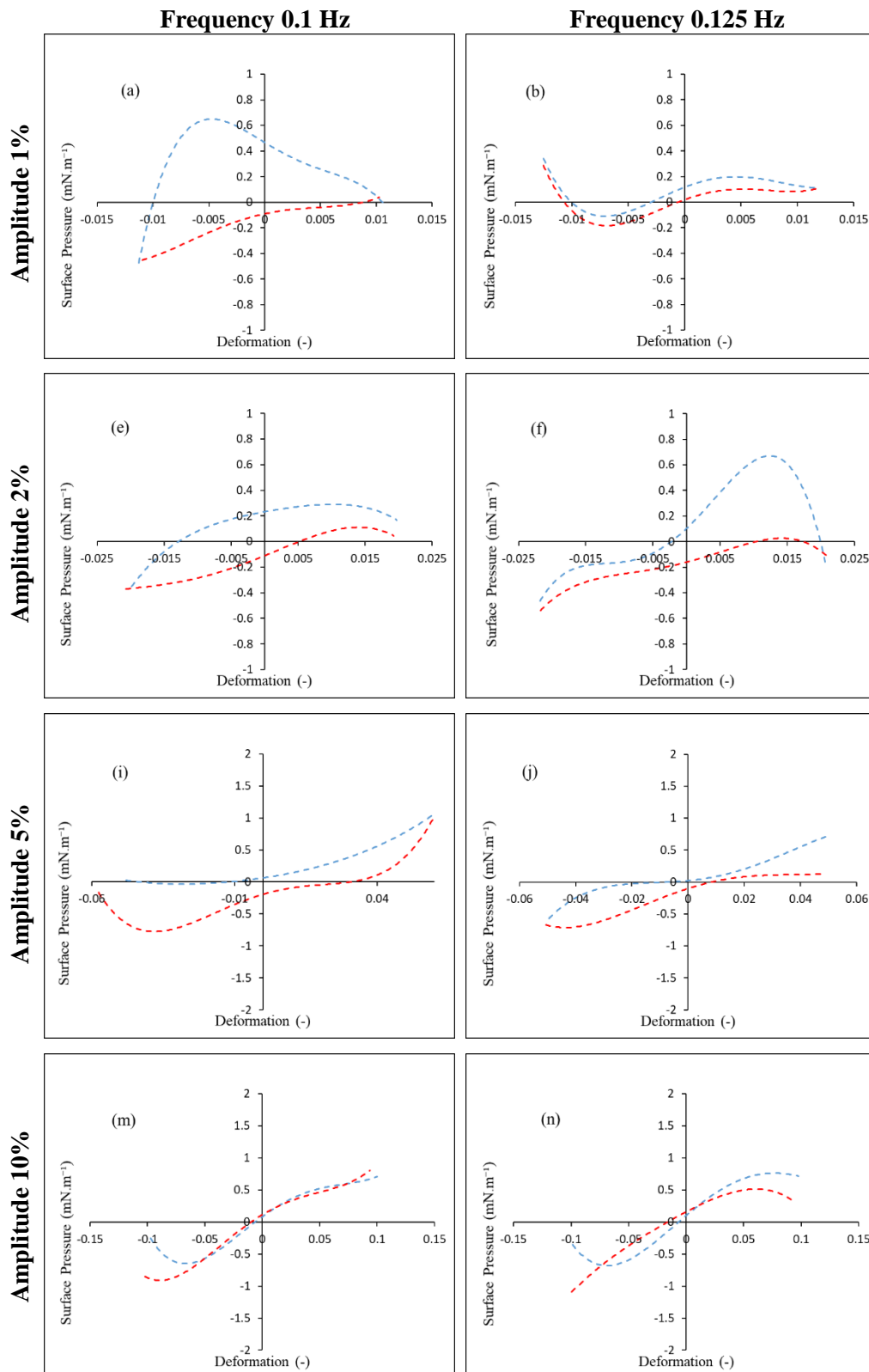


Figure C.12 Part 1 The fourth order polynomial curve fitted on the data of Lissajous plots for RTD 0.01 wt%+DPPC at the amplitudes of 1% (a-b), 2% (e-f), 5% (i-j), and 10% (m-n). The data were obtained for all frequencies including 0.1 Hz (left column) and 0.125 Hz (right column). The blue and red dashed lines are related to the expansion and compression, respectively.

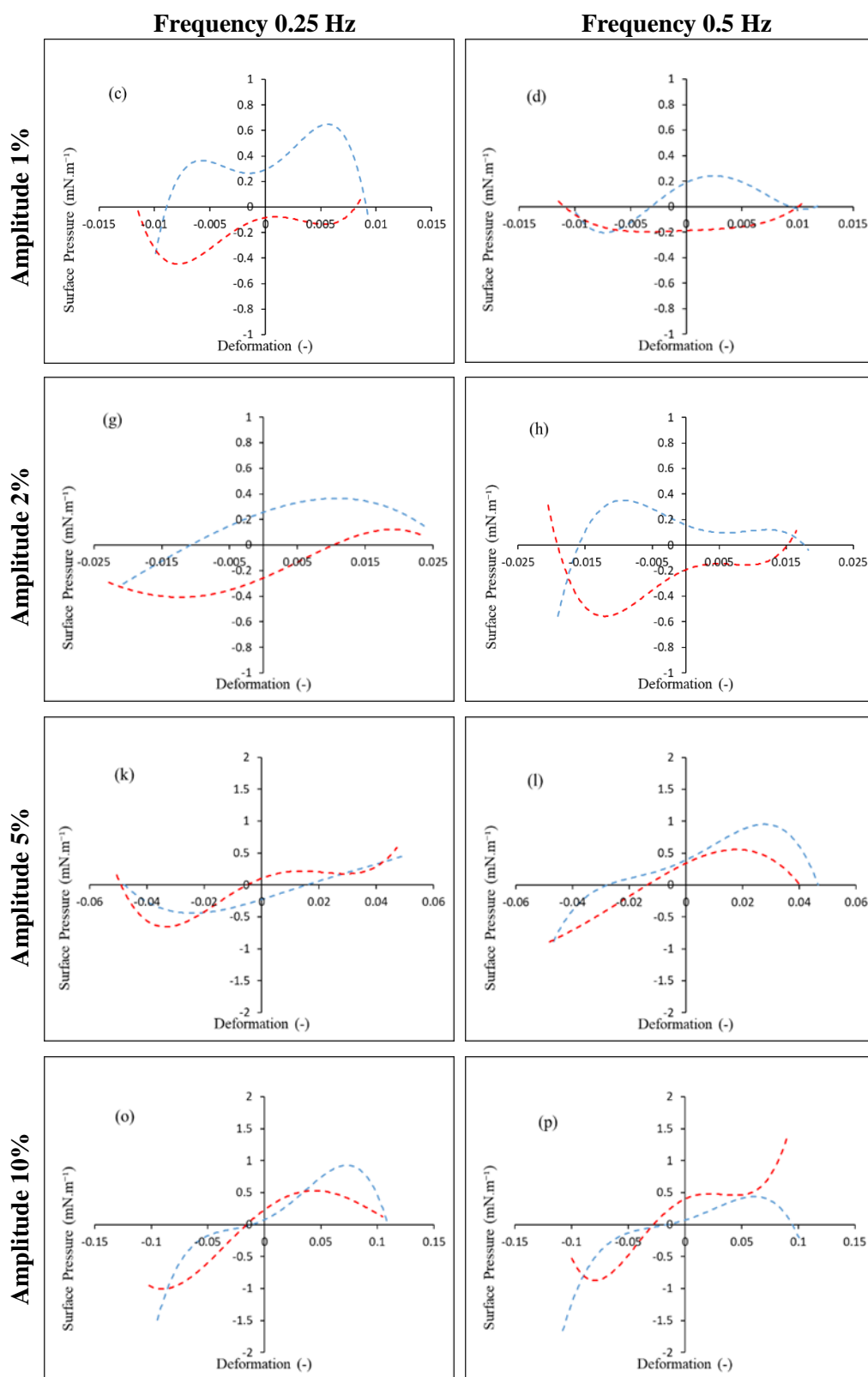


Figure C.12_Part 2 The fourth order polynomial curve fitted on the data of Lissajous plots for RTD 0.01 wt%+DPPC at the amplitudes of 1% (c-d), 2% (g-h), 5% (k-l), and 10% (o-p). The data were obtained for all frequencies including 0.25 Hz (left column) and 0.5 Hz (right column). The blue and red dashed lines are related to the expansion and compression, respectively.

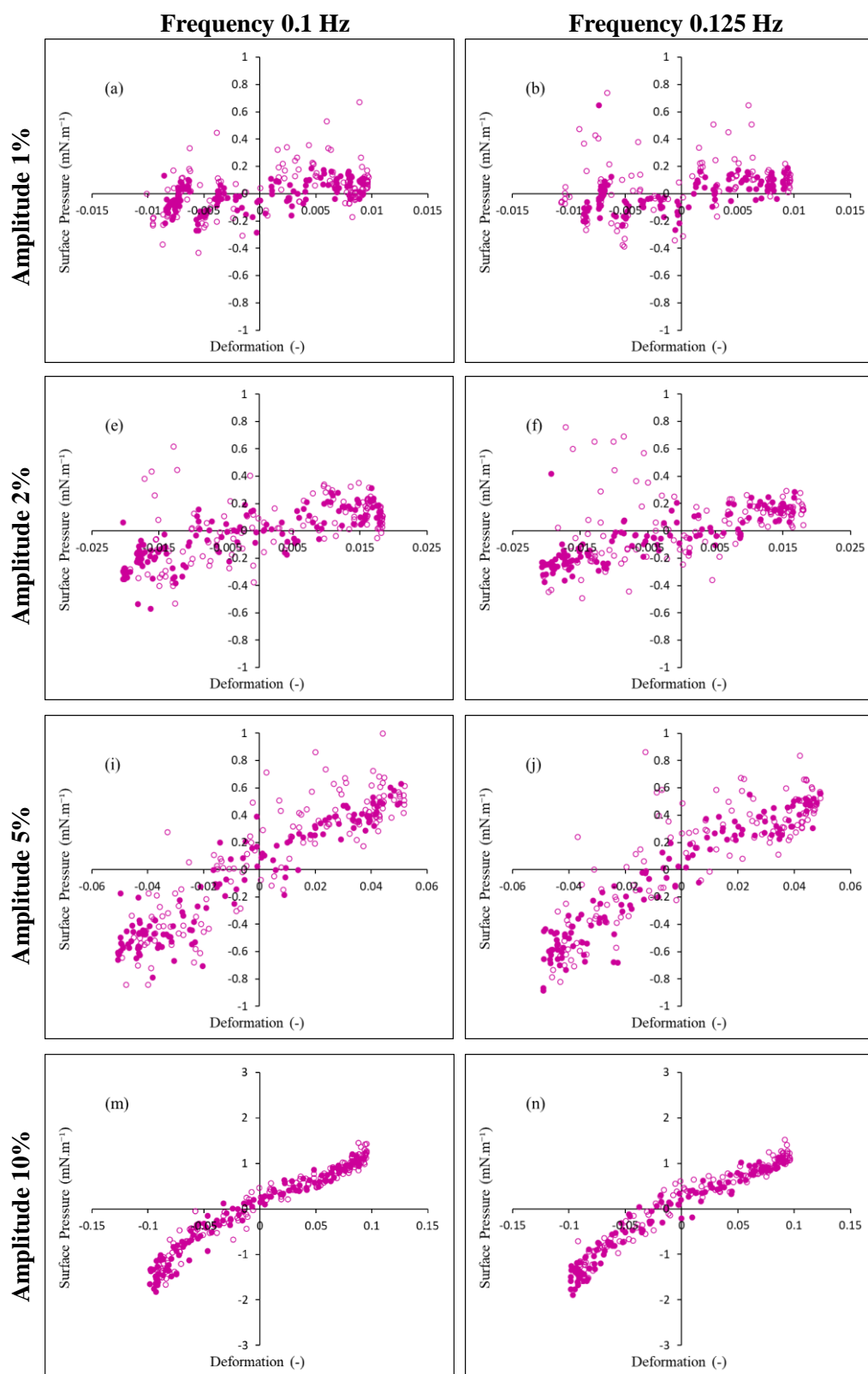


Figure C.13_Part 1 Lissajous plots for RTD 0.02 wt%+DPPC at the amplitudes of 1% (a-b), 2% (e-f), 5% (i-j), and 10% (m-n). The data were obtained for all frequencies including 0.1 Hz (left column) and 0.125 Hz (right column). The hollow dots and filled dots are related to the expansion and compression, respectively.

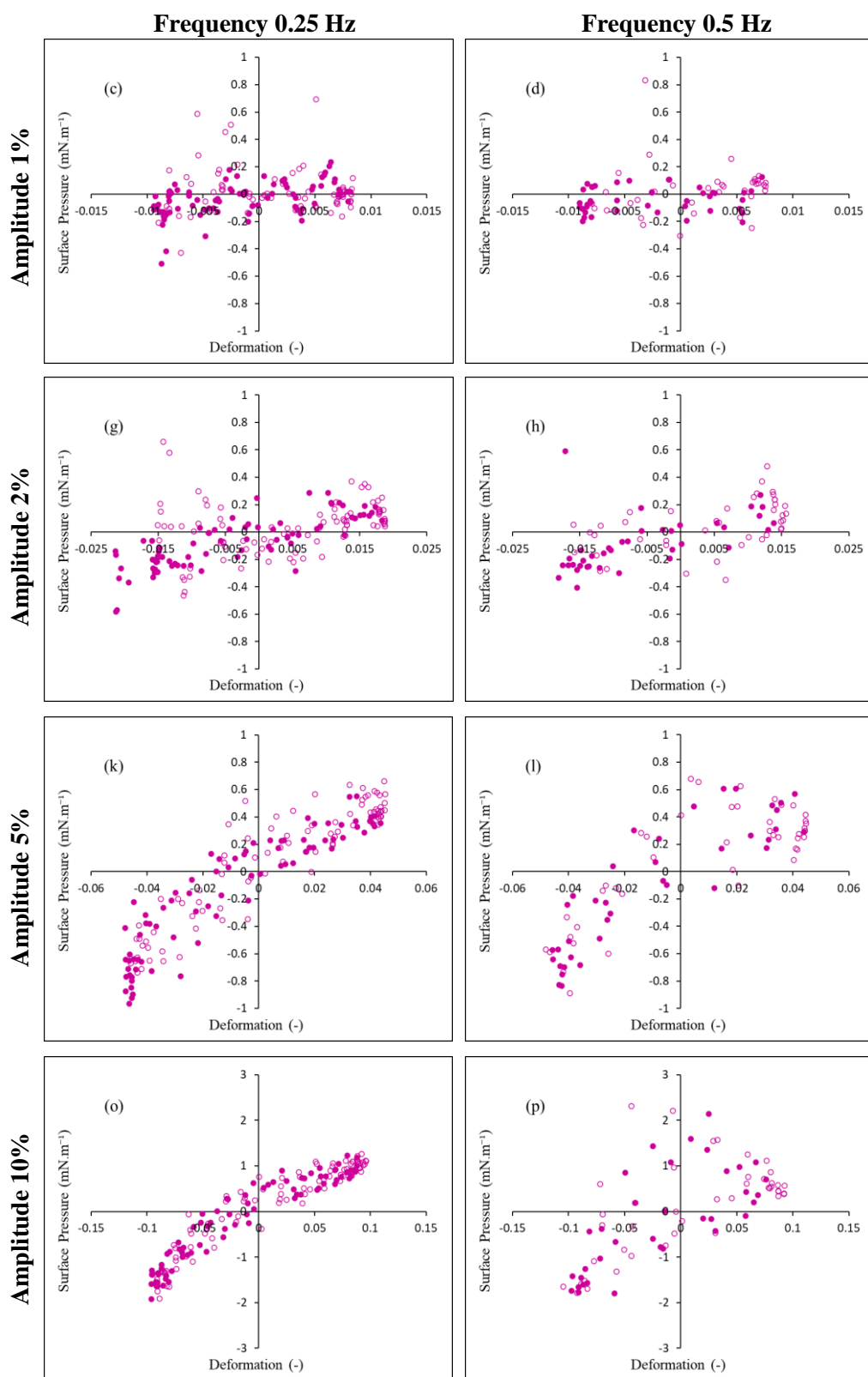


Figure C.13_Part 2 Lissajous plots for RTD 0.02 wt%+DPPC at the amplitudes of 1% (c-d), 2% (g-h), 5% (k-l), and 10% (o-p). The data were obtained for all frequencies including 0.25 Hz (left column) and 0.5 Hz (right column). The hollow dots and filled dots are related to the expansion and compression, respectively.

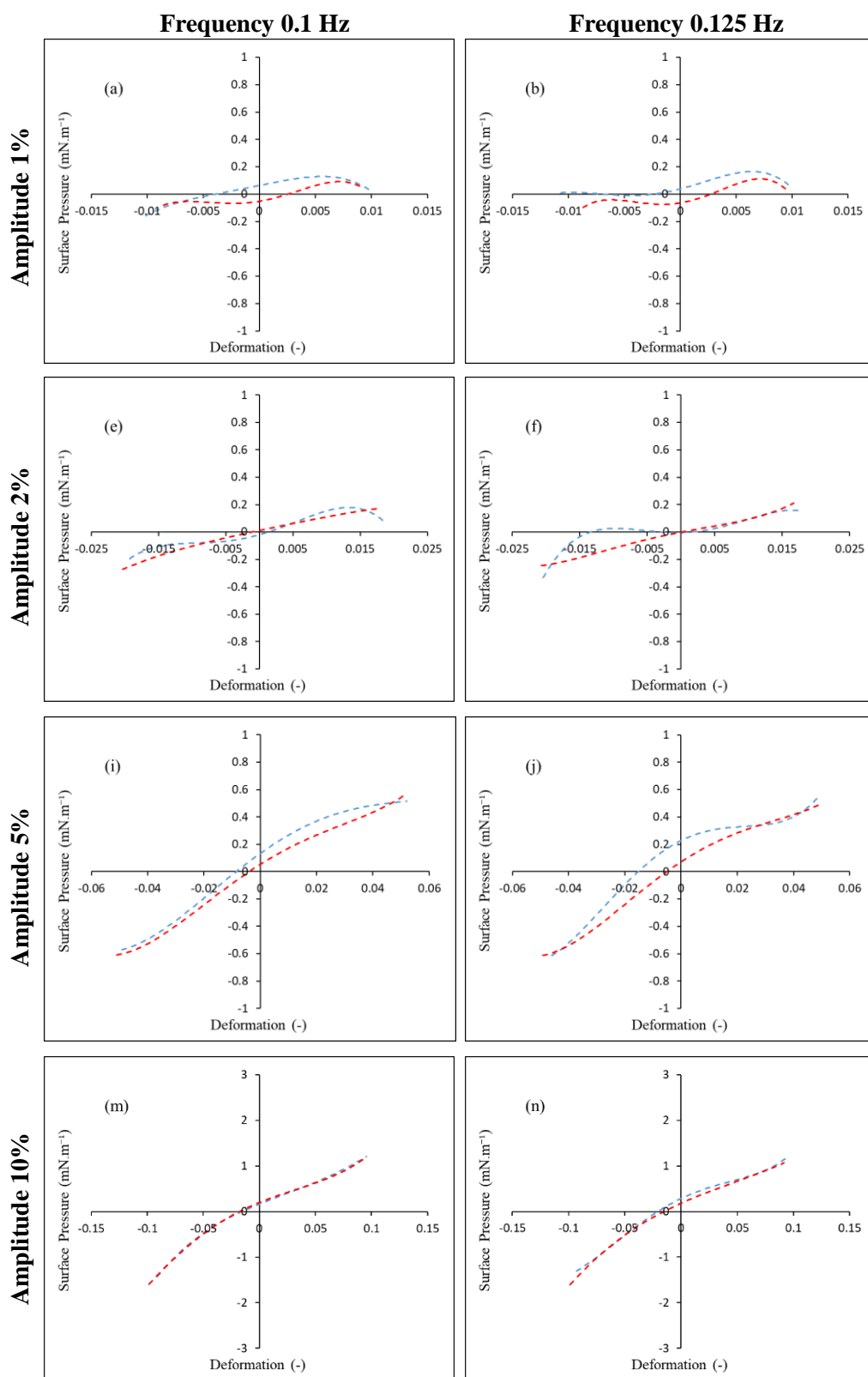


Figure C.14 Part 1 The fourth order polynomial curve fitted on the data of Lissajous plots for RTD 0.02 wt%+DPPC at the amplitudes of 1% (a-b), 2% (e-f), 5% (i-j), and 10% (m-n). The data were obtained for all frequencies including 0.1 Hz (left column) and 0.125 Hz (right column). The blue and red dashed lines are related to the expansion and compression, respectively.

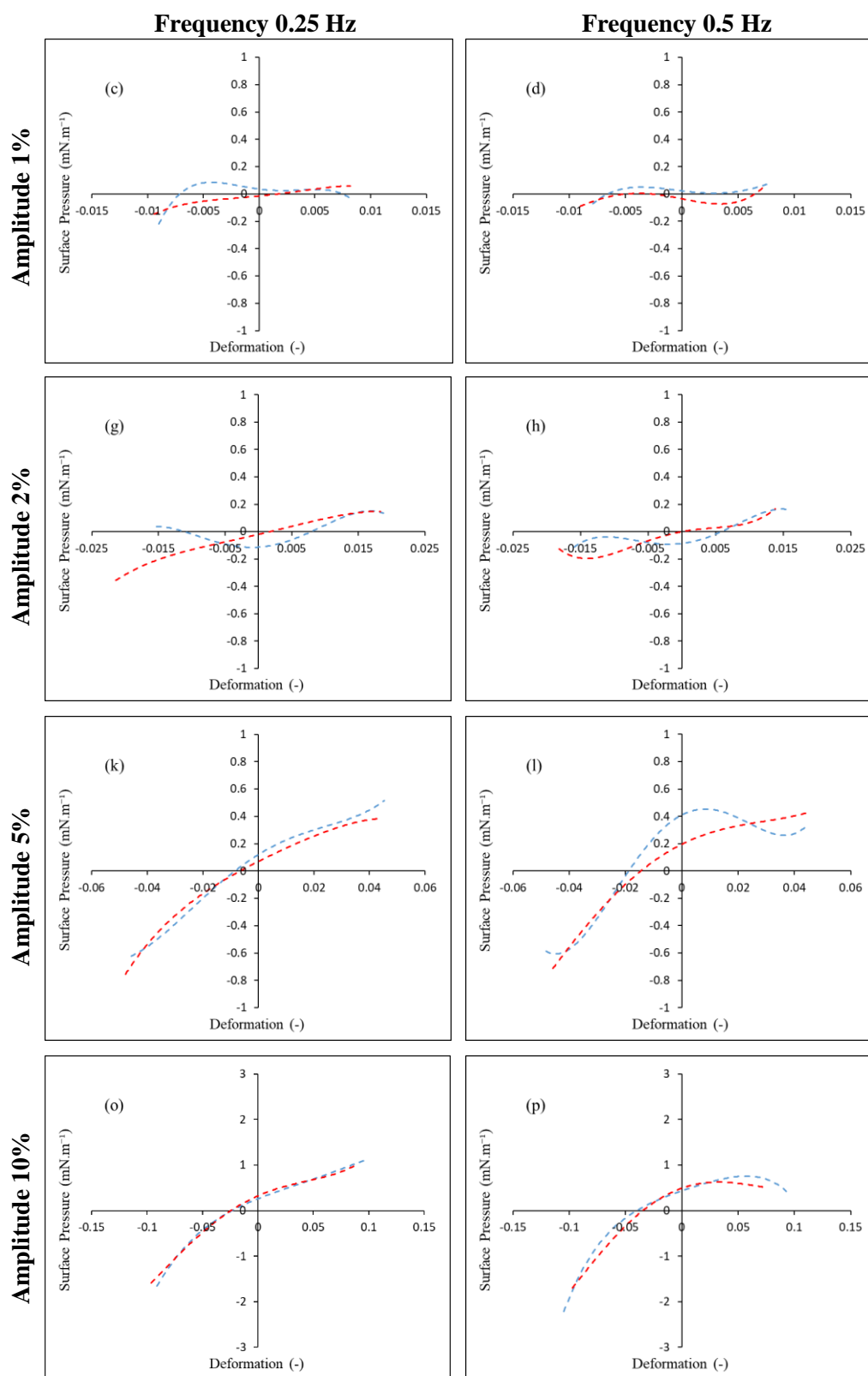


Figure C.14 Part 2 The fourth order polynomial curve fitted on the data of Lissajous plots for RTD 0.02 wt%+DPPC at the amplitudes of 1% (c-d), 2% (g-h), 5% (k-l), and 10% (o-p). The data were obtained for all frequencies including 0.25 Hz (left column) and 0.5 Hz (right column). The blue and red dashed lines are related to the expansion and compression, respectively.

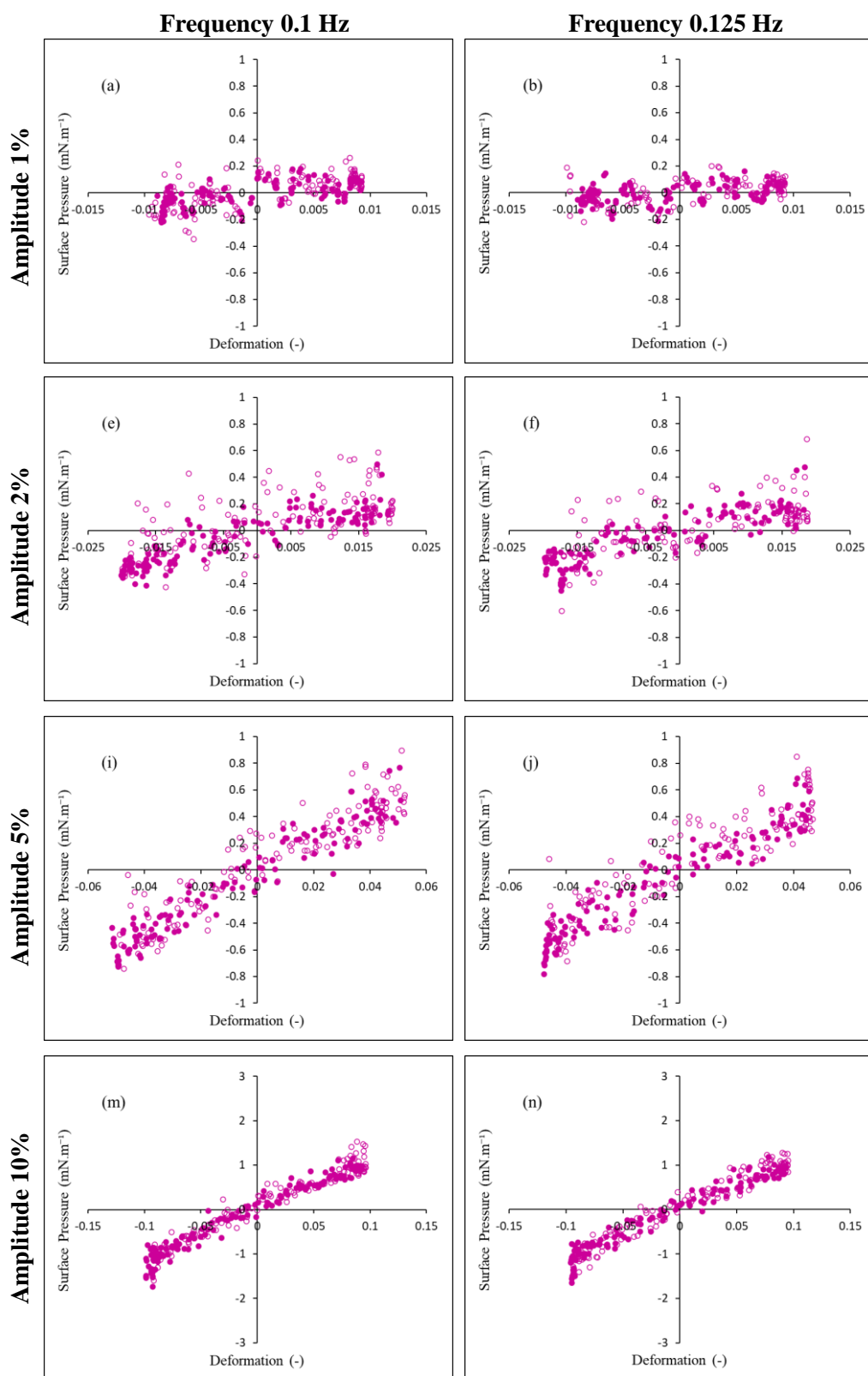


Figure C.15_Part 1 Lissajous plots for RTD 0.03 wt%+DPPC at the amplitudes of 1% (a-b), 2% (e-f), 5% (i-j), and 10% (m-n). The data were obtained for all frequencies including 0.1 Hz (left column) and 0.125 Hz (right column). The hollow dots and filled dots are related to the expansion and compression, respectively.

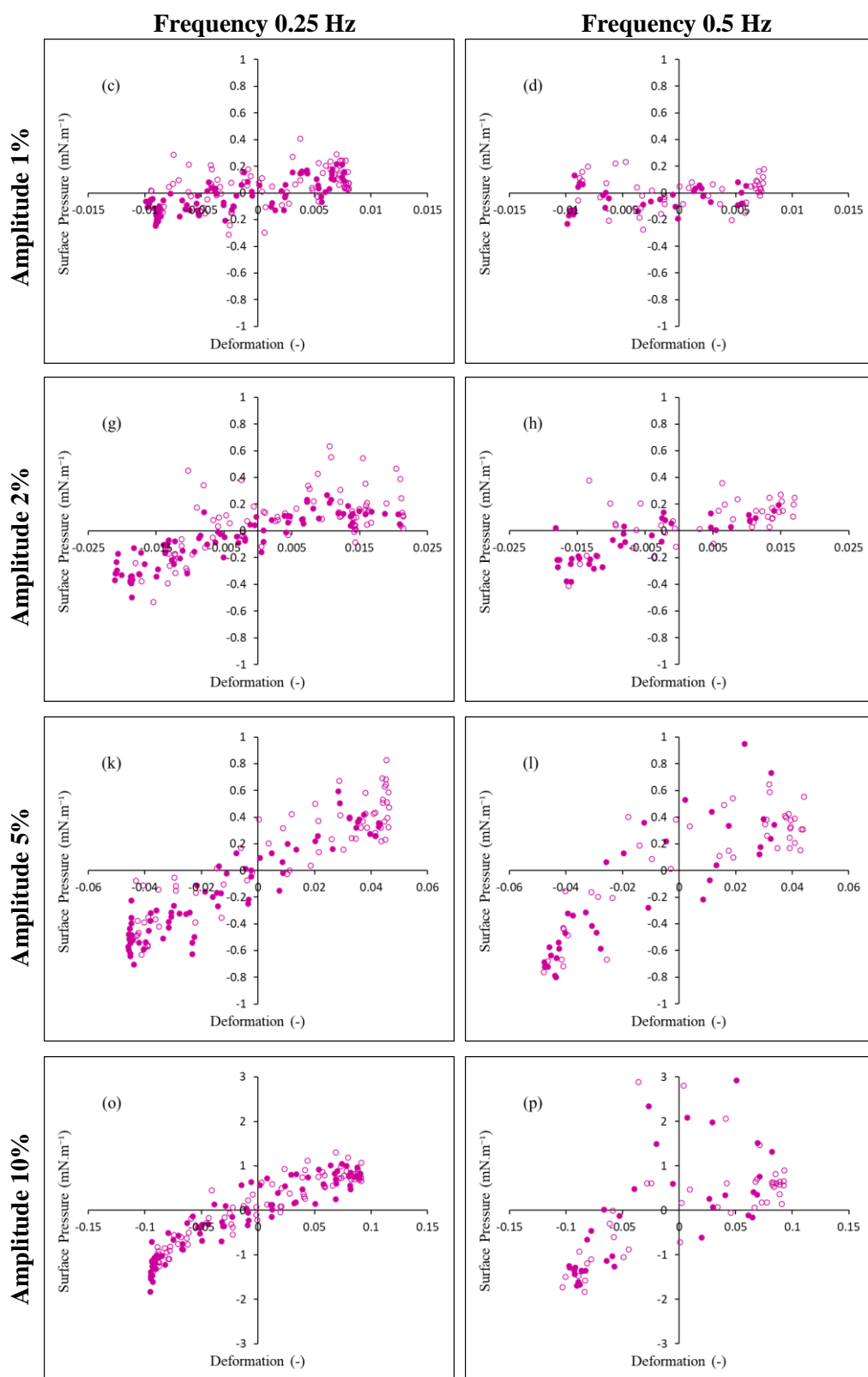


Figure C.15_Part 2 Lissajous plots for RTD 0.03 wt%+DPPC at the amplitudes of 1% (c-d), 2% (g-h), 5% (k-l), and 10% (o-p). The data were obtained for all frequencies including 0.25 Hz (left column) and 0.5 Hz (right column). The hollow dots and filled dots are related to the expansion and compression, respectively.

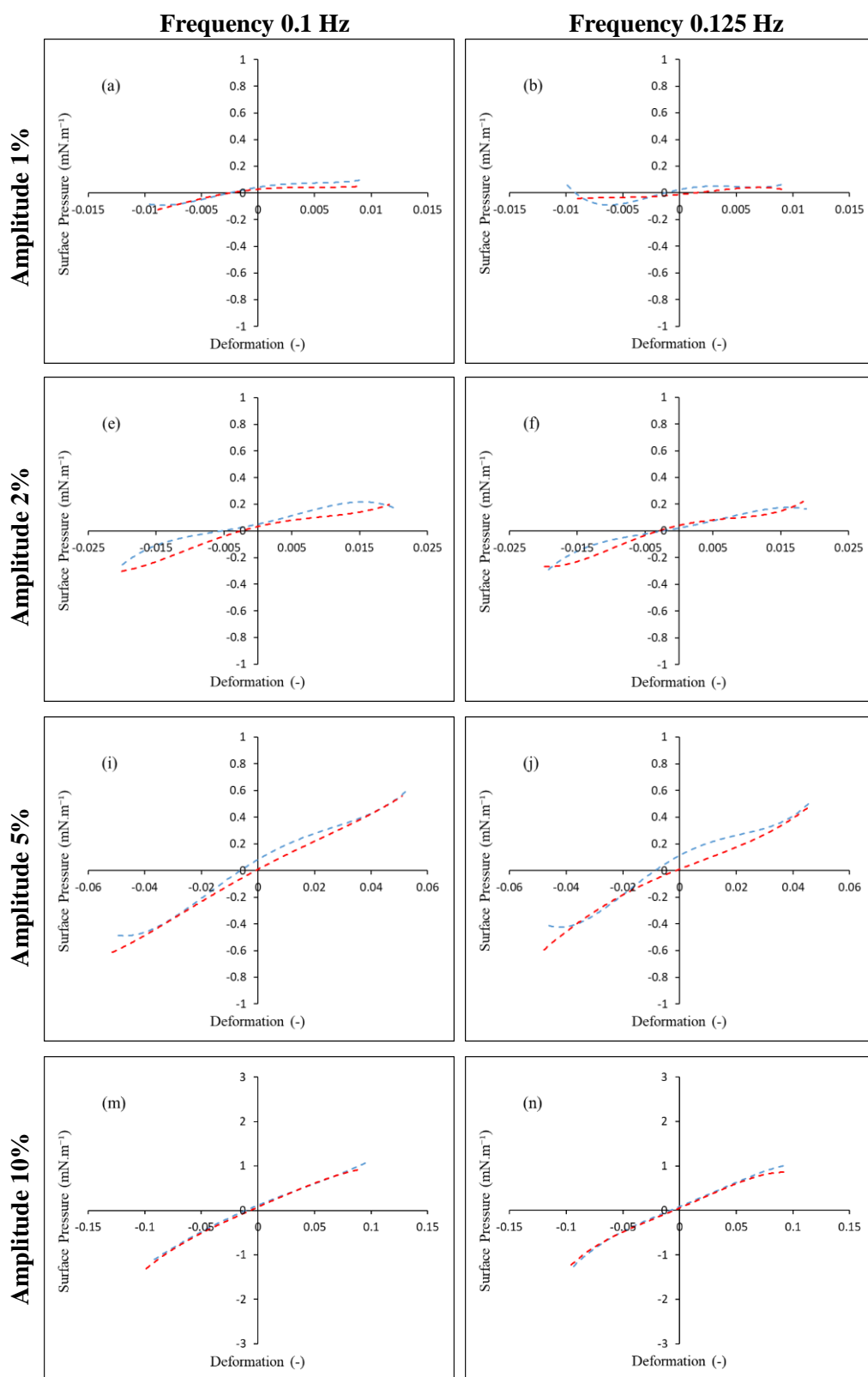


Figure C.16_Part 1 The fourth order polynomial curve fitted on the data of Lissajous plots for RTD 0.03 wt%+DPPC at the amplitudes of 1% (a-b), 2% (e-f), 5% (i-j), and 10% (m-n). The data were obtained for all frequencies including 0.1 Hz (left column) and 0.125 Hz (right column). The blue and red dashed lines are related to the expansion and compression, respectively.

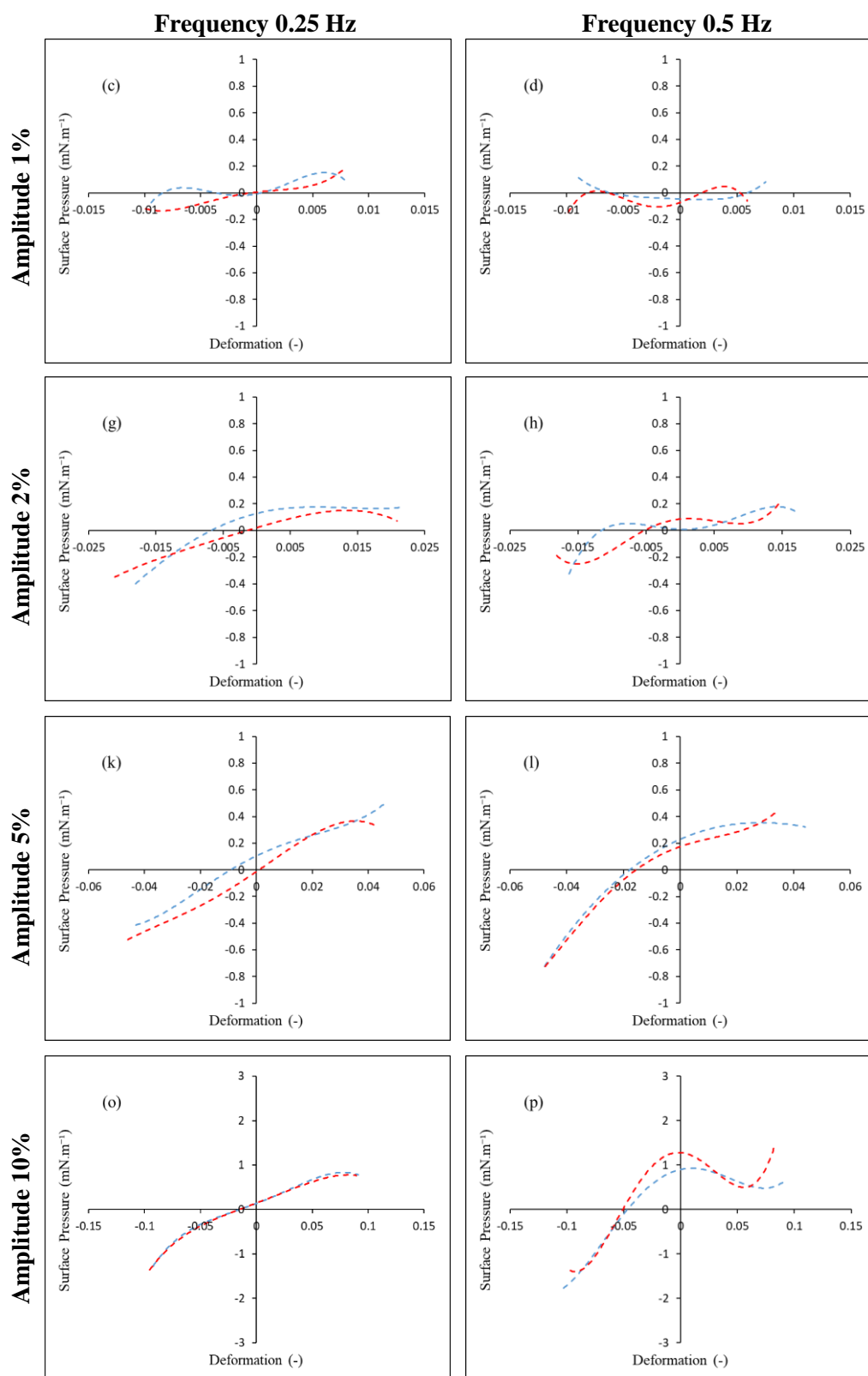


Figure C.16_Part 2 The fourth order polynomial curve fitted on the data of Lissajous plots for RTD 0.03 wt%+DPPC at the amplitudes of 1% (c-d), 2% (g-h), 5% (k-l), and 10% (o-p). The data were obtained for all frequencies including 0.25 Hz (left column) and 0.5 Hz (right column). The blue and red dashed lines are related to the expansion and compression, respectively.

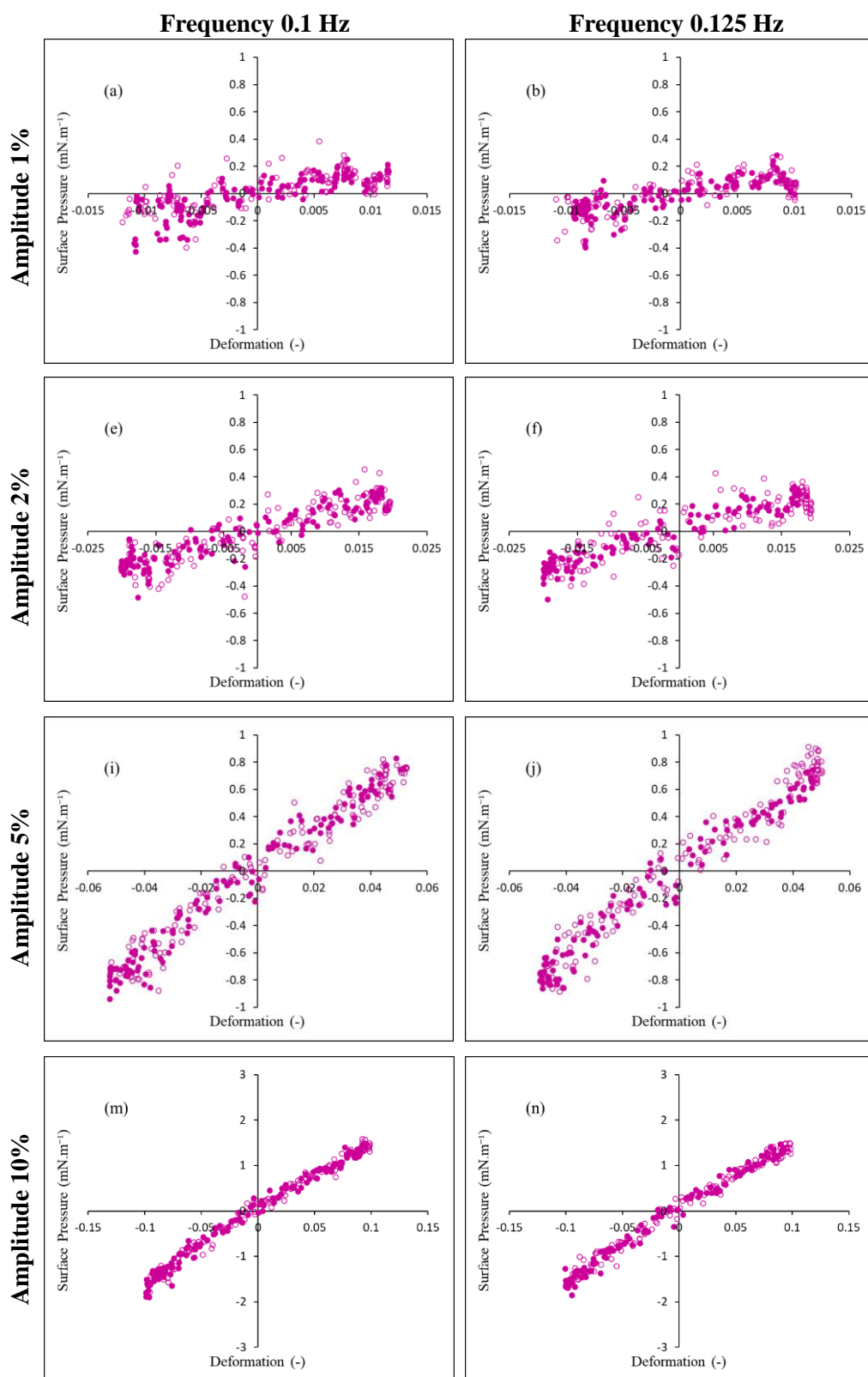


Figure C.17_Part 1 Lissajous plots for RTD 0.04 wt%+DPPC at the amplitudes of 1% (a-b), 2% (e-f), 5% (i-j), and 10% (m-n). The data were obtained for all frequencies including 0.1 Hz (left column) and 0.125 Hz (right column). The hollow dots and filled dots are related to the expansion and compression, respectively.

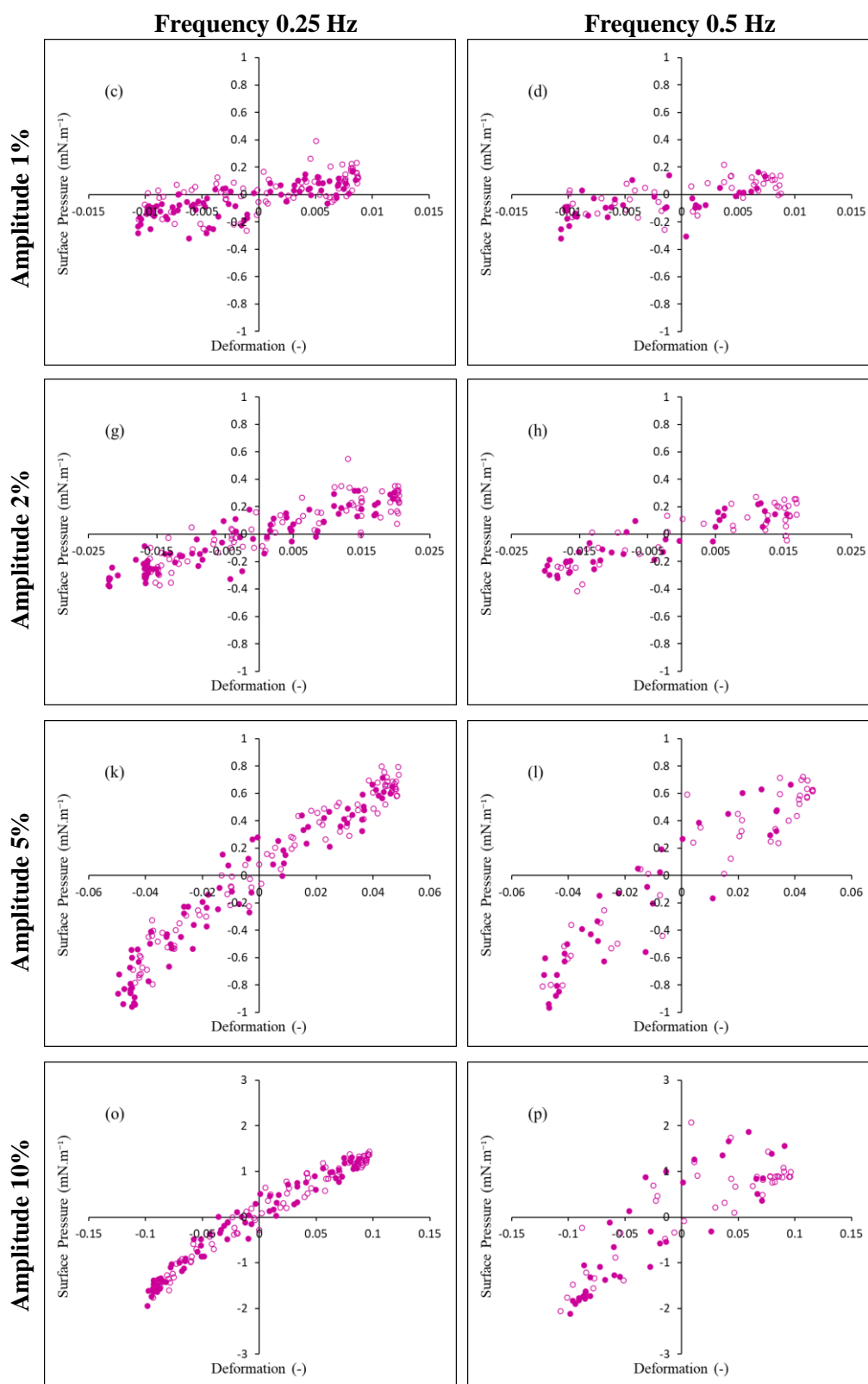


Figure C.17_Part 2 Lissajous plots for RTD 0.04 wt%+DPPC at the amplitudes of 1% (c-d), 2% (g-h), 5% (k-l), and 10% (o-p). The data were obtained for all frequencies including 0.25 Hz (left column) and 0.5 Hz (right column). The hollow dots and filled dots are related to the expansion and compression, respectively.

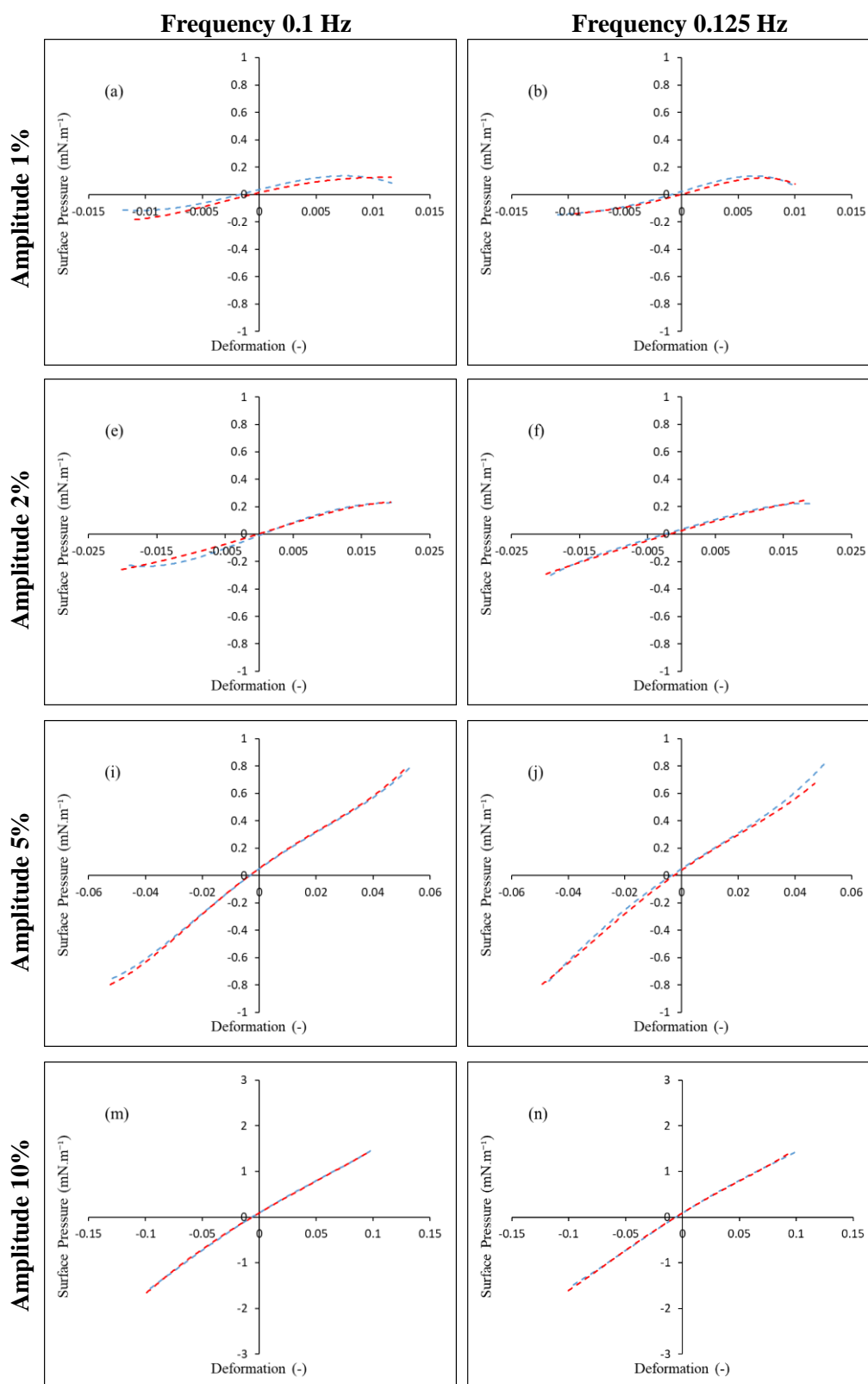


Figure C.18_Part 1 The fourth order polynomial curve fitted on the data of Lissajous plots for RTD 0.04 wt%+DPPC at the amplitudes of 1% (a-b), 2% (e-f), 5% (i-j), and 10% (m-n). The data were obtained for all frequencies including 0.1 Hz (left column) and 0.125 Hz (right column). The blue and red dashed lines are related to the expansion and compression, respectively.

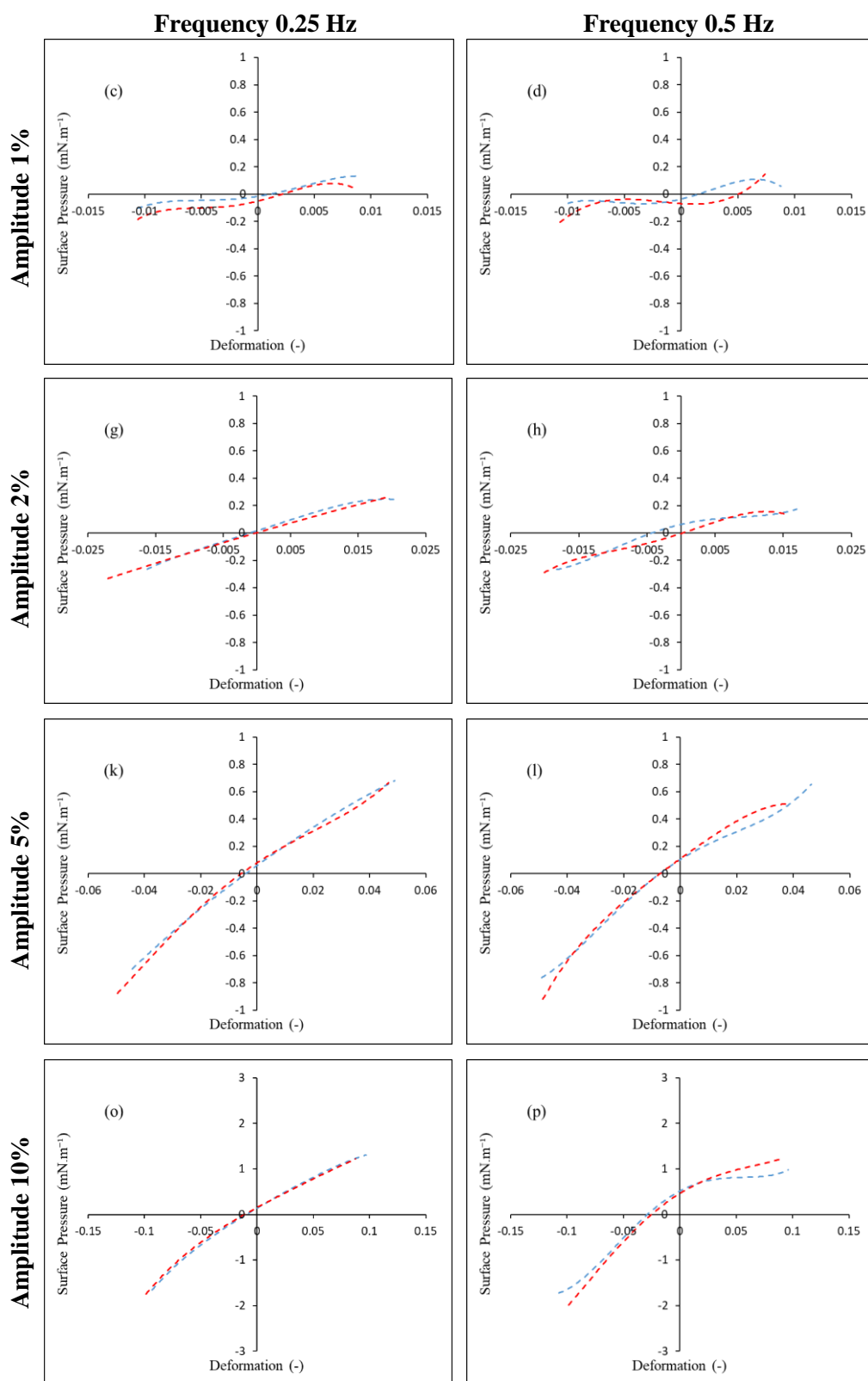


Figure C.18_Part 2 The fourth order polynomial curve fitted on the data of Lissajous plots for RTD 0.04 wt%+DPPC at the amplitudes of 1% (c-d), 2% (g-h), 5% (k-l), and 10% (o-p). The data were obtained for all frequencies including 0.25 Hz (left column) and 0.5 Hz (right column). The blue and red dashed lines are related to the expansion and compression, respectively.

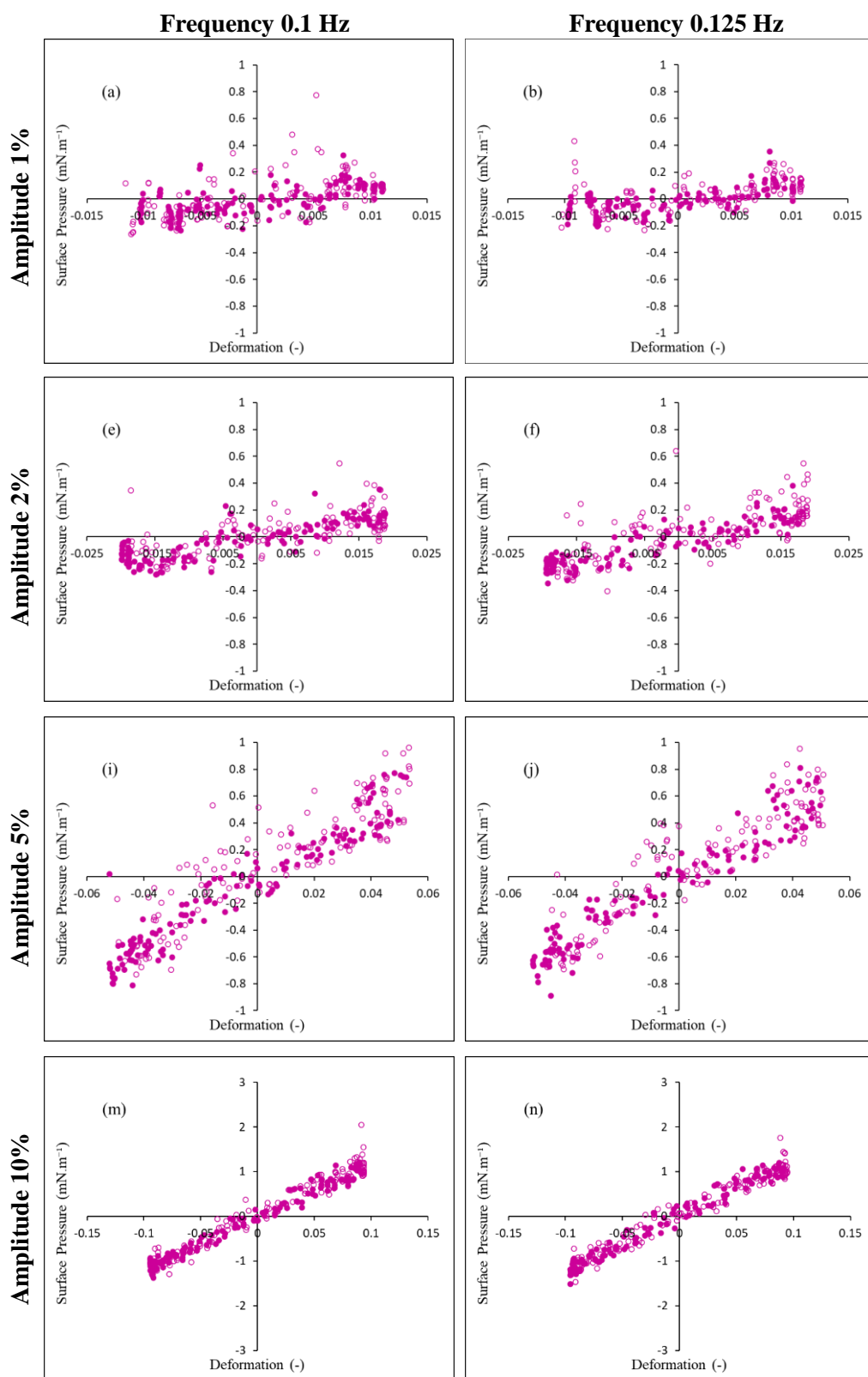


Figure C.19_Part 1 Lissajous plots for RTD 0.05 wt%+DPPC at the amplitudes of 1% (a-b), 2% (e-f), 5% (i-j), and 10% (m-n). The data were obtained for all frequencies including 0.1 Hz (left column) and 0.125 Hz (right column). The hollow dots and filled dots are related to the expansion and compression, respectively.

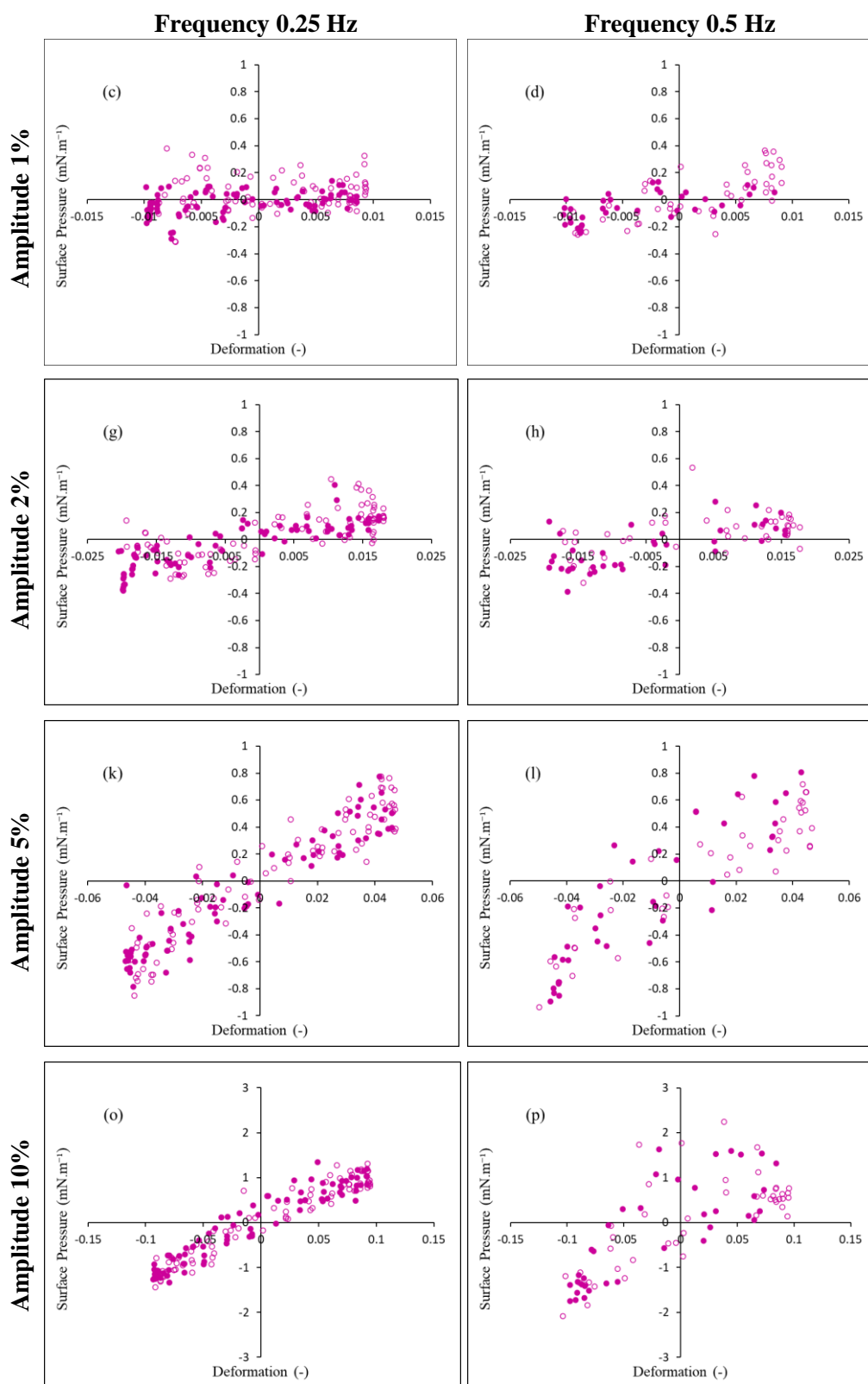


Figure C.19_Part 2 Lissajous plots for RTD 0.05 wt%+DPPC at the amplitudes of 1% (c-d), 2% (g-h), 5% (k-l), and 10% (o-p). The data were obtained for all frequencies including 0.25 Hz (left column) and 0.5 Hz (right column). The hollow dots and filled dots are related to the expansion and compression, respectively.

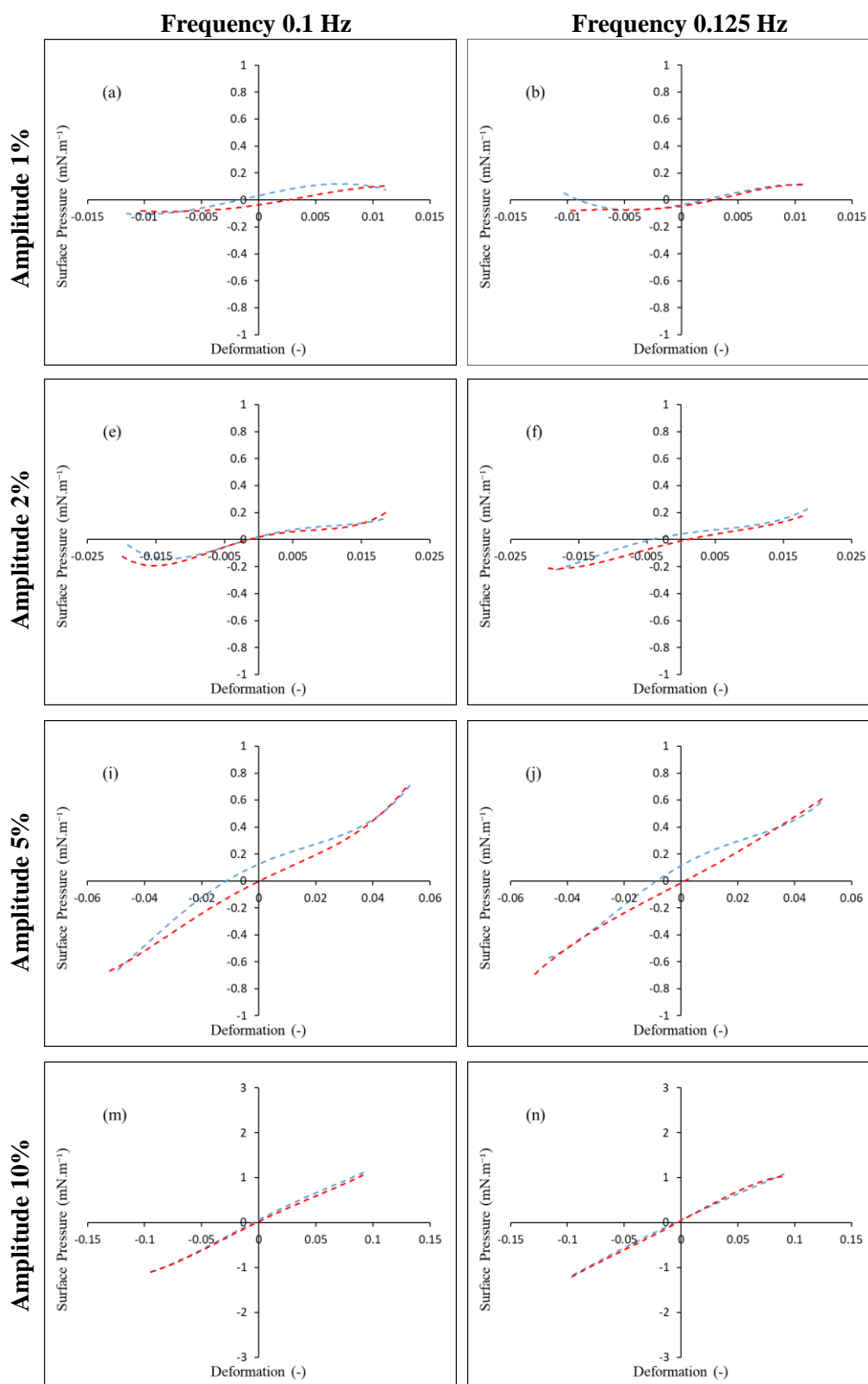


Figure C.20_Part 1 The fourth order polynomial curve fitted on the data of Lissajous plots for RTD 0.05 wt%+DPPC at the amplitudes of 1% (a-b), 2% (e-f), 5% (i-j), and 10% (m-n). The data were obtained for all frequencies including 0.1 Hz (left column) and 0.125 Hz (right column). The blue and red dashed lines are related to the expansion and compression, respectively.

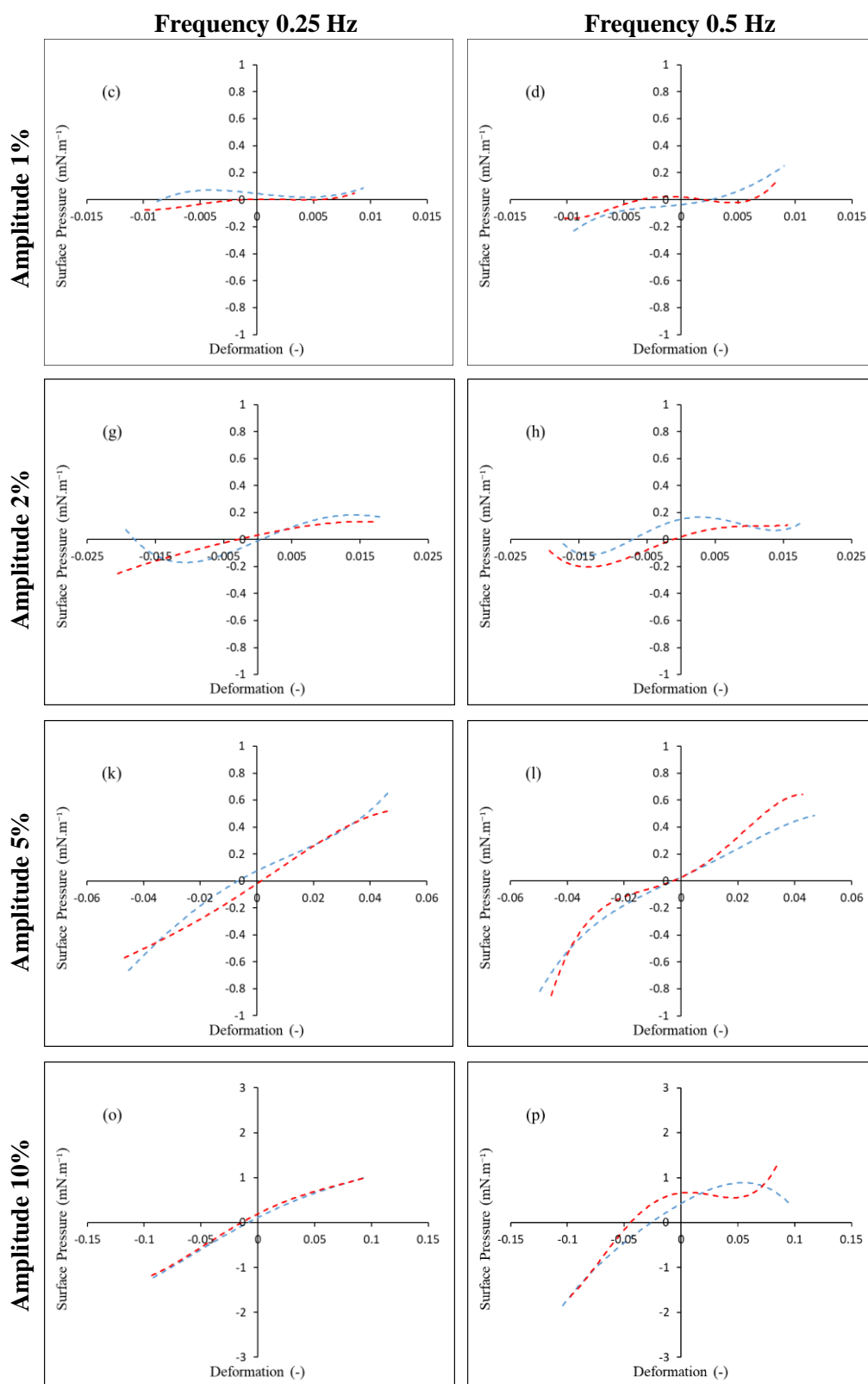


Figure C.20_Part 2 The fourth order polynomial curve fitted on the data of Lissajous plots for RTD 0.05 wt%+DPPC at the amplitudes of 1% (c-d), 2% (g-h), 5% (k-l), and 10% (o-p). The data were obtained for all frequencies including 0.25 Hz (left column) and 0.5 Hz (right column). The blue and red dashed lines are related to the expansion and compression, respectively.

Appendix D: Published Work